DTU Physics
Department of Physics

Spectroscopy Study of Low-dimensional Quantum Magnets

PhD Thesis

Wenjie Wan

Spectroscopy Study of Low-dimensional Quantum Magnets

PhD Thesis
September, 2021

By
Wenjie Wan

Published by: DTU, Department of Physics, Fysikvej, building 311, 2800 Kgs. Lyngby Denmark
https://www.fysik.dtu.dk
ISSN: [0000-0000] (electronic version)
ISBN: [000-00-0000-000-0] (electronic version)

ISSN: [0000-0000] (printed version)
ISBN: [000-00-0000-000-0] (printed version)

Approval

This thesis has been prepared over 2018-2021 at the Section for Neutrons and X-rays for Materials Physics (NEXMAP), Department of Physics, at the Technical University of Denmark, DTU, in partial fulfilment of the requirements for the degree of Ph.D. The study was funded by Department of Physics and beamtime travels were covered by the Danish Agency for Science and Higher Education under DANSCATT. The supervisors were Niels Bech Christensen from DTU physics, Kasper Steen Pedersen from DTU Chemistry and Henrik Moodysson Rønnow from EPFL.

It is assumed that the reader has a basic knowledge in the areas of quantum mechanics, condensed matter physics, magnetism and neutron scattering.

Wenjie Wan -

....

Signature

....

Date

Abstract

In this thesis the magnetic excitations in six low dimensional quantum magnets are investigated using inelastic neutron scattering complemented with thermodynamic measurements, such as magnetic susceptibility and specific heat.

- Cu(DCOO)$_2$·4D$_2$O (CFTD) is a two-dimensional $S = 1/2$ antiferromagnet on a square lattice. It is well established that in the low-temperature limit CFTD exhibits an anomaly in its spin excitation spectrum at short wavelengths on zone boundary. In the vicinity of the $(\pi, 0)$ the one-magnon excitation exhibits depression in energy, is strongly damped and attenuated. In particular, the attenuated spectral weight is transferred to an isotropic continuum of excitations extending to high energies. The origin of the anomaly is still under debate, particularly in relation to the existence of spinons in two dimensions. Here we present a study on the thermal evolution of the $(\pi, 0)$ anomaly up to finite temperatures $T/J \sim 2/3$. Our data reveal that the anomaly survives even in the absence of long-range, three-dimensional order and that it is thus a feature closely related to the two-dimensional $S = 1/2$ antiferromagnet on a square lattice. With further increase of temperature, the $(\pi, 0)$ anomaly is washed out as the zone-boundary excitations gradually softens and dampens. This is confirmed by a comparison of our data with a finite temperature Quantum Monte Carlo calculation where a good accord is found.

- It is well-established that, theoretically, magnons in a two-dimensional antiferromagnet on a square lattice exhibit spontaneous decays at high fields due to the non-zero interaction between the one-magnon branch and the two-magnon continuum. Such a decay of magnons has already been observed in a classical spin system. But the experimental evidence for magnon decays in a quantum case $S = 1/2$ is absent. Here we present the results of inelastic neutron scattering experiments and higher-order spin wave calculations on (5CAP)$_2$CuCl$_4$ (CAPCC), a quasi-two-dimensional $S = 1/2$ antiferromagnet on a square lattice with finite interlayer coupling, designed to study the field evolution of its spin excitations. Our data reveal that the one magnon response at vicinities close to $(\pi/2, \pi/2)$ dampens more heavily compared to $(\pi, 0)$ with an increasing field, in particular when the field approaches the saturation field of the system. Such an observation agrees with theoretical predictions. Compared to the higher-order spin wave results, the decays of one-magnon response are more pronounced in the experimental data. Such a discrepancy might due to the existence of other exchange interactions in the system. Nevertheless, our results provide the first experimental evidence for magnon decays in the two-dimensional $S = 1/2$ antiferromagnet on a square lattice.

- The quasi-two-dimensional honeycomb lattice antiferromagnet Na$_2$Co$_2$TeO$_6$ is proposed to be a possible platform for hosting Kitaev related physics. Here we present the results of inelastic neutron powder scattering experiments, designed to study the crystal field and spin excitations in Na$_2$Co$_2$TeO$_6$. Our analysis on the crystal field excitations reveals that the single-ion ground state for Co (II) is a spin-orbit mixed Kramers doublet characterized by an effective spin angular momentum $S_{\text{eff}} = 1/2$. Given the CoO$_6$ octahedra are arranged in an edge-sharing fashion, this confirms the potential of Na$_2$Co$_2$TeO$_6$ being a Kitaev material. The analysis of the spin excitations reveals that the Hamiltonian of Na$_2$Co$_2$TeO$_6$ deviates from a simple Heisenberg model. In particular, strong anisotropies are required to qualitatively explain the observed spectra. We analyzed the possibility of the spectra resembling a Heisenberg-Kitaev Hamiltonian. The result shows that the nearest neighbor in-plane Heisenberg interaction is heavily suppressed and significantly smaller than a

dominant ferromagnetic Kitaev interaction. This is in accord with theoretical predictions. In contrast to other similar studies, we present a complete analysis on the crystal field excitations.

- The magnetic properties of three metal-organic framework compounds, CrI$_2$(pyrazine)$_2$, GaCl$_2$(pyrazine)$_2$ and CrCl$_2$(pyrazine)$_2$ (pyrazine: C$_4$H$_4$N$_2$) are investigated. Despite the iso-structural relation, their electronic and magnetic properties vary substantially. CrI$_2$(pyrazine)$_2$ is a two-dimensional $S = 2$ antiferromagnet on a square lattice. The results of an inelastic neutron powder scattering experiment reveal that a gap ~ 0.1 meV is present in the spin wave spectrum and the data are best described by a $J_1 - J_2$ Heisenberg Hamiltonian with an easy-axis single-ion anisotropy. Unlike CrI$_2$(pyrazine)$_2$, magnetism in GaCl$_2$(pyrazine)$_2$ arises from the unpaired electrons on pyrazines. For every formula unit of GaCl$_2$(pyrazine)$_2$, an electron is transferred from Ga to one of the pyrazine ligands. Therefore GaCl$_2$(pyrazine)$_2$ manifests itself as a $S = 1/2$ system, which is supported by it magnetic susceptibility. Specific heat measurements reveal no formation of long-range order down to 2 K. The results of a polarized neutron powder diffraction experiment reveal that the total spin angular momentum $S(S+1)$ is in good accord with the $S = 1/2$ one-electron scenario. More rapid decay of the extracted magnetic form factor compared to $3d$ transition metals indicates the electron is spatially delocalized. This is consistent with the having electrons on pyrazine ligands picture. Both CrI$_2$(pyrazine)$_2$ and GaCl$_2$(pyrazine)$_2$ are well placed in an insulating limit. In contrast CrCl$_2$(pyrazine)$_2$ is electrically conductive at room temperature. Similar to GaCl$_2$(pyrazine)$_2$, the two pyrazine ligands in one formula unit of CrCl$_2$(pyrazine)$_2$ takes an electron away from the Cr ion. This gives rise to antiferromagnetically coupled Cr (III) and pyrazine spins. Below 55 K. the uncompensated $S = 1$ degree of freedoms are ferromagnetically coupled leading to a ferrimagnetic order. Results from inelastic neutron powder scattering reveal the only magnetic excitations of the system are below 1 meV. Compared to CrI$_2$(pyrazine)$_2$, the intensity of the excitations is significantly depressed. By tracking the Q-dependence of the excitation energy, a $\hbar\omega \propto Q^2$ relation is obtained. This is consistent with the ferromagnetic coupled $S = 1$ picture.

Resumé

I denne afhandling vil de magnetiske eksitationer i seks lavdimensionelle kvantemagneter blive undersøgt ved brug af inelastisk neutronspredning komplementeret af termodynamiske målinger såsom magnetisk susceptiblitet og specifik varmekapacitet.

- Cu(DCOO)$_2$·4D$_2$O (CFTD) er en todimensionel $S = 1/2$ antiferromagnet pådet kvadratiske gitter. I lavtemperatur-grænsen er det veletableret at CFTD har en anomalitet i dets spin eksitationsspektrum ved korte bølgelængder påzone grænsen. Enkelt-magnon eksitationen udviser i nærheden af $(\pi, 0)$ en dæmpning i energi, og er derudover stærkt dæmpet og attenueret. I særdeleshed er den attenuerede spektralvægt overført til et isotropt kontinuum af eksitationer, der fortsætter op til høje energier. Oprindelsen af anomalien er stadig til debat, særligt i relation til eksistensen af spinoner i to dimensioner. Her præsenterer vi et studie af den termiske udvikling af $(\pi, 0)$ anomalien op til endelige temperaturer, $T/J \sim 2/3$. Vores data afslører, at anomalien overlever selv ved manglen pålangtrækkende, tre-dimensionel orden, og er derfor nært relateret til den to-dimensionelle $S = 1/2$ antiferromagnet pådet kvadratiske gitter. Ved endnu højere temperaturer bliver $(\pi, 0)$ anomalien udvasket, da zonegrænseeksitationen langsomt bliver dæmpet. Dette er bekræftet ved en sammenligning af vores data med en endelig-temperatur kvante Monte Carlo udregning, der viser god overensstemmelse.
- Teoretisk set er det veletableret, at magnoner i en to-dimensionel antiferromgnet pådet kvadratiske gitter spontant henfalder ved høje felter pågrund af den endelige interaktion mellem enkelt-magnon eksitationen og to-magnon kontinuet. Et sådan henfald af magnoner er allerede blevet observeret i et klassisk spin system, men det eksperimentelle bevis for magnonhenfald i et kvantesystem med $S = 1/2$ mangler. Her præsenterer vi resultaterne af inelastiske neutronspredningsforsøg og højereordens spinbølgeudregninger på(5CAP)$_2$CuCl$_4$ (CAPCC), et kvasi-to-dimensionel $S = 1/2$ antiferromagnet pådet kvadratiske gitter med endelig koblinger mellem lagene, for at undersøge feltudviklingen af dets spineksitationer. Vores data viser, at enkelt-magnon responsen nær ved $(\pi/2, \pi/2)$ dæmpes kraftigere sammenlignet med $(\pi, 0)$ ved højere felter, i særdeleshed når feltet nærmer sig systemets mætningsfelt. Disse observationer er i overensstemmelse med teoretiske forudsigelser. Henfaldet af enkelt-magnon responsen er kraftigere i det eksperimentelle data sammenlignet med resultaterne fra højere-ordens spinbølge udregninger. Denne afvigelse kan stamme fra eksistensen af andre exchange interaktioner i systemet. Ikke desto mindre giver vores resultater det første eksperimentelle bevis for magnonhenfald i den to-dimensionelle $S = 1/2$ antiferromagnet pådet kvadratiske gitter.
- Den kvasi-to-dimensionelle antiferromagnet påhoneycomb-gitteret, Na$_2$Co$_2$TeO$_6$, er blevet foreslået som en mulig platform for Kitaev-relateret fysik. Her præsenterer vi resulaterne af inelastiske pulver neutronspredningseksperimenter, designet til at studere krystalfelterne og spineksitationerne i Na$_2$Co$_2$TeO$_6$. Vores analyse af krystalfeltseksitationerne afslører at enkelt-ion-grundtilstanden for Co(II) er en spin-orbit-blandet Kramers dublet, der er karakteriseret af et effektivt spin-angulært moment $S_{\text{eff}} = 1/2$. Det faktum, at CoO$_6$ oktaederne er arrangeret i en hjørnedelende facon understøtter Na$_2$Co$_2$TeO$_6$'s potentiale som Kitaev materiale. Analysen af spineksitationerne afslører, at Hamiltonen for Na$_2$Co$_2$TeO$_6$ afviger fra en simpel Heisenberg model. Særligt er kraftige anisotropier påkrævet for kvalitativt at forklare de observerede spektra. Vi analyserede muligheden for at spektrene lignede en Heisenberg-Kitaev Hamilton. Resultaterne viser, at interaktionen mellem de nærmeste naboer i planet er kraftigt undertrykt og markant mindre end

en dominerende ferromagnetisk Kitaev interaktion. Det stemmer overens med teoretiske forudsigelser. Vi præsenterer yderligere en komplet analyse af krystalfeltseksitationerne i modsætning til andre studier.

- Vi undersøger de magnetiske egenskaber af tre metal-organiske framework materialer, $\mathrm{CrI_2(pyrazin)_2}$, $\mathrm{GaCl_2(pyrazin)_2}$ og $\mathrm{CrCl_2(pyrazin)_2}$ (pyrazin: $C_4H_4N_2$). Deres elektroniske og magnetiske egenskaber varierer påtrods af deres isostrukturalitet. $\mathrm{CrI_2(pyrazin)_2}$ er en to-dimensionel $S = 2$ antiferromagnet pådet kvadratiske gitter. Resultaterne af et inelastisk pulver neutronspredningseksperiment afslører at et gab ~ 0.1 meV er tilstede i spinbølgespektret, og at data bedst beskrives af en $J_1 - J_2$ Heisenberg Hamilton med en easy-axis enkelt-ionsanistropi. Modsat $\mathrm{CrI_2(pyrazin)_2}$, såopstår magnetismen i $\mathrm{GaCl_2(pyrazin)_2}$ fra de uparrede elektroner i pyrazinerne. For hver formelenhed af $\mathrm{GaCl_2(pyrazin)_2}$, såoverføres der en Ga til en af pyrazin liganderne. Derfor manifesterer $\mathrm{GaCl_2(pyrazin)_2}$ sig som et $S = 1/2$ system, hvilket er understøttet af dens magnetisk susceptibilitet. Specifik varmekapacitetsmålinger afslører ingen langtrækkende orden ned til 2 K. Resultaterne af et polariseret inelastisk pulver neutronspredsningseksperiment afslører, at det totale spin-angulære moment $S(S+1)$ er i god overensstemmelse med $S = 1/2$ enkelt-elektron scenariet. Hurtigere henfald af den ekstraherede magnetisk formfaktor sammenlignet med $3d$ overgangsmetallerne indikerer at elektronen er rumligt delokaliseret. Det er konsistent med billedet af elektroner påpyrazin liganderne. Både $\mathrm{CrI_2(pyrazin)_2}$ og $\mathrm{GaCl_2(pyrazin)_2}$ er placeret fint i den isolerende grænse. Modsat er $\mathrm{CrCl_2(pyrazin)_2}$ elektrisk ledende ved studetemperatur. Ligesom i $\mathrm{GaCl_2(pyrazin)_2}$, såtager de to pyrazin-ligander i en formelenhed af $\mathrm{CrCl_2(pyrazin)_2}$ en elektron væk fra Cr-ionen. Det giver ophav til antiferromagnetisk koblet Cr(III) og pyrazin spins. De ukompenserede $S = 1$ frihedsgrader er ferromagnetisk koblet, hvilket leder til en ferrimagnetisk orden under 55 K. Resultater fra inelastisk pulver neutronspredning viser, at kun de magnetisk eksitationer i systemet er under 1 meV. Sammenlignet med $\mathrm{CrI_2(pyrazin)_2}$, såer intensiteten af eksitationerne undertrykt signifikant. Vi finder en $\hbar\omega \propto Q^2$ relation ved at undersøge Q-afhængigheden af eksitationsenergien. Dette er konsistent med det ferromagnetisk koblede $S = 1$ billede.

Acknowledgements

First of all, I would like to express my gratitude to my supervisor Niels Bech Christensen. Thanks for offering me the opportunity of this Ph.D. and guiding me throughout the past three years. I would also like to thank my co-supervisors Kasper Steen Pedersen for providing interesting MOF materials, and Henrik Moodysson Rønnow for allowing me to use the PPMS at EPFL and for the welcomeness during my stay at EPFL.

Many thanks to the beamline scientists who assisted me in setting up and running experiments. Without your help, it is impossible to finish this thesis. I would especially like to thank Duc Le, Alex Buts, and Toby Perring for teaching me how to use Horace and SpinW, and for their patience with my stupid questions. I would also like to thank Gøran Nilsen. Thanks for teaching me how to do fitting using SpinW and for always be patient with my questions. I would also like to thank the people I have been collaborated with during this Ph.D. Many thanks to Des McMorrow and Martin Mourigal for their help with the CFTD and CAPCC projects. Thanks to Anders Sandvik for providing QMC calculations on CFTD. Many thanks to Laura Voigt and Mariusz Kubus for synthesizing the MOF materials and for being good companies during beamtime. Thanks to Hua Chen for synthesizing 7 grams of $GaCl_2(pyz)_2$. Without your effort, the D7 experiment would be even more difficult.

At NEXMAP, thanks to Hanne Sørensen for assisting me in sorting out the new work permit application. Thanks to Peter Willendrup for setting up panda2 and Intel compilers. Thanks to Erik Bergbäck Knudsen for sharing many funny stories with me. The one with watermelon is my favourite. Thanks to Kristoffer Haldrup for giving me a ride from Lyon airport to Grenoble in the corona time, for the help during the stay (a thousand thanks for borrowing me a charger!), and for sharing very interesting and exciting X-rays physics during lunchtime at ILL. I would like to thank Mads Allerup Carlsen for always inviting me and other PhDs from the section out for cakes and board games. It was such a fun time with you all. I would also like to thank Mathias Huss-Hansen for being the best office mate. I enjoyed every time we had lunch together and it was always so much fun talking with you. Last but not the least, I would like to thank Sofie Janas for the translation of the abstract and for being supportive when I was super stressed with writing my thesis.

To my friends. Sercan, Simona, and Andreas, thanks for being supportive and always being there for me.

Finally, I want to thank my parents who have always been very supportive of my choices. Even though I live on the other side of the globe you have always been there for me. I want to especially thank my mom, thanks for always believing in me when no one else did. Without you, I could never ever get this far.

Contents

Preface . . . ii
Abstract . . . iii
Abstract . . . v
Acknowledgements . . . vii

1 Elements of Magnetism in Transition Metal Elements 1
1.1 Isolated transition metal ions . . . 1
1.2 Transition metal ions in crystals . . . 4
1.3 Magnetic ordering . . . 13
1.4 Magnetic excitations . . . 14

2 Elements of Neutron Scattering 17
2.1 Basic properties of the neutron . . . 17
2.2 Neutron-matter interaction . . . 17
2.3 Neutron scattering cross-sections . . . 18
2.4 Polarized neutrons . . . 23

3 Experimental Techniques 27
3.1 Thermodynamic material characterization methods . . . 27
3.2 Neutron scattering experiments . . . 28

4 Quantum Square Lattice Antiferromagnet 35
4.1 Temperature dependence of the excitation spectrum in a quantum square lattice antiferromagnet CFTD . . . 37
4.2 Field induced magnon decay on a quantum square lattice antiferromagnet CAPCC . . . 56

5 Possible Kitaev Physics in a d^7 Compound $Na_2Co_2TeO_6$ 91
5.1 Realization of the Kitaev model in d^7 cobalt compounds . . . 91
5.2 Crystal and magnetic structures of $Na_2Co_2TeO_6$ . . . 92
5.3 Experimental details . . . 94
5.4 Results and analysis . . . 94
5.5 Discussion and Conclusions . . . 111

6 Tailoring Magnetism by Metal-organic Framework Engineering 115
6.1 A ligand innocent quasi-2D antiferromagnet square lattice $CrI_2(pyz)_2$ . . . 115
6.2 Ligand non-innocence in $GaCl_2(pyz)_2$ . . . 126
6.3 Ligand non-innocent ferrimagnet $CrCl_2(pyz)_2$ . . . 138
6.4 Conclusions . . . 149

Bibliography 153

1 Elements of Magnetism in Transition Metal Elements

The main theme of this thesis is the magnetism of solids containing $3d$ transition elements. These materials show extremely diverse properties. Among them there are insulators, metals and superconductors with the highest critical temperature known to date. Many of these materials are magnetic but with surprisingly diverse behaviors, which provides a fantastic playground for fundamental studies of magnetism and searches for new exotic physics.

Part of the reason for the special behavior of these compounds is the strong Coulomb interaction between electrons in their partially filled $3d$-shells which tends to make them localized in space. Beyond that, when embedding these elements into a lattice their electronic degrees of freedom will be strongly modified by the neighbouring ligands, causing a change of the ground states compared to the free ion situations. In addition, the lattice degree of freedom (geometrical aspects such as dimensionalities and lattice types) will also affect how the neighbouring $3d$ transition metal ions interact with each other, hence modifying the physical properties of the compounds. Thus in general the physics involved behind the scene is quite complex as many degrees of freedom: spin, orbital and lattice, are intertwined.

This chapter tries to provide a coherent introduction to all the essential fundamental aspects relating to work performed in this thesis. As we approach the problems from a localized electron perspective, we will start by introducing the basic aspects of atomic physics from which many notations are adopted throughout the thesis. The energy spectrum of a free $3d$ transition metal ion will also be introduced as it is important to identify what is the relevant energy scale for the study at hand and the experimental techniques being used. Afterwards the free elements will be put into a more realistic environment as in solids where they are surrounded by ligands such as Oxygen and Sulphur. The static electric field produced by the ligands is called the *crystalline electric field* or CEF and we will show how it affects the energy spectrum in detail and what are the consequences. With the help of the so-called *Stevens operator formalism*, the CEF-modified single-ion magnetization and magnetic susceptibility can be calculated and compared with experimental data. In solids the transition metal ions are not completely isolated hence they may influence each other via exchange interactions. These are responsible for the development of magnetic ordering upon cooling. Last but not least, thanks to the exchange interactions, the spins on the transition metal elements can rotate collectively forming a so called *spin wave excitation* provided the ground state is magnetically ordered. In some cases [1] a single spin wave excitation can even fractionlize into two $S = 1/2$ objects, forming a so-called spinon pair.

1.1 Isolated transition metal ions

The theories presented in Section 1.1 and 1.2.1 form the theoretical basis for two MATLAB packages the author made during this PhD. They are later used to perform the analysis presented in Section 5.4.1.

In this section we will discuss the electronic states of a free transition metal ion. For detail treatments, they can be found in Refs [2, 3, 4, 5].

The state of an electron in an atom is characterized by four quantum numbers:

- The principle quantum number n.
- The orbital angular momentum l: $l \leq n-1$.
- The z-component of the orbital angular momentum m: $-l \leq m \leq l$.
- The z-component of spin σ : $\sigma = \pm\frac{1}{2}$ or ↑ and ↓.

The shells corresponding to different values of l are usually denoted as follow: s-shell for $l = 0$, p-shell for $l = 1$ and d-shell for $l = 2$. For $3d$-transition metal elements ($n = 3$), only the partially filled $3d$-shell is of interest as the inner shells are situated deeply below the Fermi level so that they are completely irrelevant or inert for the physics under consideration.

We start by introducing the Fermionic creation (annihilation) operator $c^\dagger_{n,l,m,\sigma}$ ($c_{n,l,m,\sigma}$) which creates (annihilates) an electron with principle quantum number n, orbital angular momentum l whose z-component is m, and z-component of spin σ. For brevity, we contract (n,l,m,σ) to a single index v for $3d$ transition metals, so that $c^\dagger_v = c^\dagger_{n=3,l=2,m,\sigma}$. The procedure adopted here is degenerate first order perturbation theory [4, 3]. The unperturbed Hamiltonian H_0 is the energy of $3d$-shell

$$H_0 = \epsilon_{3d} \sum_v c^\dagger_v c_v, \tag{1.1}$$

whereas the Coulomb interaction between two electrons is considered as the perturbation H_1. In second quantization, it takes the form

$$\begin{aligned} H_1 &= \frac{1}{2} \sum_{v_i,v_j,v_k,v_l} V(v_i,v_j,v_k,v_l) c^\dagger_{v_i} c^\dagger_{v_j} c_{v_k} c_{v_l} \\ V(v_1,v_2,v_3,v_4) &= \int dx \int dx' \psi^*_{v1}(x) \psi^*_{v2}(x') V_c(x,x') \psi_{v3}(x') \psi_{v4}(x) \\ V_c(x,x') &= \frac{1}{|\mathbf{r}-\mathbf{r}'|} \end{aligned} \tag{1.2}$$

Here $x = (\mathbf{r}, \sigma)$ is the combined spatial and spin coordinate with $\int dx \cdots = \sum_\sigma \int d\mathbf{r} \cdots$ and V_c is the Coulomb interaction between electrons.

For a $3d$ element with configuration d^n, all the possible states are obtained by distributing the n electrons over the 10 (2×5) spin-orbitals $|v\rangle = c^\dagger_{v1} c^\dagger_{v2} ... c^\dagger_{vn} |0\rangle$. The number of such n-electron states is $n_c = \frac{10!}{(10-n)!n!}$. If only H_0 is present, these n_c states are degenerate. The Coulomb interaction H_1 lifts this degeneracy and hence gives rise to a so-called multiplet splitting. To see this, we need to set up the matrix $h_{v_1,v_2} = \langle v_1 | H_1 | v_2 \rangle$ and diagonalize it to obtain the first order energies and wave functions. Using the multipole expansion of the Coulomb interaction, the Coulomb matrix element can be expressed as

$$\begin{aligned} V(v_1,v_2,v_3,v_4) =& \delta_{\sigma_1,\sigma_4} \delta_{\sigma_2,\sigma_3} \delta_{m1+m2,m3+m4} \times \\ & \sum_{k=0}^{\infty} c^k(l_1m_1;l_4m_4) c^k(l_3m_3;l_2m_2) R^k(n_1l_1,n_2l_2,n_3l_3,n_4l_4) \end{aligned} \tag{1.3}$$

where $c^k(l_1m_1;l_4m_4)$ and $c^k(l_3m_3;l_2m_2)$ are the Gaunt coefficients and $R^k(n_1l_1,n_2l_2,n_3l_3,n_4l_4)$ is an integral of the radical part of single electron wave functions, which has the dimension

Energy [eV]	S	L	Degeneracy	Term
0.0000	3/2	3	28	^4F
1.8000	3/2	1	12	^4P
2.1540	1/2	4	18	^2G
2.7540	1/2	5	22	^2H
2.7540	1/2	1	8	^2P
3.0545	1/2	2	10	^2D
4.5540	1/2	3	14	^2F
7.3255	1/2	2	10	^2D

Table 1.1: Energies of the $3d^7$ multiplets calculated with $R^2 = 9.7860$ eV ans $R^4 = 7.0308$ eV [3]. The standard notation of atomic terms is $^{(2S+1)}L_J$ where $2S+1$ is the spin multiplicity, L is the total orbital angular momentum and J is the total angular momentum $\mathbf{J} = \mathbf{L} + \mathbf{S}$ [7]. Conventionally $L = 0$ is denoted as S, $L = 1$ is P, $L = 2$ is D, etc.

	For an ion with several electrons on the same atomic levels
First Hund's rule	The electrons fill the levels so as to make the largest possible total spin S.
Second Hund's rule	Among the different possible configurations with the same maximal S, the configuration with the largest possible total orbital angular momentum L is the ground state.
Third Hund's rule	Due to spin-orbit coupling, the total orbital angular momentum L will mix with the total spin angular momentum S and produce a total angular momentum $\mathbf{J} = \mathbf{L}+\mathbf{S}$ characterized by the quantum number J. For the levels are less than half-filled, J takes the value $J = \lvert L - S\rvert$ whereas J is the maximum $J = \lvert L + S\rvert$ when the levels are more than half-filled.

Table 1.2: The three Hund's rules

of energy (eV).

$$c^k(lm; l'm') = (-1)^m \sqrt{\frac{4\pi}{2k+1}} \int_0^{2\pi} d\phi \int_{-1}^{1} d\cos(\theta) Y_{l,-m}(\theta,\phi) Y_{k,m-m'}(\theta,\phi) Y_{l'm'}(\theta,\phi) \tag{1.4}$$

Within a d-shell, only R^0, R^2 and R^4 [3] are relevant [4, 3] and the eigen-energy differences depend only on R^2 and R^4. The algorithm for calculating integral of three spherical harmonics in Eq.(1.4) can be found in Ref [6].

As an example, here we calculated the resulting multiplet energies for Co^{2+} ($3d^7$) with $R^2 = 9.7860$ eV and $R^4 = 7.0308$ eV, see Table 1.1. The resulting ground state is 28 fold degenerate and has maximal spin and maximal orbital angular momenta, which indeed complies with the first two Hund's rules, see Table 1.2. Notice that the energy difference between the ground state and the first excited state is of the order ~ 2 eV, much larger than the energy scale [meV] encountered in a normal neutron scattering experiment (will come back to this in the next chapter).

In addition to the Coulomb interaction between electrons in the $3d$-shell, the orbital angular

Energy [eV]	S	L	J	Degeneracy	Term
0.0000	1.4990	3.0015	9/2	10	$^4F_{9/2}$
0.0769	1.4997	3.0004	7/2	8	$^4F_{7/2}$
0.1344	1.4996	2.9995	5/2	6	$^4F_{5/2}$
0.1742	1.4991	2.9990	3/2	4	$^4F_{3/2}$

Table 1.3: Splitting of the ground state ^4F for $3d^7$ under spin-orbit coupling with $\lambda_{\text{SO}} = 0.05$ eV.

momentum can couple to the spin angular momentum via spin-orbit coupling

$$\begin{aligned}
H_{\text{SO}} =& \lambda_{\text{SO}} \sum_{i=1}^{n} \mathbf{l}_i \cdot \mathbf{s}_i = \lambda_{\text{SO}} \sum_{i=1}^{n} \left(l_i^z s_i^z + \frac{1}{2} \left(l_i^+ s_i^- + l_i^- s_i^+ \right) \right) \\
=& \lambda_{\text{SO}} \sum_{m=-l}^{l} \frac{m}{2} \left(c_{l,m,\uparrow}^\dagger c_{l,m,\uparrow} - c_{l,m,\downarrow}^\dagger c_{l,m,\downarrow} \right) + \\
& \frac{\lambda_{\text{SO}}}{2} \sum_{m=-l}^{l-1} \sqrt{(l-m)(l-m+1)} \left(c_{l,m+1,\downarrow}^\dagger c_{l,m,\uparrow} + c_{l,m,\uparrow}^\dagger c_{l,m+1,\downarrow} \right)
\end{aligned} \tag{1.5}$$

where the summation is over all $3d$ electrons, $\mathbf{l}_i$, $\mathbf{s}_i$ are the operators for orbital and spin angular momenta of ith electron, λ_{SO} is an element dependent spin-orbit coupling constant. For $3d$-shell, the spin-orbit coupling constant λ_{SO} is rather small, of the order ~ 0.05 eV [8, 3]. Due to the coupling between **l** and **s**, the *total* spin ($\mathbf{S} = \sum_{i=1}^{n} \mathbf{s}_i$) and orbital ($\mathbf{L} = \sum_{i=1}^{n} \mathbf{l}_i$) angular momenta are no longer good quantum numbers. Instead a new conserved quantity, the total angular momentum is defined $\mathbf{J} = \mathbf{L} + \mathbf{S}$. As an example, we assume the spin-orbit coupling constant for Co^{2+} to be 0.05 eV and in Table 1.3 we list the splittings of the ground state manifold ^4F (the excited states are well above the ground state and can be ignored). Evidently, both S and L are no longer conserved and fluctuate around $S = 3/2$ and $L = 3$ respectively. The value of J decreases with the increase of the state energy. For the new ground state J is fully maximized ($J = L + S$), which is in accord with Hund's third rule, see Table 1.2.

1.2 Transition metal ions in crystals

In the last section we only discussed the electronic properties of isolated transition metal ions. Now we turn to a more realistic scenario where the ions are embedded in solids. Normally they are locked in different polyhedron cages, such as tetrahedra and octahedra, of which the vertices are placed with ions (ligands) such as Oxygen or Sulfur. In principle there are two effects need to be considered: the static electric field produced by ligands, the so-called *crystalline electric field* or CEF, and the charge transfer between transition metal ions and ligands due to the overlapping of their wavefunctions. For now we will focus on the treatment of CEF, and will comment on the charge transfer process at the end of Section 1.2.1.

The simplest approximation one can come up with is treating all the ligands as point charges. Similar to the Coulomb interaction discussed previously, application of the mul-

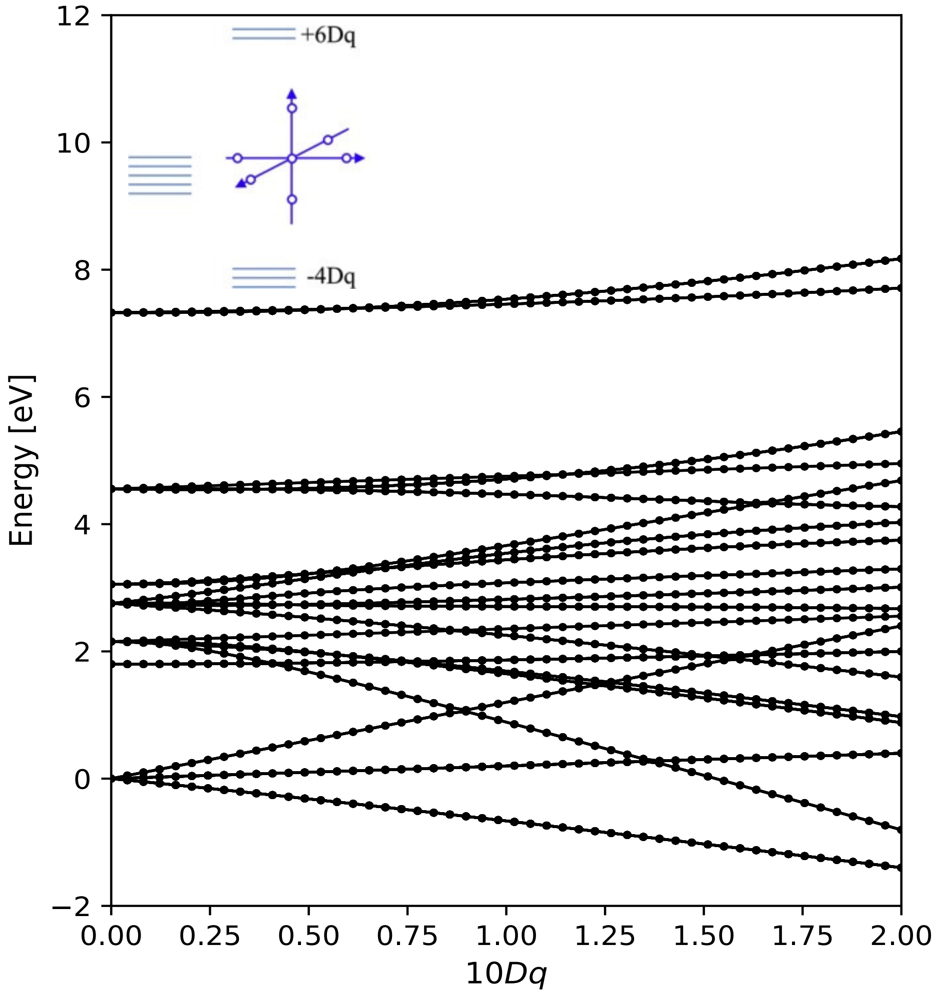

Figure 1.1: Splitting of the multiplets in $3d^7$ with $R^2 = 9.7860$ eV and $R^4 = 7.0308$ eV under an ideal octahedral crystal field whose strength is characterized by $10Dq$ (in eV). At $10Dq = 0$ eV, from bottom to top (in energy), the illustrated seven energy levels correspond to the eight eigenstates listed in Table 1.1, i.e. $^4F \rightarrow ^2D$. The two states ^2H and ^2P are degenerate as seen in Table 1.1, hence only seven energy levels are shown in the figure. The inset [9] illustrates the splitting of the five degenerate d-orbitals into the lower t_{2g} manifold and the higher e_g manifold in an ideal octahedral crystal field with energies $-4Dq$ and $6Dq$ respectively.

tipole expansion yields the CEF Hamiltonian

$$H_{\text{CEF}} = \sum_{l_1,l_2} \sum_{m_1=-l_1}^{l_1} \sum_{m_2=-l_2}^{l_2} \sum_{k=0}^{\infty} \sum_{-m}^{m} A_{k,m} \langle Y_{l_1,m_1}(\theta,\phi)| \sqrt{\frac{4\pi}{2k+1}} Y_{k,m}(\theta,\phi) |Y_{l_2,m_2}(\theta,\phi)\rangle \times c^{\dagger}_{l_1,m_1,\sigma} c_{l_2,m_2,\sigma} \tag{1.6}$$

where the coefficients $A_{k,m}$ depend on the symmetry of the crystal. For a cubic symmetry group (O_h) where an $3d$-element sits in the center of an octahedral cage, the only non-vanishing terms are [3]:

$$\begin{aligned} A_{4,0} &= \frac{21}{10} \times 10Dq \\ A_{4,4} = A_{4,-4} &= \frac{3}{2}\sqrt{\frac{7}{10}} \times 10Dq \end{aligned} \tag{1.7}$$

and $10Dq$ is the energy splitting of the $3d$-orbitals under an octahedral CEF, of which the higher and lower energy ones are called e_g ($d_{x^2-y^2}$, $d_{3z^2-r^2}$) and t_{2g} (d_{xy}, d_{xz}, d_{yz}) [10] respectively. In Fig.1.1, we show the splitting of multiplets for a d^7 ion Co (II) for increasing $10Dq$. Noticeably, even when $10Dq$ is as large as 2 eV, the newly formed ground state still belongs to the previously identified ground state ^4F obtained in the absence of CEF. From the calculation, the degeneracy of the new ground state is found to be 12 and its spin angular momentum is $S = \frac{3}{2}$. Moreover the orbital angular momentum of the new ground state is calculated to be 3 fold degenerate. Thus we can assign an effective angular momentum $l_{\text{eff}} = 1$ to the ground state. The two quantum numbers (S, l_{eff}) complies with the found 12-fold degeneracy of the new ground state ($(2l_{\text{eff}} + 1)(2S + 1) = 12$).

As illustrated in Fig.1.1, when excluding the spin-orbit coupling λ_{SO} of $3d$ electrons, the ground states of the transition metal ions in solids are one of the CEF-split states from the ground state manifolds obtained in the isolated ion limit. With the further inclusion of the spin-orbit coupling λ_{SO}, the CEF-present ground state manifolds of the transition metal ions continue splitting. Due to the comparable strength of CEF and the spin-orbit coupling λ_{SO} for $3d$ transition metals, the first few low lying states after the splitting still belong to the ground state manifolds obtained in the isolated ion limit. For neutron scattering, it is the transitions between these low lying states that are probed. Hence is there a way to effectively describe that how the ground states obtained in the isolated ion limit split under SOC and CEF when embedding $3d$-elements in solids, without invoking the full-fledged formalism as explained in Section 1.1 and 1.2 and in the meantime still give interpretable results? The *Stevens operators formalism* is the answer.

1.2.1 Stevens operators and crystal field splitting

In this section, we will introduce the Stevens operator formalism [11, 12, 13] and present general formulas for calculation crystal field parameters using a point charge model [11, 14].

When restricted to the ground state of a given $3d$-element obtained in the isolated ion limit, the orbital and spin angular momentum **L**, **S** are fixed. Here we work in the so-called intermediate coupling scheme where $|L, m_l, S, m_s\rangle$ are chosen as the basis states. Stevens showed [12] that in such a scenario the CEF Hamiltonian can be equivalently written as a summation of the so-called *Stevens operators* $\hat{O}_n^m$ [12, 11, 8], composed of polynomial sums of $\{L_x, L_y, L_z, L\}$ up to order n

$$H_{\text{CEF}} = \sum_{n} \sum_{m=-n}^{n} B_n^m \hat{O}_n^m \tag{1.8}$$

where n is the rank of the operator and the associated crystal field parameters B_n^m are real numbers. Hermiticity and time reversal invariance of the CEF Hamiltonian ensures that only crystal field parameters of even rank are non-zero [13]. Hence for $3d$-shell elements n takes the values 0, 2, 4 and only the last two determine how large the energy splittings are [11, 13]. The parameters B_n^m can usually be fitted to experimental data or calculated from a point charge model as a starting point of the fit.

In a point charge model [11, 14], as the name suggests the surrounding ligands are treated as static point charges and the crystal field parameters are (in units of meV)

$$B_n^m = -\frac{a_0^n}{4\pi\epsilon_0}\gamma_{nm} N_Z F_{nm} \langle r^n \rangle \theta_n \times 10^3 \tag{1.9}$$

where ϵ_0 is the vacuum permittivity (in units $e^2 \cdot \text{GeV}^{-1} \cdot \text{fm}^{-1}$), a_0 is the Bohr radius and N_Z is the number of unpaired electrons on the central ion. $\langle r^n \rangle$ is the expectation value of the radial wavefunction (in units a_0^n and the values for all $3d$ transition elements are reported in [8]). F_{nm} are numerical factors occurring in the tesseral harmonics $Z_{nm}(x, y, z)$, e.g. $F_{20} = \frac{1}{4}\sqrt{\frac{5}{\pi}}$ for $Z_{20}(x, y, z) = \frac{1}{4}\sqrt{\frac{5}{\pi}} \cdot \frac{3z^2 - r^2}{r^2}$. γ_{nm} is a weighted summation of tesseral harmonics over all ligands

$$\gamma_{nm} = \sum_{j=1}^{N} \frac{4\pi}{2n+1} q_j \frac{Z_{nm}(x_j, y_j, z_j)}{R_j^{n+1}} \tag{1.10}$$

where N is the number of ligands under consideration, q_j is the charge (in units e) carried by the ligand j and R_j (in units Å) is the distance between the central ion and the ligand j. The last term θ_n in Eq.(1.9) is a multiplicative factor associated with the orbital angular momentum of the central ion.

Apart from θ_n, all the other parameters in Eq.(1.9) can be easily obtained. In the following, we present a general scheme to numerically evaluate the value of θ_n for different electron configurations.

We again take the Co^{2+} ion as an example, which has seven electrons in its $3d$-shell and has a free ion ground state characterized by $L = 3$ and $S = 3/2$. Further assume that the ion is in a maximally polarized state with $L_z = L = 3$ and $S_z = S = 3/2$. From the operator equivalents [12, 15] it follows

$$\begin{aligned} \sum_i \frac{Z_{n0}(x_i, y_i, z_i)}{F_{n0}} \cdot r_i^n &\equiv \theta_n \langle r^n \rangle \left\langle L, L \right| \hat{O}_n^0 \left| L, L \right\rangle \\ \sum_i \frac{Z_{n0}(x_i, y_i, z_i)}{F_{n0}} \cdot r_i^n &\equiv \tilde{\gamma} \sum_i \left\langle l, m_l^i \right| \hat{O}_n^0 \left| l, m_l^i \right\rangle \end{aligned} \tag{1.11}$$

where $\tilde{\gamma}$ is a constant depending on an angular momentum l. The first equation is obtained when the left-hand side is evaluated in a manifold with $L = 3$ and the second equation is valid in a manifold with $l = 2$ (d electrons). The index i indicates the ith unpaired electron and the corresponding orbital angular momentum is m_l^i. For Co (II), m_l^i take values 2, 1 and 0 for electron $i = 1$, 2 and 3 respectively. To find $\tilde{\gamma}$, assume that an electron is in a $|l, m_l = l\rangle$ state. Again from the operator equivalents [12, 15] the following identity holds

$$\begin{aligned} \frac{Z_{n0}(x, y, z)}{F_{n0}} r^n &= \frac{(-1)^l \int_0^{2\pi} d\phi \int_{-1}^{1} d\cos(\theta) Y_{l,-l}(\theta, \phi) Y_{n,0}(\theta, \phi) Y_{l,l}(\theta, \phi)}{F_n^0} \langle r \rangle^n \\ &= \tilde{\gamma} \left\langle l, l \right| \hat{O}_n^0 \left| l, l \right\rangle \end{aligned} \tag{1.12}$$

B_n^m	Value [meV]
B_4^0	-0.7165
B_4^4	-3.5825

Table 1.4: The non-vanishing crystal field parameters B_n^m for a Co^{2+} ion in an ideal octahedral crystal field composed of O^{2-}..

from which the analytical expression for $\tilde{\gamma}$ can be derived

$$\tilde{\gamma} = \frac{(-1)^l \int_0^{2\pi} d\phi \int_{-1}^{1} d\cos(\theta) Y_{l,-l}(\theta,\phi) Y_{n,0}(\theta,\phi) Y_{l,l}(\theta,\phi)}{F_n^0 \langle l,l| \hat{O}_n^0 |l,l\rangle} \langle r\rangle^n \tag{1.13}$$

and the evaluation of the integral in the nominator can be found in Ref [6]. Combining Eq.(1.11) with Eq.(1.13), we arrive at the general formula for θ_n.

$$\theta_n = \frac{\sum_i \langle l,m_l^i| \hat{O}_n^0 |l,m_l^i\rangle}{\langle L,L| \hat{O}_n^0 |L,L\rangle} \cdot \frac{(-1)^l \int_0^{2\pi} d\phi \int_{-1}^{1} d\cos(\theta) Y_{l,-l}(\theta,\phi) Y_{n,0}(\theta,\phi) Y_{l,l}(\theta,\phi)}{F_n^0 \langle l,l| \hat{O}_n^0 |l,l\rangle} \tag{1.14}$$

For Co^{2+}, the only non-vanishing terms are θ_2 and θ_4 and their values are $\theta_2 = -0.0190476$ and $\theta_4 = -0.00634921$ respectively.

Having introduced the Stevens operator formalism and the calculation of the related crystal field parameters B_n^m from a static point charge perspective, now we will show how to use them in practice. As an example, we consider a Co^{2+} ion ($3d^7$ with three unpaired electrons) sitting in the center of an ideal octahedron surrounded by six O^{2-}. The global Z axis is chosen such that it aligns with a four-fold rotation axis of the octahedron. The Co^{2+} is at the origin. Hence the coordinates of the six oxygen ions are: $(\pm a, 0, 0)$, $(0, \pm a, 0)$ and $(0, 0, \pm a)$ and here we set $a = 2$ Å. Application of Eq.(1.9)-(1.14), the only non-vanishing terms are B_4^0 and B_4^4. Their values are listed in Table 1.4. The ratio $B_4^4/B_4^0 = 5$ coincides with the group theory result [16].

In Table 1.5, we list the splittings of the ground state ^4F of Co^{2+} for the determined crystal field parameters. The new ground state is 12-fold degenerate and from the calculation, its orbital angular momentum can be written as $\mathbf{L} = -\frac{3}{2}\mathbf{l}_{\text{eff}}$ with $l_{\text{eff}} = 1$. When further including the spin-orbit coupling $H_{\text{SO}} = \lambda_{\text{SO}}\mathbf{L}\cdot\mathbf{S}$, the 12-fold degenerate ground state splits into three states, see Table 1.6 and Fig.(1.2), characterized by an effective total angular momentum j_{eff}. This is because the ground state has an effective angular momentum $l_{\text{eff}} = 1$ and a spin angular momentum $S = 3/2$. Owing to the minus sign in $\mathbf{L} = -\frac{3}{2}\mathbf{l}_{\text{eff}}$, even though the d-shell is more than half-filled, the total angular momentum for the lowest energy state is $j_{\text{eff}} = |l_{\text{eff}} - S| = \frac{1}{2}$ and $|l_{\text{eff}} + S| = \frac{5}{2}$ for the highest excited state. This is in contrast to the third Hund's rule. The two-fold $j_{\text{eff}} = \frac{1}{2}$ state is a *Kramers doublet* where the two degenerate states are related by time reversal symmetry [8].

As a final remark, the crystal field parameters extracted from fitting to experimental data contains the contributions from both the charge transfer process between transition metal ions and ligands, and the static electric field generated by ligands. This is in contrast to the crystal field parameters calculated from a point charge model, in which only the static electric field effect is considered. Hence the Stevens operator formalism can be regarded as an effective Hamiltonian for describing the single-ion properties of transition elements in solids.

Energy [meV]	Degeneracy
0.0000	12
343.9258	12
773.8332	4

Table 1.5: Splitting of the ground state ^4F for a Co^{2+} ion in an ideal octahedral crystal field composed of O^{2-}, which corresponds to the three splittings from the ground state ^4F with increasing $10Dq$ in Fig.1.1. Notice as long as $10Dq$ is smaller than 0.75 meV as illustrated in Fig.1.1, the three splittings are the three lowest eigenstates.

Energy [meV]	Degeneracy	j_{eff}
0.0000	2	1/2
40.7129	4	3/2
110.6266	6	5/2

Table 1.6: Futher splitting of the 12-fold degenerate ground state manifold shown in Table 1.5 upon the spin-orbit coupling $\tilde{\lambda}_{\text{SO}} = -22$ meV.

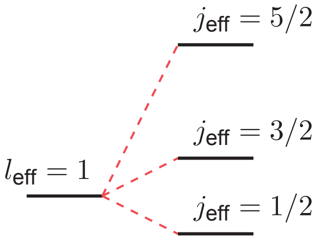

Figure 1.2: Splitting of the $l_{\text{eff}} = 1$, $S = 3/2$ ground state due to spin-orbit coupling. The resulting three states are characterized by j_{eff}: 1/2, 3/2 and 5/2 as listed in Table 1.6.

1.2.2 Magnetization and magnetic susceptibility

It can be useful to calculate the magnetization and magnetic susceptibility from a CEF Hamiltonian, especially for fitting and comparison with experimental data. To achieve this, first we need to define the total magnetization operator

$$\mathbf{M} = \eta \mathbf{L} + g\mathbf{S} \tag{1.15}$$

where $g = 2.0$ (ignoring the QED correction) and η is introduced to account for the hybridization or charge transfer between a central ion and ligands. Normally $\eta = 1$ but for most $3d$-transition metals in solids, η is estimated around 0.8 [8].

In the presence of an external magnetic field **B**, the Hamiltonian reads

$$H = H_{\text{CEF}} + H_{\text{SO}} + \mu_B \mathbf{B} \cdot \mathbf{M} \tag{1.16}$$

where $\mu_B = 5.7883818012 \times 10^{-2}$ meV·T^{-1} is the Bohr magneton. After projecting the Hamiltonian onto the basis state manifold $|L, m_L, S, m_S\rangle$, it can be diagonalized and the corresponding eigenstates $|v_i\rangle$ and eigenenergies E_i can be easily obtained ($i = 1 \ldots N$, N is the total number of states). Hence the total magnetization (in units μ_B per ion) can be expressed as follow

$$\langle \mathbf{M} \rangle = -\frac{\sum_{i=1}^{N} \langle v_i| \mathbf{M} |v_i\rangle \, \text{exp}\left(-E_i/k_B T\right)}{\sum_{i=1}^{N} \text{exp}\left(-E_i/k_B T\right)} \tag{1.17}$$

where the summation is over all the eigenstates and $k_B = \frac{1}{11.604505}$ meV· K^{-1} is the Boltzmann constant. As for calculating a spherical average of magnetization (or the magnetization for a powder sample), the following formula is applied

$$\langle M \rangle_{\text{powder}} = \frac{1}{3}\left(\langle M_{B_x}\rangle + \langle M_{B_y}\rangle + \langle M_{B_z}\rangle\right) \tag{1.18}$$

where M_{B_i} ($i = x, y, z$) represents the magnetization with the external magnetic field applied along the corresponding i-direction.

The single-ion magnetic susceptibility $\chi^{(0)}$ is calculated using a perturbative approach and the final expression [17] (units in emu·mol^{-1}·Oe^{-1}) is

$$\begin{aligned}\chi^{(0)}_{\alpha\beta} =& \frac{N_A \mu_B^2 \mu_0}{4\pi \times 1.60218 \times 10^{-28}} \times \\ &\left[\sum_{i=1}^{N}\sum_{i'=1}^{N} \mathbb{I}_{E_{i'} \neq E_i} \cdot \frac{\langle v_i| M_\alpha |v_{i'}\rangle \langle v_i'| M_\beta |v_i\rangle}{E_{i'} - E_i}\left(e^{-E_i/k_B T} - e^{-E_{i'}/k_B T}\right) + \right. \\ &\left. \sum_{i=1}^{N} \frac{\langle v_i| M_\alpha |v_i\rangle \langle v_i| M_\beta |v_i\rangle}{k_B T} e^{-E_i/k_B T} - \frac{1}{k_B T}\langle M_\alpha\rangle\langle M_\beta\rangle\right]\end{aligned} \tag{1.19}$$

where $\alpha, \beta = x, y, z$, N_A is Avogadro's constant, $\mu_0 = 4\pi \times 10^{-7}$ T·m·A^{-1} is vacuum permeability, and $\mathbb{I}_{E_{i'} \neq E_i}$ is an indicator enforcing $E_{i'} \neq E_i$ for any two eigen-states $|v_i\rangle$, $|v_{i'}\rangle$. The first term in Eq.(1.19) is the *Van Vleck* contribution, which becomes constant at zero temperature. The second term, the so-called *Curie* contribution, diverges as $\frac{1}{T}$ in the low-temperature limit [17].

In a realistic system, there are always interactions between neighbouring transition metal ions, the so-called *exchange interactions*, which will be discussed in the next section. In addition, the inner filled shells have a negative contribution to the susceptibility, yielding a *diamagnetic* term χ_{dia}. To take both of these contributions into account, at a mean field (MF) level, the susceptibility can be written as [17]

$$\underline{\underline{\chi}}^{MF} = \chi_{\text{dia}} + \frac{\underline{\underline{\chi}}^{(0)}}{1 + 2\underline{\underline{J}} \times \underline{\underline{\chi}}^{(0)}} \tag{1.20}$$

where $\underline{\underline{\cdots}}$ indicates a matrix form and $\underline{\underline{J}}$ represents the sum over all neighbouring exchange interactions. Similar to the total magnetization $\langle \mathbf{M} \rangle$, a spherical average of susceptibility $\underline{\underline{\chi}}^{\text{MF}}$ is its trace

$$\chi^{MF}_{\text{powder}} = \frac{1}{3}\text{Tr}\left[\underline{\underline{\chi}}^{MF}\right] \tag{1.21}$$

1.2.3 Exchange interactions

As mentioned above, in a real material, there are always interactions between neighboring transition metal ions. Here we will introduce two, the most common *Heisenberg* type, and a more exotic one, the so-called *Kitaev* exchange interaction.

Heisenberg interaction

For simplicity, we only consider two electrons. Assume their total spin angular momenta are $\mathbf{S}_1$ and $\mathbf{S}_2$ respectively. The Hamiltonian reads

$$H_{\text{Heisenberg}} = J\mathbf{S}_1 \cdot \mathbf{S}_2 \tag{1.22}$$

which originates from (i) a direct Coulomb exchange [2, 18] between the two electrons which results in a negative J and (ii) a kinetic exchange [18] process where the hopping of the electrons to neighbouring sites is allowed. This gives rise to a positive J. The sign of J determines the interaction type, for $J < 0$, it is ferromagnetic (FM) such that in the ground state the spins form a triplet: $|\uparrow\uparrow\rangle$, $|\downarrow\downarrow\rangle$ and $\frac{1}{\sqrt{2}}\left(|\uparrow\downarrow\rangle + |\downarrow\uparrow\rangle\right)$. It is antiferromagnetic (AFM) if $J > 0$. In this case the ground state is a singlet $\frac{1}{\sqrt{2}}\left(|\uparrow\downarrow\rangle - |\downarrow\uparrow\rangle\right)$.

The Heisenberg interaction is the most simple and common type of exchange interaction encountered in nature. It will be predominantly considered throughout the thesis, together with its anisotropic generalizations, such as a XXZ type with $\Delta \neq 0$.

$$H_{\text{XXZ}} = J\mathbf{S}_1 \cdot \mathbf{S}_2 + \Delta S_1^z S_2^z \tag{1.23}$$

Kitaev interaction

In a seminal work [19], A. Kitaev proposed an exactly solvable spin model in two dimension which is called now the Kitaev honeycomb model. In short, Kiaev considered the following situation: In a two-dimensional honeycomb lattice, there is a spin 1/2 degree of freedom assigned to each lattice site. The interaction among them are restricted to a nearest neighbour (NN). In addition, these interactions are bond-dependent, see Fig.1.3. The full Hamiltonian reads

$$H = \sum_{\langle i,j \rangle} K_x S_i^x S_j^x + K_y S_i^y S_j^y + K_z S_i^z S_j^z \tag{1.24}$$

where the summation is over all the NNs and K_x, K_y, K_z are the so-called Kitaev exchange interactions.

Contrary to the Heisenberg type introduced in this section, it introduces a strong frustration on the central spin: In a honeycomb lattice, there are three bonds {X, Y, Z} associated with one lattice site, which are labeled by red, green and blue solid lines respectively in Fig.1.3. Each bond carries an Ising-type interaction constraining the spins to align along the Ising

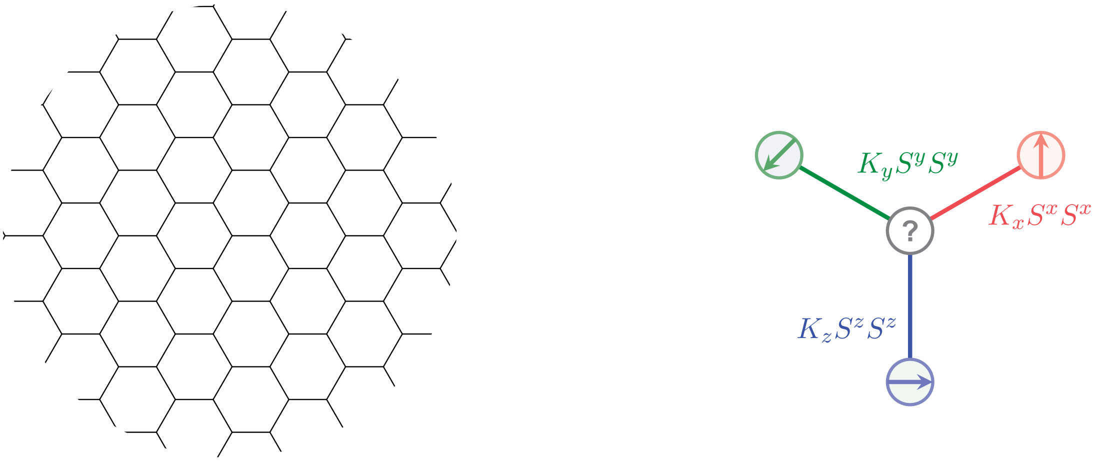

Figure 1.3: Left panel: A honeycomb lattice as considered in the original Kitaev model where each lattice point is assigned a spin 1/2 degree of freedom. Right panel: A schematic drawing of the bond-dependent exchange interactions at each site. Each bond is associated with an Ising-type interaction which introduces strong frustration on the central spin.

easy axis, e.g. the interaction on the X bond is $K_x S^x S^x$, thus the spins are forced to be parallel along the x-direction. As a result, the central spin cannot decide which direction to point to because the Ising type interactions carried by the three bonds dictate it to align itself to three orthogonal directions. One might naively speculate the ground state of the Kitaev model is highly disordered and in fact Kitaev showed that the ground state is a quantum spin liquid without any broken symmetries (can be either gapped or gapless depending on the relative strengths of K_x, K_y and K_z [19]).

Due to the exotic bond-dependent interaction form of the Hamiltonian, it initially seems impossible to realize such a model in real material. However in 2008, G. Jackli and G. Khaliulin [20] first realized such a non-trivial model is indeed possible provided two essential ingredients are present:

- The orbital and spin angular momenta of a transition metal ion is mixed, forming a spin-orbit entangled ground state such that it is a Kramers doublet.
- The neighbouring transition metal ions must be connected via an edge sharing octahedral fashion where the metal-ligand-metal angle is 90° in an ideal case.

As an example, we consider Ir^{4+} (5d^5) in a cubic crystal field following the original paper [20] where the six corners of the octahedron are taken up by O^{2-}. The crystal field splits the d-orbitals into the doublet e_g and the triplet t_{2g}. The t_{2g} levels can be effectively treated as occupied by a hole, characterized by an effective orbital angular momentum $l_{\text{eff}} = 1$ and a spin angular momentum $S = 1/2$. Upon spin-orbital coupling, the t_{2g} hole further splits into $j_{\text{eff}} = 1/2$ and $j_{\text{eff}} = 3/2$ states, where $j_{\text{eff}} = 1/2$ is the ground state (Kramers doublet), see the left panel of Fig.(1.4). An edge sharing geometry of two octahedra is sketched in the right panel of Fig.(1.4) where Ir^{4+} and O^{2-} are represented by black and red circles respectively. Of special interest, in such a geometry a destructive quantum interference of the two Ir-O-Ir paths in the super-exchange process occurs [21], which completely suppresses the conventional Heisenberg type exchange interaction. Instead an Ising ferromagnetic exchange, $-KJ^z_{\text{eff}}J^z_{\text{eff}}$ ($K > 0$), with easy axis perpendicular to the Ir-O$_2$-Ir plane (indicated by the blue plaquette in Fig.1.4) emerges. Hence the final

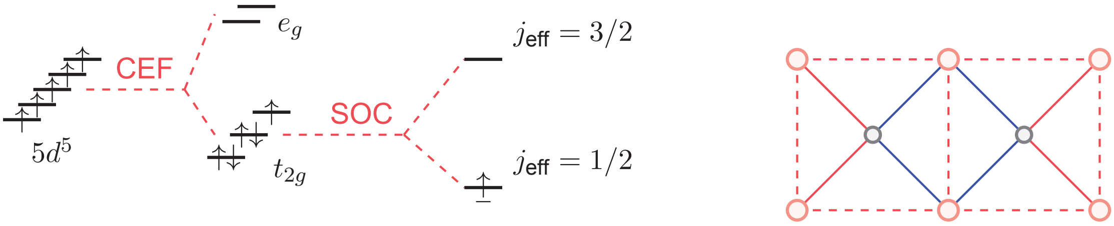

Figure 1.4: Left panel: The splitting of $5d^5$ under CEF and SOC. The resulting ground state is an effective j_{eff} state occupied by a hole. $\uparrow$ and $\downarrow$ represent spin-up and spin-down states of an electron, and $\underline{\uparrow}$ represents a spin-up hole. Right panel: The edge sharing geometry of two neighbouring octahedra, indicated by the two red dashed plaquette, when looking from above. The black and red circles represent Ir^{4+} and O^{2-} respectively (the two out-of-plane O^{2-} for each octahedron are ignored for clarity).

Hamiltonian in the local cubic coordinate system reads

$$H_{ij}^{(\gamma)} = -K\tilde{S}_i^{\gamma}\tilde{S}_j^{\gamma} \tag{1.25}$$

where $\gamma = x, y, z$ for X, Y and Z bonds respectively, and $\tilde{S}$ is a pseudo-spin 1/2 operator due to the Kramers doublet ground state.

1.3 Magnetic ordering

The exchange interactions introduced above can give different types of magnetic ordering. Two most common types are:

- Ferromagnetic where all spins are parallel $\uparrow\uparrow\uparrow\cdots\uparrow$.
- Antiferromagnetic where the neighbouring spins are of opposite directions $\uparrow\downarrow\uparrow\cdots\downarrow\uparrow$ (Néel state).

For probing magnetic ordering, several experimental techniques can be applied, of which magnetic susceptibility χ, specific heat and neutron diffraction are always the go-to choices. Since magnetic ordering normally belongs to the family of second-order phase transition, specific heat diverges at the ordering temperature [7]. This gives rise to the so-called λ-anomaly. As pointed out by Fisher [22], the first-order derivative of χT is approximate to magnetic specific heat C_m: $C_m \approx \frac{d\chi T}{dT}$. Hence the signature of magnetic ordering is also observable in magnetic susceptibility data. Neutron diffraction for probing magnetic order will be discussed in the next chapter.

When temperature is far above the magnetic ordering temperature, the material under study is in a fully paramagnetic state in which the magnetic moments are randomly aligned. In this region, the magnetic susceptibility of the material can be described by the well-known Curie-Weiss law, see Eq.(1.26).

$$\chi(T) = \frac{C}{T - T_{CW}} \tag{1.26}$$

C is a material specific Curie constant given by [7]

$$C = \frac{\mu_0\mu_B^2}{3k_B}g^2S(S+1) \tag{1.27}$$

where g is the Landé g-factor, S is the spin angular momentum of the magnetic ion in the material. T_{CW} is the Curie-Weiss temperature which is associated with the sum of all exchange interactions inside the material. Assuming the exchange interactions are Heisenberg like, T_{CW} is given by the expression [7]

$$T_{CW} = -\frac{S(S+1)}{3k_B}\sum_j J_{ij} \tag{1.28}$$

where the summation goes over all neighbours with which a given spin interacts.

1.4 Magnetic excitations

In this section, we will introduce two types of excitations mostly encountered in real materials, namely spin waves and spinons. For detail treatments and discussions on these two excitations, see Ref [23, 24].

1.4.1 Spin waves

A magnetically ordered ground state breaks the spin-rotation symmetry, of which the most important collective excitations are spin waves. The standard procedure for finding the spin wave dispersions of any ordered ground states [24] starts with rotating the ordered spins such that the moment directions are parallel to the **Z** axis in a global Cartesian coordinate system. Then apply the Holstein-Primakoff expansion of the spin operators and restrict the Hamiltonian up to a quadratic order form. The resulting quadratic Hamiltonian can be diagonalized by performing a Bogoliubov transformation and the obtained eigenenvalues are the desired spin wave energies. Here we summarize the important aspects of spin wave dispersions for ferromagnetic and antiferromagnetic ground states respectively, assuming a Heisenberg type Hamiltonian:

- Ferromagnetic ground state: in the long wavelength limit, i.e. $\mathbf{q} \to 0$, the dispersion is quadratic $\hbar\omega_{\mathbf{q}} \sim \mathbf{q}^2$.
- Antiferromagnetic ground state: close to the zone center (for a square lattice it corresponds to $\mathbf{q} = (\pi, \pi)$ assuming the lattice constant is 1), the dispersion is linear in **q** for small deviations $\delta\mathbf{q}$: $\hbar\omega E_{\mathbf{q}} \sim \delta\mathbf{q}$.

The spin wave dispersions calculated in the thesis were carried out using a MATLAB package SpinW [24] which is a numerical implementation of the linear spin wave theory (LSWT) for a single **Q** ordered ground state.

1.4.2 Spinons

Spin waves represent a type of elementary excitations that changes the total spin angular momenta of ground states by 1, i.e. $\Delta S = 1$. In some special cases, such a $S = 1$ excitation is able to fractionize into two $S = 1/2$ objects, known as spinons.

To illustrate this idea, the nearest neighbor Heisenberg antiferromagnet $S = 1/2$ chain is taken as an example. Owing to the ground state spin-spin correlation decays as a power law [23],

$$\langle 0|\, \mathbf{S}_i \cdot \mathbf{S}_j \,|0\rangle \sim \frac{(-1)^{i-j} \log^{1/2}|i-j|}{|i-j|^2} \tag{1.29}$$

if one were to take a snap shot of a local spin configuration of the spin chain, it would look like a Néel state.

A $\Delta S = 1$ excitation in such a Néel state corresponds to a local spin flip. By doing so, two independent domain walls are created separating two possible stagger-order states as shown in Fig.1.5. It is these domain walls are called spinons in such a 1D scenario and each carries a $S = 1/2$ degree of freedom.

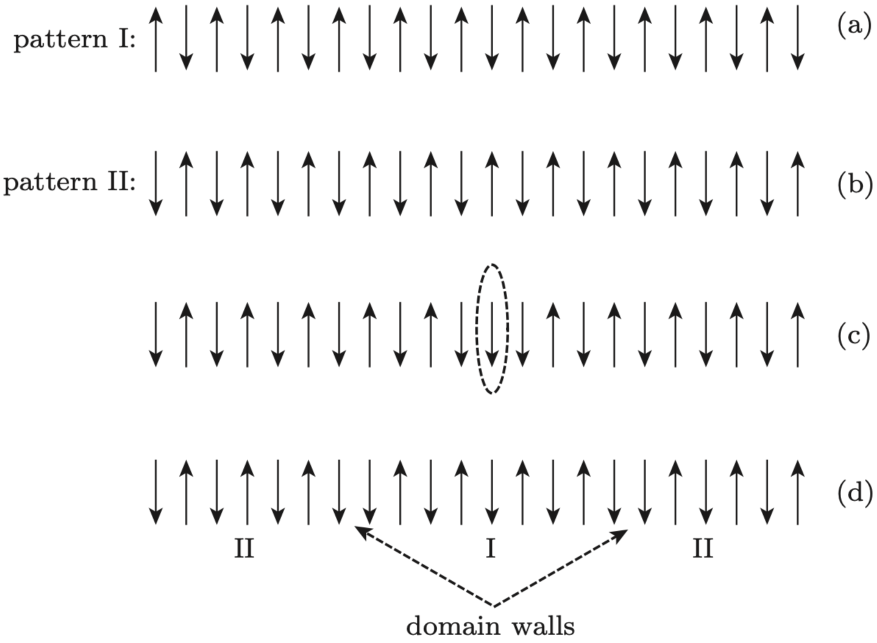

Figure 1.5: A pair of spinon excitations in the nearest neighbor Heisenberg antiferromagnetic $S = 1/2$ chain. (a)(b) Two opposite-stagger ordered states in 1D. (c) A spin flip excitation occurs at the center of the chain. (d) Fractionalization of the single flipped spin into two $S = 1/2$ domain walls which separate pattern I and pattern II ordering. The figure is taken from [23].

2 Elements of Neutron Scattering

The basic properties of neutron and how it interacts with matter are discussed in this chapter. More detailed and rigorous theoretical treatments and derivations can be found in [25, 26, 27, 28]. The related instrumental setups used in this thesis will be presented in the next chapter.

2.1 Basic properties of the neutron

As the name suggests, neutron is a charge-neutral particle. Unlike another charge-less particle, the photon, it has a finite mass, $m_n = 1.675 \times 10^{-27}$ kg. Further it is a fermion with spin $S = 1/2$, which allows it to interact with magnetic fields. Finally the lifetime of a free neutron is close to 15 minutes, which is long enough for it to interact with matters before decaying into an electron, a proton and an electron neutrino: $n^0 \rightarrow e^- + p^+ + \bar{v}_e$. The basic properties of the neutron are summarized in Table 2.1.

There are two ways to produce neutrons in the field of neutron scattering: either via a nuclear fission process or a spallation process. Nuclear fission takes place in a nuclear reactor where a heavy and unstable nucleus, e.g. U^{235} is bombarded by slow neutrons. The nucleus then splits into smaller parts and generates more neutrons. Whereas for spallation, protons are accelerated to hit a heavy metal target, such as Hg or W. The target nuclei are excited and expel neutrons and other particles. In both cases, the generated neutrons are of high energies ([MeV]). Hence it is necessary to slow them down to the desired energies ([meV]) for conducting scattering experiments via modulators [28].

2.2 Neutron-matter interaction

Neutron scattering has several advantages:

- A neutron can penetrate deeply into solids as there is no Coulomb interaction between the electrons in the solids and the neutron. Hence it is an excellent tool for characterizing the bulk properties of materials.
- As a spin 1/2 particle, a neutron can interact with the magnetic fields created by the orbital and spin angular momenta of the ions in solids. Consequently, neutrons can be directly used to study magnetic properties of materials.

There are two types of interactions that we will encounter when neutrons pass through materials. One is the interaction with the nuclei via strong forces and the other is the magnetic dipole interaction between the unpaired electrons and the neutrons. The strengths of the two interactions are of a similar order of magnitude. This is an advantage for studying magnetic scattering using neutrons as opposing to using X-rays, due to the magnetic cross-section is very small in X-ray scattering [29].

Properties	Value
Mass	1.675×10^{-27} kg
Charge	0
Spin	1/2
Magnetic dipole moment	$9.6623647 \times 10^{-27}$ J·T^{-1}
Lifetime	881.5 ± 1.5 s

Table 2.1: Basic properties of neutrons.

2.2.1 Strong force

The interaction between a nucleus and a neutron has a very short range, much smaller than the wavelength of neutrons used for scattering experiments (for thermal neutron scattering the wavelength lies in between 1.3 Å and 4.0 Å [28]). Moreover, the nuclear scattering is isotropic and can therefore be characterized by a single parameter b, called the scattering length. The Fermi pseudo-potential takes the form [25, 28]

$$V_N(\mathbf{r}) = \frac{2\pi\hbar^2}{m_n} b\delta(\mathbf{r} - \mathbf{R}) \tag{2.1}$$

where **R** is the position of the nucleus and **r** is the position of the neutron. The scattering length b not only depends on the isotope of the atom, but also is associated with the relative orientations between the neutron spin and the nuclear spin I of the isotope. For a natural nucleus interacting with an unpolarized neutron beam, the scattering length is an average of all the natural isotope populations it has and all the spin directions of the neutron. Thus the scattering length is normally denoted as $\bar{b}$.

2.2.2 Magnetic dipole interaction

The magnetic interaction arises from the coupling between the neutron magnetic moment and the magnetic fields created by unpaired electrons. Since electrons have both spin and orbital angular momenta, the potential felt by the neutron at **r** due to N unpaired electrons whose positions are $\mathbf{R}_i$ takes the form [30, 31]

$$\begin{aligned} V_M(\mathbf{r}) &= -\boldsymbol{\mu}_n \cdot \mathbf{H} \\ \mathbf{H} = \mathbf{H}_S + \mathbf{H}_L &= \sum_{i=1}^{N} \left(\nabla \times \frac{\boldsymbol{\mu}_i \times (\mathbf{r} - \mathbf{R}_i)}{(r - R_i)^3} - \frac{2\mu_B}{\hbar} \frac{\mathbf{p}_i \times (\mathbf{r} - \mathbf{R}_i)}{(r - R_i)^3} \right) \end{aligned} \tag{2.2}$$

where $\boldsymbol{\mu}_n = \gamma\mu_N\boldsymbol{\sigma}$ is the magnetic moment of neutron ($\gamma = 1.76 \times 10^{11}$ s^{-1} T^{-1} and μ_N are the gyromagnetic ratio and nuclear Bohr magneton respectively) and $\boldsymbol{\mu}_i = -2\mu_B \boldsymbol{s}_i$ is the magnetic moment of the ith electron. $\boldsymbol{s}_i$ is the spin angular momentum for the ith electron and $\boldsymbol{p}_i$ is its momentum. The two contributions H_S and H_L comes from the dipolar interaction with the electron spins, and the electron orbital motions respectively.

2.3 Neutron scattering cross-sections

In neutron scattering, cross-section is a measure of the probability that neutrons are scattered from a target. In practice the three most frequently quoted cross-sections are list as follow [31]:

- Total cross-section σ:

  $$\sigma = \frac{\text{total number of neutrons scattered in all direction per second}}{\text{incident flux}} \tag{2.3}$$

  It serves as the effective area of the target as viewed by the incident neutrons, which is in units of [barn] (1 barn = 10^{-28} m^2).

- Differential cross-section $\frac{d\sigma}{d\Omega}$:

  $$\frac{d\sigma}{d\Omega} = \frac{\text{total number of neutrons scattered in solid angle } d\Omega \text{ per second}}{\text{incident flux} \cdot d\Omega} \tag{2.4}$$

  The differential cross-section is from the view of a detector whose solid angle coverage is $d\Omega$. Note it has the unit of [barn·sr^{-1}].

- Double differential cross-section $\frac{d^2\sigma}{d\Omega dE}$:

  Suppose detectors can analyze the energy of the scattered neutrons. The double differential cross-section is needed as it describes the differential cross-section of neutrons in a final energy interval $[E_f, E_f + dE]$,

  $$\frac{d^2\sigma}{d\Omega dE} = \frac{\text{total number of neutrons scattered in solid angle } d\Omega \text{ per second with final energies between } E_f \text{ and } E_f + dE}{\text{incident flux} \cdot d\Omega \cdot dE} \tag{2.5}$$

  which is in units of [barn·sr^{-1}·meV^{-1}].

The last two, the differential cross-section and the double differential cross-section, are relevant for elastic and inelastic scattering, respectively.

2.3.1 Elastic scattering

The elastic scattering refers to a process where an incident beam of neutrons characterized by a wavevector $\mathbf{k}_i$ and spin σ_i, impinges on a target and scatters into a final state characterized by a wavevector $\mathbf{k}_f$ and spin σ_f with $k_i = k_f$. In such a process, there is no energy transfer. Define the scattering vector $\mathbf{Q} = \mathbf{k}_i - \mathbf{k}_f$. The general expression for the differential cross-section takes the form [30]

$$\frac{d\sigma}{d\Omega}(\mathbf{k}_f\sigma_f, \mathbf{k}_i\sigma_i) = \left(\frac{m}{2\pi\hbar^2}\right) \langle\mathbf{k}_f| V(\mathbf{r}) |\mathbf{k}_i\rangle \tag{2.6}$$

where $V(\mathbf{r})$ is the potential felt by neutrons.

In turn the differential cross-section for the nuclear coherent scattering part from an unpolarized neutron beam for a natural nucleus is [30]

$$\left.\frac{d\sigma_{N\text{coh}}}{d\Omega}\right|_{\text{elastic}} = |\bar{b}|^2 \tag{2.7}$$

and in addition, the fluctuation of the scattering length due to its natural isotopes, denoted as Δb, gives rise to the nuclear incoherent scattering [30].

$$\left.\frac{d\sigma_{N\text{inc}}}{d\Omega}\right|_{\text{elastic}} = |\Delta b|^2 \tag{2.8}$$

If the nucleus has unpaired electrons in its outer shells. Due to the finite spatial spread in real space of the unpaired electrons, the magnetic scattering intensity in **Q** space decays as the increase of **Q**. This effect can be summarized in a single term, the so-called magnetic form factor $f(Q)$ [25]. Moreover, neutrons can only couple to the magnetic moment perpendicular to the scattering vector **Q** [25, 30], denoted as $\mu_\perp$, hence the differential scattering cross-section for the magnetic scattering of an unpolarized neutron beam from a pure paramagnetic ion reads [25, 30]

$$\left.\frac{d\sigma_M}{d\Omega}\right|_{\text{elastic}} = p^2 f(Q)^2 \mu_\perp^2 \tag{2.9}$$

where $p = 0.2696 \times 10^{-14}$ m is a constant.

In the above discussion, we only considered the scattering from a single ion. Inside a crystal, billions of ions align with each other and form a periodic structure. Such periodicity gives rise to both constructive and destructive interference in the final scattering pattern. The Bragg condition is satisfied in situations where constructive interference occurs. The derivation of the differential cross-sections for coherent nuclear scattering and magnetic scattering for an unpolarized neutron beam scattered from a crystal can be found in Refs [26, 27, 25]. In the following, we summarized the main results (for simplicity we ignore the Debye-Waller factor [25] in the nuclear/magnetic structure factors).

The expression for the differential cross-section for coherent nuclear scattering reads [25, 30]

$$\left.\frac{d\sigma_{N\text{coh}}}{d\Omega}\right|_{\text{elastic}} = \frac{(2\pi)^3}{V}\mathcal{N}\sum_{\mathbf{H}}|F_N(\mathbf{Q})|^2\delta(\mathbf{Q}-\mathbf{H}) \tag{2.10}$$

where **H** is a reciprocal lattice vector, V is the volume of one unit cell, $\mathcal{N}$ is the total number of unit cells inside the crystal and $F_N(\mathbf{Q})$ is the unit cell nuclear structure factor defined as [25, 30]

$$F_N(\mathbf{Q}) = \sum_v b_v e^{i\mathbf{Q}\cdot\mathbf{r}_v} \tag{2.11}$$

and the index v denotes the v-th atom inside the unit cell. In Eq.(2.10), the δ-function encodes the Bragg condition: for a perfect crystal, constructive interference occurs if the scattering vector **Q** coincides with a reciprocal lattice vector **H**. These special reciprocal lattice vectors are called (nuclear) Bragg peaks.

The differential cross-section for magnetic scattering can be written in a similar fashion, but with a few complications [30]:

$$\left.\frac{d\sigma_M}{d\Omega}\right|_{\text{elastic}} = \frac{(2\pi)^3}{V}\mathcal{N}\sum_{\mathbf{H}}\sum_{\mathbf{k}}|F_{M\perp}(\mathbf{Q})|^2\delta(\mathbf{Q}-\mathbf{H}-\mathbf{k}) \tag{2.12}$$

Any ordered ground state can be expanded as a sum of Fourier series [30], see Eq.(2.13), where $\boldsymbol{\mu}_{n,v}$ is the magnetic moment associated with the site index (n, v) (n for unit cells, v for atoms), and $\boldsymbol{m}_{v,\mathbf{k}}$ is the Fourier component associated with the propagation vector **k**. Taken as an example, a 2D square lattice antiferromagnet has a propagation vector $\mathbf{k} = (1/2, 1/2)$. Thus now we can define the magnetic structure factor $F_M(\mathbf{Q})$, see Eq.(2.14) [30]. As before, the summation is carried out over all the atoms inside one nuclear unit cell and $f_v(Q)$ are the associated magnetic form factors.

$$\boldsymbol{\mu}_{n,v} = \sum_{\mathbf{k}}\boldsymbol{m}_{v,\mathbf{k}}e^{-i\mathbf{k}\cdot\mathbf{R}_n} \tag{2.13}$$

$$F_M(\mathbf{Q}=\mathbf{H}+\mathbf{k}) = p\sum_v f_v(Q)\boldsymbol{m}_{v,\mathbf{k}}e^{i\mathbf{Q}\cdot\mathbf{r}_v} \tag{2.14}$$

With Eq.(2.13) and Eq.(2.14), we can finally interpret Eq.(2.12). The double summations are carried out not only for the reciprocal lattice vectors **H**, but also for the propagation vectors **k** (for complex structures there might be one than one **k**). With the δ-function constraint, the (magnetic) Bragg peaks can only locate at $\mathbf{H}+\mathbf{k}$; And because $\boldsymbol{\mu}_{n,v}$ must be real, **k** always shows up in pairs $\pm\mathbf{k}$ and the magnetic Bragg peaks $\mathbf{H}\pm\mathbf{k}$ are a pair of satellite peaks around the nuclear Bragg peak **H**. Moreover, as in the single ion case, see Eq.(2.9), neutrons only couple to the magnetic moment perpendicular to **Q** ($F_{M\perp}$).

2.3.2 Inelastic scattering

In inelastic scattering, the energy $\mathcal{E}$ and momentum **Q** transfers are defined as follow

$$\begin{aligned}\mathcal{E} &= E_i - E_f = \frac{\hbar k_i^2}{2m_n} - \frac{\hbar k_f^2}{2m_n}\\ \mathbf{Q} &= \mathbf{k}_i - \mathbf{k}_f\end{aligned} \tag{2.15}$$

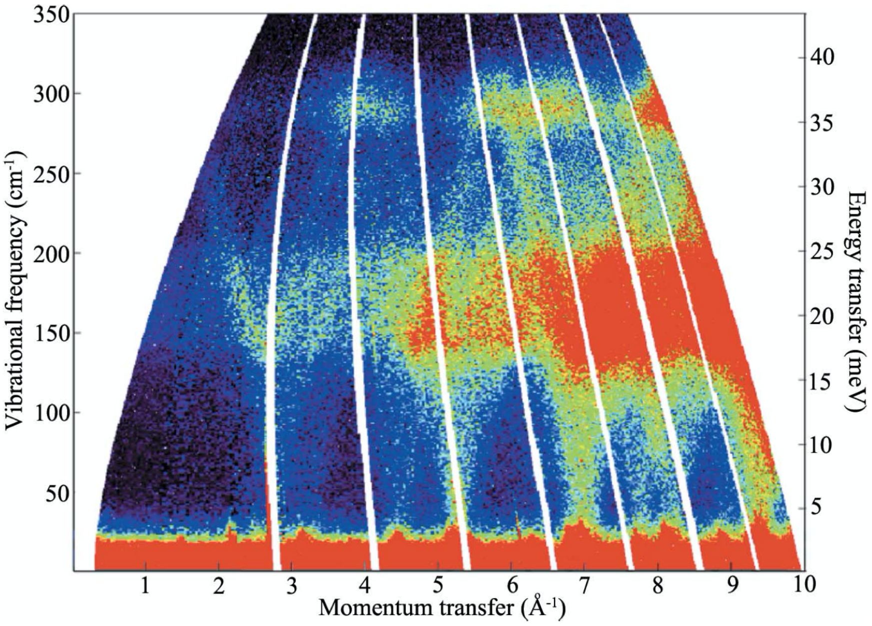

Figure 2.1: Inelastic neutron scattering spectrum for phonon excitations of a Aluminium powder sample collected at 10 K on the MARI spectrometer at the ISIS Neutron and Muon Source [32].

E_i and E_f are the energies of the neutrons before and after being scattered from a sample, and $\mathbf{k}_i$ and $\mathbf{k}_f$ are the associated wavevectors. Throughout the thesis's work, only two situations were encountered in which either the E_i or the E_f of an scattering event is fixed. The kinematic constraint for each situation is illustrated as follow.

- E_i is fixed:
$$\frac{\hbar Q^2}{2m_n} = 2E_i - \mathcal{E} + 2\sqrt{E_i(E_i - \mathcal{E})}\cos 2\theta \tag{2.16}$$
- E_f is fixed:
$$\frac{\hbar Q^2}{2m_n} = 2E_f + \mathcal{E} + 2\sqrt{E_f(E_f + \mathcal{E})}\cos 2\theta \tag{2.17}$$

The double differential cross-section for inelastic scattering can be written as [31]

$$\frac{d^2\sigma}{d\Omega dE_f} = \frac{k_f}{k_i} S(\mathbf{Q}, \mathcal{E}) \tag{2.18}$$

where $S(\mathbf{Q}, \mathcal{E})$ is the response function carrying all the information on the physics of the system [31]. For scattering from lattice vibrations or phonons, the response function $S_N(\mathbf{Q}, \mathcal{E})$ for one-phonon scattering for a Bravais lattice varies according to [28]

$$S_N(\mathbf{Q}, \mathcal{E}) \propto \sum_{\mathbf{H}} \frac{(\mathbf{Q}\cdot\mathbf{e}_q)^2}{\mathcal{E}_{\mathbf{q}}} \left[(n_{\mathbf{q}}+1)\delta(\mathcal{E}-\mathcal{E}_{\mathbf{q}})\delta(\mathbf{Q}-\mathbf{H}-\mathbf{q}) + n_{\mathbf{q}}\delta(\mathcal{E}+\mathcal{E}_{\mathbf{q}})\delta(\mathbf{Q}-\mathbf{H}+\mathbf{q})\right] \tag{2.19}$$

where $\mathbf{q}$ is a reciprocal lattice vector with respect to $\mathbf{H}$, $\mathcal{E}_{\mathbf{q}}$ is the phonon energy at $\mathbf{q}$, $e_{\mathbf{q}}$ is the associated polarization vector, and $n_{\mathbf{q}}$ is the phonon occupation number at temperature T: $n_{\mathbf{q}} = \frac{1}{e^{\mathcal{E}_{\mathbf{q}}/k_B T}-1}$. Notice that the response function has a prefactor $(\mathbf{Q}\cdot\mathbf{e}_q)^2$.

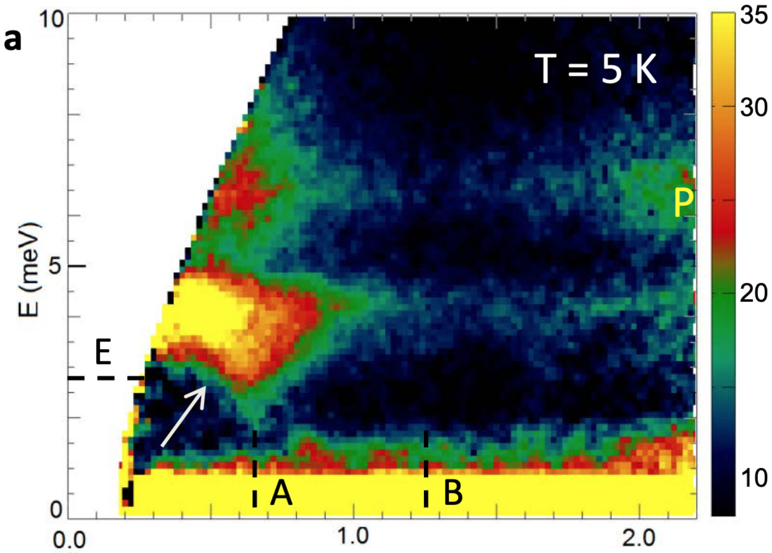

Figure 2.2: Inelastic neutron scattering spectrum measured on a α-RuCl$_3$ powder sample collected at 5 K on the SEQUOIA spectrometer at the Spallation Neutron Source [33].

Due to this term, phonons dominate high Q regions in spectra as their intensities increase quadratically in Q. As illustrated in Fig.2.1 where the experimental inelastic neutron scattering spectrum of phonon excitations in a polycrystalline Aluminium is shown [32], the spectrum is dominated by the pronounced scattering features locating at large momentum transfers $Q \geq 5$ Å^{-1}, in contrast to the weak scattering signals recorded at momentum transfers $Q \leq 4$ Å^{-1}.

The response function for magnetic scattering $S_M(\mathbf{Q}, \mathcal{E})$ for a Bravais lattice is proportional to [28]

$$\begin{aligned} S_M(\mathbf{Q}, \mathcal{E}) &\propto f(Q)^2 \sum_{\alpha,\beta} \left(\delta_{\alpha\beta} - \frac{Q_\alpha Q_\beta}{Q^2}\right) \sum_{i,j} \int_{-\infty}^{+\infty} e^{-i\mathcal{E}t/\hbar} \langle S_i^\alpha(0) S_j^\beta(t)\rangle e^{-i\mathbf{Q}\cdot(\mathbf{R}_i - \mathbf{R}_j)} dt \\ &= f(Q)^2 \sum_{\alpha,\beta} \left(\delta_{\alpha\beta} - \frac{Q_\alpha Q_\beta}{Q^2}\right) \int_{-\infty}^{+\infty} e^{-i\mathcal{E}t/\hbar} \langle S_{\mathbf{Q}}^\alpha(0) S_{-\mathbf{Q}}^\beta(t)\rangle dt \end{aligned} \tag{2.20}$$

where $\alpha, \beta = x, y, z$, $f(Q)$ is the magnetic form factor and $\langle S_i^\alpha(0) S_j^\beta(t)\rangle$ is the thermal average of the time-dependent spin operators, which essentially describes the probability that, if the magnetic moment of the ith site has a specific vector $\mathbf{S}_i$ at time zero, then the magnetic moment at site j at time t takes another specific vector $\mathbf{S}_j$ [28]. The factor $\left(\delta_{\alpha\beta} - \frac{Q_\alpha Q_\beta}{Q^2}\right)$ highlights the fact that, neutrons only couple to the spin fluctuations perpendicular to the scattering vector $\mathbf{Q}$, e.g. if the magnetic fluctuation is along the x-direction, then at $\mathbf{Q} = (1, 0, 0)$ neutrons are unable to couple to it whereas at $\mathbf{Q} = (0, 1, 0)$ one can probe it directly. As an example, in Fig.2.2 we illustrate the measured magnetic excitations in a polycrystalline α-RuCl$_3$ collected in its magnetic ordered phase [33]. It is evident that, in contrast to phonon scattering whose intensity is most prominent at large momentum transfers as illustrated in Fig.2.1, magnetic excitations dominate small momentum transfer regions in an inelastic neutron scattering spectrum. This is due to the magnetic form factor $f(Q)$ has an exponential decay in momentum space.

For scattering from polycrystalline material, the double differential cross-section is a spherical average of $\frac{k_f}{k_i}S(\mathbf{Q},\mathcal{E})$ over all possible momentum transfers $\mathbf{Q}_k$ that share the same length $|Q|$ (($k = 1, 2, \ldots, N_{\mathbf{Q}_k}$ and $N_{\mathbf{Q}_k}$ is the number of momentum transfers that have the length $|Q|$), which can be written as follow

$$\left.\frac{d^2\sigma}{d\Omega dE_f}\right|_{\text{powder}} = \frac{1}{N_{\mathbf{Q}_k}} \times \frac{k_f}{k_i} \sum_{\mathbf{Q}_k \in |Q|} S(\mathbf{Q}_k, \mathcal{E}). \tag{2.21}$$

Due to the spherical average, majority of the information regarding the physics of the system is lost. Whereas such an average is absent in the spectra taken on single crystals, which offer a direct view of the response function $S(\mathbf{Q},\mathcal{E})$ in full $(\mathbf{Q},\mathcal{E})$ space. Thus it is less straightforward to interpret powder spectra compared to the spectra measured on single crystals.

In Chapter 1 we introduced the multiplet splitting of transition metal ions under CEF and SOC when embedding into solids. With the application of the Stevens operator formalism explained in Section 1.2.1, the energy levels E_i and the corresponding wavefunctions $|v_i\rangle$ of the split states ($i = 1, 2, \ldots, N$ where N is the total number of the states) from the ground state manifold obtained in the isolated ion limit for a transition metal ion can be calculated. Due to the selection rule of neutron scattering, the only allowed transitions between these states are those whose total angular momentum changes ΔJ satisfy: $\Delta J = 1$ and $\Delta J_z = 0, \pm 1$ [28]. In Eq.(2.22), a general formula for computing the double differential cross-section for such transitions is presented [28]

$$\frac{d^2\sigma}{d\Omega dE_f} \propto \frac{k_f}{k_i} f(Q)^2 \sum_{i,j} \frac{e^{-E_i/k_BT}}{Z} |\langle v_i| \mathbf{M}_\perp |v_j\rangle|^2 \cdot \delta\left(\mathcal{E} - (E_i - E_j)\right) \tag{2.22}$$

where k_B is the Boltzmann constant, T is temperature and Z is the partition function $Z = \sum_i e^{-E_i/k_BT}$. $\mathbf{M}_\perp$ represents the part of the total magnetization operator $\mathbf{M}$ (defined in Section 1.2.2) that is perpendicular to the momentum transfer $\mathbf{Q}$. For scattering from polycrystalline material, the calculation of $|\langle v_i| \mathbf{M}_\perp |v_j\rangle|^2$ can be simplified to [28]

$$|\langle v_i| M_\perp |v_j\rangle|^2 = \frac{2}{3}\left(|\langle v_i| M_x |v_j\rangle|^2 + |\langle v_i| M_y |v_j\rangle|^2 + |\langle v_i| M_z |v_j\rangle|^2\right). \tag{2.23}$$

2.4 Polarized neutrons

A detailed treatment of neutron polarization analysis can be found in [27], [34] and [25]. Here we only summarize the main results regarding XYZ-polarization analysis, as it is of the most relevance to the thesis's work in Section 6.2.

During a scattering event, it is possible for a neutron to flip its spin state when scattered from a sample. Due to its spin 1/2 nature, a neutron spin can either be in a "up" state $|+\rangle$ or in a "down" state $|-\rangle$. Thus four different spin-state transitions could happen during a scattering event for an unpolarized neutron beam: $|+\rangle \rightarrow |+\rangle$, $|+\rangle \rightarrow |-\rangle$, $|-\rangle \rightarrow |-\rangle$ and $|+\rangle \rightarrow |+\rangle$. Even though these are not particular useful for unpolarized neutron scattering experiments, it turns out, by measuring these transition event separately, it is possible to obtain the nuclear-coherent (it also contains the isotope incoherent cross-section, hence denoted as nuc+ii), nuclear spin-incoherent (si) and magnetic (mag) cross-sections individually. To determine the polarization of neutron beam during an experiment, a quantity called flipping ratio, $F = \frac{N_+}{N_-}$ is introduced, where N_+ and N_- are the numbers of neutrons in the spin-up and spin-down states, respectively. Using the flipping ratio, the beam

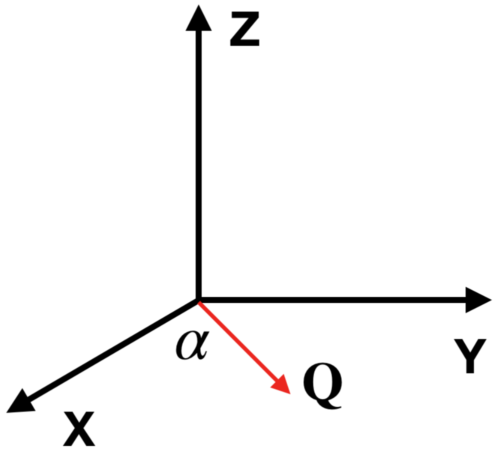

Figure 2.3: The geometry of an XYZ polarization analysis experiment. The incident neutron polarization alternates in the X-, Y- and Z- directions. The Schärpf angle α is defined as the angle between the X-axis and the scattering vector **Q**.

polarization P can be obtained:

$$P = \frac{N_+ - N_-}{N_+ + N_-} = \frac{F-1}{F+1}. \tag{2.24}$$

A typical value for a polarized neutron expeiment is $F = 20 - 30$, correspondingly $P = 90 - 95$ %.

The method we will be introducing is the so-called XYZ-polarization analysis. Here we only considered the most simple situation in which the scattering is limited within the XY plane only, as illustrated in Fig.2.3. For the treatment of an arbitrary scattering direction, it can be found in Ref [35]. The geometry of the XYZ polarization analysis is illustrated in Fig.2.3. The angle between the scattering vector **Q** and the X axis is called the Schärpf angle, denoted as α. Thus the unit scattering vector is **Q** $= (\cos\alpha, \sin\alpha, 0)$. We further assume the polarization of the neutrons received by the planar detectors is fixed, e.g. $|+\rangle$, and by varying the incident neutrons' polarization states, either $|+\rangle$ or $|-\rangle$, this gives rise to non spin-flip (NSF) $|+\rangle \rightarrow |+\rangle$ and spin-flip (SF) $|-\rangle \rightarrow |+\rangle$ events. Moreover, by alternating the polarization of the incident neutrons along three directions (X, Y and Z), we end up have six scattering cross-sections recorded by the detectors, and their compositions are listed as follow.

$$
\begin{aligned}
\left(\frac{d\sigma}{d\Omega}\right)_x^{\text{NSF}} &= \frac{1}{2}\sin^2\alpha\left(\frac{d\sigma}{d\Omega}\right)_{\text{mag}} + \frac{1}{3}\left(\frac{d\sigma}{d\Omega}\right)_{\text{si}} + \left(\frac{d\sigma}{d\Omega}\right)_{\text{nuc+ii}} \\
\left(\frac{d\sigma}{d\Omega}\right)_x^{\text{SF}} &= \frac{1}{2}\left(\cos^2\alpha + 1\right)\left(\frac{d\sigma}{d\Omega}\right)_{\text{mag}} + \frac{2}{3}\left(\frac{d\sigma}{d\Omega}\right)_{\text{si}} \\
\left(\frac{d\sigma}{d\Omega}\right)_y^{\text{NSF}} &= \frac{1}{2}\cos^2\alpha\left(\frac{d\sigma}{d\Omega}\right)_{\text{mag}} + \frac{1}{3}\left(\frac{d\sigma}{d\Omega}\right)_{\text{si}} + \left(\frac{d\sigma}{d\Omega}\right)_{\text{nuc+ii}} \\
\left(\frac{d\sigma}{d\Omega}\right)_y^{\text{SF}} &= \frac{1}{2}\left(\sin^2\alpha + 1\right)\left(\frac{d\sigma}{d\Omega}\right)_{\text{mag}} + \frac{2}{3}\left(\frac{d\sigma}{d\Omega}\right)_{\text{si}} \\
\left(\frac{d\sigma}{d\Omega}\right)_z^{\text{NSF}} &= \frac{1}{2}\left(\frac{d\sigma}{d\Omega}\right)_{\text{mag}} + \frac{1}{3}\left(\frac{d\sigma}{d\Omega}\right)_{\text{si}} + \left(\frac{d\sigma}{d\Omega}\right)_{\text{nuc+ii}} \\
\left(\frac{d\sigma}{d\Omega}\right)_z^{\text{SF}} &= \frac{1}{2}\left(\frac{d\sigma}{d\Omega}\right)_{\text{mag}} + \frac{1}{3}\left(\frac{d\sigma}{d\Omega}\right)_{\text{si}}
\end{aligned}
\tag{2.25}
$$

With some algebra manipulations, the magnetic differential cross-section can be calculated independently in two different ways, see Eq.(2.26), and in practice we are mostly interested in the average of the two.

$$
\begin{aligned}
\left(\frac{d\sigma}{d\Omega}\right)_{\text{mag}} &= 2\left[\left(\frac{d\sigma}{d\Omega}\right)_x^{\text{SF}} + \left(\frac{d\sigma}{d\Omega}\right)_y^{\text{SF}} - 2\left(\frac{d\sigma}{d\Omega}\right)_z^{\text{SF}}\right] \\
\left(\frac{d\sigma}{d\Omega}\right)_{\text{mag}} &= 2\left[2\left(\frac{d\sigma}{d\Omega}\right)_z^{\text{NSF}} - \left(\frac{d\sigma}{d\Omega}\right)_x^{\text{NSF}} - \left(\frac{d\sigma}{d\Omega}\right)_y^{\text{NSF}}\right]
\end{aligned}
\tag{2.26}
$$

For the nuclear-coherent and nuclear spin-incoherent cross-sections, we have

$$
\begin{aligned}
\left(\frac{d\sigma}{d\Omega}\right)_{\text{nuc+ii}} &= \frac{1}{6}\left[2\left(\frac{d\sigma}{d\Omega}\right)^{\text{Tol NSF}} - \left(\frac{d\sigma}{d\Omega}\right)^{\text{Tol SF}}\right] \\
\left(\frac{d\sigma}{d\Omega}\right)_{\text{si}} &= \frac{1}{2}\left(\frac{d\sigma}{d\Omega}\right)^{\text{Tol SF}} - \left(\frac{d\sigma}{d\Omega}\right)^{\text{mag}}
\end{aligned}
\tag{2.27}
$$

where the upperscripts Tot NSF and Tot SF refer to the total NSF and total SF cross-sections respectively.

3 Experimental Techniques

Throughout the project, a number of experimental techniques were employed. These include not only thermodynamic material characterization methods, such as DC magnetic susceptibility, magnetization and specific heat, but also involves various scattering techniques for an in-depth understanding on a microscopic level regarding systems' structures and Hamiltonians. In this thesis's work, neutron diffraction, inelastic and polarization neutron scattering experiments were performed. All these techniques are described in this chapter.

3.1 Thermodynamic material characterization methods

As mentioned in Section 1.3, characterizing materials' properties such as their specific heats or susceptibilities are effective ways to extract physical quantities such as magnetic ordering temperatures, effective moments and Curie-Weiss temperatures. Moreover, by varying external physical quantities in these measurements, such as magnetic field, temperature or pressure, the measured results can be used to obtain the phase diagram of a material with the external quantities as independent variables. Most of these kinds of experiments can be done at university laboratories and are relatively easy to conduct. In general, the measurements are also fast, producing a large amount of data in a short time scale. However only macroscopic physical quantities are measurable in these type of experiments. In order to interpret the results, an understanding on a microscopic level is often of necessity. For this purpose, additional measurements such as neutron scattering experiments and theoretical calculations are often needed.

Vibrating sample magnetometer. The vibrating sample magnetometer (VSM) for conducting magnetization and DC magnetic susceptibility measurements in Chapter 5 and 6 is a Quantum Design Physical Properties Measurement System (PPMS) at DTU Chemistry.

The magnetometer consists of a cryostat able to cool down to 1.5 K and a DC magnetic field up to 9 T along the vertical direction, together with a linear motor for vibrating the sample under study and a pickup coilset for detection. The measurement is accomplished by oscillating the sample around the pickup coil and synchronously measuring the voltage induced [36]. The basic theory behind the scene for a VSM is Faraday's law of induction: a changing magnetic flux will induce a voltage in the pickup coil, which is given by the following equation:

$$V_{\text{coil}} = \frac{d\Phi}{dt} = \left(\frac{d\Phi}{dz}\right)\left(\frac{dz}{dt}\right) \tag{3.1}$$

where Φ is the magnetic flux through the pickup coil and z is the vertical position of the sample with respect to the coil, controlled by the linear motor. For a sinusoidally oscillating sample position, the induced voltage takes the form [36]

$$V_{\text{coil}} = 2\pi f C m A \sin\left(2\pi f t\right) \tag{3.2}$$

where C is a coupling constant, A is the amplitude of oscillation and f is the associated frequency. These are the known quantities for a given measurement. For acquiring the DC magnetic moment m of the sample, the measuring of the coefficient $2\pi f C m A$ in the sinusoidal voltage response from the pickup coil is thus required [36].

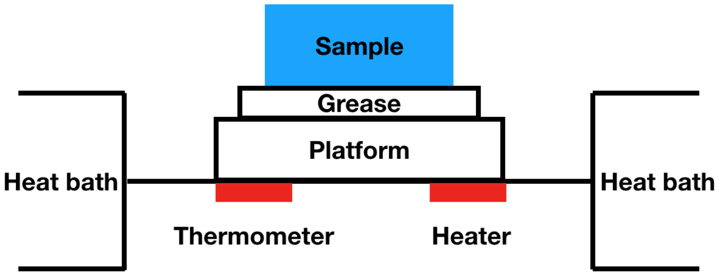

Figure 3.1: Schematic of heat capacity experimental setup in the PPMS. Adapted from Ref [37].

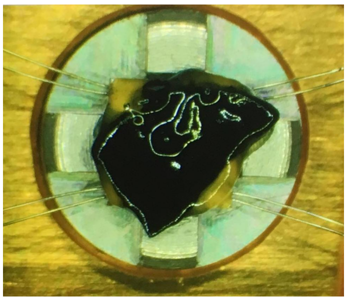

Figure 3.2: A $GaCl_2$(pyrazine)$_2$ powder pellet as mounted in the PPMS.

Heat capacity measurement. The heat capacity measurements presented in Chapter 6 were using a Quantum Design PPMS at EPFL Lausanne with applying external magnetic field from 0 T to 14 T. As shown in Fig.3.1, a sample is mounted on a platform to which the wires provide electric connection, and thin layer of grease is placed in between the sample and the platform for ensuring thermal contact. In Fig.3.2, the sample under study is a powder pellet of $GaCl_2$(pyrazine)$_2$ of the mass of 5.7 mg. Due to the air sensitive nature of the material, the sample was covered with a thick layer of grease to protect it from oxidisation.

Heat capacity measuring process is similar to the charging and discharging processes of a capacitor. For conducting measurements on a material, during each measurement cycle, a heating period followed by a cooling period is performed [37]. The obtained temperature response of the platform from this entire heating-and-cooling process is fitted to a model which takes into account both the thermal relaxation of the platform to the bath temperature and the relaxation between the platform and the sample itself [37]. From the fit, the correct heat capacity of the sample and the associated errorbar can be obtained.

3.2 Neutron scattering experiments

The neutrons generated from either a nuclear fission or a spallation process are too high in energy (in the MeV range) to perform any scattering experiments. To slow the hot neutrons down, collisions with other atoms or substances is needed to shift the energy down to the meV range required for scattering experiments in condensed matter research. This can be accomplished by using moderators made of light substances such as liquid H_2O or methane [28], with which the neutrons become thermally equilibrial when the moderator is kept at a constant temperature T. After the moderator the neutrons follow a Maxwellian

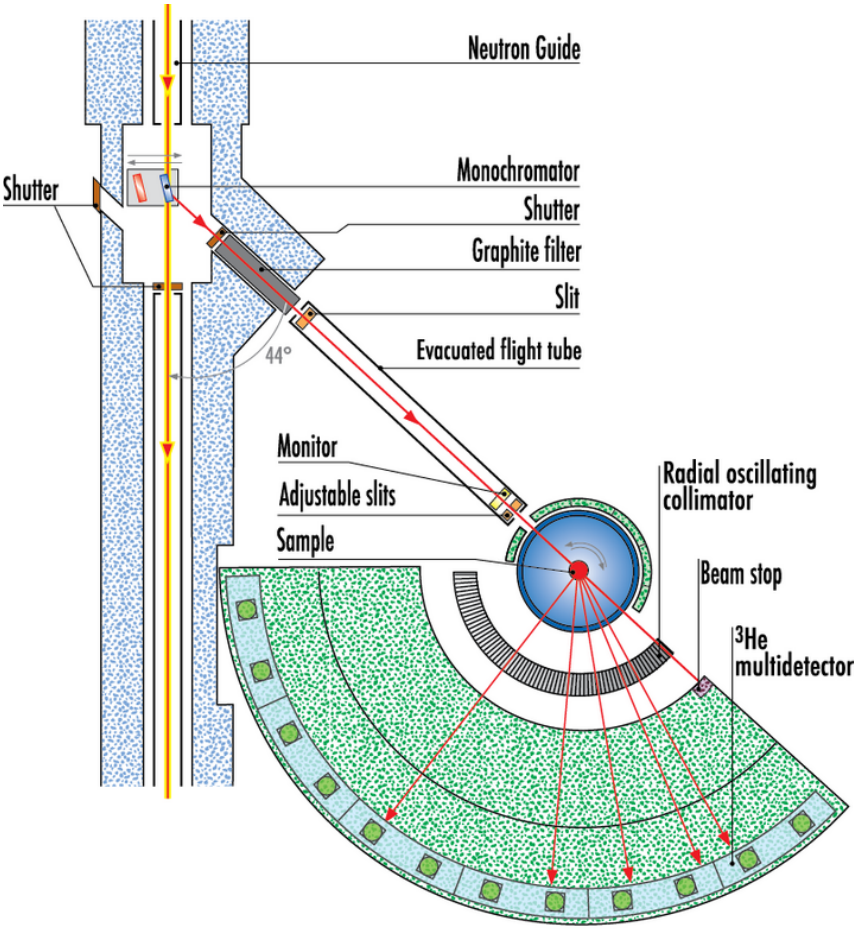

Figure 3.3: The instrument layout of D1B at the Institut Laue-Langevin, France

distribution [28]

$$\text{Dist}(\lambda) \propto \frac{1}{\lambda^3} \exp\left(-\frac{h}{2k_B T m_n \lambda^3}\right) \tag{3.3}$$

where λ is the wavelength of the neutrons.

Once the neutrons have been produced and moderated, it is necessary to transport them to the required beamline positions. The neutron flux at an instrument at a distance r from the source reduces dramatically according to the well-known law for isotropic radiation [28]: flux $\propto r^{-2}$. To overcome this, neutrons are transported inside neutron guides, which are made of so-called supermirrors consisting of a sequences of alternating layers of high positive (e.g. Ni) and negative (e.g. Ti) scattering length materials [28]. When neutrons impinge on the mirrors with an scattering angle below the critical angle γ_c, total external reflection occurs and the flux at the instrument position is increased significantly compared to a conventional beam tube.

3.2.1 Neutron diffraction

The diffraction experiments included in this thesis were nearly all performed on continuous source based powder diffractometers. In Fig.3.3, we show a typical layout of such an instrument taken from the powder diffractometer D1B at the Institut Laue-Langevin. Once the neutrons have been transported to the instrument position, they first impinge on a monochromator where only neutrons of the desired wavelength λ_0 or the higher-orders $(\lambda_0/2, \lambda_0/3, \dots)$ are reflected. To eliminate the high order reflections, a beam filter is

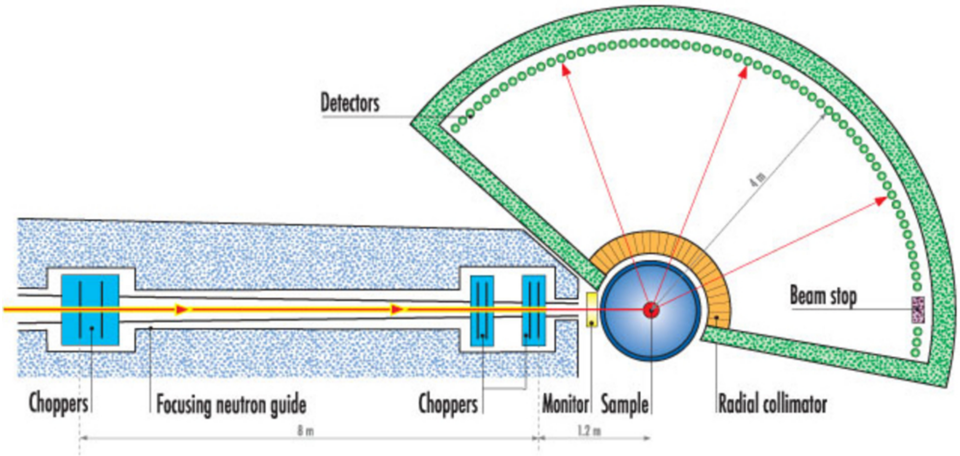

Figure 3.4: The instrument layout of IN5 at the Institut Laue-Langevin, France

placed in the beam, such as a Be filter. For a Be filter, neutrons with wavelengths below the cutoff wavelength (4 Å) are completely scattered out of the beam, whereas the large-wavelength neutrons pass the filter almost intact [28]. Afterwards, the neutron beam is transported to the sample position through a evacuated flight tube with the beam size controlled by adjustable slits. The scattered neutrons from the sample are collected by ^{3}He detectors. The Radial Oscillating Collimator (ROC) eliminates the parasitic diffraction from the sample environment.

The recorded scattering pattern from the detectors is a function of the scattering angle 2θ and is proportional to the differential scattering cross-section of the material. On top of that, the scattering intensity is also modulated by a geometric factor relating to the instrument itself, the so-called Lorentz factor [25].

$$\text{Lorz}(2\theta) = \frac{1}{4\sin\theta \times 2\pi \sin 2\theta} \tag{3.4}$$

As a final remark, the data obtained from a neutron powder diffractometer as illustrated in Fig.3.3 contains contributions from both elastic and inelastic channels. However compared to the elastic part, the inelastic signals are extremely weak and mostly contribute to the background only. Therefore even though the detectors cannot distinguish the contributions from the two channels, it is not a big concern in practice as the collected full spectrum is dominated by the elastic contribution.

3.2.2 Neutron spectroscopy

The inelastic experiments included in the thesis were taken from pulse source based inelastic scattering spectrometers, all of which are operated according to the so-called time-of-flight (TOF) method [28]. In Fig.3.4, we show a representative layout of a TOF inelastic neutron scattering spectrometer IN5 at the Institut Laue-Langevin.

Owing to the fact that, in scattering experiments neutrons normally have velocities of the order of a few hundred to a few thousand m/s, their energies can be determined by measuring the time taken to travel from one position to another given the known distance between the two positions. To quantify the energy transfers during a scattering event, either E_i or E_f needs to be known in advance. This distinguishes direct and indirect geometry spectrometers.

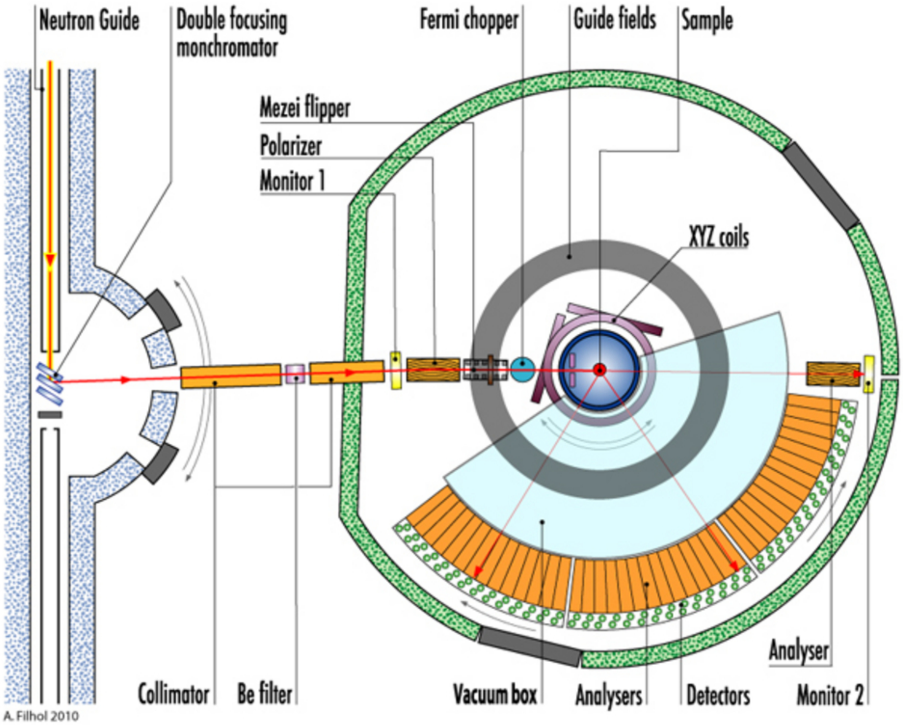

Figure 3.5: The instrument layout of D7 at the Institut Laue-Langevin, France

- **E_i is fixed (direct geometry).** In such a geometry, by measuring the time taken by a scattered neutron to travel from the sample position to the detector bank, it is possible to determine the final energy E_f of the neutron. The energy transfer $\mathcal{E}$ and the amplitude of the final wavevector k_f thus can be determined by $\mathcal{E} = E_i - E_f$ and $k_f = \sqrt{\frac{2m_n E_f}{\hbar^2}}$. Given the position of each detector in a laboratory coordinate system and the amplitude of the final wavevector $\mathbf{k}_f$, the final wavevetor $\mathbf{k}_f$ can be deduced, hence the scattering vector $\mathbf{Q} = \mathbf{k}_i - \mathbf{k}_f$ is found as well.

- **E_f is fixed (indirect geometry).** For indirect geometry spectrometers it is the final energy E_f that being fixed. By measuring the time taken by an incident neutron to travel from the choppers to the sample position, the incident energy E_i and wavevector $\mathbf{k}_i$ can be determined. Given the prior knowledge of $\mathbf{k}_f$ and E_f, it is easy to determine the energy transfer $\mathcal{E} = E_i - E_f$ and the scattering vector $\mathbf{Q} = \mathbf{k}_i - \mathbf{k}_f$ respectively.

For shaping neutron pulse width and filter out the undesired wavelengths from incident neutrons, several choppers are placed in front of the sample position to fulfill such purpose. Moreover, modern time-of-flight inelastic scattering spectrometers use with the so-called Repetition Rate Multiplication (RRM) technique[38] in which the choppers are configured to allow the passage of several monochromatic beams onto the sample. This scheme allows efficient use of the pulsed neutron source and permits the simultaneous interrogation of the excitation spectrum over different momentum and energy transfer ranges, $\mathbf{Q}$ and $\mathcal{E}$.

3.2.3 XYZ-polarization analysis

In this thesis'work, there was a single diffraction experiment conducted on the spectrometer D7 at the Institut Laue-Langevin with polarized neutrons and XYZ-polarization analysis. D7 is a diffuse scattering spectrometer dedicated to study the often neglected portions of

Supermirror polarizer [28]	The total reflection from a supermirror polarizer has constructive interference for one spin state of incident neutrons and destructive interference for the other.
Spin flipper [28]	A spin flipper is a set of coils inside which the magnetic field is perpendicular to both the polarization and the flight direction of the neutrons. With the application of the Larmor procession, neutrons passing through the coil experience a sudden field change and perform a procession with respect to the field direction. The resultant polarization direction depends on the incoming neutron velocity, the thickness of the coil and the applied field strength.

Table 3.1: Concepts of supermirror polarizer and spin flipper.

neutron scattering patterns of crystalline materials: the regions between the nuclear and magnetic Bragg peaks where the information on nuclear and magnetic structural disorder that is usually hidden. To achieve this purpose, D7 fulfills a number of stringent criteria [34]: (i) Relaxed the Q resolution in favour of high neutron flux; (ii) Relatively low instrumental background; (iii) Equipped with the ability to perform polarization analysis, so that the nuclear coherent, nuclear spin incoherent and magnetic scattering contributions can be separate unambiguously as explained in Section 2.4.

The instrument layout of D7 is shown in Fig.3.5. A double focusing graphite monochromator, both vertically and horizontally, is applied for selecting neutrons of wavelength 3.1, 4.8 or 5.8 Å. The focused monochromatic beam is polarized using a supermirror polarizer, see Table 3.1. To ensure the neutron polarization of the beam is transported through the instrument, a magnetic guide field of around 10-20 G is applied. The neutron polarization is manipulated via a spin flipper, see Table 3.1, followed by a set of orthogonal Helmholtz xyz field coils placed around the sample position, which alternate the neutron polarization in x, y and z directions adiabatically. The detector bank is equipped with supermirror analysers (polarizers), allowing to perform XYZ-polarization analysis.

3.2.4 Expeiments conducted throughout this thesis's work

In Table 3.2, we list the materials presented in this thesis and the corresponding instruments conducting the investigations.

Material	Instrument
$Cu(DCOO)_2{\cdot}4D_2O$	A direct geometry spectrometer MAPS at the ISIS Neutron and Muon Source.
$(5CAP)_2CuCl_4$	An indirect geometry back-scattering spectrometer OSIRIS at the ISIS Neutron and Muon Source.
$Na_2Co_2TeO_6$	A direct geometry spectrometer MARI at the ISIS Neutron and Muon Source.
CrI_2(pyrazine-D_4)$_2$	A direct geometry spectrometer MARI at the ISIS Neutron and Muon Source.
$GaCl_2$(pyrazine-D_4)$_2$	A direct geometry diffuse scattering spectrometer D7 at the Institut Laue-Langevin.
$CrCl_2$(pyrazine-D_4)$_2$	A direct geometry spectrometer LET at the ISIS Neutron and Muon Source.
$CrCl_2$(pyrazine-D_4)$_2$	A direct geometry spectrometer MAPS at the ISIS Neutron and Muon Source.
CrI_2(pyrazine)$_2$	A powder diffractometer SPODI at the Heinz Maier-Leibnitz Zentrum.

Table 3.2: List of materials presented in this thesis and the corresponding instruments for conducting the experiments.

4 Quantum Square Lattice Antiferromagnet

The problem in which we are interested in this chapter is Heisenberg model on a square lattice

$$H = J \sum_{\langle i,j \rangle} \mathbf{S}_i \cdot \mathbf{S}_j \tag{4.1}$$

where the summation is over all nearest neighbour sites and J represents an isotropic Heisenberg exchange interaction. In particular, we focus on the scenario where J is antiferromagnetic ($J > 0$). In the classical limit, where spins **S** are treated as ordinary vectors, the neighbouring spins on the square lattice tend to be antiparallel to each other, in favor of minimizing the total energy of the system. Hence the ground state is an Néel state characterized by the propagation vector (π, π). The spin wave dispersion for the system along the high-symmetry directions in the Brillouin zone of a 2D square lattice is shown in Fig.4.1b. Due to the spontaneously antiferromagnetic ordering in the ground state, the SO(3) rotation symmetry imposed by the Hamiltonian is broken, which gives rise to the so-called Goldstone gapless energy modes at the zone center (π, π) and the equivalent positions. Moreover, along the zone-boundary direction, i.e. from $(\pi, 0)$ to $(\pi/2, \pi/2)$, the excitation is dispersion-less, which is a consequence of the fact that at these momenta the low-order spin wave Hamiltonian vanishes [39]. This also means due to the absence of the Bogoliubov rotation, the Bosons at the two sublattices of the square lattice are not mixed [39]. Hence within linear spin wave theory the spin waves are localized on a single sublattice [39].

When spins reclaim the quantum nature back, i.e. the commutation relations between its Cartesian components are preserved, and here we only consider the most quantum case with $S = 1/2$. Whereas no formal proof exists, numerical evidence unanimously indicates that the 2D quantum Heisenberg antiferromagnet on a square lattice (2DQHAFSL) orders only at T = 0 [40]. Similar to the classical case, the ordering wavevector is (π, π) but the sublattice magnetization is reduced to 60% of its classical expectation value, $\mu \approx 0.6\mu_B$. Moreover, the spin wave spectrum of a square lattice antiferromagnet undergoes a renormlization, (i) In the long wavelength limit, i.e. $\mathbf{q} \to (\pi, \pi)$, the spin wave velocity or the stiffness $\partial\omega_{\mathbf{q}}/\partial\mathbf{q}$ is modified by multiplying a constant $Z_c = 1.18$; (ii) In the short wavelength limit or along the zone boundary direction, the excitation is no longer flat. It has been demonstrated both experimentally and numerically [41, 42, 43, 39, 44] that there is a 6% - 7% depression of the spin wave energy and 50% loss of spectral weight of the spin wave peak at $(\pi, 0)$. In addition, the lost spectral weight is transferred to the continuum above the spin wave peak and it occurs in both transverse (1, 3, 5, ... odd number of magnon excitations) and longitudinal (2, 4, 6, ... even number of magnon excitations) fluctuation channels such that the continuum appears spin-isotropic at $(\pi, 0)$ even in the symmetry-broken antiferromagnetically ordered state. No consensus has been reached so far regarding why such dramatic changes occur. The essence of the debate lies in whether spinons or multi-magnons interact with the low lying (in energy) single magnon branch along the zone boundary direction. We will come back to this in section 4.1.2.

It is interesting to further investigate how the spin excitation spectrum of the 2DQHAFSL responds to any external influences. In this chapter, we touch upon the following two

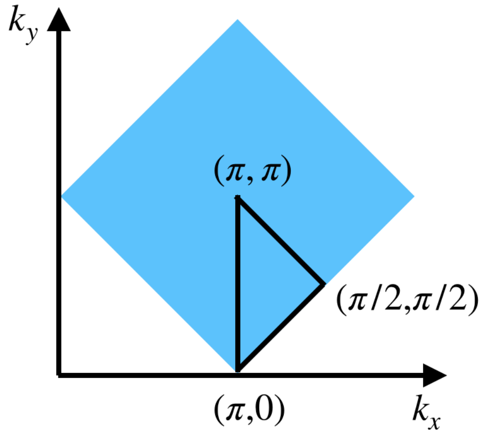

(a) High symmetry directions in the reciprocal space of a 2D square lattice.

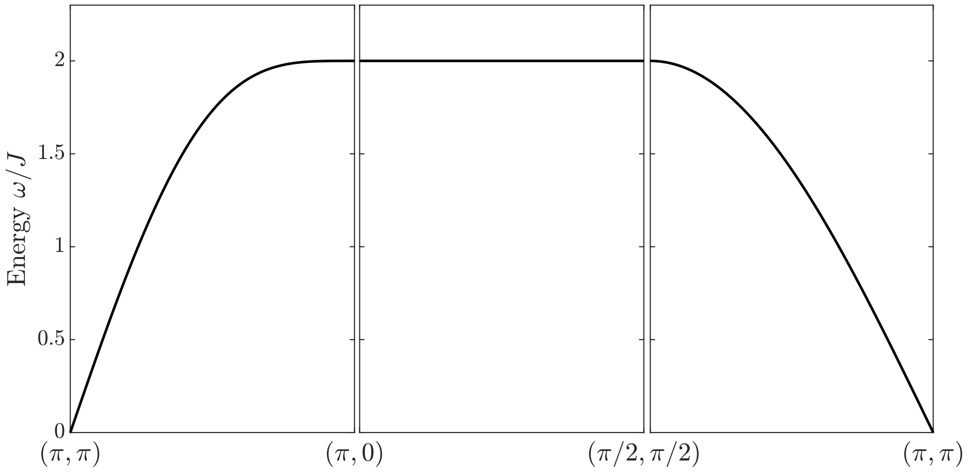

(b) Spin wave spectrum of the 2D classical Heisenberg antiferromagnetic square lattice along the high symmetry directions illustrated in Fig.4.1a.

Figure 4.1: (a) High symmetry directions in the reciprocal space of a 2D square lattice and (b) the spin wave dispersion along these directions calculated from linear spin wave theory.

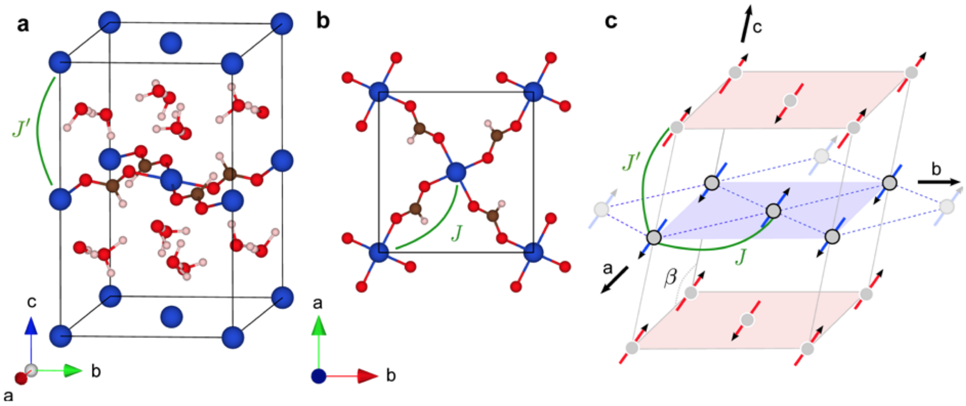

Figure 4.2: Crystal and magnetic structures of CFTD [42]. **a**, Three dimensional crystal structure of CFTD with Cu, O, C and D in blue, red, brown and grey spheres respectively. J' indicates the interlayer exchange interaction. **b**, Top view of CFTD. J is the dominant nearest neighbour exchange interaction. **c**, A sketch of the three dimensional magnetic structure with the spin directions slightly tilted away from a axis towards c axis.

J [meV]	J'	DM
6.19(2)	$10^{-5}J$	$0.05J$

Table 4.1: The exchange interactions in CFTD determined by various experimental methods as explained in the text. J stands for the nearest neighbour superexchange interaction which is also the dominant one in the material; J' is the interlayer coupling between the neighbouring copper-formate planes and DM represents the norm of the DM vector which is close to the **c** axis.

aspects, thermal fluctuations (section 4.1) and application of magnetic fields (section 4.2). We will present detailed studies of their direct impacts on the spectrum.

4.1 Temperature dependence of the excitation spectrum in a quantum square lattice antiferromagnet CFTD

To date, the best physical realization of the 2DQHAFSL is a metallo-organic compound Cu(DCOO)$_2$·4D$_2$O (CFTD). At room temperature, CFTD is monoclinic (space group P2$_1$/a), but under cooling undergoes an antiferroelectric transition at 246 K, which involves a doubling of the unit cell along the crystallographic **c** axis. At 100 K the space group is P2$_1$/n (non-standard setting of space group 14) with lattice constants $a = 8.113$ Å, $b = 8.119$ Å, $c = 12.45$ Å, and $\beta = 100°$. Within the **a** − **b** plane, the Cu^{2+} ions are coordinated by four oxygens from the formate molecules and form an almost ideal square lattice arrangement with nearest neighbor lattice constant 5.739 Å. The octahedral coordination is completed by oxygens from the crystal bound water molecules between the planes, see Fig.4.2a and Fig.4.2b.

Upon cooling, CFTD undergoes an antiferromagnetic transition at $T_N = 16.5$ K with a staggered magnetic moment of size $0.48(2)\ \mu_B$ determined by Burger *et al* [45], who also found that the spins are rotated $8°$ away from the **a** axis towards the **c** axis. The magnetic structure is shown in Fig.4.2c. The Curie-Weiss temperature of CFTD is $T_{\text{CW}} = -175$ K [46], and inelastic neutron scattering experiments have determined the antiferromagnetic exchange interaction $J = 6.19(2)$ meV [41] and no significant long range interactions were found within the copper-formate plane. Magnetization data [47, 48] revealed that the interlayer interaction J' is only of the order 10^{-5} of J and the symmetry allowed Dzyaloshinskii-Moriya (DM) interaction is around 5% of J with the DM vector close to the **c** axis. In Table 4.1, we summarize all the exchange interactions in CFTD.

The reciprocal space of CFTD is spanned by **a***, **b*** and **c***. For an arbitrary reciprocal lattice vector **Q**, it can be written as **Q** $= h$**a**$^* + k$**b**$^* + l$**c*** with h, k and l in reciprocal lattice units (r.l.u). Owing to the extremely weak interlayer interaction J', we only need to focus on the 2D plane in reciprocal space with $l = 0$. To be consistent with the theoretical notations, we re-define the reciprocal lattice vectors as **x**$^* := ($**a**$^* +$ **b**$^*)/2\pi$ and **y**$^* := ($**a**$^* -$ **b**$^*)/2\pi$. Any vectors on the 2D plane can be expressed as **q** $= q_x$**x**$^* + q_y$**y*** with $q_x = \pi(h+k)$ and $q_x = \pi(h-k)$.

4.1.1 The $(\pi, 0)$ anomaly in the excitation spectrum

The $(\pi, 0)$ anomaly refers to the aforementioned $6\% - 7\%$ softening in energy of the single magnon pole at $(\pi, 0)$ compared to $(\pi/2, \pi/2)$. Piazza and Mourigal *et al* [42] performed a detailed study of the magnetic fluctuations at both $(\pi, 0)$ and $(\pi/2, \pi/2)$ in CFTD utilizing the power of polarized neutrons. What they found is rather striking, see Fig.4.3. At $(\pi/2, \pi/2)$, the total dynamical structure is dominated by a resolution-limited single magnon peak (centered at $\omega = 2.38(2)J$) in the transverse channel, in accord with the conventional spin wave picture. The fluctuation in the longitudinal channel represents a weak continuum extending from $\omega/J \approx 2.3$ to 3.4 and only carries a small fraction of the total spectral weight compared to the sharp one-magnon peak in the transverse channel. In contrast, at $(\pi, 0)$ not only is the single magnon peak softened to $\omega = 2.19(2)J$, but there also exists a pronounced tail in the transverse channel starting right above the magnon peak maximum, and extending to $\omega/J \approx 3.8$. This tail together with the broad continuum in the longitudinal channel contributes $40(12)$% of the total spectral weight at $(\pi, 0)$ and the single magnon intensity is significantly reduced compared to $(\pi/2, \pi/2)$. To further compare the continua in both transverse and longitudinal channels at $(\pi, 0)$, the resolution limited magnon peak is subtracted from the transverse channel and the resultant is plotted on top of the scaled interpolated longitudinal fluctuation spectrum, see Fig.4.3d. Surprisingly, the two coincide with each other within error bars. The continuum at $(\pi, 0)$ therefore arises from isotropic correlations in spin space with $S^{\perp}(\mathbf{q}, \omega) = S^{xx}(\mathbf{q}, \omega) + S^{yy}(\mathbf{q}, \omega) = 2S^{zz}(\mathbf{q}, \omega)$, in sharp contrast to the continuum at $(\pi/2, \pi/2)$ which is essentially fully contained in the longitudinal channel.

4.1.2 Spinons or magnons?

Unlike La_2CuO_4 [49], the cause of the non-flat single magnon dispersion along the zone boundary direction in CFTD cannot attribute to long range interactions. As seen from Table 4.1, the second nearest neighbor interaction J' is five orders of magnitude smaller than J. Its effect on the dispersion is therefore negligible. The DM interaction on the nearest neighbor bonds, whose value is listed in Table 4.1, can only affect the spin excitations in the long wavelength limit and the short wavelength dynamics along the zone boundary direction stays intact, i.e. dispersionless. As the result, the observed $(\pi, 0)$ anomaly is a pure quantum mechanical effect directly associated with the quantumness in the 2DQHAFSL. To explain such a quantum effect, two possible pictures from drastically different views, i.e. spinons and magnons, are proposed as we shall discuss below.

A variational Monte Carlo [42] study based on the Gutzwiller-projected variational wavefunctions method indicated the isotropic continuum excitation at $(\pi, 0)$ arises from a deconfined pair of spinons. Whereas at $(\pi/2, \pi/2)$, the spinon pairs are confined spatially to form a single magnon [42]. Hence the physical pictures at $(\pi, 0)$ and $(\pi/2, \pi/2)$ were sug-

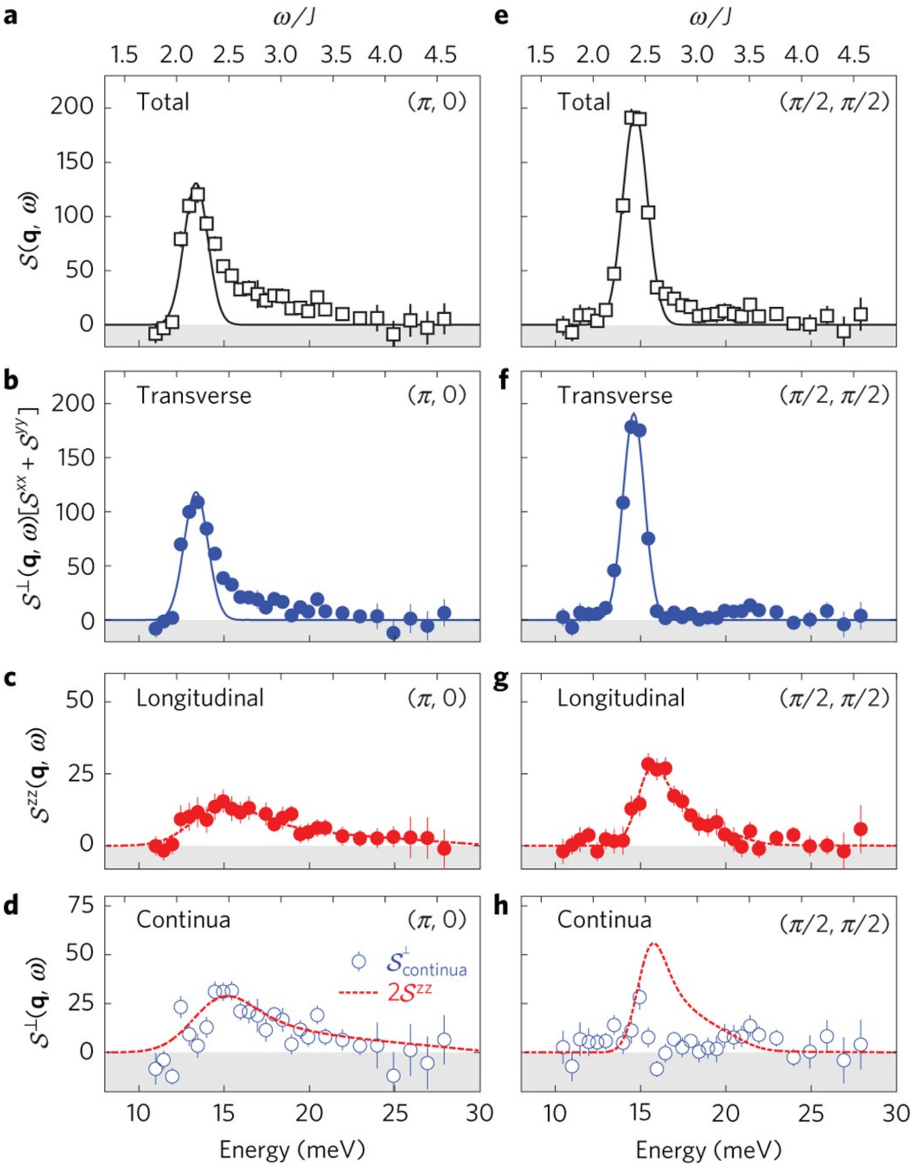

Figure 4.3: Polarized neutron scattering data at $(\pi, 0)$ and $(\pi/2, \pi/2)$ in CFTD [42]. **a**-**c**, Energy dependence of the total, transverse and longitudinal dynamical structure factors at $(\pi, 0)$ respectively. **e**-**g**, Energy dependence of the total, transverse and longitudinal dynamical structure factors at $(\pi/2, \pi/2)$ respectively. **d**,**h**, The resolution-limited one-magnon peak subtracted transverse dynamical structure factors at $(\pi, 0)$ and $(\pi/2, \pi/2)$ respectively, together with the scaled longitudinal dynamical structure factors.

gested to be drastically different. In recent years, due to the rapid development of both theoretical and numerical tools, more rigorous theoretical studies of this long-standing puzzle emerged. Although no consensus has been reached to date regarding the nature of the continuum excitation, it is worth noting that both magnon and spinon pictures can give a self-consistent description of the observed anomaly at $(\pi, 0)$.

Shao *et al* applied quantum momnte carlo (QMC) with the newly developed stochastic analytical continuation method to obtain the dynamical structure factor of the 2DQHAFSL [44]. Their results agree well with the extracted single-magnon dispersion from INS studies on CFTD [42], see Fig.4.4a, and the measured total dynamical structure factors at (π, 0) and ($\pi/2$, $\pi/2$), see Fig.4.4b. To elucidate the physical mechanism behind the anomaly, they added a four-spin interaction term Q in the Hamiltonian and observed a rapid reduction of the magnon weight at $(\pi, 0)$ upon its increasing, before the system undergoes a phase transition to a nonmagnetic spontaneously dimerized state [44]. Hence in their study, the anomaly at $(\pi, 0)$ is interpreted as a precursor to deconfined quantum criticality where one magnon fractionalizes into two nearly-deconfined spinon pairs. Motivated by the numerical results, they constructed an effective model where the spinons lie above the one magnon branch. The energy difference between the one-magnon and one-spinon branches reaches a minimum at $(\pi, 0)$ and a maximum at $(\pi/2, \pi/2)$. Hence upon including the interaction between the magnons and spinons, at $(\pi, 0)$, a single magnon splits into two inseparable spinons that fluctuate in and out of the magnon space [44]. Such an effective model not only reproduces the softening of one-magnon energy at $(\pi, 0)$, but also the spectral weight transfer from the magnon peak at $(\pi, 0)$ to the high energy continuum excitations as observed in the polarized neutron experiment [42], see Fig.4.3.

Powalski *et al* [43] approached the $(\pi, 0)$ anomaly from a pure magnon perspective without resorting to spinons. They adopted the so-called continuous similarity transformation (CST) which is performed in a non-perturbative fashion and applied it to the 2DQHAFSL. In their calculation, both the dispersion anomaly and the broad high energy continuum arise from strong magnon-magnon interactions in the system, see Fig.4.5. The attractive interaction between magnons is attributed to the two-magnon Higgs resonance (the excitations associated with the amplitude fluctuation of the order parameter) in the longitudinal channel. The broad spectral profile implies the Higgs resonance only lives for a short time as its energy lies within the two-magnon continuum into which it decays. The one-magnon softening and the high energy tail in the transverse channel at $(\pi, 0)$ is due to the attraction between the one magnon state and the three magnon continuum. The strong hybridization between them forbids the full decay of the magnon [50]. Instead it repels the one magnon state out of the three magnon continuum, giving rise to the observed anomaly [39, 50].

Although the two approaches from seemingly different perspectives both offer satisfactory descriptions of the experimental data, they could actually have a same origin, as pointed out in Ref [44]. The strong attraction between magnons in the 2DQHAFSL might be mediated by spinon pairs. In this case it is possible to give a accurate description of the spin excitation without invoking spinons.

4.1.3 Temperature evolution of the excitation spectrum

In this context, it is interesting to investigate how the thermal fluctuation influences the spin excitation in CFTD as the long range antiferromagnetic order is destroyed, leading to a paramagnetic state with only short range correlations [51]. For such purpose, an inelastic neutron scattering experiment was performed to offer the insight into the thermal evolution of the spin excitation spectrum. The sample used in the inelastic neutron scattering

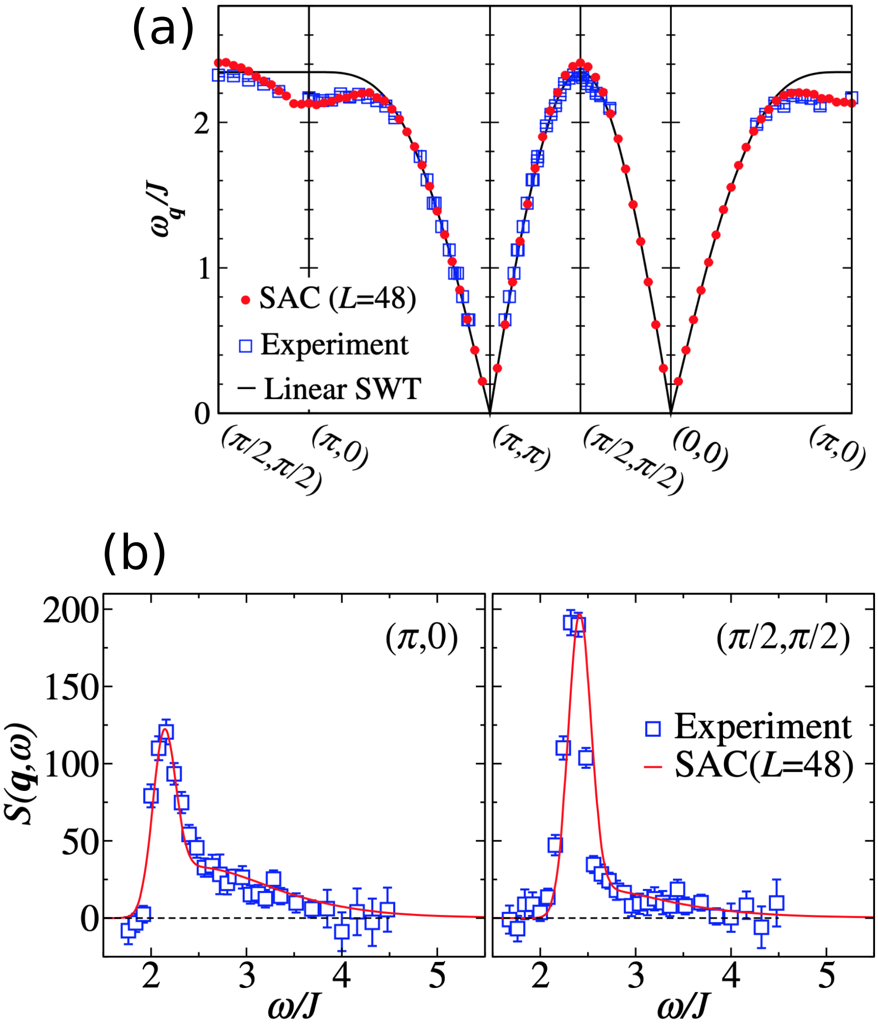

Figure 4.4: Prediction from spinon picture: the comparison between the experimental data on CFTD and numerical results obtained from QMC+SAC, taken from Ref [44]. **a**, The one-magnon dispersion calculated from SAC and the extracted experimental dispersion. **b**, The total dynamical structure factors obtained from SAC and the experimentally determined counterparts at $(\pi, 0)$ and $(\pi/2, \pi/2)$ respectively [44].

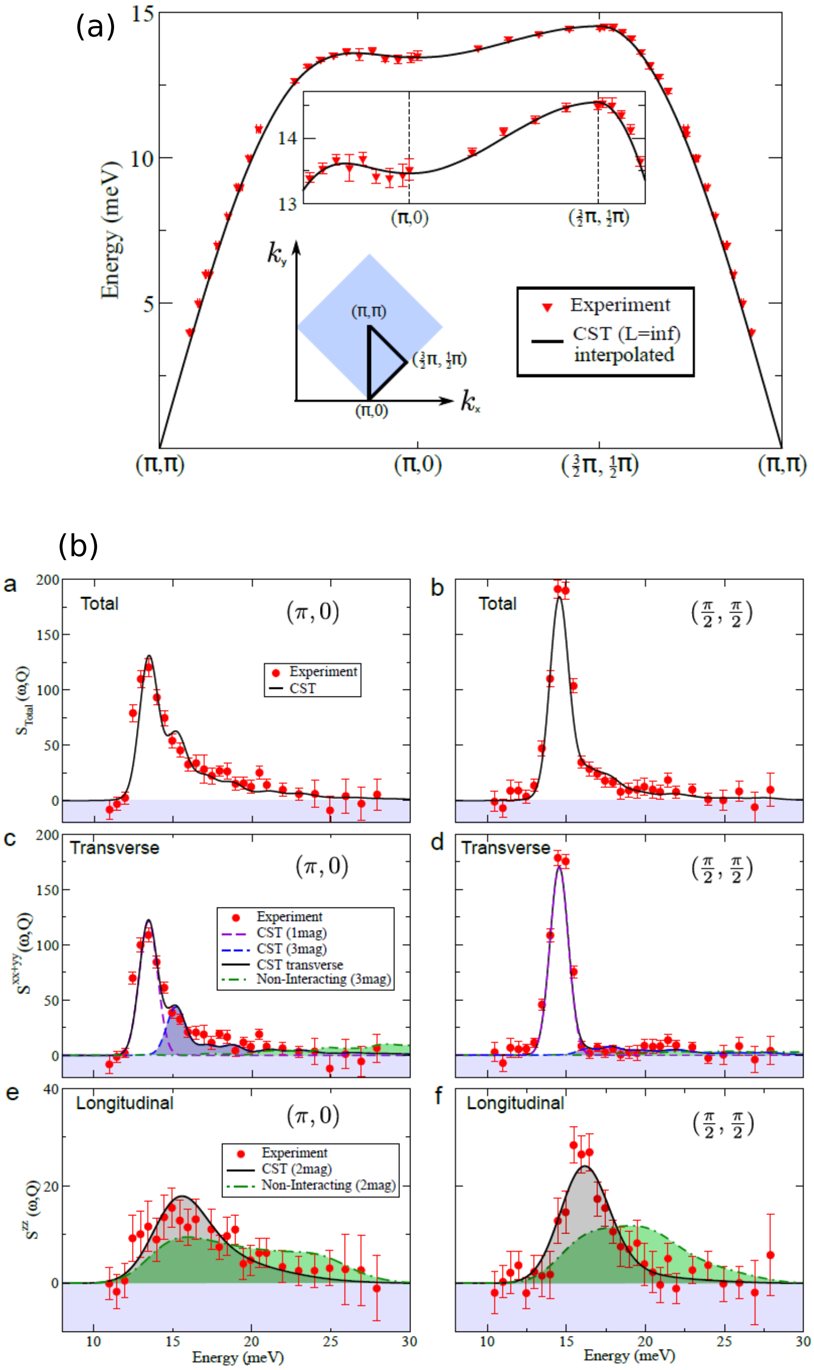

Figure 4.5: Prediction from magnon picture: comparison between the experimental data on CFTD [42] and theoretical results obtained from CST, taken from Ref [43]. **a**, The extracted one-magnon dispersion [42] from INS measurement together with the theoretical dispersion. **b**, Comparison between the measured dynamical structure factors and the theoretical lineshapes obtained from CST at both $(\pi, 0)$ and $(\pi/2, \pi/2)$ respectively.

experiment consisted of three co-aligned high-quality solution grown single crystals. The total weight of the crystals was approximately 12 grams. The experiment was conducted on a direct geometry TOF spectrometer MAPS at the ISIS Facility, Rutherford Appleton Laboratory (UK) by Mourigal, Christensen *et al* before the start of this PhD project. For exploring the two-dimensional nature of the spin correlation in CFTD, the reciprocal directions $\mathbf{a}^*$ and $\mathbf{b}^*$ were kept perpendicular to the neutron beam direction. The incident neutron energy was set to 36.25 meV during the experiment with the Fermi chopper spinning at 200 Hz. The energy resolution at the energy of the zone boundary magnon, $\omega = 2Z_cJ = 14.5$ meV, was 1.3 meV (FWHM). This configuration allowed a detailed study of the full dynamics of the spin correlation function $S(\mathbf{Q}, \omega)$, where **Q** is the projection of the three dimensional scattering vector on the $\mathbf{a}^* - \mathbf{b}^*$ plane. Six sets data were collected at 6 K, 20 K, 35 K, 40 K, 50 K and 80 K, corresponding to T/J =0.08, 0.28, 0.49, 0.56 and 1.11 respectively.

The thermal evolution below and above the Néel temperature $T_N = 16.5$ K of the spin and lattice excitations along the high-symmetry directions in the Brillouin zone is illustrated in Fig.4.6. To produce these plots, the raw data were symmetrized over four equivalent quadrants in the Brillouin zone covered by the central detector bank on MAPS. To further increase the statistical quality of the data, two highly similar data sets taken at 35 K and 40 K, see Fig.4.7a and b, were combined (averaged with respect to the total flux) and labelled as the 38 K data. In Fig.4.7c, we also illustrated the spectrum collected at 80 K. Below 4 meV, there is a broad diffuse scattering in the spectrum which might have a magnetic origin. Apart from that, the 80 K spectrum is dominated by scattering from lattice vibrations. This justifies the suitability of treating 80 K spectrum as an effective phonon background for subtraction purpose as we shall see later. The most prominent feature in the data obtained at 6 K (Fig.4.6a) is the dispersive spin excitation emanating from the zone center (π, π) and reaching the maximum energy 14.5 meV at $(\pi/2, \pi/2)$. The spin excitations along the zone boundary direction, from $(\pi/2, \pi/2)$ to $(\pi, 0)$, are immediately evident to be dispersive and softened in energy at $(\pi, 0)$, as reported in previous studies on the spin exitations in the ordered phase of CFTD [41, 42]. The depression in intensity of the magnon peak at $(\pi, 0)$ compared to the peak at $(\pi/2, \pi/2)$ is also identifiable, illustrated by the clear difference in the 2D colormap. Besides the spin excitations, Fig.4.6 also illustrates the contributions from phonons. Notably two nearly flat bands of phonon scattering with weakly momentum dependence, are observed at 7.5 meV and 20 meV respectively.

Comparing Fig.4.6a and Fig.4.6b, it is evident the dispersion of the spin excitations at 6 K, below $T_N = 16.5$ K, is similar to the dispersion at 20 K, above T_N. A slight broadening of the excitations is discernible at low energy transfers, whereas the excitations along the zone boundary direction experience an overall intensity decrease. At higher temperatures, 38 K (Fig.4.6c) and 50 K (Fig.4.6d), the high energy excitations start losing definition, as they gradually become indistinguishable from the phonon scattering signals, which dominate the spectra at high temperatures. In the long wavelength limit, the spin excitations are further broadened and become diffuse at 50 K.

The evolution of the spin excitations above 20 K becomes clearer after subtraction of the 80 K spectrum (with its Bose occupation factor being corrected) from the low temperature spectra. The result is shown in Fig.4.8. Although the subtraction appears to be not perfect, as evident from the residual phonon scattering at 7.5 meV and 20 meV which cannot be eliminated completely, the remnant contribution is easily identifiable and its weak **Q**-dependent dispersion and intensity do not impair the credibility of the analysis presented below.

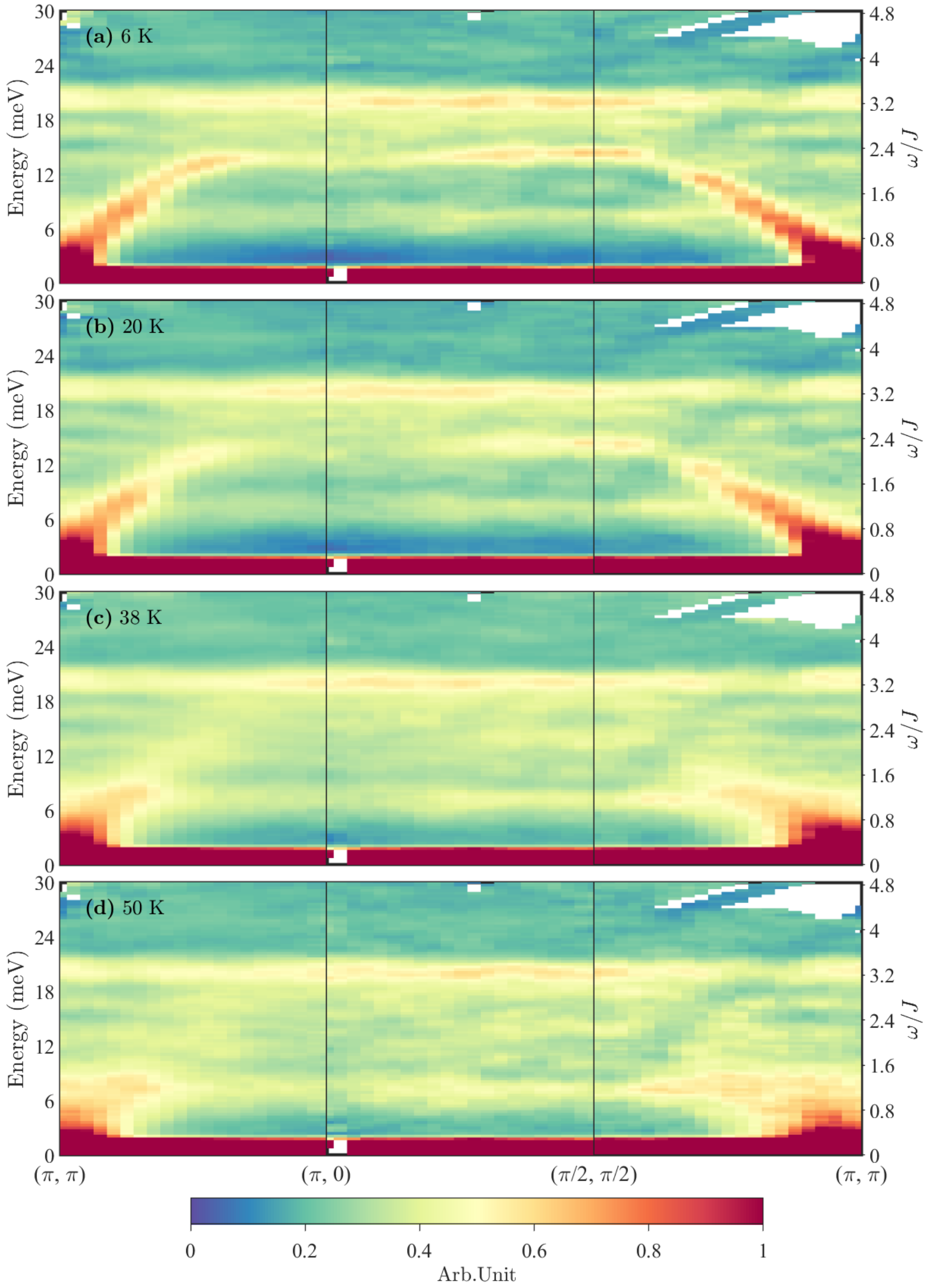

Figure 4.6: Overview of the magnetic and lattice excitation spectra of CFTD at (a) 6 K, (b) 20 K, (c) 38 K and (d) 50 K (The 38 K data set in panel (c) is the average of raw data obtained at 35 K and 40 K as explained in the text) measured by time-of-flight inelastic neutron scattering. The momentum axis follows the standard path around the Brillouin zone of a 2D square lattice as shown in Fig.4.1a. Intensities are shown in arbitrary units.

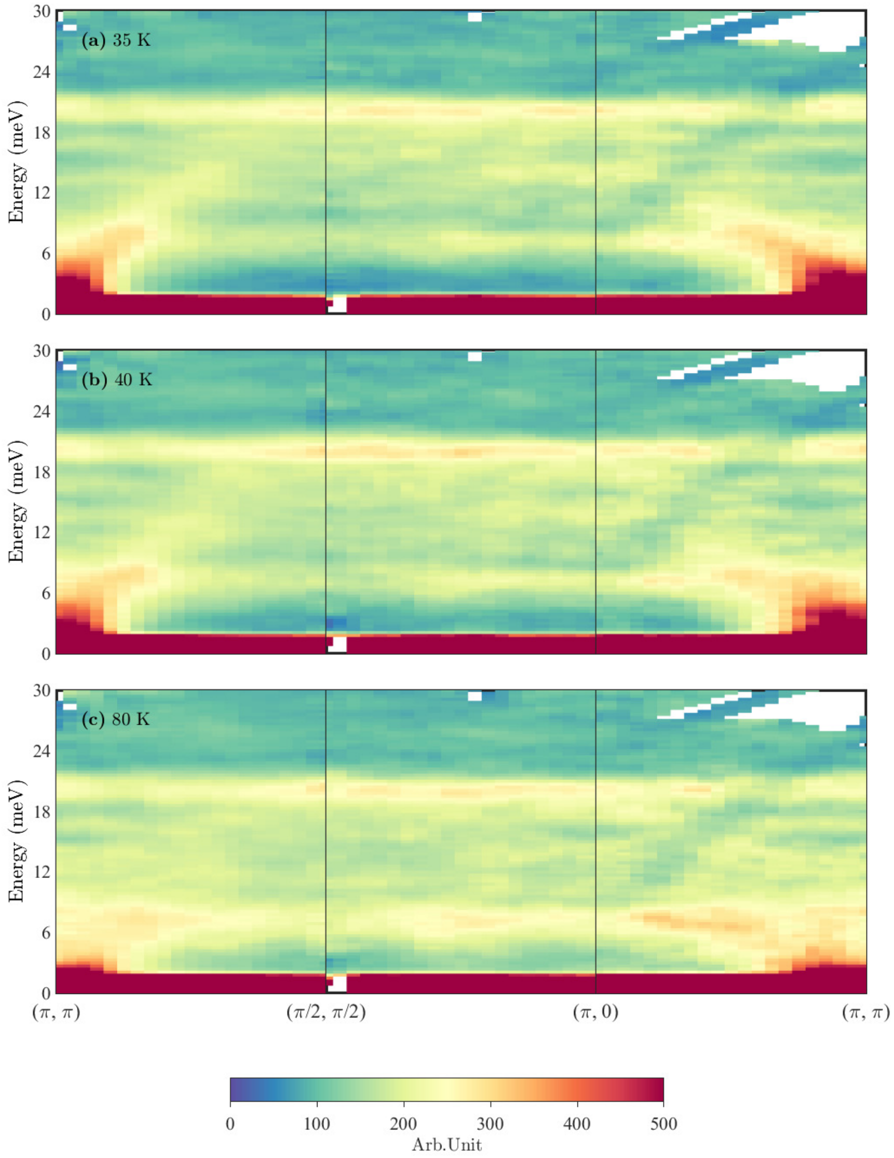

Figure 4.7: Color spectra of the magnetic and lattice excitation spectra of CFTD at (a) 35 K, (b) 40 K and (c) 80 K measured by time-of-flight inelastic neutron scattering. The momentum axis follows the standard path around the Brillouin zone of a 2D square lattice as shown in Fig.4.1a. Intensities are shown in arbitrary units.

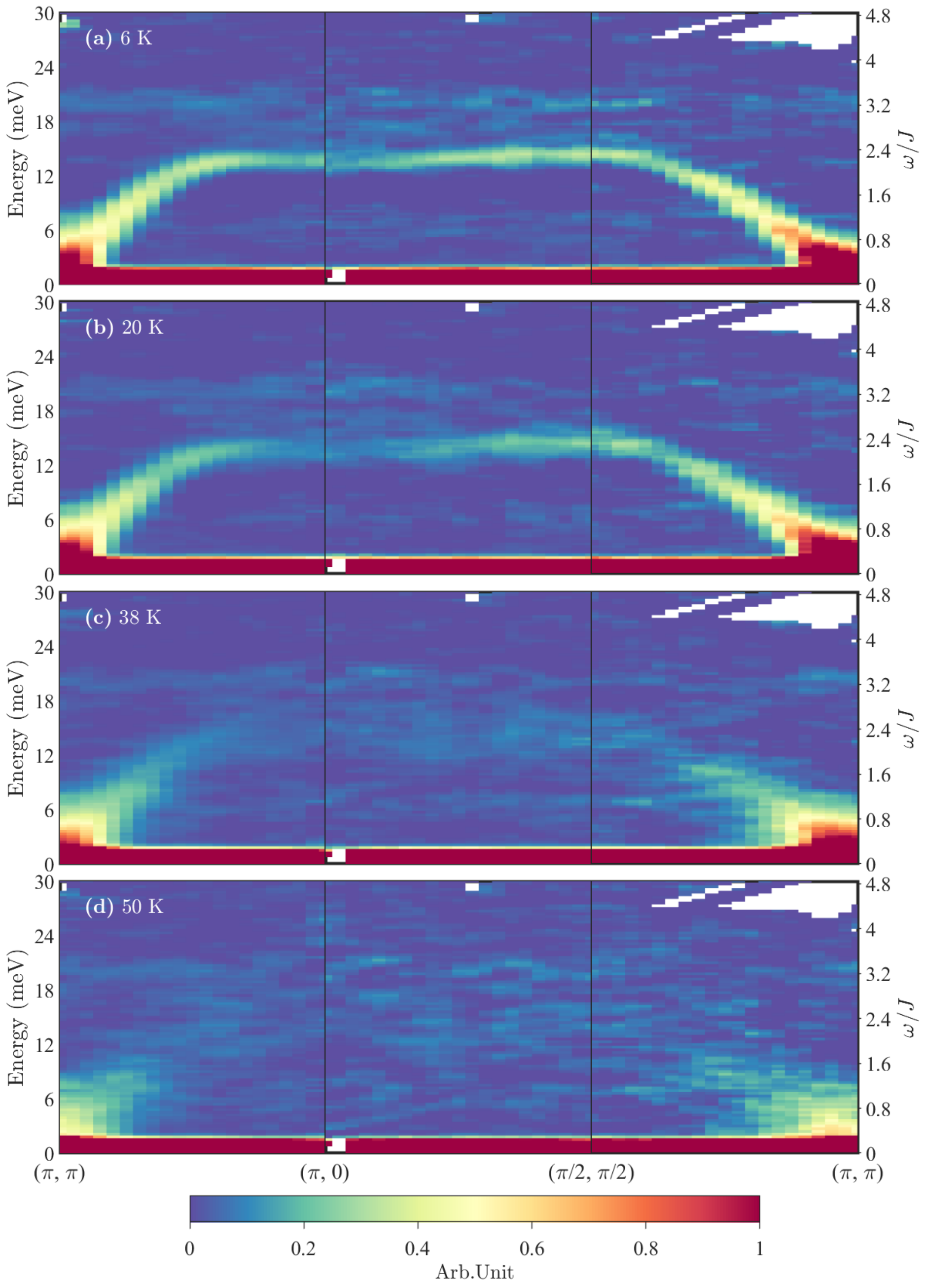

Figure 4.8: Magnetic excitation spectra, S(**Q**,ω), of CFTD for temperatures (a), 6 K. (b), 20 K, (c), 38 K and (d), 50 K after subtracting the 80 K spectrum corrected for the Bose occupation factor.

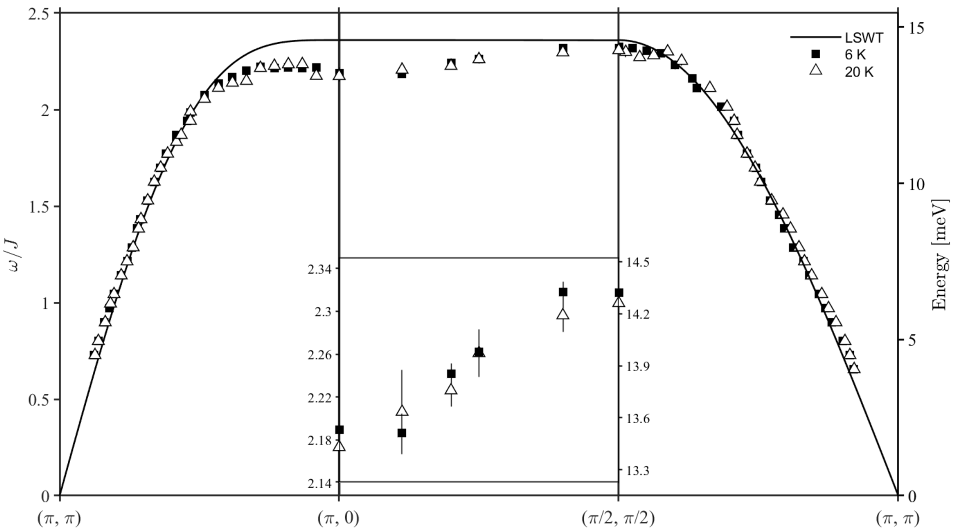

Figure 4.9: The extracted dispersion of the magnetic excitations along the high-symmetry directions in the Brillouin zone at 6 K (filled squares) and 20 K (open triangles), respectively. The inset shows the detailed dispersion along the zone boundary. The solid line represents linear spin wave theory with $J = 6.19$ meV.

Fig.4.8a and Fig. 4.8b confirm the conclusion drawn from Fig.4.6a and Fig.4.6b, i.e. neither the existence of $(\pi, 0)$ anomaly, nor the decrease of single-magnon intensity at $(\pi, 0)$ compared to $(\pi/2, \pi/2)$ are dependent on whether the sample is in a magnetically ordered state or at a temperature just above T_N. As the temperature keeps increasing, the previous difficult-to-identify high energy excitations now becomes visible, manifesting as broad and diffuse intensity bands. This can be seen from Fig.4.8c and Fig.4.8d.

To further quantify the evolution of spin excitation dispersion through the antiferromagnetic to paramagnetic phase transition, the spectra in Fig.4.6a and Fig.4.6b were separated into low and high energy regions. Gaussian lineshapes and linear backgrounds were fitted to constant energy cuts for the low energy part, and constant momentum cuts for the high energy regions. Fig.4.9 shows the results of the fitting. Here the plotted dispersion is normalized by the exchange energy $J = 6.19$ meV. Evidently, the magnon dispersion is essentially indistinguishable at 6 K and 20 K, implying the anomaly at $(\pi, 0)$ and the zone boundary dispersion manifest themselves as intrinsic properties of the 2DQHAFSL and are not dependent on the existence of 3D long range order.

4.1.4 Results and analysis

Thermal evolution of the zone boundary spectra

In order to investigate the thermal evolution of the spectrum at $(\pi, 0)$ relative to $(\pi/2, \pi/2)$, a different phonon-subtraction method beyond a simple scaled subtraction of the high temperature data (here we used 80 K) was developed. The reason behind it is due to the rapid diminishing of the magnetic excitation intensities at the zone boundary as the material is heated, see Fig.4.8. The relatively weak spin excitation signals require extra care to avoid being over-subtracted. Several alternative methods were attempted, all of which yielded a qualitatively similar result. The method we presented below is believed to be the most accurate, judged by the residue intensities of phonon peaks after the subtraction.

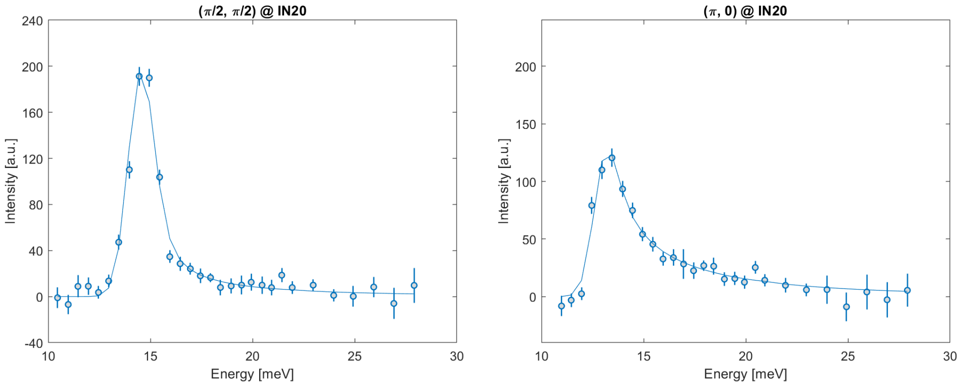

Figure 4.10: Pure spin excitations at $(\pi/2, \pi/2)$ and $(\pi, 0)$ obtained from an polarized neutron experiment at IN20 [42]. Solid lines are the fitted lineshapes with the application of Eq.(4.2).

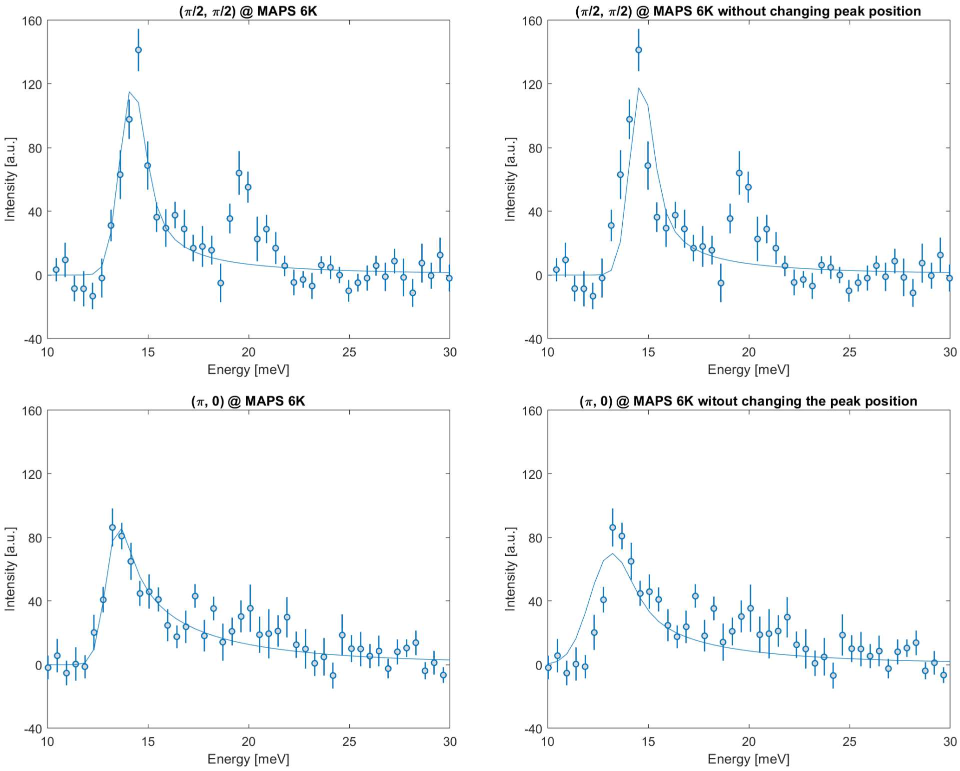

Figure 4.11: Constant momentum cuts at $(\pi/2, \pi/2)$ (upper panel) and $(\pi, 0)$ (lower panel) obtained from the MAPS 80 K subtracted 6 K spectrum. The intense peak at 20 meV in the $(\pi/2, \pi/2)$ spectrum is a residual phonon peak resulting from the direct 80 K subtraction procedure. The two cuts are integrated over a circular momentum range centered at $(\pi/2, \pi/2)$ and $(\pi, 0)$, respectively, with a radius $r = 0.1175$ r.l.u. Left panel: the solid lines represent fitted results using Eq.(4.2) with only η_1 and η_2 fixed to the values obtained from the fitting to the IN20 data shown in Fig.4.10. Right panel: apart from η_1 and η_2, $\omega_{\mathbf{Q}}$ is also fixed when fitting to the constant momentum cuts from the MAPS 80 K subtracted spectrum at 6 K. The results are illustrated as solid lines.

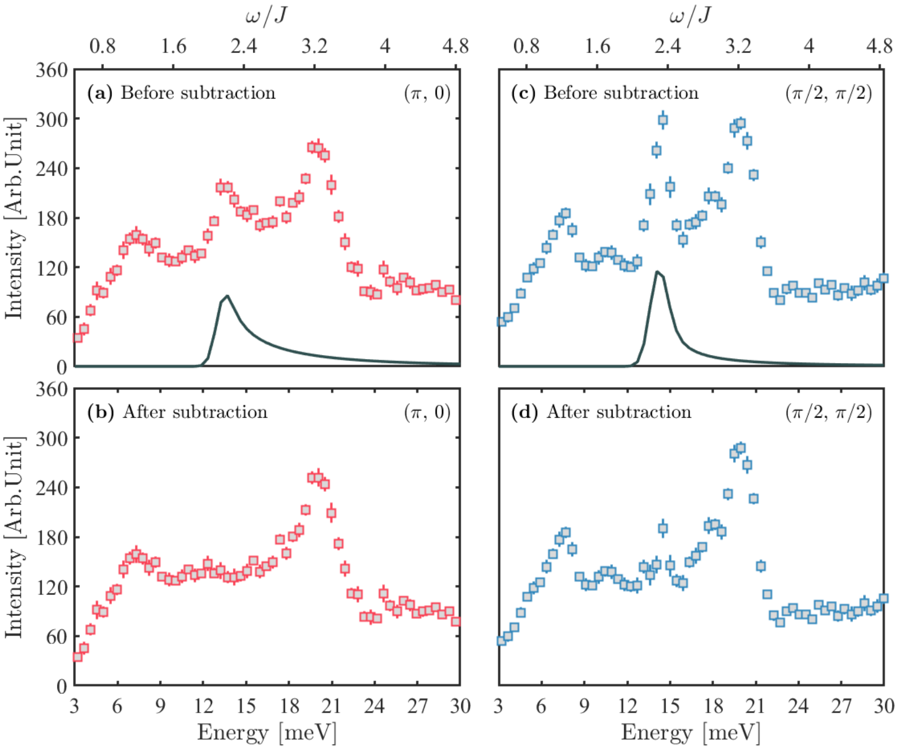

Figure 4.12: Subtraction of the extrapolated polarized neutron data from the MAPS 6 K data. Panels (a) and (c) show raw data at $(\pi, 0)$ and $(\pi/2, \pi/2)$, respectively, along with the corresponding magnetic scattering lineshapes (solid lines) extracted from fitting to the 80 K data subtracted 6 K spectra obtained from MAPS as explained in the text. Panels (b) and (d) show the non-magnetic background spectra at the same wavevectors, obtained by subtraction of these lineshape fsrom the data in (a) and (c). After rescaling by the appropriate Bose occupation factors, the spectra in (b) and (d) were subtracted from the raw zone boundary spectra at 20, 38, 50 and 80 K to yield the results in Fig.4.13

The methodology we adopted is as follow: with the prior knowledge of the pure magnetic spectra at both wavevectors $(\pi, 0)$ and $(\pi/2, \pi/2)$ obtained from previous polarized neutron scattering (IN20) [42], a phenomenological description of the complete lineshapes of the spin excitations at both wavevectors can be established by fitting the excitation spectra to convolutions of power-law decay functions [52] with a Gaussian instrumental energy resolution function, see Eq.(4.2).

$$S(\mathbf{Q}, \omega) = \text{Amp} \times \left(\frac{\Theta(\omega - \omega_{\mathbf{Q}})}{\left(\omega^{\eta_1} - \omega_{\mathbf{Q}}^{\eta_1}\right)^{1-\eta_2}} \circledast \text{Gauss}\left(\omega, \omega_{\mathbf{Q}}, \sigma_{\text{instrument}}\right) \right) \tag{4.2}$$

Here $\Theta(\omega - \omega_{\mathbf{Q}})$ is a Heaviside function, Gauss $(\omega, \omega_{\mathbf{Q}}, \sigma_{\text{instrument}})$ represents a normalized Gaussian resolution function centered at $\omega_{\mathbf{Q}}$ with a FWHM $\sim 2.355\sigma_{\text{instrument}}$, and Amp is the amplitude of the scattering intensity. In Fig.4.10 we illustrate the experimental polarized neutron data and the corresponding fitted lineshapes at $(\pi/2, \pi/2)$ and $(\pi, 0)$, respectively.

After obtaining the best description to the polarized neutron data with the application of Eq.(4.2), the next step is to adjust the obtained model lineshapes to adapt to the constant momentum cuts from the MAPS 80 K subtracted spectrum at 6 K at $(\pi/2, \pi/2)$ and $(\pi, 0)$. Due to IN20 and MAPS have different energy resolutions (IN20: $\Delta\omega = 1.47(5)$ meV $= 0.24(1)J$, MAPS: $\Delta\omega = 1.3$ meV at the energy of the zone boundary magnons), $\sigma_{\text{instrument}}$ is allowed to be varied in the adaption. The two constant momentum cuts from the MAPS data are integrated over a circular momentum range with a radius $r = 0.1175$ r.l.u (in the current notation, $(0, 0) \rightarrow (\pi, \pi)$ corresponds to 1 r.l.u) centered at $(\pi/2, \pi/2)$ and $(\pi, 0)$, respectively. While the data obtained from IN20 are directly measured at $(\pi/2, \pi/2)$ and $(\pi, 0)$. As the result, the peak positions of the linshapes from MAPS have slight shifts compared to the peak positions obtained from IN20. Along the zone boundary direction, i.e. $(\pi/2, \pi/2) \rightarrow (\pi, 0)$, the one magnon excitation energy reaches a maximum at $(\pi/2, \pi/2)$ and a minimum at $(\pi, 0)$. Therefore the large momentum integration range of MAPS causes the peak position at $(\pi.2, \pi/2)$ to shift downwards and the peak position to move upwards at $(\pi, 0)$. This means $\omega_{\mathbf{Q}}$ in Eq.(4.2) is allowed to vary as well in the adaption. The rest parameters η_1 and η_2 in Eq.(4.2) are fixed in the adaption as the power-law decay is instrument independent. For the adaption to the constant momentum cuts from the MAPS 80 K subtracted spectum at 6 K at $(\pi, 0)$ and $(\pi/2, \pi/2)$, the lineshapes obtained from the fitting to the IN20 data are fitted again to the constant momentum cuts at $(\pi/2, \pi/2)$ and $(\pi, 0)$ from MAPS. As explained before, during the fitting only Amp, $\sigma_{\text{instrument}}$ and $\omega_{\mathbf{Q}}$ are allowed to vary and the results are shown in Fig.4.11. As seen from the right panel of Fig.4.11, if the peak positions are fixed in the fitting as well, the resultant fitted lineshapes have a slight higher peak position at $(\pi/2, \pi/2)$ and a lower peak position at $(\pi, 0)$ just as previously explained. Having identified the effective lineshapes describing the spin excitations at $(\pi/2, \pi/2)$ and $(\pi, 0)$, illustrated as the solid lines in Fig.4.12a and Fig.4.12b. They are subtracted from the raw MAPS 6 K data to produce the effective nonmagnetic background spectra shown in Fig.4.12c and Fig.4.12d. Notice that besides the intense phonon contributions near 7.5 meV and 20 meV, the nonmagnetic background at $(\pi/2, \pi/2)$ contains a weaker lattice excitation near 15 meV. This is consistent with observations from the previous polarized neutron study [42], hence further validating the accuracy of the new subtraction procedure. Finally, after re-scaling of the Bose occupation factors, the nonmagnetic background spectra were subtracted from the raw 20 K, 38 K and 50 K data, respectively.

The spectra at wavevectors $(\pi, 0)$ and $(\pi/2, \pi/2)$ resulting from the above subtraction procedure are shown in Fig.4.13. An inspection of the subtracted 80 K linesshapes reveals

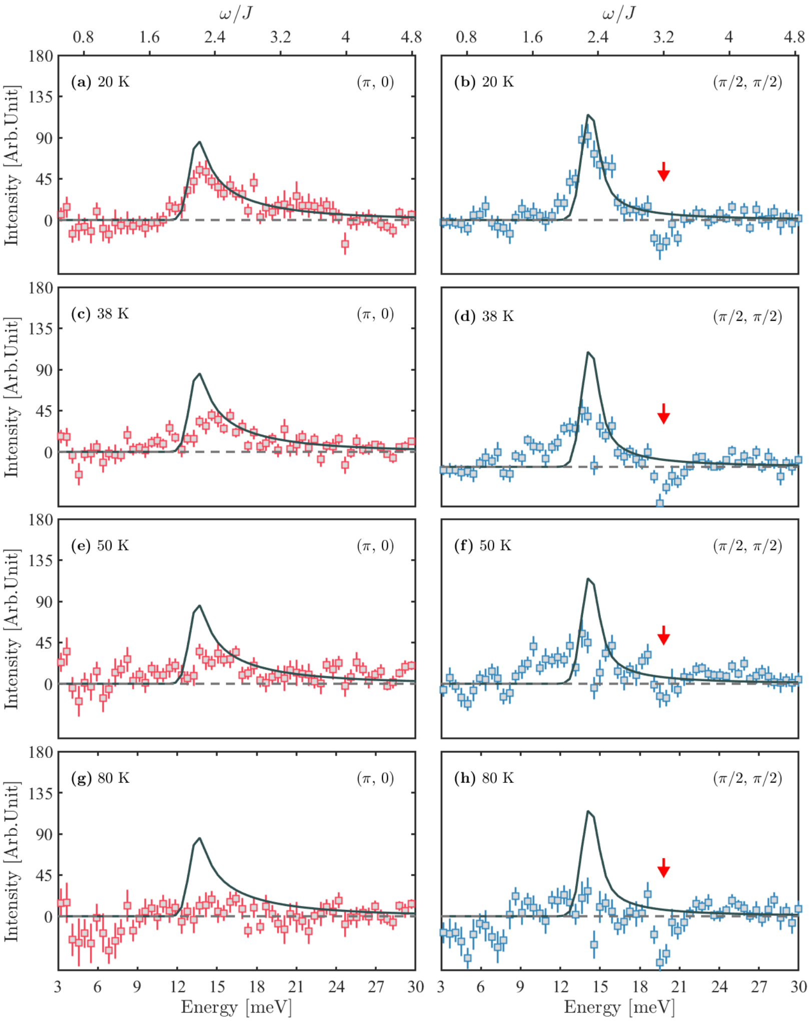

Figure 4.13: Energy dependence of the measured total magnetic dynamical structure factors at **Q** = $(\pi, 0)$ and **Q** = $(\pi/2, \pi/2)$ for different temperatures (a)-(b), 20 K, (c)-(d), 38 K, (e)-(f), 50 K, and (g)-(h), 80 K. The solid lines represent the best fitted lineshapes of the 80 K data subtracted 6 K spectra obtained from MAPS as explained in the text. The red arrows indicate positions of an over-subtracted phonon mode.

both the strength and weakness of the subtraction procedure. At such high temperature ($\sim 5T_N$), the excitation spectra at both $(\pi,0)$ and $(\pi/2,\pi/2)$ are expected to be extremely weak, which indeed agrees with essentially flat lineshapes over the energies of interest produced by the subtraction method. However, it is clear at $(\pi/2,\pi/2)$ the phonon contributions were overestimated for energies below 9 meV as well as around 20 meV, leading to negative intensities after the subtraction. Nevertheless, we believe the subtraction method is robust enough to allow us to make reliable inference on the thermal evolution of the magnetic spectra at wavevectors $(\pi,0)$ and $(\pi/2,\pi/2)$ for temperatures below 80 K. As shown in Fig.4.13, the analysis establish that the zone-boundary magnetic excitation persists up to 50 K $\sim 3T_N$ but vanishes at 80 K $\sim 5T_N$. We notice that the linshapes of the zone boundary magnetic excitations at 6 K (the solid lines in Fig.4.13) and 20 K are rather similar apart from the slightly broadened peak widths at 20 K. Such close resemblance of the two temperatures could already be inferred from the color plots in Fig.4.8. As the temperature increases, the zone boundary magnetic excitations are further weakened. Moreover at $(\pi/2,\pi/2)$, there is a softening of the excitation energies and a substantial broadening towards low energy transfers.

To compare with theory, finite temperature QMC calculations were conducted by A. Sandvik. The numerical results for $S(\mathbf{Q},\omega)$ were obtained by stochastic analytic continuation [53, 54, 44] of imaginary-time correlation functions $G(\mathbf{Q},\tau)$ computed with the stochastic series expansion QMC method, implemented according to Ref. [55]. The lattices sizes ranged from 32×32 for $T/J = 2/3$ to 128×128 for $T/J = 1/4$, and tests for other sizes indicate that no significant finite-size effects are left for the **Q** points considered here. Tests with synthetic data with the same noise level as in the QMC data indicate that broadening and other spectral distortions should be rather mild in the results presented here. We have not carried out any further Gaussian convolution to account for the instrumental resolution.

The results of the QMC calculations of $S(\mathbf{Q},\omega)$ at $(\pi/2,\pi/2)$ and $(\pi,0)$ are summarized in Fig.4.14a, where T/J was set to 1/4, 1/2, 2/3 for the QMC calculations which correspond to 18 K, 36 K and 48 K respectively. The values are very close to the experimental temperatures 20 K, 38 K and 50 K. With increasing temperature, $S(\mathbf{Q},\omega)$ obtained from QMC is rapidly weakened in intensity, softened in energy and broadened in lineshape to become more symmetric with an increase of the intensity of the tail towards lower energies. It is noticeable thermal fluctuations tend to make the spectral lineshapes at the two wavevectors more similar, hence removing the zone boundary anomaly. In Fig.4.14b to Fig.4.14g, we compare the experimental data to the QMC lineshapes. It is evident there is in general a good agreement, even though the QMC predicts relatively broader lineshapes compared to the experimental observations, especially at higher temperatures. Further theoretical work and a high resolution INS study will be necessary to understand such discrepancy.

Temperature dependence of the zone-centre dispersion

Apart from the short-wavelength zone boundary spin excitations, we also investigate the temperature dependence of the long-wavelength zone center spin excitations emanating from (π,π) along the $(1,0)$ and $(1,0)$ directions. Fig.4.15 compares representative constant energy cuts of the 80 K subtracted spectra at 6 K and 38 K (Fig.4.8a and Fig.4.8c respectively). Panels (a) and (b) display cuts along the $(1,0)$ direction averaged over the energy range [5.5, 6.5] meV and [9.0,10.0] meV, respectively. In panels (c) and (d) the constant energy cuts are along the $(1,1)$ direction averaged over the same energy range. In both cases, the counter-propagating magnetic excitation modes were fitted to Voigt lineshapes, see the black solid lines in Fig.4.15. As expected, the thermal fluctuation

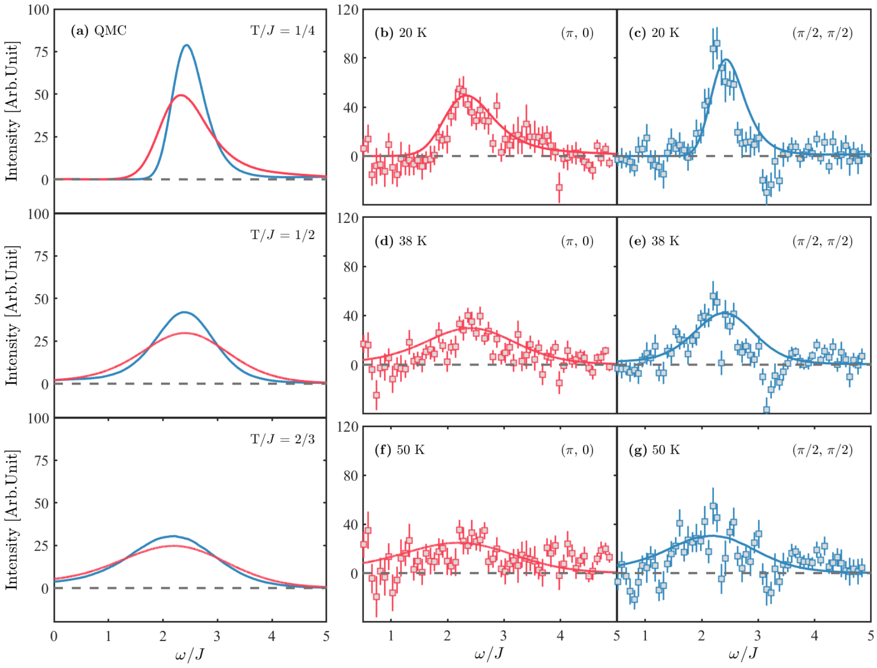

Figure 4.14: (a) Quantum Monte Carlo calculations of the excitation spectra at $(\pi/2, \pi/2)$ (blue lines) and $(\pi, 0)$ (red lines) at $T/J = 1/4$, $1/2$ and $2/3$, respectively. With the exchange constant $J = 6.19$ meV, relevant for CFTD, this corresponds to temperatures 18, 36 and 48 K. (b)-(g), Comparison of the QMC dynamical structure factors with the experimental data at (b)-(c) 20 K, (d)-(e) 38 K and (f)-(g) 50 K for both $(\pi, 0)$ and $(\pi/2, \pi/2)$.

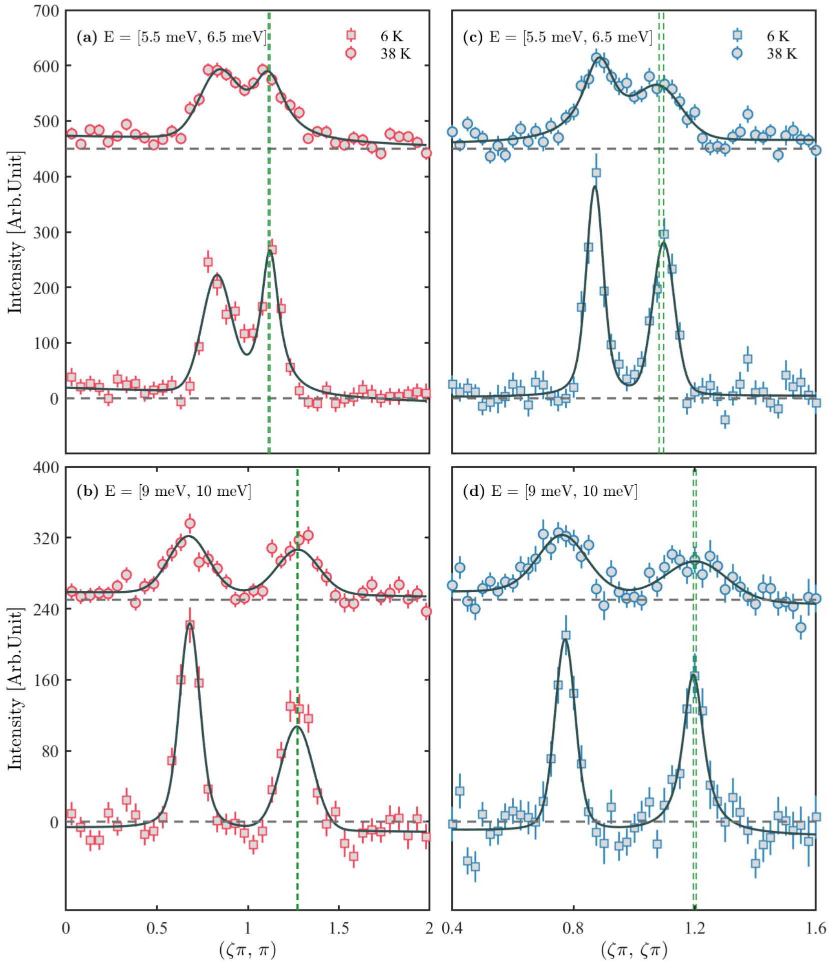

Figure 4.15: Constant energy cuts through the 80 K background subtracted data at 6 K (squares) and 38 K (circles) seen in Figs.4.8(a) and (c). The cuts in panels (a) and (c) correspond to the energy range 5.5 to 6.5 meV, while those in (b) and (d) correspond to the range 9 to 10 meV. In the left hand and right hand panels, the cuts through (π, π) run along the $(1, 0)$ and $(1, 1)$ directions, respectively. In all panels the solid lines represent fits to a lineshape consisting of two Voigt functions and the green dashed lines indicate the fitted peak positions at 6 K and 38 K.

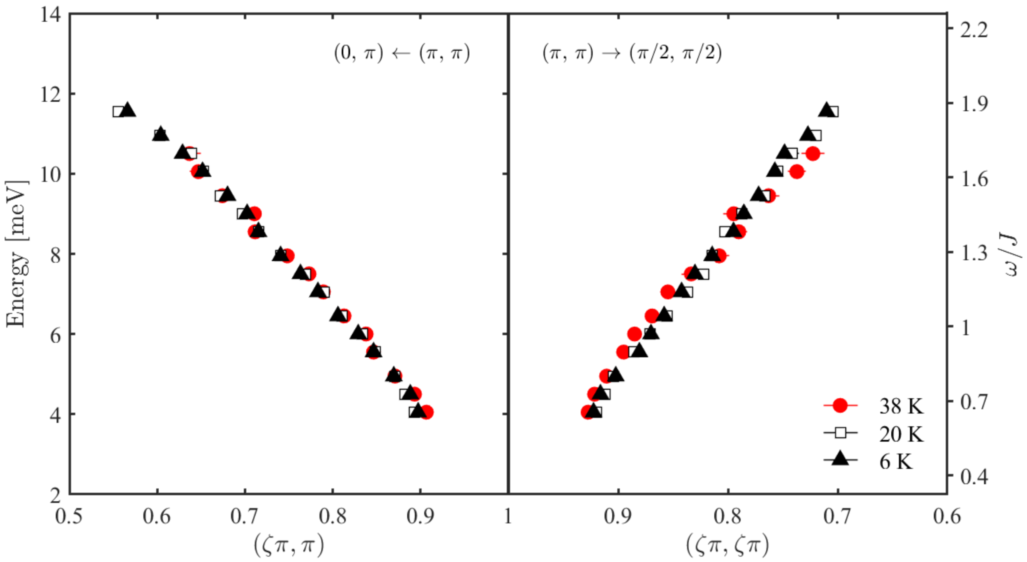

Figure 4.16: Dispersion of the low energy spin excitations at 6 K (black triangles), 20 K (open squares), and 38 K (red cicles), respectively, obtained from fits to cuts such as those in Fig. 4.15

induced excitation broadening is evident when comparing the 6 K and 38 K representative cuts, whereas there is a small shift in wavevectors with respect to the temperature change along both $(1,0)$ and $(1,1)$ directions. The green dashed lines in Fig.4.15 indicate the fitted peak positions.

Fig.4.16 summarizes the dispersion of the magnetic excitations between 4 meV and 11.5 meV at 6 K, 20 K, 38 K and 50 K. As there is a broad diffuse scattering below 4 meV in the spectrum at 80 K, see Fig.4.7c, the dispersion of the lowest energy excitations (< 4 meV) could not be extracted reliably. Overall, the results show dispersion is relatively robust against thermal fluctuations up to $T/J \sim 2/3$, except for the weak indications of hardening (softening) at low (high) energies for magnetic excitations along the $(1,1)$ direction.

4.1.5 Conclusions

Our analysis of the thermal evolution of the spin excitations in CFTD, which is known to be an excellent representative of the 2DQHAFSL, has revealed several novel results:

- The 6 K and 20 K magnetic excitation spectra are remarkably similar. In particular the $(\pi,0)$ anomaly survives through the phase transition from the ordered Néel state to the paramagnetic state.
- Thermally induced excitation broadening is observed along the zone boundary direction $(\pi,0) \rightarrow (\pi/2,\pi/2)$. In addition, the spectral weights of the spin excitations at both $(\pi/2,\pi/2)$ and $(\pi,0)$ gradually diminish due to heating but remain visible up to temperatures $T/J \approx 2/3$.
- As the zone boundary excitations broaden with temperature increase, the lineshape at $(\pi,0)$ becomes more symmetric. Only until $T/J \approx 1$, the lineshapes at $(\pi,0)$ and $(\pi/2,\pi/2)$ are essentially indistinguishable, which is consistent with the QMC calculations.
- The dispersion of the spin excitations in the long wavelength limit shows little changes up to $T/J \approx 1/2$, which is remarkably robust against thermal fluctuations.

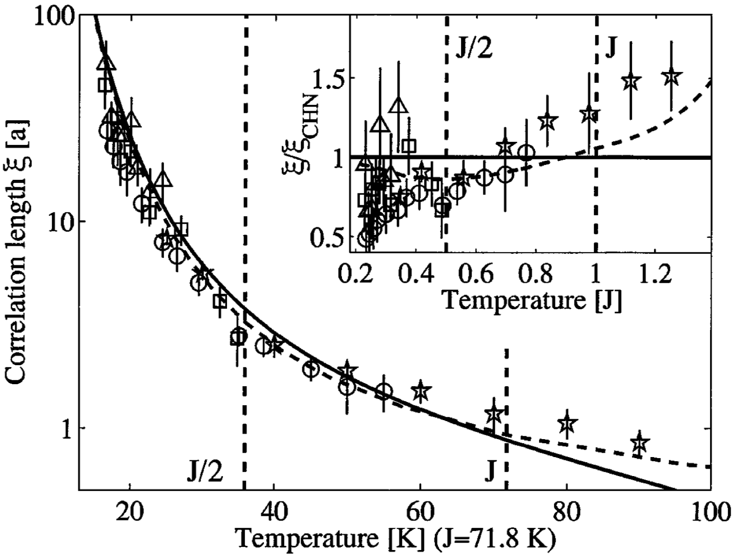

Figure 4.17: The measured spin-spin correlation length ξ in CFTD compared to the prediction by CHN (solid) [56] and QMC (dahsed) [57] results. The figure is taken from Ref [58].

These results highlight the interplay between quantum and thermal effects. Naively, the persistence of the well-defined zone boundary excitations at $\omega \approx 2J$ up to $T/J \approx 2/3$, a temperature at which the spin-spin correlation length is short-ranged, as pointed out in Ref [58], see Fig.4.17, suggests a simple interpretation in real space. In a localized picture, due to a given spin is surrounded by four neighbouring antiparallel spins, the spin flip excitation costs an energy $2J$. In other words, the zone boundary excitations reflect the energy of a localized spin flip, regardless of which sublattice the flipped spin resides on. The similarity of the lineshapes between $(\pi, 0)$ and $(\pi/2, \pi/2)$ above $T/J \approx 2/3$ further supports this naive picture, which closely resembles the linear spin wave theory scenario where spin waves are localized on a single sublattice [50]. However, beyond this simple picture, the broadened zone boundary magnetic excitations are centered at an energy higher than $2J$ even at $T/J = 2/3$. Remembering in the zero temperature limit, the bandwidth of the spin wave excitations ($2JZ_c$) is enhanced by a renormalization factor $Z_c = 1.18$ directly stemming from quantum corrections to the excitation energies. Therefore, our results implies even at finite temperatures, quantum renormalization effect might still remain active.

4.2 Field induced magnon decay on a quantum square lattice antiferromagnet CAPCC

In this section, we study the spin dynamics of the 2DQHAFSL under magnetic field. When applying a magnetic field perpendicular to the 2D plane of a Néel ordered square lattice, see Fig.4.18. The energy per spin to the lowest order reads [59],

$$H_0(\theta) = 4JS^2 \sin^2\theta - g\mu_B HS \sin\theta - 2JS^2. \tag{4.3}$$

Here J is the nearest neighbor exchange constant, H is the applied magnetic field, S is the spin angular momentum per site and θ denotes the angle between spin directions and the $\hat{\mathbf{x}}_0$ axis as illustrated in Fig.4.18.

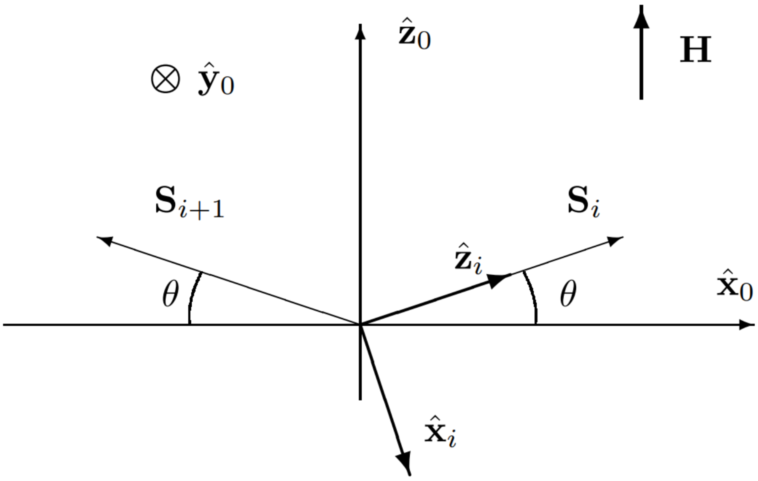

Figure 4.18: Schematic of applying magnetic field perpendicular to the 2D plane of a Néel ordered square lattice. $\mathbf{S}_i$ and $\mathbf{S}_{i+1}$ are the spin angular momenta at site i and $i+1$, respectively. $\{\hat{\mathbf{x}}_0, \hat{\mathbf{y}}_0, \hat{\mathbf{z}}_0\}$ represents a laboratory reference of frame. $\{\hat{\mathbf{x}}_i, \hat{\mathbf{y}}_i, \hat{\mathbf{z}}_i\}$ represents a local rotating frame at site i. The figure is taken from [59].

The minimum of Eq.(4.3) occurs at $\sin\theta_0 = \frac{g\mu_B H}{8JS}$. This implies that spins smoothly cant towards the field direction and are ferromagnetically aligned when the field is above $8JS$. Therefore, $8JS$ here is denoted as the saturation field of the system.

The evolution of the spin excitation spectrum in the 2DQHAFSL under magnetic field has long been an active research field within theoretical community [51, 60, 61, 62, 63, 64]. Essentially what has been discovered in the past decade is, when the applied field is above a threshold field H^*, the single magnon branch will decay into the two magnon continuum. This so-called magnon instability has been observed in the classical $S = 5/2$ square lattice system $Ba_2MnGe_2O_7$ at high magnetic fields, highlighted by the unambiguous broadening of the one magnon excitation spectrum for some momenta [65], see Fig.4.19. However, to date direct experimental evidence of magnon decay in the 2DQHAFSL is absent. This is due to the stringent requirements imposed by the practical difficulties on both material and experimental sides:

- The material under study must be a good realization of the 2DQHAFSL, as any additional exchange interactions will impair the decay tendency [63].
- The saturation field H_{sat} of the material has to be accessible by the current superconducting magnets at neutron facilities.
- A high resolution spectrometer is required as probing lineshape broadening is the primary focus.
- We need a large crystal and/or a high flux spectrometer due to the small spin angular momentum size ($S = 1/2$) of the 2DQHAFSL.

Although CFTD is so far the best realization of the 2DQHAFSL, its saturation field ($\frac{4J}{g\mu_B} \sim 214$ T) is far beyond the current superconducting magnet's capability. To this end, another square lattice compound $(5CAP)_2CuCl_4$ (CAPCC) became our primary candidate, due to its relatively low saturation field $H_{\text{sat}} = 3.62$ T.

CAPCC crystallizes in the monoclinic space group $C2/c$. Structural analysis shows that,

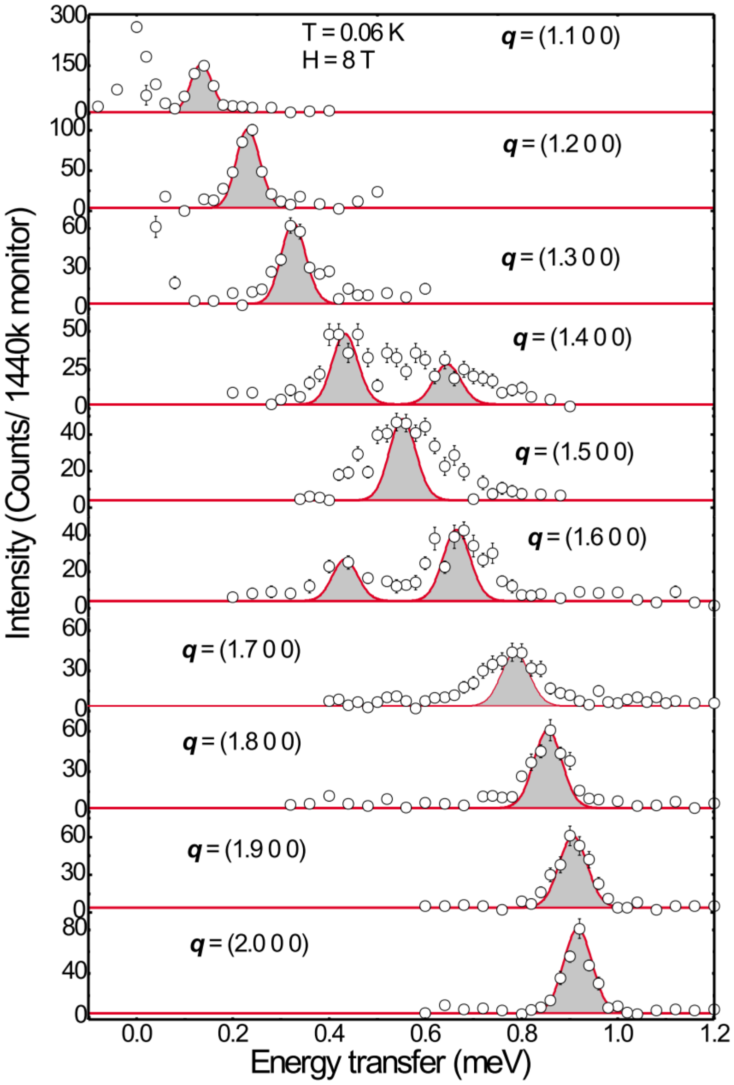

Figure 4.19: Constant **q** scan at 8 T from **q** $= (1.1, 0, 0)$ to **q** $= (2.0, 0, 0)$. The shaded areas indicate energy resolution. As **q** approaches $(1.5, 0, 0)$, the widths of the spin excitations increase significantly. The figure is taken from Ref [65].

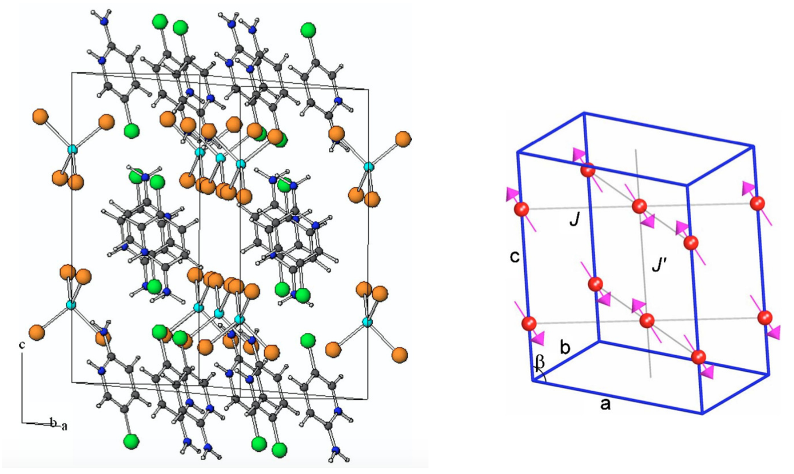

(a) (b)

Figure 4.20: Crystal and magnetic structures of CAPCC [67]. **a**. Three dimensional crystal structure of CAPCC with Cu, Cl, C, N and H in cyan, orange, grey, blue and white spheres. **b**. A proposed magnetic structure of CAPCC. The red spheres represent Cu (II) ions and J, J' indicate the nearest neighbor in-plane and out-of-plane exchange interactions, respectively.

at 143 K, the lattice constants are $a = 12.850(2)$ Å, $b = 8.375(1)$ Å, $c = 15.711(2)$ Å, and $\beta = 94.37(3)^\circ$ [66]. For a single layer, the Cu^{2+} ions are surrounded by four Cl^- to complete the tetrahedral coordination, and these $CuCl_4^{2-}$ anions form an effective square planar lattice within the $\mathbf{a} - \mathbf{b}$ plane. The magnetic exchange paths within the layers are mediated by the overlap of chlorides between the neighboring tetrahedra. The exchange coupling strength J depends upon the distance between the chlorides and the dihedral angle Cu(1)-Cl(1)$\cdots$Cu(2)-Cl(2) where 1 and 2 represent the adjacent tetrahedra within the same layer [66]. Along the crystallographic **c** direction, organic cations 5CAP (5CAP=5-chloro-2-aminopyridinium) set in between the close-by $CuCl_4^{2-}$ tetrahedra and separate the adjacent layers. Due to the large spatial separation between the layers, the interlayer exchange coupling J' is expected to be much weaker than the intralayer one J. The crystal structure of CAPCC is shown in Fig.4.20.

Upon cooling, CAPCC undergoes an antiferromagnetic phase transition at $T_N = 0.754$ K with an ordering vector (π, π, π). Although the number of observed reflections in the neutron diffraction experiment were insufficient for a refinement of the magnetic structure and its spin orientation angle, Coomer *et al* [67] determined the saturation field H_{sat} at the base temperature 30 mK to be $H_{\text{sat}} = 3.62(3)$ T, by tracking the dependence of intensity of the $(1, 1, 0)$ Bragg peak on magnetic field applied perpendicular to the $\mathbf{a}^* - \mathbf{b}^*$ plane, see Fig.4.21. Detailed heat capacity and magnetic susceptibility measurements indicated [66, 67], that unlike CFTD, the interlayer exchange coupling in CAPCC is non-negligible. The estimated exchange couplings are summarized in Tab.(4.2), where J and J' represent the nearest-neighbor in-plane and out-of-plane exchange couplings respectively.

4.2.1 Magnon decay on a quantum square lattice antiferromagnet in high fields

The 2DQHAFSL has a Néel order at zero field, as discussed in the CFTD section, the spin excitation spectrum is well described by the LSWT with a renormalization factor $Z_c = 1.18$ apart from the anomaly at $(\pi, 0)$, which highlights the quantum dynamics of spins in the short wavelength limit. However, An external field perpendicular to the 2D plane induces

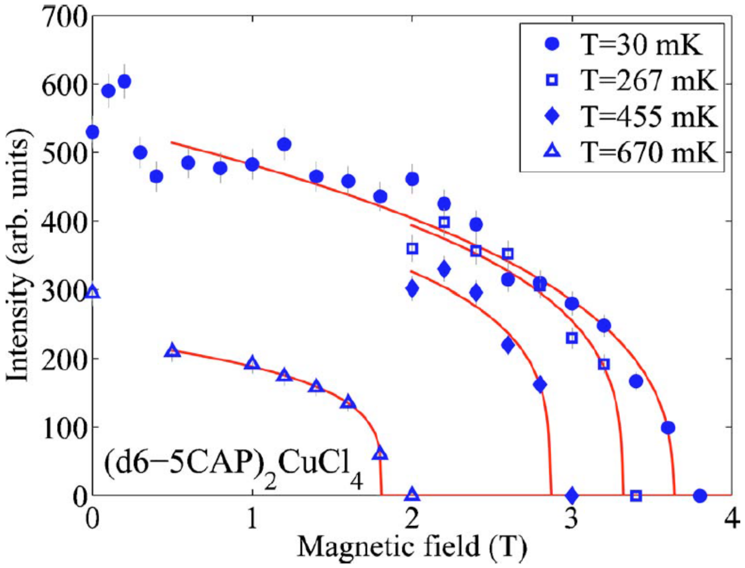

Figure 4.21: Field dependence of the intensity of the $(1, 1, 0)$ Bragg peak at 30 mK, 267 mK, 455 mK and 670 mK. The figure is taken from [67].

Compound	J [meV]	J'/J
(5CAP)$_2$CuCl$_4$	0.11	0.25

Table 4.2: The estimated exchange interactions in CAPCC from specific heat and magnetic susceptibility measurements [66, 67]. J and J' are the nearest neighbor in-plane and out-of-plane exchange couplings respectively.

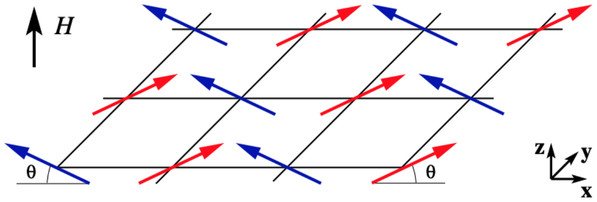

Figure 4.22: Noncollinear magnetic structure of the 2DQHAFSL in a magnetic field. The canting angle θ is controlled by the external magnetic field H. The figure is taken from Ref [60]

a noncollinear spin configuration, see Fig.4.22, resulting in non-zero three-magnon interactions in the Hamiltonian [51, 60, 64, 59], as we shall discuss below. Simply by tuning the external field strength, these three-magnon interaction strengths varies. Such interactions open a channel for magnons to couple to the two-magnon continuum, inducing the so-called magnon decay for the one-magnon branch where substantial damping in the spectrum occurs. This has been verified by the QMC [61] and the exact diagonalization [62]. In addition, the QMC study pointed out a non-trivial distribution of the spectral weight which gives rise to non-Lorentzian ”double-peak” features in the dynamical structure factor, which were also observed in the previous analytical studies [51, 60].

The theoretical work [51, 60, 64] only deals with magnon decays in a pure antiferromagnetic Heisenberg square lattice model without interlayer coupling. In practice, the interlayer exchange J' is finite otherwise no long-range ordering would occur at finite temperatures. To address the magnon decay dynamics in the three dimensional coupling scenario, Fuhrman *et al.* [63] carried out a detailed calculation regarding the dynamical structure factors with the standard $1/S$ expansion technique. Compared to the pure 2D case, a non-zero 3D interlayer coupling largely mitigates the singularities of high field corrections without invoking any self-consistency approaches. In the following, we will review Fuhrman's formalism and introduce the main contributions that renormalizing the excitation spectrum.

We start with the Heisenberg Hamiltonian of nearest neighbor interacting spins in the presence of external magnetic field H along the Z axis in the laboratory reference frame (Fig.4.18),

$$H = \sum_{\langle i,j \rangle} J_{ij} \mathbf{S}_i \cdot \mathbf{S}_j - g\mu_B H \sum_i S_i^z, \tag{4.4}$$

where the in-plane exchange coupling is $J_{ij} = J$ and the interplane exchange interaction is $J_{ij} = J'$. The coupling ratio is denoted by $\alpha := J'/J$ and assumed to be between 0 and 1. In the local rotating frame, we apply the standard Holstein-Primakoff transformation to spin operators and rewrite the Hamiltonian in terms of the newly introduced boson operators. Afterwards, we apply the Fourier transform to the Hamiltonian and subsequently

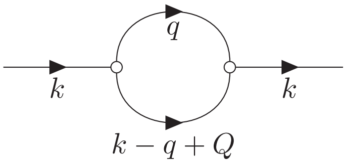

Figure 4.23: The lowest order of self-energy from the decay vertex.

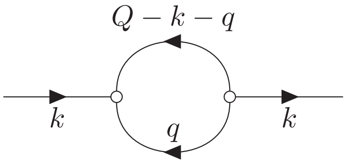

Figure 4.24: The lowest order of self-energy from the source vertex.

diagonalize it via the Bogoliubov transformation. The yielded Hamiltonian reads

$$\begin{aligned} H = \sum_{\mathbf{k}} \tilde{\epsilon}_{\mathbf{k}} b^{\dagger}_{\mathbf{k}} b_{\mathbf{k}} + & \underbrace{\frac{1}{2!} \sum_{\mathbf{k},\mathbf{q}} \Phi_1(\mathbf{k},\mathbf{q}) \left(b^{\dagger}_{\mathbf{k}-\mathbf{q}+\mathbf{Q}} b^{\dagger}_{\mathbf{q}} b_{\mathbf{k}} + \text{H.c} \right)}_{\text{Decay}} + \\ & \underbrace{\frac{1}{3!} \sum_{\mathbf{k},\mathbf{q}} \Phi_2(\mathbf{k},\mathbf{q}) \left(b^{\dagger}_{\mathbf{Q}-\mathbf{k}-\mathbf{q}} b^{\dagger}_{\mathbf{q}} b_{\mathbf{k}} + \text{H.c} \right)}_{\text{Source}} + \cdots , \end{aligned} \tag{4.5}$$

where the ordering vector $\mathbf{Q} = (\pi, \pi, \pi)$ enters the momentum conservation condition because of the staggered canting of the spins. The quadratic energy term, $\tilde{\epsilon}_{\mathbf{k}} = \epsilon_{\mathbf{k}} + \delta\epsilon^{(1)}_{\mathbf{k}} + \delta\epsilon^{(2)}_{\mathbf{k}}$, contains the bare magnon dispersion given by LSWT and corrections $\delta\epsilon^{(1)}_{\mathbf{k}}$ and $\delta\epsilon^{(2)}_{\mathbf{k}}$. $\delta\epsilon^{(1)}_{\mathbf{k}}$ is due to Hartree-Fock decoupling of the cubic and quartic perturbations, and $\delta\epsilon^{(2)}_{\mathbf{k}}$ arises from the $1/S$ correction to the canting angle. The three boson terms are decay and source vertices that govern the anomalous dynamics in the high-field regime. The dynamical features of the system are obtained from the interacting magnon Green's function

$$G(\mathbf{k},\omega) = \frac{1}{\omega - \tilde{\epsilon}_{\mathbf{k}} - \Sigma_1(\mathbf{k},\omega) - \Sigma_2(\mathbf{k},\omega)}, \tag{4.6}$$

where $\Sigma_1(\mathbf{k},\omega)$ and $\Sigma_2(\mathbf{k},\omega)$ are the decay and source self-energies presented in Fig.4.23 and Fig.4.24, respectively. Their explicit expressions up to a second order are

$$\begin{aligned} \Sigma_1(\mathbf{k},\omega) &= \frac{1}{2} \sum_{\mathbf{q}} \frac{|\Phi_1(\mathbf{k},\mathbf{q})|^2}{\omega - \epsilon_{\mathbf{q}} - \epsilon_{\mathbf{k}-\mathbf{q}+\mathbf{Q}} + i0} \\ \Sigma_2(\mathbf{k},\omega) &= -\frac{1}{2} \sum_{\mathbf{q}} \frac{|\Phi_2(\mathbf{k},\mathbf{q})|^2}{\omega + \epsilon_{\mathbf{q}} + \epsilon_{\mathbf{k}+\mathbf{q}-\mathbf{Q}} - i0}. \end{aligned} \tag{4.7}$$

In contrast to $H = 0$ scenario where the energy dependent magnon interactions beyond Hartree-Fock only show up in the $1/S^2$ order, they already occurred in the $1/S$ corrections for $H \neq 0$ due to couplings between longitudinal and transverse spin excitations that renders three-magnon vertices non-zero [51, 60, 63, 64]. Above the threshold field $H^* \approx 0.76 H_{\text{sat}}$ for magnon instability [51], the self-energy $\Sigma_1(\mathbf{k},\omega)$ acquires a finite imaginary component, allowing the occurrence of spontaneous magnon decays.

4.2.2 Dynamical structure factor calculation from 1/S SWT

Dynamical structure factor $S^{\alpha\beta}$ is defined as

$$S^{\alpha\beta}(\mathbf{k},\omega)=\int_{-\infty}^{\infty}\frac{dt}{2\pi}\langle S^{\alpha}_{\mathbf{k}}(t)S^{\beta}_{-\mathbf{k}}\rangle e^{i\omega t}, \tag{4.8}$$

where $\alpha,\beta=x,y,z$ generally refer to the local rotating frame (xyz) in the spin-wave calculation [51, 60, 63, 59]. Converting to the laboratory reference frame (XYZ), to a lowest order, the new dynamical structure factors can be expressed as a linear combination of the structure factors in the rotating frame [63, 60],

$$\begin{aligned}S^{XX}(\mathbf{k},\omega)&=\sin^2\theta S^{xx}(\mathbf{k},\omega)+\cos^2\theta S^{zz}(\mathbf{k}-\mathbf{Q},\omega)\\ S^{ZZ}(\mathbf{k},\omega)&=\cos^2\theta S^{xx}(\mathbf{k}-\mathbf{Q},\omega)+\sin^2\theta S^{zz}(\mathbf{k},\omega)\\ S^{YY}(\mathbf{k},\omega)&=S^{yy}(\mathbf{k},\omega)\end{aligned} \tag{4.9}$$

where θ is the spin canting angle induced by external magnetic field. Here we omitted the cross terms ($S^{\alpha\beta}(\mathbf{k},\omega)$ with $\alpha\neq\beta$), as they only contribute to the order $1/S^2$ or higher [59].

Due to the fluctuation-dissipation theorem [68] at zero temperature, the dynamical structure factor and the interacting magnon Green's function, Eq.(4.6), is linked via [63, 60]

$$\begin{aligned}S^{xx}(\mathbf{k},\omega)&=-\frac{1}{2S}\Lambda_{+}(u_{\mathbf{k}}+v_{\mathbf{k}})^2\mathrm{Im}G(\mathbf{k},\omega)\\ S^{yy}(\mathbf{k},\omega)&=-\frac{1}{2S}\Lambda_{-}(u_{\mathbf{k}}-v_{\mathbf{k}})^2\mathrm{Im}G(\mathbf{k},\omega)\\ S^{zz}(\mathbf{k},\omega)&=\frac{1}{2}\sum_{\mathbf{q}}\left(u_{\mathbf{q}}v_{\mathbf{k}-\mathbf{q}}+v_{\mathbf{q}}u_{\mathbf{k}-\mathbf{q}}\right)^2\times\delta(\omega-\epsilon_{\mathbf{q}}-\epsilon_{\mathbf{k}-\mathbf{q}})\end{aligned} \tag{4.10}$$

where $S=1/2$ is the spin value, $u_{\mathbf{k}}$ and $v_{\mathbf{k}}$ are parameters of the Bogoliubov transformation, and $\Lambda_{\pm}=[1-(2n\pm\delta)/2S]$ [63].

In Fig.4.25, we show the intensity plots of transverse, $S_{\perp}(\mathbf{k},\omega)=S^{xx}(\mathbf{k},\omega)+S^{yy}(\mathbf{k},\omega)$, and longitudinal, $S^{zz}(\mathbf{k},\omega)$, dynamical structure factors at zero field and $H=0.9H_{\text{sat}}$, for several representative paths in the Brillouin zone with $k_z=0$. The model parameters chosen here are $J=0.1$ meV, $\alpha=0.2$ and $g=2.0$, respectively. The longitudinal channel $S^{zz}(\mathbf{k},\omega)$ contains only two-magnon continuum excitations, see the lower pannels of Fig.4.25a and Fig.4.25b. It is evident that, at both zero field and $H=0.9H_{\text{sat}}$, the intensities of the two-magnon continuum are much smaller than the single-magnon excitations in the transverse channel $S^{\perp}(\mathbf{k},\omega)$. The complex lineshapes in the transverse channel $S^{\perp}(\mathbf{k},\omega)$ at $H=0.9H_{\text{sat}}$ (the upper panel of Fig.4.25b) are very much distinct from the well-defined single-magnon lineshapes at zero field (the upper panel of Fig.4.25a). Compared to the transverse fluctuation at zero field, there is clear evidence of spectral weight broadening and redistribution occurring in the $H=0.9H_{\text{sat}}$ transverse spectrum due to the magnon decays. Such a decay trend is most obvious at $(\pi/2,\pi/2,0)$ (see the middle point of $(\pi,\pi,0)$ and $(0,0,0)$ in the upper panel of Fig.4.25b), where a single-magnon excitation is substantially broadened giving rise to a long tail extending from ~ 0.2 meV to ~ 0.4 meV. This signifies the crucial role of spontaneous magnon decays in terms of substantially reshaping the excitation spectrum and such effects should readily be observed in experiment. At $(\pi,0,0)$, the magnon decay is less pronounced. This is readily seen from the intense well-defined one magnon excitation at ~ 0.2 meV in the upper panel of Fig.4.25b. The intensity of the high energy excitations extending from 0.2 meV to 0.4 meV at $(\pi,0,0)$ in the transverse channel (the upper panel of Fig.4.25b) is significantly weaker

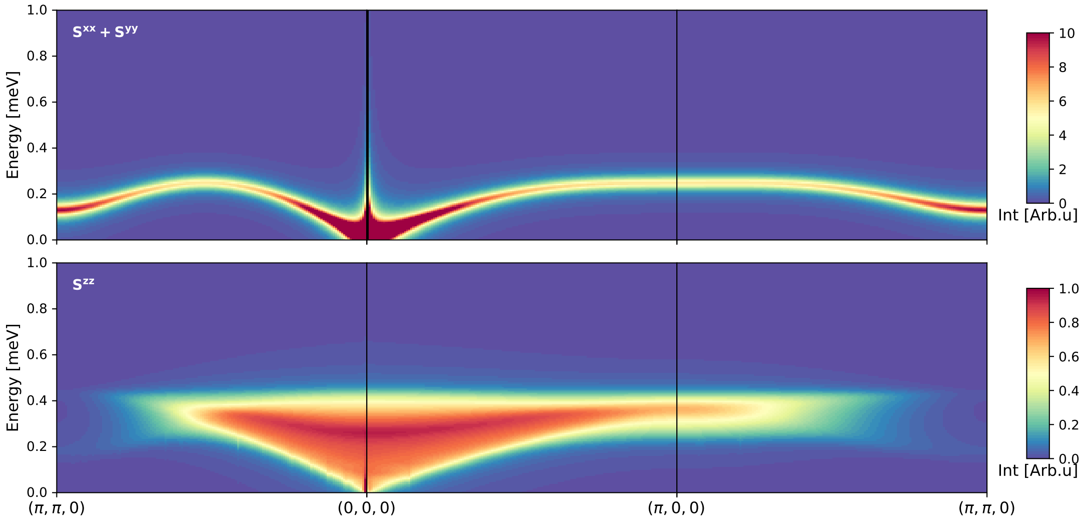

(a) Intensity color plots of **upper panel** the transverse dynamical structure factor, and **lower panel** the longitudinal dynamical structure factor at zero field. The intense feature extending from zero energy to 1 meV at $(0, 0, 0)$ in the transverse channel is non-physical, which arises from the numerical divergence in the calculation.

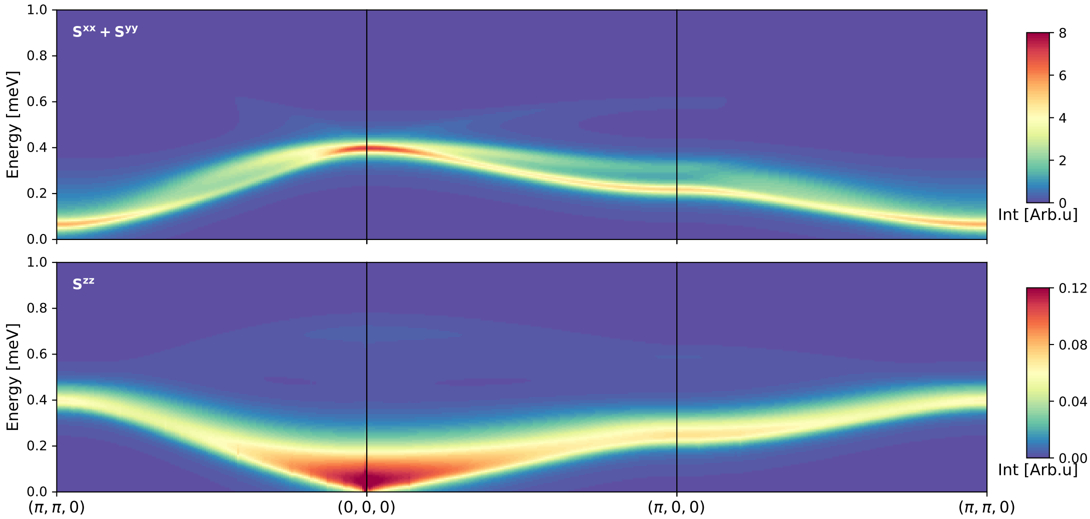

(b) Intensity color plots of **upper panel** the transverse dynamical structure factor, and **lower panel** the longitudinal dynamical structure factor at $H = 0.9H_{\text{sat}}$.

Figure 4.25: Illustration of the transverse, $S_{\perp}(\mathbf{k}, \omega)$, and longitudinal, $S^{zz}(\mathbf{k}, \omega)$, dynamical structure factors at (a) zero field and (b) $H = 0.9H_{\text{sat}}$. The calculations were performed for the parameters: $J = 0.1$ meV, $\alpha = 0.2$ and $g = 2.0$. The spectra are broadened by a lorentzian resolution function with $\Gamma = 0.0220$ meV.

than the single-magnon response. This is very distinct from what happens at $(\pi/2, \pi/2, 0)$ as explained above.

Recall that the double differential cross-section $\frac{d\sigma}{d\Omega dE}(\mathbf{k}, \omega)$ for unpolarized neutron scattering experiment is a linear combination of dynamical structure factors, weighted by the square of a material dependent magnetic form factor $f(\mathbf{k})$ and a polarization factor $\left(\delta_{\alpha\beta} - \frac{k_\alpha k_\beta}{k^2}\right)$, signifying that only the fluctuations perpendicular to the momentum transfer **k** can be probed by neutrons. In the laboratory reference frame, the expression is

$$\frac{d^2\sigma}{d\Omega dE}(\mathbf{k}, \omega) \propto \frac{k_f}{k_i} \times f^2(\mathbf{k}) \times \sum_{\alpha,\beta=X,Y,Z} \left(\delta_{\alpha\beta} - \frac{k_\alpha k_\beta}{k^2}\right) S^{\alpha\beta}(\mathbf{k}, \omega), \tag{4.11}$$

where k_f and k_i are the norm of the final and the initial wavevectors of the neutron, respectively, $k_{\alpha(\beta)}$ is the corresponding component of the scattering vector **k** and k is its norm.

4.2.3 Evidence for field induced magnon decay

Having reviewed theoretically how spontaneous magnon decays could be induced by varying external magnetic field in the quasi-2DQHAFSL with non-zero interlayer coupling, the next phase is to observe the decay signature experimentally in a suitable quantum antiferromagnet to elucidate the accuracy of the theoretical prediction. Owing to its easily accessible saturation field $H_{\text{sat}} = 3.62$ T, CAPCC is a suitable candidate for this study. As illustrated in the upper panel of Fig.4.25b, the magnon decay process occurs at several momenta in the Brillouin zone, inelastic neutron scattering is the ideal tool for this purpose.

The spin wave dispersion at zero field for the quasi-2DQHAFSL with finite interlayer coupling reads [63]

$$\hbar\omega_{\mathbf{k}} = J(2+\alpha)\sqrt{(1+\gamma_{\mathbf{k}})(1-\cos 2\theta\gamma_{\mathbf{k}})}. \tag{4.12}$$

where $\gamma_{\mathbf{k}} = \frac{\cos(k_x)+\cos(k_y)+\alpha\cos(k_z)}{\alpha+2}$. In Table 4.2, we list the estimated J and α based on thermodynamic measurements [66, 67]. Substitute them ($J = 0.1$ meV and $\alpha = 0.25$) into Eq.(4.12), we find the bandwidth of the spin wave excitations at zero field is around 0.23 meV. Such a low energy scale imposes stringent requirements on the spectrometers: it has to be able to resolve excitaitons below 1 meV, and its energy resolution has to be sharp enough to identify any magnon decay signatures. The ultimate choice of spectrometer was a back-scattering TOF spectrometer OSIRIS [69, 70] at the ISIS facility, Rutherford Appleton Laboratory (UK). Due to the incoming white neutron beam,it also has a high flux.

Experimental details

The sample for the inelastic neutron scattering experiment was a single high-quality crystal, and the experiment was conducted by Christensen and Nilsen *et al* before the start of this PhD project with the final analyzer energy 1.8463 meV for a PG002 analyzer and the chopper spinning at 50 Hz. The obtained energy resolution at zero energy transfer is around 22 μeV. The total mass of the crystal was 2 grams and it was aligned such that the incident neutron wavevector $\mathbf{k}_i$ was parallel to the reciprocal lattice plane $\mathbf{a}^* - \mathbf{b}^*$. To fully explore the excitation spectrum in reciprocal space, the crystal was further rotated within the $\mathbf{a}^* - \mathbf{b}^*$ plane with $\Psi = -71.0^\circ, -66.2^\circ, -52.2^\circ, -64.7^\circ, -74.8^\circ$ and -78.6°. In Fig.4.26, we illustrate the reciprocal space coverage for CAPCC at each Ψ. The measurements were conducted at 50 mK with magnetic field applied perpendicular to the $\mathbf{a}^* - \mathbf{b}^*$ plane. Spectra at six different fields 0.0 T, 2.0 T, 2.7 T, 3.2 T, 3.5 T and 7.0 T were collected. The details are summarized in Tab.(4.3).

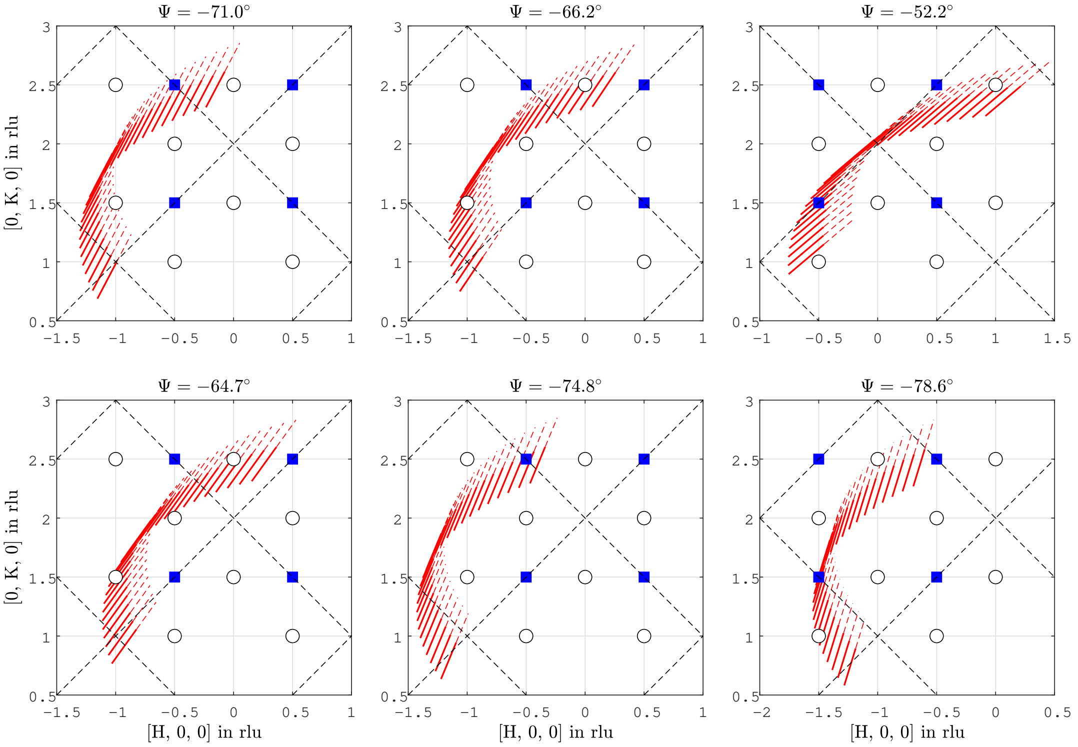

Figure 4.26: Reciprocal space coverage of OSIRIS at different sample rotation angles $\Psi = -71.0°$, $-66.2°$, $-52.2°$, $-64.7°$, $-74.8°$ and $-64.7°$, respectively, with the final analyzer energy $E_f = 1.8463$ meV. The red solid lines represent the momenta accessed by the neutrons with energy transfers below 1 meV, while the red dashed lines are the regions in reciprocal space seen by neutrons with energy transfers above 1 meV. The blue filled squares and white circles represent the momenta $(\pi, 0, 0)$ and $(\pi/2, \pi/2, 0)$, respectively.

No.	Temperature [mK]	Field [T]	Ψ
1	50	0.0	$-64.7°$
2	50	0.0	$-74.8°$
3	50	0.0	$-78.6°$
4	50	2.0	$-71.0°$
5	50	2.7	$-71.0°$
6	50	3.2	$-71.0°$
7	50	3.5	$-71.0°$
8	50	7.0	$-71.0°$
9	50	3.2	$-66.2°$
10	50	3.5	$-66.2°$
11	50	7.0	$-66.2°$
12	50	3.2	$-52.2°$
13	50	3.5	$-52.2°$
14	50	7.0	$-52.2°$

Table 4.3: The complete list of measured spectra at different fields and rotation angles Ψ.

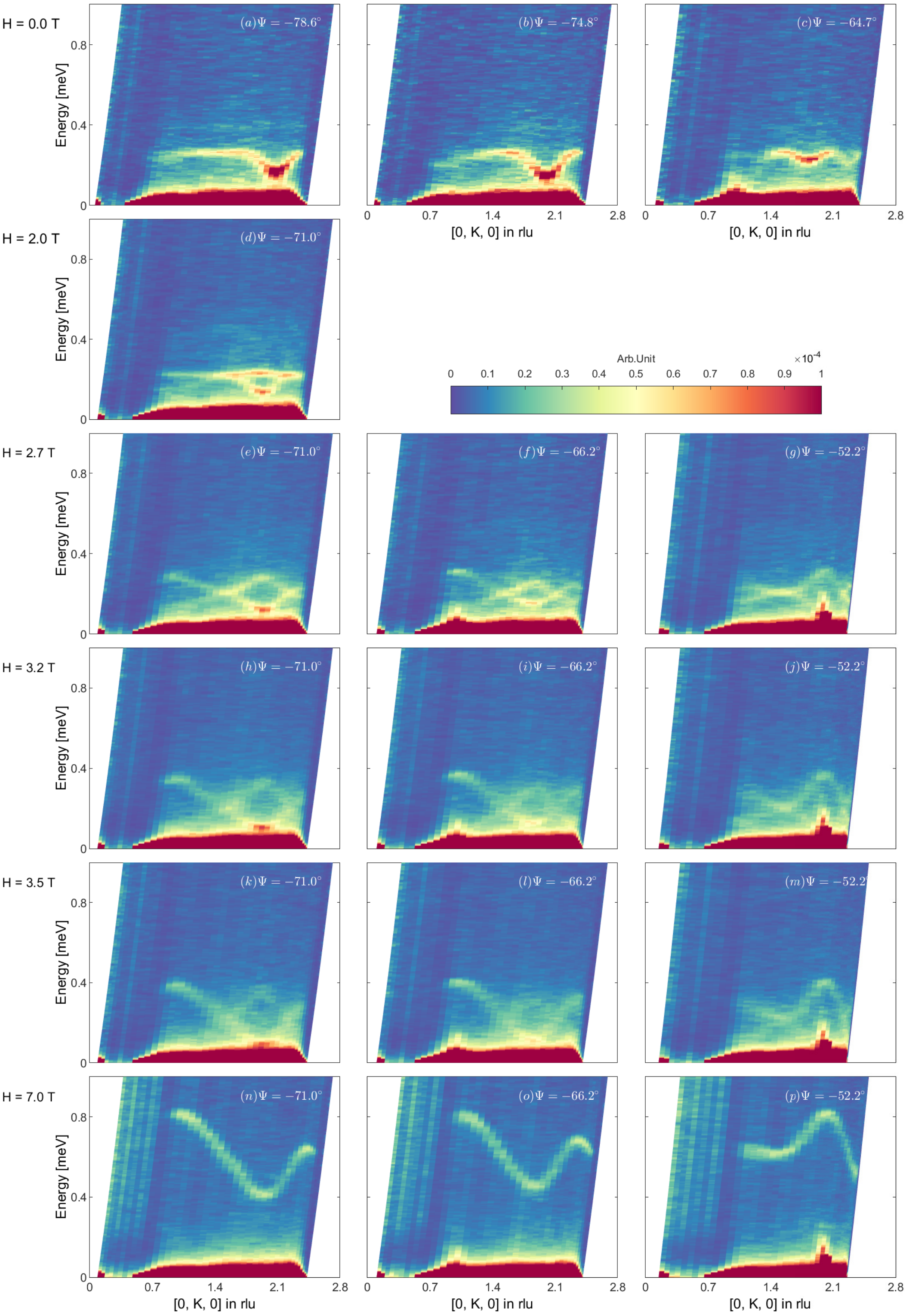

Figure 4.27: Field evolution of the spin excitation in CAPCC where the spectra are projected onto the $[0, \mathrm{K}, 0]$ axis. (a)-(c) Spectra collected at $H = 0.0$ T at $\Psi = -78.6°, -74.8°$ and $-64.7°$, respectively. (d) The spectrum when the field was ramped up to 2.0 T. (e)-(p) A complete view of the spectral evolution from 2.7 T to 7.0 T. (e)(h)(k)(n) $\Psi = -71.0°$, (f)(i)(l)(o) $\Psi = -66.2°$ and (g)(j)(m)(p) $\Psi = -52.2°$.

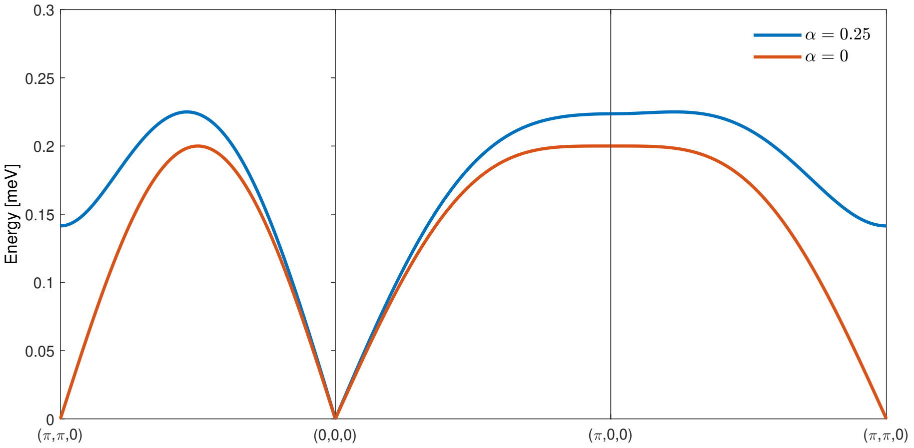

Figure 4.28: Zero field spin wave dispersions along several representative paths in the Brillouin zone with $k_z = 0$ for α = 0 and $\alpha = 0.25$, respectively. Both of the dispersions are calculated with $J = 0.1$ meV and $\theta = 0$ using Eq.(4.12).

Results and analysis

The field evolution of spin excitation spectrum below and above the saturation field $H^* \approx 0.76H_{\text{sat}} \approx 2.75$ T is presented in Fig.4.27. To produce these color plots, the spectra were projected onto the $[0, \text{K}, 0]$ axis and visualized in the MATLAB package Mslice. As the magnet significantly restricted the accessible range of neutron scattering angles, the scattering from the sample was invisible to several detectors. Even though the resultant visible K range also depends on the rotation angle Ψ, as illustrated in Fig.4.27, overall the spin excitations are absent at K below ~ 0.7 r.l.u in all collected spectra. Below K ~ 0.7 r.l.u, only background scattering was collected.

The most prominent feature in the zero field data is that, a well-defined spin wave dispersion is clearly visible in the spectra. At $\Psi = -78.6°$ (Fig.4.27(a)) and $-74.8°$ (Fig.4.27(b)), the spin wave dispersion has a minimum in energy (~ 0.13 meV) at around K $\simeq 2$ r.l.u. As illustrated in Fig.4.26, at $\Psi = -78.6°$ and $-74.8°$, the trajectories of the detector coverage are close to $(\pi, \pi, 0)$ at this K position. In Fig.4.28, we show the zero field spin wave dispersions calculated with $\alpha = 0$ and 0.25 using Eq.(4.13) given $J = 0.1$ meV. It is evident that, due to the presence of α, a spin wave gap is open at $(\pi, \pi, 0)$. Therefore, the observed spin wave minimum at K $\simeq 2$ r.l.u is a reflection of the spin wave gap at $(\pi, \pi, 0)$ and directly indicates α is finite for CAPCC. As K decreases, following the trajectories shown in Fig.4.26 for $\Psi = -78.6°$, the spin wave dispersion reaches $(\pi, 0, 0)$ at K $= 1.5$ r.l.u. Since $(\pi, 0, 0)$ is at the Brillouin zone boundary, the energy transfer value at this position directly reflects the bandwidth of the spin excitation spectrum of CAPCC at zero field. With a rough estimate, the energy transfer at K $= 1.5$ r.l.u in the $\Psi = -74.8°$ spectrum (Fig.4.27(b)) is around 0.25 meV. Compared to the spin wave dispersion shown in Fig.4.28, the nearest neighbor exchange constant J should be around 0.1 meV. For the spectrum collected at $\Psi = -64.7°$ (Fig.4.27(c)), the two maxima of the spin wave dispersion, i.e. one is at $K \simeq 1.5$ r.l.u and the other is around 2.1 r.l.u, both reflect the spin excitation energy at another zone boundary point $(\pi/2, \pi/2, 0)$ according to the trajectories shown in Fig.4.26. The excitation energies of the two maxima are comparable with the previously identified maximum energy 0.25 meV in the $\Psi = -74.8°$ spectrum (Fig.4.27(b)).

When the field becomes finite, there are two spin wave branches existing in the collected spectra, see Fig.4.27(d). We label the lower branch (has a minimum at K $= 2$ r.l.u) as normal mode and the upper branch as ghost mode. The labelling of normal and ghost modes is the same for $\Psi = -66.2°$ but reversed for $\Psi = -52.2°$. As illustrated in Fig.4.27(g), the branch has a maximum at K $\simeq 2$ r.l.u is the normal mode and the ghost mode is the lower branch. The existence of two modes can be explained by Eq.(4.9). The ghost mode can be obtained from the normal mode directly by giving momenta a π shift (**Q** $\rightarrow$ **Q**$+(\pi, \pi, \pi)$). At 2 T (Fig.4.27(d)), both normal and ghost modes are well-defined. This is consistent with our expectation that, below the threshold field $H^* \approx 2.75$ T, magnon decay is not allowed. As the field keeps increasing, the spin excitations at three orientations $\Psi = -71.0°$, $-66.2°$ and $-52.2°$ (Fig.4.27(c)-(m)) follow a general trend: the minimum (maximum) of the normal mode decreases (increases) with increasing field at $\Psi = -71.0°$ and $-66.2°$ ($\Psi = -52.2°$) , while the maximum (minimum) of the ghost mode increases (decreases) as the field strength grows. Intensity-wise, the ghost mode gradually diminishes in intensity with increasing field. At the field close to the saturation value $H_{\text{sat}} = 3.62$ T, the ghost mode is barely discernible in the spectra. This is most evident in the 3.5 T spectrum collected at $\Psi = -71.0°$ (Fig.4.27(k)).

At 2.7 T (Fig.4.27(e)-(g)), both normal and ghost modes are still well-defined even though the applied field 2.7 T is only slightly below the threshold field $H^* \approx 2.75$ T. As soon as the field value is above H^*, see the spectra collected at 3.2 T (Fig.4.27(h)-(j)), the previous well-defined spin wave excitations now become diffuse. It is evident that, compared to the 2.7 T data, the widths of both normal and ghost modes are broadened significantly. In the data shown in Fig.4.27(i), at K $\simeq 1.5$ r.l.u where the two modes cross, the spin excitation is very broad and diffuse without showing any sharp features. According to Fig.4.26, K $= 1.5$ r.l.u at $\Psi = -66.2°$ corresponds to the momentum $(\pi/2, \pi/2, 0)$. As illustrated in Fig.4.25b, theoretically the magnon at $(\pi/2, \pi/2, 0)$ should have a substantial decay when field is above H^*. This is consistent with our experimental observations. On the contrary, in the data shown in Fig.4.27(j), the spin excitation at K $\simeq 1.5$ r.l.u is less broadened compared to the K $\simeq 1.5$ spin excitation in the $\Psi = -66.2°$ spectrum (Fig.4.27(i)). According to Fig.4.26, K $= 1.5$ r.l.u at $\Psi = -52.2°$ corresponds to the momentum $(\pi, 0, 0)$. In theory [51, 60, 63], the magnon decay at $(\pi, 0, 0)$ is less pronounced compared to that at $(\pi/2, \pi/2, 0)$ as demonstrated in Fig.4.25b. Our experimental observation seems to support the theoretical prediction. At 3.5 T, see Fig.4.27(k)-(m), both normal and ghost modes get more diffuse compared to 3.2 T. Apart from that, the general spectral features of the 3.5 T spectra are very similar to what we've found at 3.2 T.

When the field is eventually above the saturation field $H_{\text{sat}} = 3.62$ T, the system is in a quantum paramagnetic state in which magnon decay is not allowed. This is supported by the collected spectra at 7 K (Fig.4.27(n)-(p)), where the spin wave excitations at three different orientations are well-defined. It is evident that No diffuse features nor broadening of the excitations are visible in the collected 7 T spectra.

Fitting to the 7 T data The magnon dispersion in a fully polarized quantum square lattice antiferromgnet reads [71]

$$\hbar\omega_{\mathbf{Q}} = g\mu_B H + 2J(\gamma_{\mathbf{Q}} - 1) + J'(\gamma'_{\mathbf{Q}} - 1), \tag{4.13}$$

where $\gamma_{\mathbf{Q}} = \cos\pi\text{H}\cos\pi\text{K}$ and $\gamma'_{\mathbf{Q}} = \cos\pi\text{L}$. As illustrated in Fig.4.26, the collected spin excitation spectra are centered at L $= 0$ and restricted in the **a*** $-$ **b*** plane. Hence the only extractable parameters from the 7.0 T spectra are J and g. In the following, we list the relevant procedures for conducting the fitting to the 7 T data.

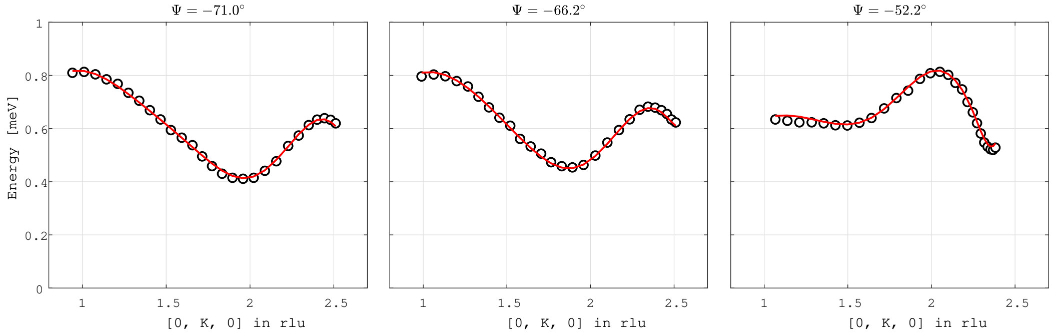

Figure 4.29: The magnon dispersion extracted from the experimental $H = 7.0$ T data. The black open circles are the peak positions extracted from the Gaussian fits. The red solid lines represent the fitted dispersion calculated from Eq.(4.13).

	Value
J	0.102(2) meV
g	2.025(1)

Table 4.4: Values of J and g determined from the least χ^2 fitting to the extracted dispersion collected at $H = 7.0$ T.

- The data was projected onto the $[\mathrm{H}, 0, 0]$, $[0, \mathrm{K}, 0]$ and energy transfer axes in MSlice respectively to extract the corresponding values of H, K and $\hbar\omega_{\mathbf{Q}}$.
- Followed a detector by detector inspection principle, at each detector, the collected spectrum was fitted to a Gaussian lineshape with a linear background model, from which the momentum transfer $\mathbf{Q} = (\mathrm{H}, \mathrm{K}, 0)$ and the energy transfer $\hbar\omega_{\mathbf{Q}}$ were obtained.
- The extracted dispersion $(\mathrm{H}, \mathrm{K}, \hbar\omega_{\mathbf{Q}})$ was fitted to Eq.(4.13). Here we adopted the least-square fitting routine to deduce the parameters J and g. The fitted result is presented in Fig.4.29, see the solid red lines. The fitted J and g are summarized in Tab.(4.4), and are consistent with the values estimated from susceptibility and specific heat measurements [66, 67], see Tab.(4.2). The best-fitted value of $J = 0.102$ meV is also consistence with the observed excitation bandwidth (Fig.4.27(a) and (b)) as explained in the last section.

Width analysis Magnon decay manifest itself through broadening of excitation lineshapes, see Fig.4.25a and Fig.4.25b. Spectroscopy wise for CAPCC, tracking the field evolution of lineshape widths is a feasible way to capture the signature of decays. Owing to the asymmetric spectral linshapes induced by the mixing of the single-magnon branch with the two magnon continuum, to correctly account for such a decay process and extract the corresponding one magnon linewidths, the normal mode for each detector was fitted to the phenomenological lineshape [71]

$$y(\omega) = 2G(\omega; \omega_0, \sigma)\left(1 + \mathrm{erf}\left(\alpha\frac{\omega - \omega_0}{\sqrt{2}\sigma}\right)\right), \tag{4.14}$$

where $G(\omega; \omega_0, \sigma)$ is a Gaussian lineshape centered at ω_0 with width σ, $\mathrm{erf}(\dots)$ is an error function and α adjusts the degree of asymmetry of the lineshape.

As explained in the last section, the magnon decay at $(\pi/2, \pi/2, 0)$ seems stronger than that at $(\pi, 0, 0)$ at elevated fields. To get a more clear view on this, in this section, we extract the excitation linewidths of the normal mode for detectors close to these two **Q** positions. However there are two main issues associated with this which are not avoidable:

- Ideally we only want to extract the widths of the normal mode. However both normal and ghost modes exist in the collected spectra at fields below H_{sat}. To make matters worse, the two modes overlap at K close to 1.5 r.l.u in the spectra measured at $\Psi = -66.2°$ and $-52.2°$ (for $\Psi = -66.2°$: Fig.4.27(f), (i) and (l), for $\Psi = -52.2°$: Fig.4.27(g), (j) and (m)), and K = 1.5 r.l.u is exactly the position where $(\pi/2, \pi/2, 0)$ and $(\pi, 0, 0)$ sit (Fig.4.26). Such an overlap makes the extraction of the excitation widths of the normal mode at $(\pi/2, \pi/2, 0)$ and $(\pi, 0, 0)$ difficult.
- The spectrum for each detector is a constant 2θ (scattering angle) cut, This is in contrast to the commonly adopted strategy of using constant **Q** cuts as illustrated in Fig.4.19. Under such a condition, the extracted excitation linewidths depend on the slope of the spin wave dispersion and also the slope of the detector coverage. As the result, it is not possible to obtain the true linewidths of the spin excitations in the current dataset.

In Fig.4.30a (detector 22) and Fig.4.31a (detector 21), we show the representative fitted results for $\Psi = -66.2°$ and $-52.2°$, respectively. The trajectory of detector 22 at $\Psi = -66.2°$ lies close to $(\pi/2, \pi/2, 0)$ as illustrated in Fig.4.30b(b). Clearly, as the field increases, the spin excitation at $\simeq 0.2$ meV at 2.7 T gets broadened significantly. When the field is above H_{sat}, i.e. $H = 7$ T, the energy of the spin excitation increases to $\simeq 0.55$ meV and the lineshape becomes well-defined again. In Fig.4.30b(a), we summarize the variation of the FWHM of the normal mode from detector 12 to 23 at different fields. The trajectory of each detector is shown in Fig.4.30b(b) with a pink solid line. The widths of the normal mode at 2.7 T and 7 T vary only slightly at different detectors and their values all lie below 0.1 meV. When moving away from detector 12, the width increases substantially at 3.2 T and 3.5 T. This signifies that as **Q** getting closer to $(\pi/2, \pi/2, 0)$, the magnon decay becomes more pronounced. At detector 21, 22 and 23, the widths at 3.2 T and 3.5 are almost identity. With a rough estimate, the mean value is found to be ~ 0.25 meV. Compared to the widths at 2.7 T at detector 21 and 22 whose mean value is around 0.05 meV, the spin excitation width at $(\pi/2, \pi/2, 0)$ increases 4 times larger.

In Fig.4.31a we show the fitted results for detector 21 at $\Psi = -52.2°$. As seen from the plots, the 0.2 meV spin excitation at 2.7 T is very sharp. As the field grows, the excitation starts damping at 3.2 T and 3.5 T. At 7 T, the energy of the excitation moves up to 0.7 meV and the lineshape is more well-defined compared to 3.2 T and 3.5 T. In Fig.4.31b(a), we summarize the widths of the normal mode from detector 17 to 22 at different fields. As illustrated in Fig.4.31b(b), these detectors lie close to $(\pi, 0, 0)$ where less magnon decay is expected compared to $(\pi/2, \pi/2, 0)$. As seen in Fig.4.31b(a), the extracted widths show very little variations at different detectors for all fields. Moreover the width of the normal mode does not increases significantly when changing the field from 2.7 T to 7 T, in contrast to the results shown in Fig.4.30b. We estimate the mean widths at 2.7 T and 3.5 T are $\simeq 0.05$ meV and $\simeq 0.14$ meV, respectively. This corresponds to 1.8 times increase in width at $(\pi, 0, 0)$, which is much smaller than the previously found 4 times increase at $(\pi/2, \pi/2, 0)$. The slightly larger widths for detectors 21 and 22 at 7 T compared to at 2.7 T, is due to the larger slop of the spin wave dispersion in between K $= 1.4$ r.l.u and 2 r.l.u at 7 T compared to at 2.7 T.

In the above analysis, we quantitatively described the magnon decays at $(\pi/2, \pi/2, 0)$ and

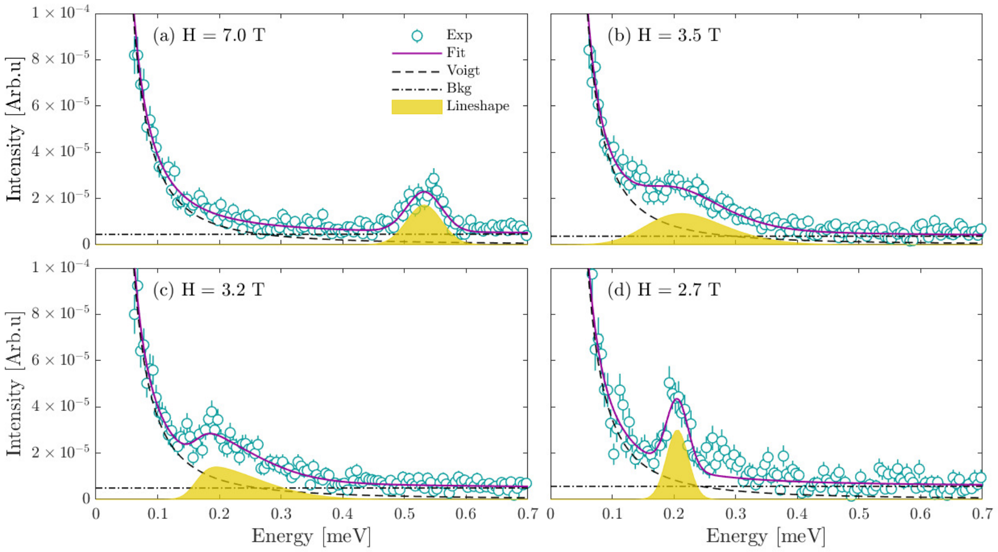

(a) The fitted lineshapes and the experimental spectra for detector 22 at four different fields: **(a)**, 7.0 T, **(b)**, 3.5 T, **(c)**, 3.2 T and **(d)**, 2.7 T. Here the rotation angle Ψ is $-66.2°$.

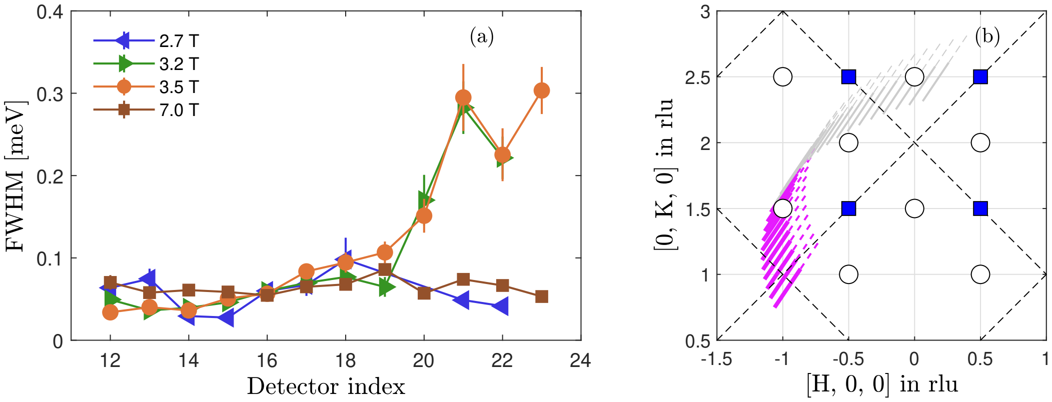

(b) **(a)**, The extracted FWHMs of the lineshapes from detector 12 to detector 23 taken at $\Psi = -66.2°$ at different fields: 7.0 T, 3.5 T, 3.2 T and 2.7 T. **(b)**, The pink solid lines represent the detector trajectories from which the FWHMs are extracted. Here the rotation angle Ψ is $-66.2°$.

Figure 4.30: $\Psi = -66.2°$: (a) Fitted results for detector 22. (b) The extracted FWHMs from detector 12 to 23.

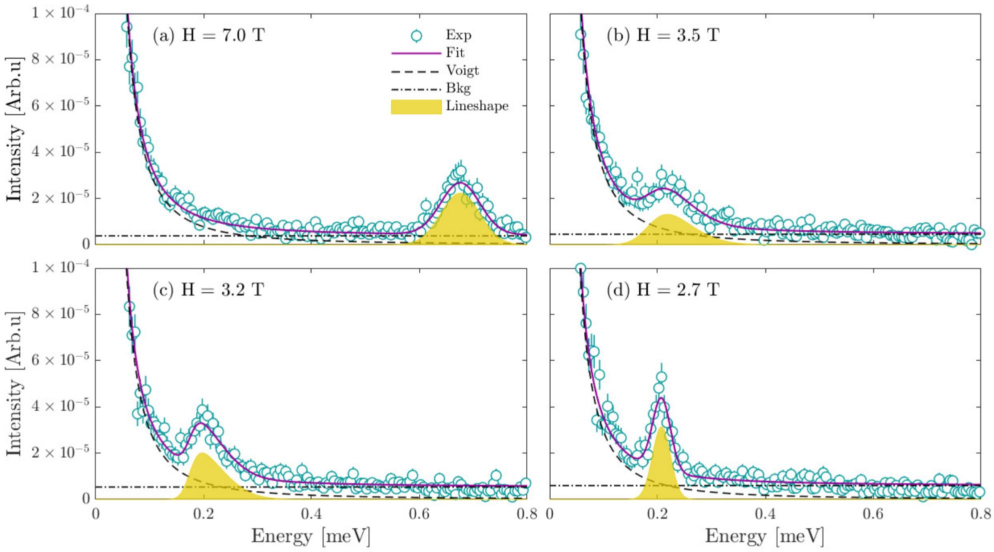

(a) The fitted lineshapes and the experimental spectra for detector 21 at four different fields: **(a)**, 7.0 T, **(b)**, 3.5 T, **(c)**, 3.2 T and **(d)**, 2.7 T. Here the rotation angle Ψ is $-52.2°$.

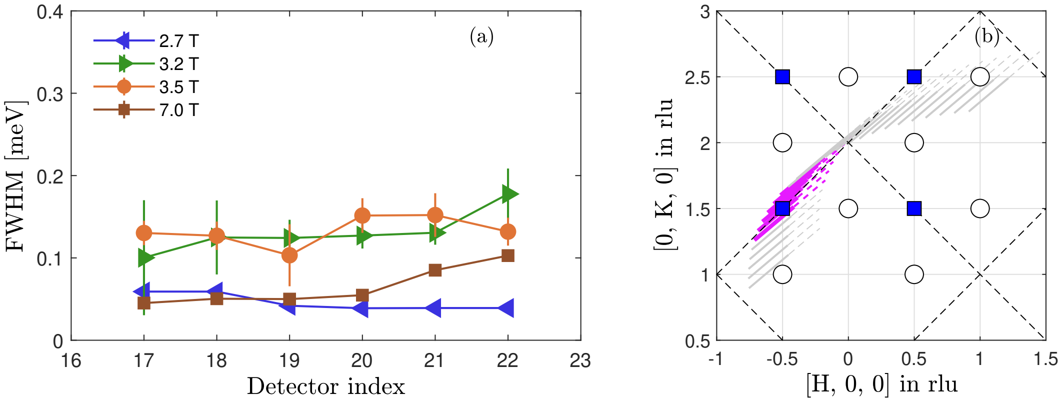

(b) **(a)**, The extracted FWHMs of the lineshapes from detector 17 to detector 22 taken at $\Psi = -52.2°$ at different fields: 7.0 T, 3.5 T, 3.2 T and 2.7 T. **(b)**, The pink solid lines represent the detector trajectories from which the FWHMs are extracted. Here the rotation angle Ψ is $-52.2°$.

Figure 4.31: $\Psi = -52.2°$: (a) Fitted results for detector 21. (b) The extracted FWHMs from detector 17 to 22.

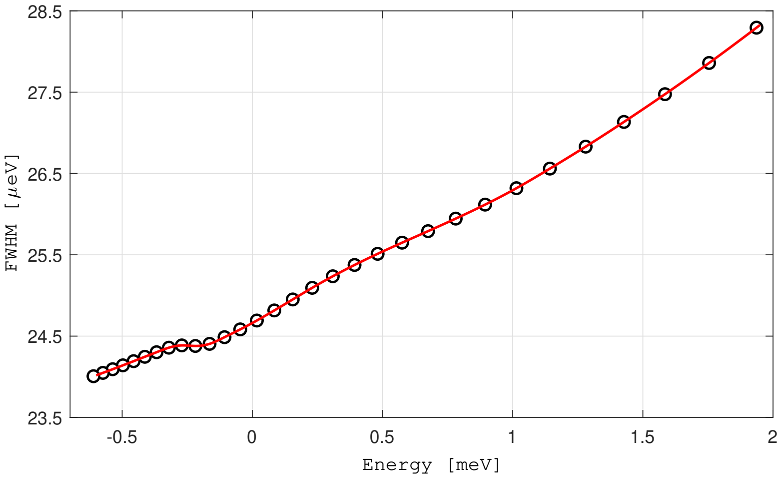

Figure 4.32: Resolution of OSIRIS as a function of energy transfers. The black unfilled circles represent the simulated resolution function obtained from McStas [73] and the red solid line is the interpolated result.

$(\pi, 0, 0)$ in terms of the linewidth of the normal mode, and found the linewidth increase at $(\pi/2, \pi/2, 0)$ is more pronounced than at $(\pi, 0, 0)$ when the field is above H^*. Such a result agrees with the theoretical prediction made in Refs [51, 60, 63], which is also illustrated in Fig.4.25b as previously explained. Even though the two issues mentioned at the beginning of this section would impair the accuracy of this analysis, our results still provide an evidence for magnon decays in CAPCC.

Comparison with the theory

The width analysis presented in the last section provides an evidence for magnon decays in CAPCC. In this section, we ask our self a question: how well can the theory (Section 4.2.1 and 4.2.2) describe the data collected at different fields? To see this, first, we need to address several technicalities as shall be discussed in the following.

The energy resolution of OSIRIS Since OSIRIS is an indirect geometry TOF spectrometer, its instrumental resolution is hard to calculate analytically. Here we used the numerical result from Ref [72], in which the resolution was simulated in McStas [73] up to an energy transfer of 20 meV for a PG002 analyzer, see the black unfilled circles in Fig.4.32. We spline interpolated the simulated resolution (see the red solid line in Fig.4.32) and the result will be reserved for later use when comparing the $1/S$ spin wave spectra to the experimental data.

Account for the integration along the azimuthal direction Fig.4.26 illustrates the reciprocal space probed by OSIRIS as limited to the $\mathbf{a}^* - \mathbf{b}^*$ plane only. This is due to a horizontal scattering configuration of OSIRIS in which the out-of-plane azimuthal scattering angle ψ is assumed to be zero. However, due to the finite height of the analyzer, such an assumption is only valid on a statistical average. In practice, the detector bank collects neutrons reflected from the whole analyzer bank, resulting in the final spectrum being integrated over a certain range along the azimuthal direction (the **y** direction in Fig.4.33). The effect of such an integration is normally negligible as the azimuthal range is small and centered around $\psi = 0°$. However as both magnon decay and the azimuthal integration manifest themselves through broadening of the spectral lineshapes, it is crucial to take the integration effect into account when conducting a quantitative comparison.

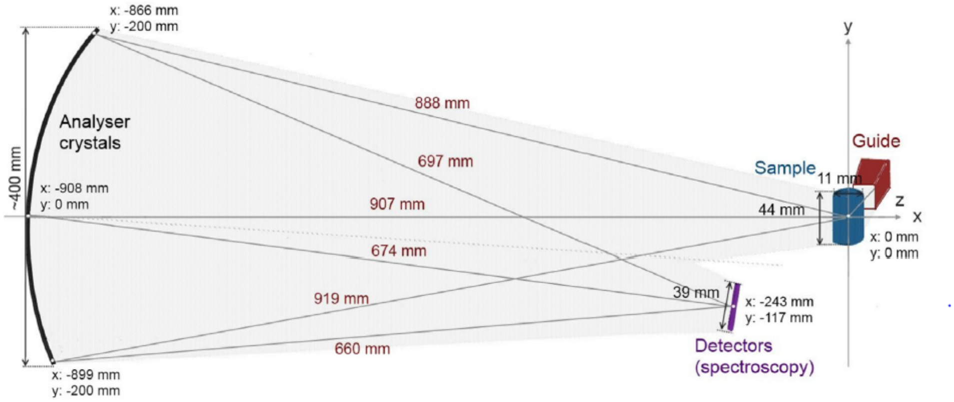

Figure 4.33: The schematic of the secondary spectrometer in OSIRIS, taken from Ref.[72]. Here the horizontal scattering plan is the **x** − **z** plane. Incident neutrons are along the **x** direction.

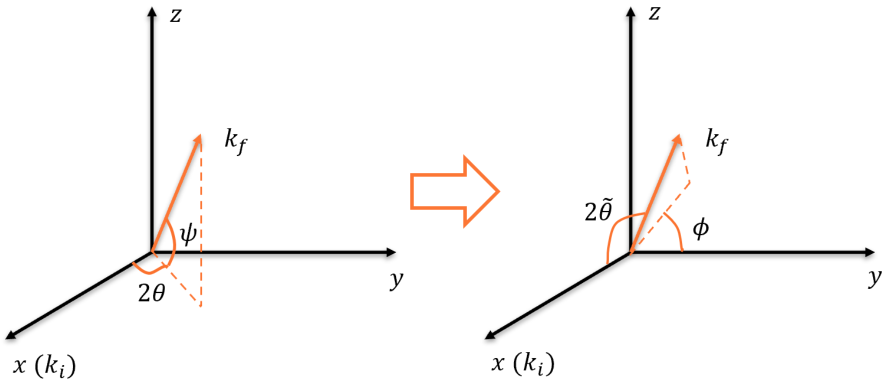

Figure 4.34: Laboratory reference frame for OSIRIS used in Section ”Account for the integration along the azimuthal direction”. Incident neutrons are along the **x** direction and the horizontal scattering plane is the **x** − **y** plane.

To determine how the integration along the azimuthal direction affects H, K and L compared to when scattering is limited to the horizontal plane only, a general formalism is developed as we shall introduce in the following.

We first define a global coordinate system as illustrated in Fig.4.34, where the incident neutron wavevector $\mathbf{k}_i$ is along the **x** direction. The neutron final wavevector is denoted as $\mathbf{k}_f$. As we shall see soon, the main goal of this section is to express $\mathbf{k}_f$ in terms of $(2\tilde{\theta}, \phi)$.

Given that the analyzer bank sits on a segment of a circle and the sample is at the center, thus each row of the analyzer bank shares the same azimuthal angle ψ (in the current situation, each analyzer position corresponds to an unique $\mathbf{k}_f$). ψ is defined as the angle between $\mathbf{k}_f$ and its projected vector onto the horizontal $\mathbf{x} - \mathbf{y}$ plane, as illustrated in Fig.4.34). But the horizontal scattering angle 2θ along the row varies and it is defined as the angle between the **x** axis and the projection of $\mathbf{k}_f$ onto the $\mathbf{x} - \mathbf{y}$ plane, as shown in Fig.4.34.

We start with defining the unit vector **u** of $\mathbf{k}_f$ at $(2\theta, \psi)$:

$$\begin{aligned} u_x &= \cos\psi \cos 2\theta, \\ u_y &= \cos\psi \sin 2\theta, \\ u_z &= \sin\psi, \end{aligned} \tag{4.15}$$

from which the total scattering angle $2\tilde{\theta}$, as illustrated in Fig.4.34, can be obtained

$$2\tilde{\theta} = -\arccos\left([1,0,0] \times [u_x, u_y, u_z]^T\right). \tag{4.16}$$

Now the new azimuthal angle ϕ (see Fig.4.34), defined as the angle between and the **y** axis and the projection of $\mathbf{k}_f$ onto the $\mathbf{y} - \mathbf{z}$ plane, can be calculated as follow

$$\phi = \pi - \text{sgn}(\psi) \times \arccos\left(\frac{[1,0] \times [u_y, u_z]^T}{\sqrt{u_y^2 + u_z^2}}\right), \tag{4.17}$$

where sgn(ψ) is 1 for $\psi > 0$ and -1 for $\psi < 0$, respectively. When $\psi = 0$, ϕ is assigned to be 0 as well.

Now we managed the most crucial step: to represent $\mathbf{k}_f$ in terms of a new set of variables $(2\tilde{\theta}, \phi)$. It is in this step that the azimuthal degree of freedom is taken into account.

The next step is to express the momentum transfer $\mathbf{Q} = \mathbf{k}_i - \mathbf{k}_f$ in terms of $(2\tilde{\theta}, \phi)$. This can be achieved via

$$\begin{aligned} Q_x &= k_i - \cos 2\tilde{\theta} \times k_f, \\ Q_y &= -\sin 2\tilde{\theta} \cos\phi \times k_f, \\ Q_z &= -\sin 2\tilde{\theta} \sin\phi \times k_f. \end{aligned} \tag{4.18}$$

If the sample is further rotated anti-clockwise by an angle Ψ in the horizontal $\mathbf{x} - \mathbf{y}$ plane (the $\mathbf{a}^* - \mathbf{b}^*$ plane for CAPCC), follow a simple coordinate transformation, the final momentum transfer transfer **Q** reads

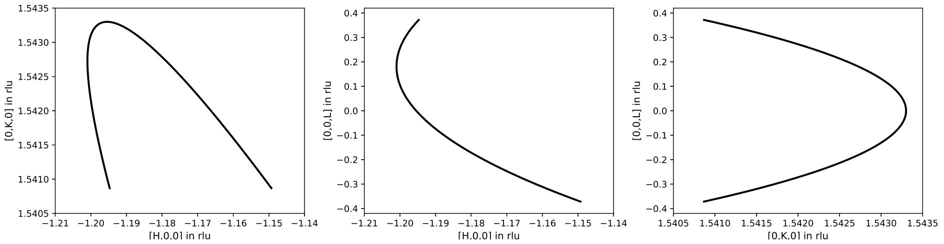

Figure 4.35: The accessible $(\mathsf{H}, \mathsf{K}, \mathsf{L})$ (black solid lines) in reciprocal space for CAPCC for a particular scattering angle, 2θ, and a particular energy transfer, $\hbar\omega = 0.5$ meV, given $E_f = 1.8463$ meV and the azimuthal angle range is from -9° to 9°.

$$\begin{aligned}
\tilde{Q}_x &= Q_x \cos\Psi + Q_y \sin\Psi, \\
\tilde{Q}_y &= -Q_x \sin\Psi + Q_y \cos\Psi, \\
\tilde{Q}_z &= Q_z,
\end{aligned} \tag{4.19}$$

As the last step, in order to transform the momentum transfer **Q** from the laboratory frame to the reciprocal lattice basis of the sample, the following transformation is applied

$$[\mathsf{H}, \mathsf{K}, \mathsf{L}]^T = \mathsf{inv}\,(\mathsf{U}) \times \left[\tilde{Q}_x, \tilde{Q}_y, \tilde{Q}_z\right]^T, \tag{4.20}$$

where U is the lattice basis matrix of the sample in the laboratory frame and inv(U) represents the inverse of U.

It can be calculated from Fig.4.33 that azimuthal angles for the upper and lower edges of analyzer in OSIRIS are around $\psi_{\mathsf{upper}} = 13.00^\circ$ and $\psi_{\mathsf{lower}} = -12.54^\circ$, respectively. However due to the installment of magnet at the sample position, the true accessible azimuthal range was limited to $[-9^\circ, +9^\circ]$ during the experiment [74]. In Fig.4.35, we illustrate the calculated accessible $(\mathsf{H}, \mathsf{K}, \mathsf{L})$ in reciprocal space for CAPCC given the final analyzer energy $E_f = 1.8463$ meV, the horizontal scattering angle $2\theta = -80^\circ$ and the energy transfer $\hbar\omega = 0.5$ meV. In this particular situation, the curved trajectories span the ranges (units in rlu) H : $[-1.201, -1.149]$, K : $[1.541, 1.543]$ and L : $[-0.372, 0.372]$. Hence the finite height of analyzer contributes mostly to the integration along the L direction. The asymmetric ranges in H and K are a result of (i) the monoclinic crystal structure ($\beta = 94.37^\circ$) and (ii) the difference in lattice constants, $a = 12.85$ Å and $b = 8.37$ Å.

Comparison between the theory and the experiment Having determined the energy resolution of OSIRIS, and established the formalism to account for the integration along azimuthal direction due to the finite height of analyzer bank. Combining them with the previously explained $1/S$ spin wave theory for calculating the double differential cross-section $\frac{d^2\sigma}{d\Omega dE}$ at different fields, see Eq.(4.11), now it's time to compare the theoretical result with the experimental data to elucidate its accuracy.

As the first step, we need to set up a work flow to efficiently simulate the neutron scattering patterns collected by OSIRIS at different magnetic fields. Even though the essential formulas for achieving it have already been explained in the previous sections, there are still some technical difficulties that need to be addressed:

- When evaluating the self-energy $\Sigma_1(\mathbf{k},\omega)$ or $\Sigma_2(\mathbf{k},\omega)$ (Eq.(4.7)), a summation over momenta in the Brillouin zone needs to be carried out. To calculate it accurately with low variance, the Quasi-Monte Carlo integration method [75] was applied, in which 10,000 three dimensional Sobol sequences [75] (q_x, q_y, q_z) were generated to fill the cubic region $[0,2\pi]\times[0,2\pi]\times[0,2\pi]$ with low discrepancy. This allows us to fast calculate the double differential cross-section $\frac{d^2\sigma}{d\Omega dE}$. Here we denote the calculated cross-section as Spec $(\mathbf{k}(\psi),\omega,\psi)$ ($\mathbf{k}$ is momentum transfer and ω is energy transfer). ψ represents the angle in the azimuthal direction, see Fig.4.34.The ψ dependence of **k** comes from that, when taking the azimuthal direction into account, **k** becomes a function of ψ. This can be seen from the "Account for the integration along the azimuthal direction" Section.
- For the integration along the azimuthal direction, the integration is represented as

  $$\text{Spec}_{\text{final}}(\mathbf{k},\omega) = \frac{1}{\psi_{\text{max}}-\psi_{\text{min}}}\int_{\psi_{\text{min}}}^{\psi_{\text{max}}} \text{Spec}\left(\mathbf{k}(\psi),\omega,\psi\right) d\psi \tag{4.21}$$

  where ψ_{min} and ψ_{max} are -9° and $+9^\circ$, respectively. Applying the trapezoidal rule, Eq.(4.21) can be approximated by

  $$\text{Spec}_{\text{final}}(\mathbf{k},\omega) \approx \frac{1}{\psi_{\text{max}}-\psi_{\text{min}}}\sum_{i=0}^{N-1} \text{Spec}\left(\mathbf{k}(\psi_{\text{min}}+i\delta\psi),\omega,\psi_{\text{min}}+i\delta\psi\right)\delta\psi, \tag{4.22}$$

  where $N\in\mathbb{Z}$ is the grid size in ψ and the step size $\delta\psi$ is defined as $\delta\psi := \frac{\psi_{\text{max}}-\psi_{\text{min}}}{N}$. In our calculation, N is set to 100, thus $\delta\psi = 0.18^\circ$.
- Even though we have now taken into account the integration along the azimuthal direction, the simulated "bare" spectra still cannot compare with the experimental data directly, as the energy resolution effect plays another crucial role and hasn't been considered yet. The energy resolution function of OSIRIS is assumed to be represented by a Gaussian $G\left(\omega;\omega_0,\text{FWHM}(\omega_0)\right)$

  $$G\left(\omega;\omega_0,\text{FWHM}(\omega_0)\right) = \frac{2.355}{\sqrt{2\pi}\text{FWHM}(\omega_0)} e^{-\frac{2.355^2}{2}\times\frac{(\omega-\omega_0)^2}{\text{FWHM}^2(\omega_0)}}, \tag{4.23}$$

  where ω is the energy transfer, ω_0 is the center of the Gaussian profile, and FWHM(ω_0) is the previously interpolated energy dependent FWHM at ω_0 (Fig.4.32). The convolution of the simulated spectrum Spec$_{\text{final}}(\mathbf{k},\omega)$, Eq.(4.22), with the resolution function can be approximated by

  $$\begin{aligned}\text{Spec}_{\text{conv}}(\mathbf{k},\omega) &= \int_{-\infty}^{\infty} \text{Spec}_{\text{final}}(\mathbf{k},\omega-\omega_0) G\left(\omega;\omega_0,\text{FWHM}(\omega_0)\right) d\omega_0 \\ &\approx \sum_{i=0}^{M-1} \text{Spec}_{\text{final}}(\mathbf{k},\omega_i) G\left(\omega;\omega_i,\text{FWHM}(\omega_i)\right)\end{aligned} \tag{4.24}$$

  where $M = 210$ is the number of energy bins recorded by the detector bank of OSIRIS.

For the next step, we need to determine which set of parameters (J,α,g) provides the best description to the collected spectra. As explained before, the gap observed in the zero field data (Fig.4.27(a) and (b)) can be used to determine the size of α, and the bandwidth of the spin excitations can determine J. Thus we need to include at least one zero field spectrum in the fitting process. To estimate g, several spectra at different fields are included. Hence the following fitting routine was conducted for the parameter estimation:

Label	J [meV]	α	J
1	0.1003	0.2761	2.0271
2	0.102(2)		2.025(1)
3	0.11	0.25	

Table 4.5: Values of J, α and g obtained from **1** minimizing the cost function Eq.(4.26), **2** fitting to the 7 T data, and **3** thermodynamic measurement [66, 67].

- The following spectra were chosen for the fitting process: ($H = 0.0$ T, $\Psi = -74.8°$), ($H = 2.0$ T, $\Psi = -71.0°$), ($H = 2.7$ T, $\Psi = -71.0°$) and ($H = 7.0$ T, $\Psi = -71.0°$).
- Set the saturation field for later simulations to the theoretical value: $H_{\text{sat}} = \frac{4J+2J\alpha}{g\mu_B}$.
- Set up the simulation workflow as introduced above to calculate the magnetic scattering contribution $y^{\text{mag}}(J, \alpha, g) \equiv \text{Spec}_{\text{conv}}(\mathbf{k}, \omega)$ for a given parameter set (J, α, g), where the resolution effect and the integration along the azimuthal direction were both taken into account. In addition, for numerically implementing Green's function (Eq.(4.7)), the imaginary part $i0$ in the denominator was replaced by a finite value $i\Gamma$ with $\Gamma = 0.01 \times 2J(\alpha + 2)$, which is much smaller than the energy resolution of OSIRIS.
- To properly account for the non-magnetic scattering $y^{\text{non-mag}}$ in the experimental spectra, for each detector, we introduced a Voigt lineshape Voigt $\left(\omega; \text{amp}, \omega^0_{\text{Voigt}}, \sigma, \gamma\right)$ to model the incoherent elastic scattering centered at $\omega = 0$ and a linear function $A\omega + B$ to account for the background intensity at non-zero energy transfers. The six unknown parameters $\left(\text{amp}, \omega^0_{\text{Voigt}}, \sigma, \gamma, A, B\right)$ were determined via the Levenberg - Marquardt method [76] where the cost function for each detector is defined as

$$\chi^2_{2\theta}(J, \alpha, g) = \sum_i \left(\frac{y_i^{\text{exp}} - y_i^{\text{mag}}(J, \alpha, g) - y_i^{\text{non-mag}}}{e_i^{\text{exp}}} \right)^2, \tag{4.25}$$

  in which 2θ is the horizontal scattering angle for labelling different detectors, y^{exp} and e^{exp} are the experimental scattering intensities and error bars respectively, and the summation is over all the collected data points.
- The total cost function Cost(J, α, g) is defined as the mean of $\chi^2_{2\theta}(J, \alpha, g)$ over all feasible detectors

$$\text{Cost}(J, \alpha, g) = \frac{1}{N_{2\theta}} \sum_{\{2\theta\}} \chi^2_{2\theta}(J, \alpha, g), \tag{4.26}$$

  where $N_{2\theta}$ is the total number of detectors included in the fitting process for each spectrum. Constrained by the limited horizontal opening angle of magnet, only 27 out of all 42 detectors in OSIRIS were useful, of which the indices are from 12 to 38. The minimization of Cost(J, α, g) was solved by the Nelder-Mead method [76] after ~ 50 iterations.

Results The parameters (J, α, g) obtained from the optimization process are summarized in the first row of Table 4.5. Due to the inclusion of the zero field data, the value of α can be estimated reliably. According to the optimization, with $\alpha = 0.2761$, the simulated spectra provide the best description of the experimental data. The estimation of the associated errors for J, α and g has not been performed. This will be left for future study. Compared to the results extracted from fitting to the 7.0 T magnon dispersion (shown in

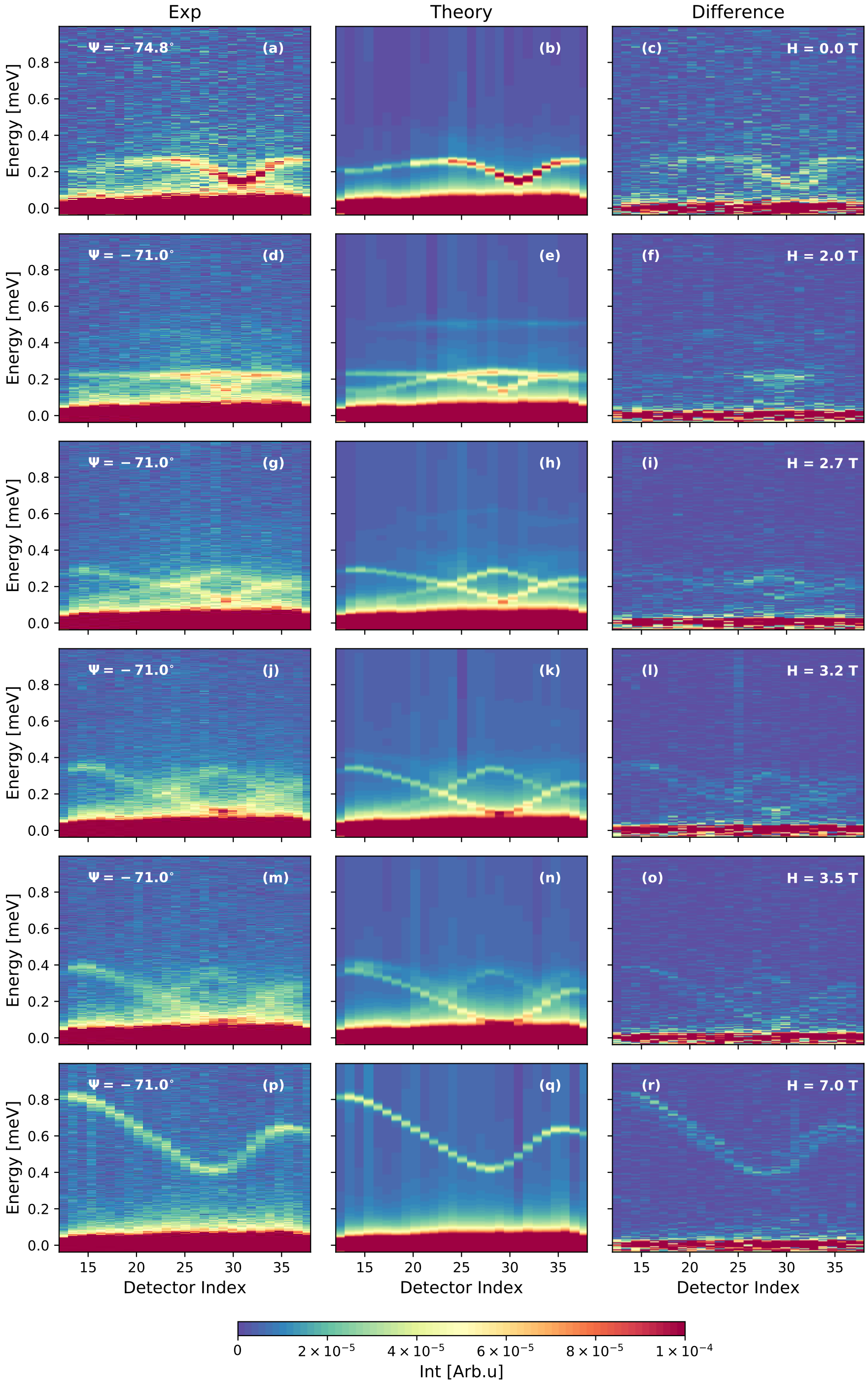

Figure 4.36: Comparison between the fitted theoretical results and the experimental data. The left most column illustrates the experimental spectra, the middle column is the fitted theoretical results and the right most column is the absolute difference between the two. From top to bottom, the spectra are collected/simulated at ($\Psi = -74.8°, H = 0.0$ T), ($\Psi = -71.0°, H = 2.0$ T), ($\Psi = -71.0°, H = 2.7$ T), ($\Psi = -71.0°, H = 3.2$ T), ($\Psi = -71.0°, H = 3.5$ T) and ($\Psi = -71.0°, H = 7.0$ T), respectively.

the second row of Table 4.5), J and g are nearly the same. Clearly, as shown in the third row of Table 4.5, the values obtained from magnetic susceptibility and magnetization [66, 67] underestimate J and overestimate g. Such a discrepancy is also readily seen when comparing the theoretical saturation field strength (calculated with the parameters listed in the first row of Table 4.5), $H_{\text{sat}}^{\text{theory}} = 3.89$ T, with the experimental value, $H_{\text{sat}}^{\text{exp}} = 3.61$ T. The difference between them might due to the existence of other interactions in the system, which shall be discussed in Conclusion.

The fitted results are illustrated in Fig.4.36, where the third column presents the absolute difference between the theory and the experiment, Difference $:= |\text{Spec}^{\text{Exp}} - \text{Spec}^{\text{Theory}}|$. To provide a more clear view, we show the fitted spectrum for each detector as shown in Fig.4.37 ($\Psi = -74.8°$, H = 0.0 T), Fig.4.38 ($\Psi = -71.0°$, H = 2.0 T), Fig.4.39 ($\Psi = -71.0°$, H = 2.7 T), Fig.4.40 ($\Psi = -71.0°$, H = 3.2 T), Fig.4.41 ($\Psi = -71.0°$, H = 3.5 T), and Fig.4.42 ($\Psi = -71.0°$, H = 7.0 T).

As illustrated in Fig.4.36, when the field is much lower than the threshold field $H^* \approx 2.75$ T where no magnon decays occur, i.e. H $= 0$ T (Fig.4.36(a)-(b)) and 2T (Fig.4.36(d)-(e)), the $1/S$ spin wave theory provides an overall good description of the experimental data. Even though the difference spectra illustrated in Fig.4.36(c) and (f) show some evident residual intensities especially at 0 T (Fig.4.36(c)), they are much smaller than the intensities of the experimental data (Fig.4.36(a) and (d)). To find out where the differences come from, we turn to the detector cuts shown in Fig.4.37 and Fig.4.38. At 0 T, the peak positions at different detectors are captured quite well by the $1/S$ spin wave theory and the main difference arises when comparing the width. The excitation lineshapes in the experimental data are slightly broader than the theoretical calculations, giving rise to the evident residual features observed in the difference spectrum (Fig.4.36(c)). At 2 T, the positions and widths of the normal mode (the lower branch which has a minimum close to detector 28) are captured quite well by the $1/S$ spin wave theory. Whereas for the ghost mode (the upper branch which is relatively flat), the theory predicts slightly higher energies compared to the experimental data, as illustrated in the detector cuts at $2\theta = -108°$, $-111.4°$ and $-114.7°$ in Fig.4.38. Overall the differences between the $1/S$ spin wave theory and the experiment data are not significant, justifying the claim that the theory and the experiment are in good accord.

As the field approaches the threshold field, i.e. H $= 2.7$ T, $1/S$ spin wave theory again captures the peak positions of the excitations relatively well. This can be directly seen from the difference spectrum Fig.4.36(i), in which no evident residual features for the normal mode are observed (the lower branch which has a minimum close to detector 30). However, there are some residual intensities for the ghost mode (the upper branch which has a maximum close to detector 30) in the difference spectrum (Fig.4.36(i)). Such differences are readily seen in the detector cuts illustrated in Fig.4.39. Similar to what we found at 2 T, the theory predicted energies for the ghost mode are slightly higher than the observations. This is readily seen from, such as, the detector cuts at $2\theta = -91.4°$, $-94.73°$ and $-98.06°$. In addition, the widths for both normal and ghost modes are slightly underestimated by the $1/S$ spin wave theory. This can be seen from some of the detector cuts, such as $2\theta = -91.4°$ and $-108°$. In general, the differences between the theory and the experiment are not severe and the two are still in good accord.

When the field is finally above the threshold field, i.e. H $= 3.2$ T and 3.5 T, we enter the regime where magnon decays are expected to occur. Compared the theoretical spectra to the experimental data at 3.2 T (Theory: Fig.4.36(j), Exp: Fig.4.36(k)) and 3.5 T (Theory: Fig.4.36(m), Exp: Fig.4.36(n)), it is immediately clear that the excitations in the theoretical spectra are much sharper than the experimental data. This can seen more clearly from the detector cuts (3.2 T: Fig.4.40 and 3.5 T: 4.41). For instance, the experimental $2\theta = -91.4°$ detector cut at 3.5 T shows no sharp features in its lineshape besides a broad continuum of excitations. Whereas the $1/S$ spin wave theory predicts two clear sharp peaks in the spectrum. Similar situations are encountered in the detector cuts at 3.5 T. For example, $2\theta = -118°$, the intense sharp peak below 0.2 meV predicted by the theory is replaced by a much weaker and broader feature in the experimental data. Besides the width differences, peak position-wise, the $1/S$ spin wave theory captures relatively well where the excitations should locate as seen from different detector cuts shown in Fig.4.40 and Fig.4.41. Even though there are small discrepancies, such as the $2\theta = -101.40°$ at 3.2 T cut where the theory predicts slightly higher energy of the excitation, and the $2\theta = -121.40°$ at 3.5 T in which the theory underestimates the excitation energy. In general the differences in peak positions between the theory and the experiment are acceptable.

At 7 T, the system is in a fully polarized phase where no magnon decays are allowed and the excitations' linewidths are expected to be resolution limited. Even though, as illustrated in Fig.4.36(p) the excitations in the experimental data are well defined, they appear to broader than the calculated results from the $1/S$ spin wave theory shown in Fig.4.36(q). This is also evident from the detector cuts illustrated in 4.42. Even though the peak positions of the excitations are captured relatively well by the theory, the theory largely underestimates the size of the excitation linewidths. Because when performing calculations in a fully polarized phase, the widths of the excitaions are solely determined by the energy resolution of OSIRIS (Fig.4.32). The observed width discrepancy could indicate that we might underestimate the energy resolution of OSIRIS.

4.2.4 Conclusions

Our width analysis presented in Section 4.2.3 shows that, compared to the widths obtained at 2.7 T where no magnon decays are expected, the excitation linewidths increase ~ 4 times at $(\pi/2, \pi/2)$ and only ~ 1.8 times at $(\pi, 0, 0)$ for both 3.2 T and 3,5 T. This signifies that, the one magnon response at vicinities close to $(\pi/2, \pi/2)$ dampens more heavily compared to $(\pi, 0)$ with field increasing, in particular when the field approaches the saturation field of CAPCC, $H_{\text{sat}} = 3.62$ T. This is in good accord with theoretical predictions [51, 60, 61, 62, 63].

We also carried out $1/S$ spin wave calculations and compared the results with the experimental data. This gives us an estimation of the exchange constants and the g-factor of the Hamiltonian, which are found to be $J = 0.1003$ meV, $J'/J = 0.2761$ and $g = 2.0271$. These are in good accord with the estimated values from the thermodynamic measurement [66, 67] and the fitting to the spin wave disperisions at 7 T (Section 4.2.3). With the obtained parameters, the peak positions of the excitations in the experimental data can be relatively well reproduced by the $1/S$ spin wave theory. Whereas for the excitation linewidths, the theory tends to underestimate their sizes. Such an underestimation is most significant at 3.2 T and 3.5 T, where the observed excitations heavily dampen and broaden, in contrast to having relative sharp features predicted by the $1/S$ spin wave theory.

Such a deviation between the theory and the experiment may arise from:

- There is an underestimation of the energy resolution of OSIRIS. This can be seen from the comparison between the experimental data and the $1/S$ spin wave theory results at 7 T (Fig.4.36(p) and (q)), where the experimental spectra are broader than the simulations.

- In the $1/S$ spin wave theory, the renormalized single magnon branch escapes from the two magnon continuum as the one-loop approximation takes into account the correction of the real part of the energy as well [63]. As the result, the magnon decay is likely underestimated in theory.
- There is a large difference between the experimental saturation field strength, $H_{\text{sat}}^{\text{exp}} = 3.62$ T, and the theoretical value calculated from the best fitted J, α and g, $H_{\text{sat}}^{\text{theory}} = 3.89$ T. As the result, decays are less pronounced in the theoretical calculation as the ratio between the external field and the saturation field becomes smaller compared to that in reality, e.g $H/H_{\text{sat}}^{\text{theory}} < H/H_{\text{sat}}^{\text{exp}}$. The overestimation of the saturation field might relate to the $J - J'$ Heisenberg Hamiltonian is not the full story. Other exchange interactions may also be present in the Hamiltonian. Thus the saturation field will be modified and potentially can give rise to larger decays.
- In an external magnetic field, besides the Zeeman coupling $H_{\text{Zeeman}} = g\mu_B \mathbf{H} \cdot \sum_i \mathbf{S}_i$, an additional spin chirality term $H_{\text{chiral}} = J_\chi \sum_\Delta \mathbf{S}_i \cdot (\mathbf{S}_j \times \mathbf{S}_k)$ is also present where the summation is over all elementary triangular plaquettes, denoted by Δ and its strength J_χ is proportional to the magnetic flux penetrating through the triangular plaquette [77]. Usually such a chiral term is extremely small [78] and ignored more of the time. But it can drive the antiferromagnetic order close to a critical point (but still in the antiferromagnetic order), hence one can imagine the magnons would have a larger decay [79].

Nevertheless, here we provide the first experimental evidence for magnon decays in the two-dimensional $S = 1/2$ antiferromagnet on a square lattice. Despite there are some discrepancies between the $1/S$ spin wave theory and the experimental data, the theory still provides an overall relatively well description of the experimental data. This is summarized in Fig.4.43 where we illustrate both the experimental and theoretical spectra at 3.5 T. The difference between them is less than 10% of the raw data. Finally a full understanding of the discrepancies will be left for future study.

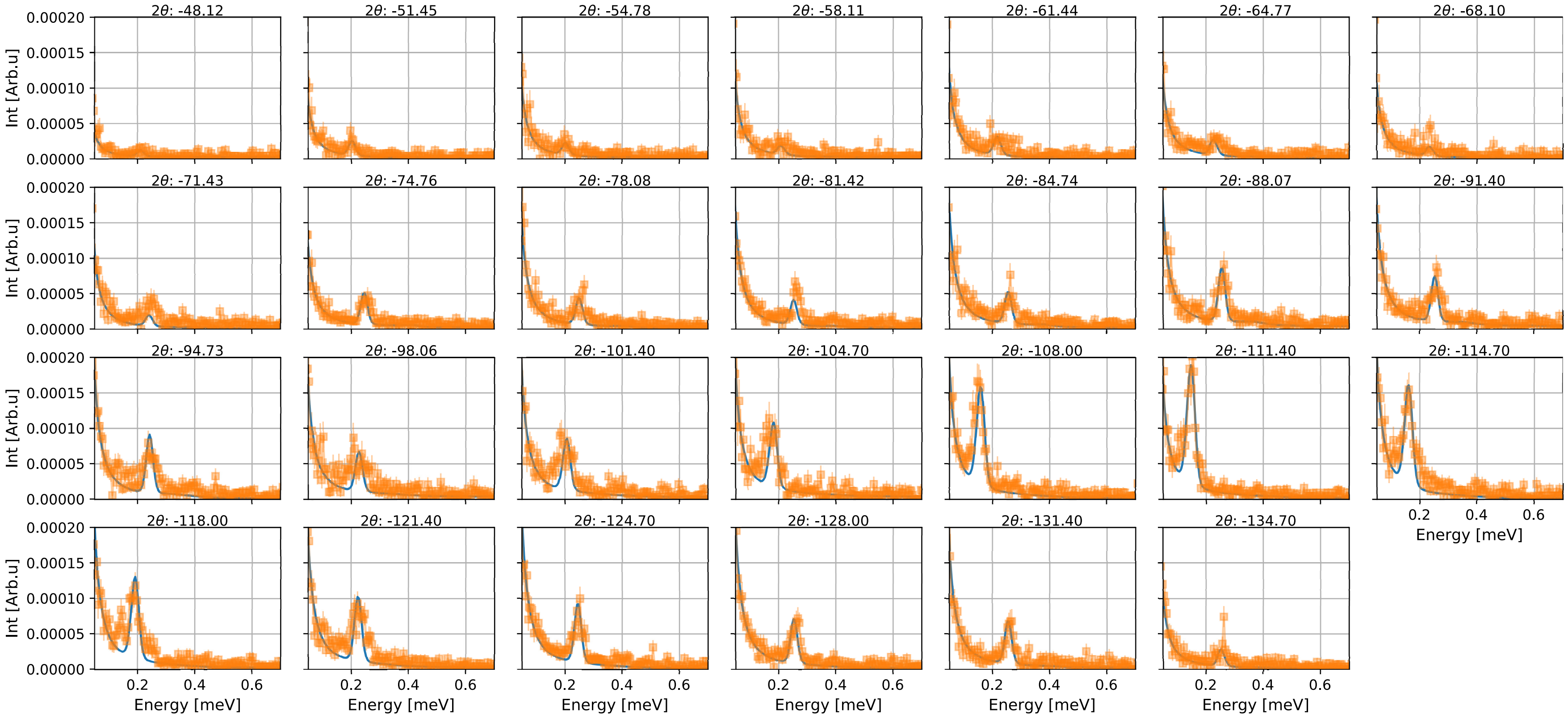

Figure 4.37: Lineshape comparison between the theory and the experiment at ($\Psi = -74.8°$, H=0.0 T) for different detectors labelled by the corresponding scattering angle 2θ.

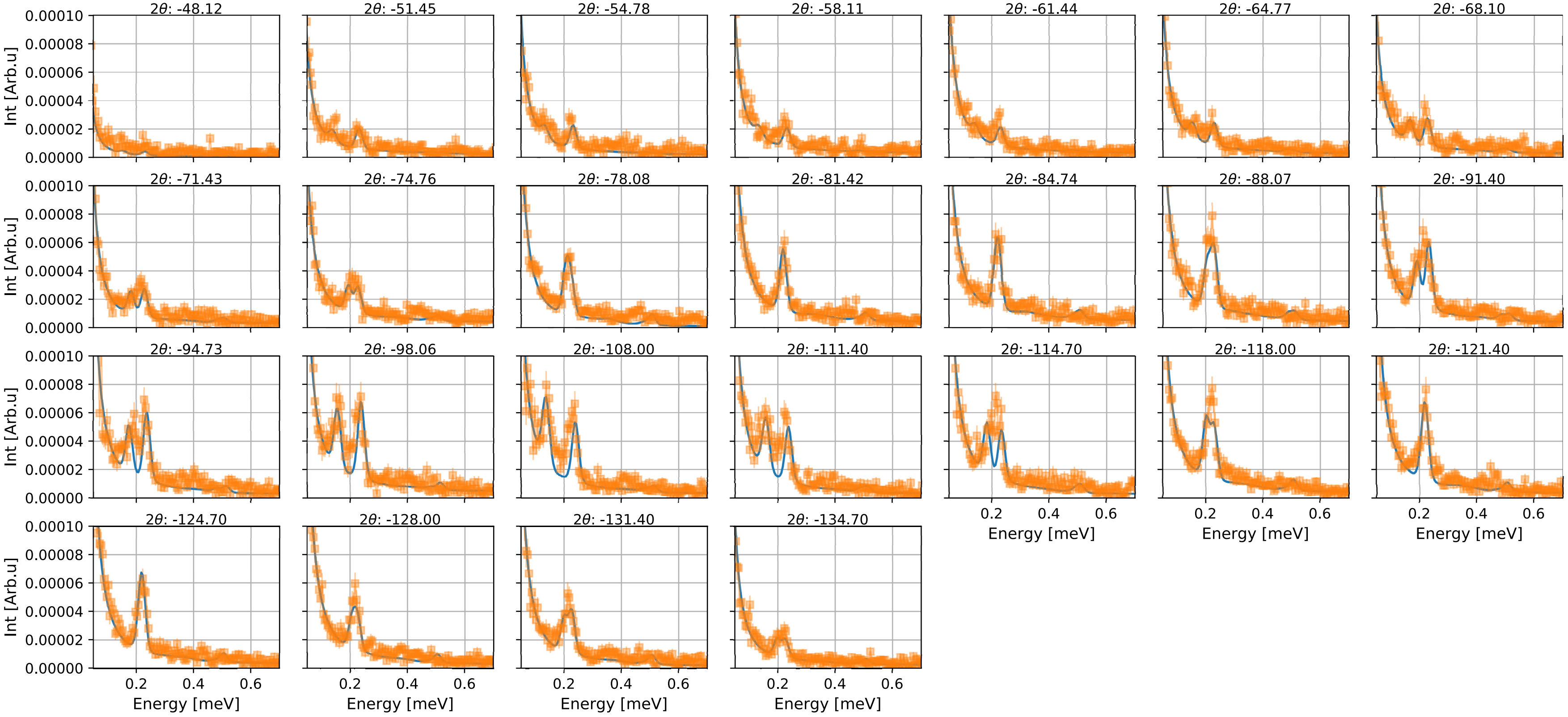

Figure 4.38: Lineshape comparison between the theory and the experiment at ($\Psi = -71.0°$, H=2.0 T) for different detectors labelled by the corresponding scattering angle 2θ.

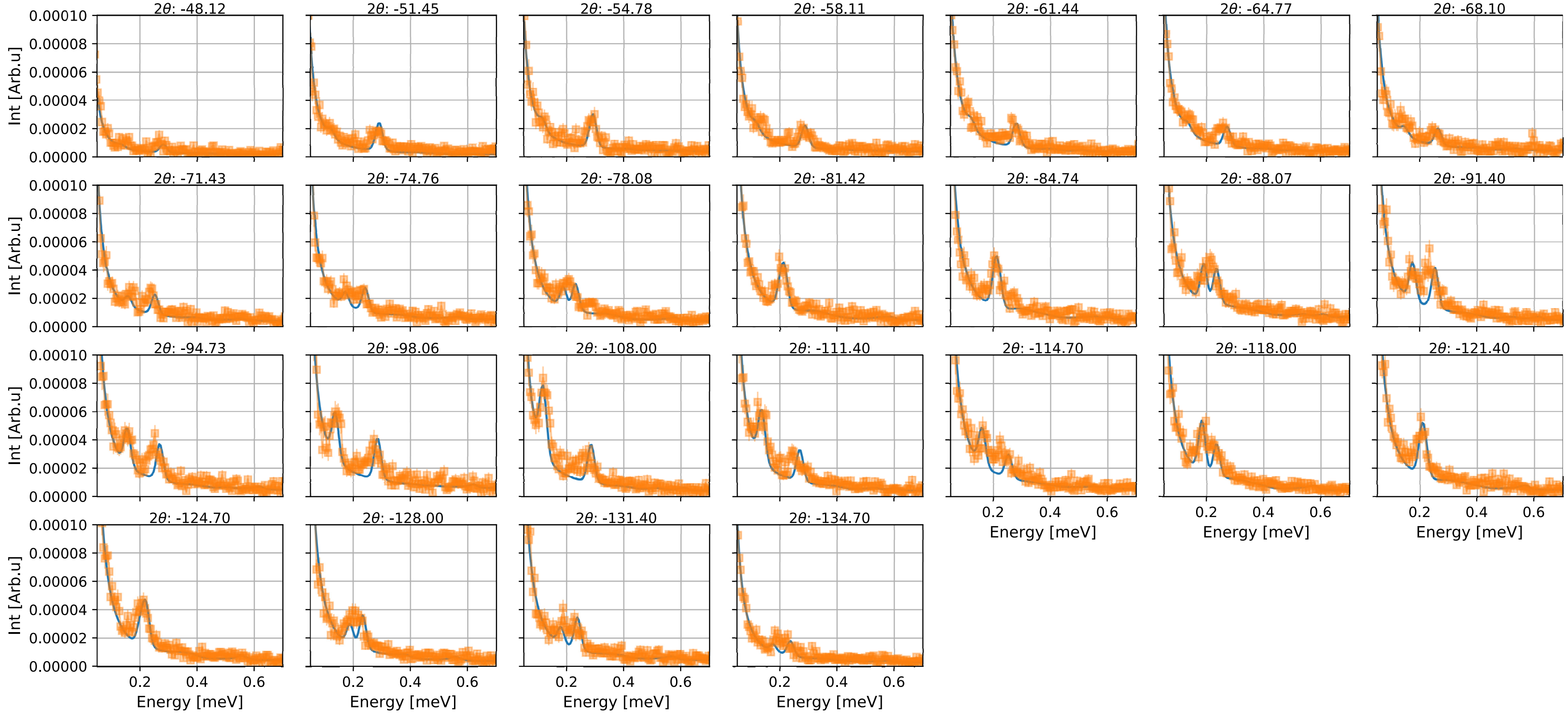

Figure 4.39: Lineshape comparison between the theory and the experiment at ($\Psi = -71.0°$, H=2.7 T) for different detectors labelled by the corresponding scattering angle 2θ.

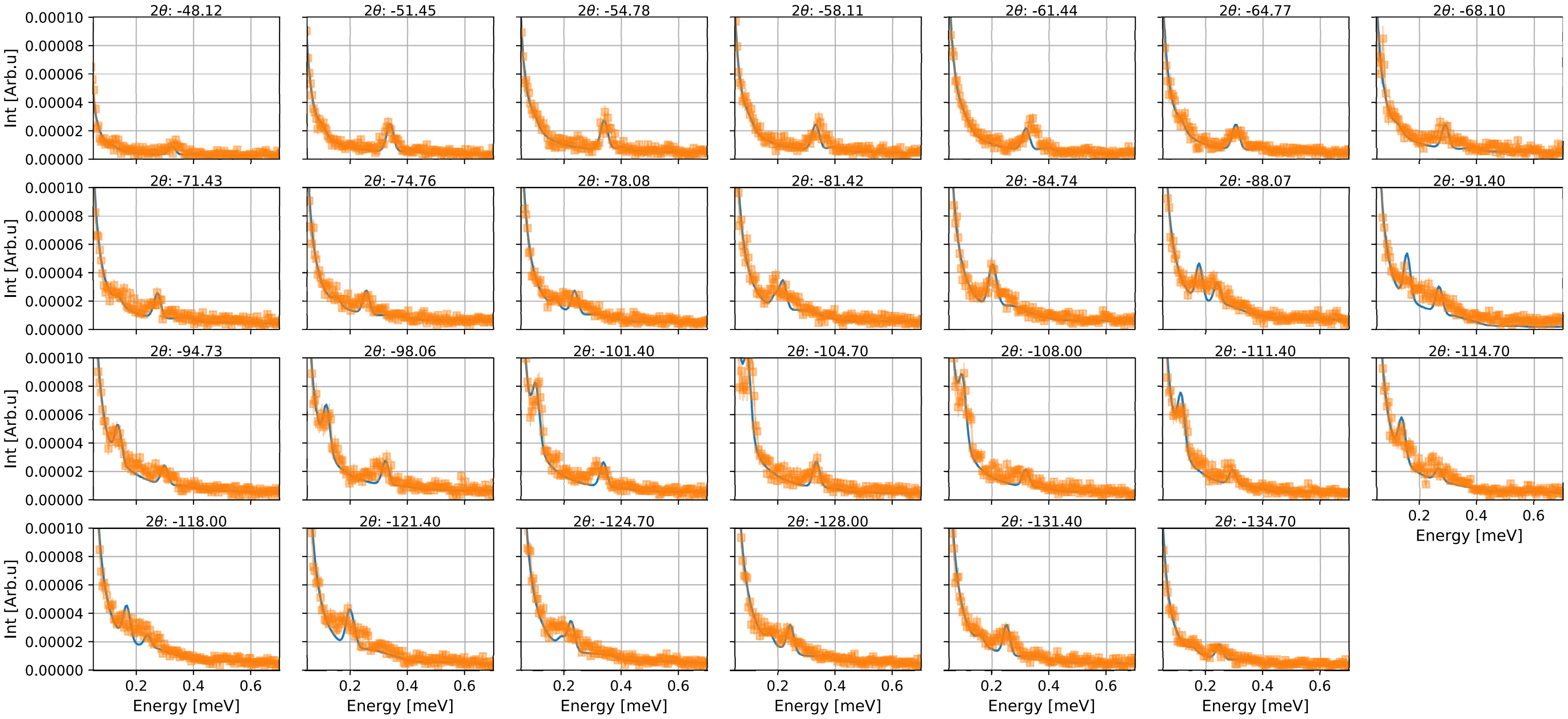

Figure 4.40: Lineshape comparison between the theory and the experiment at ($\Psi = -71.0^\circ$, H=3.2 T) for different detectors labelled by the corresponding scattering angle 2θ.

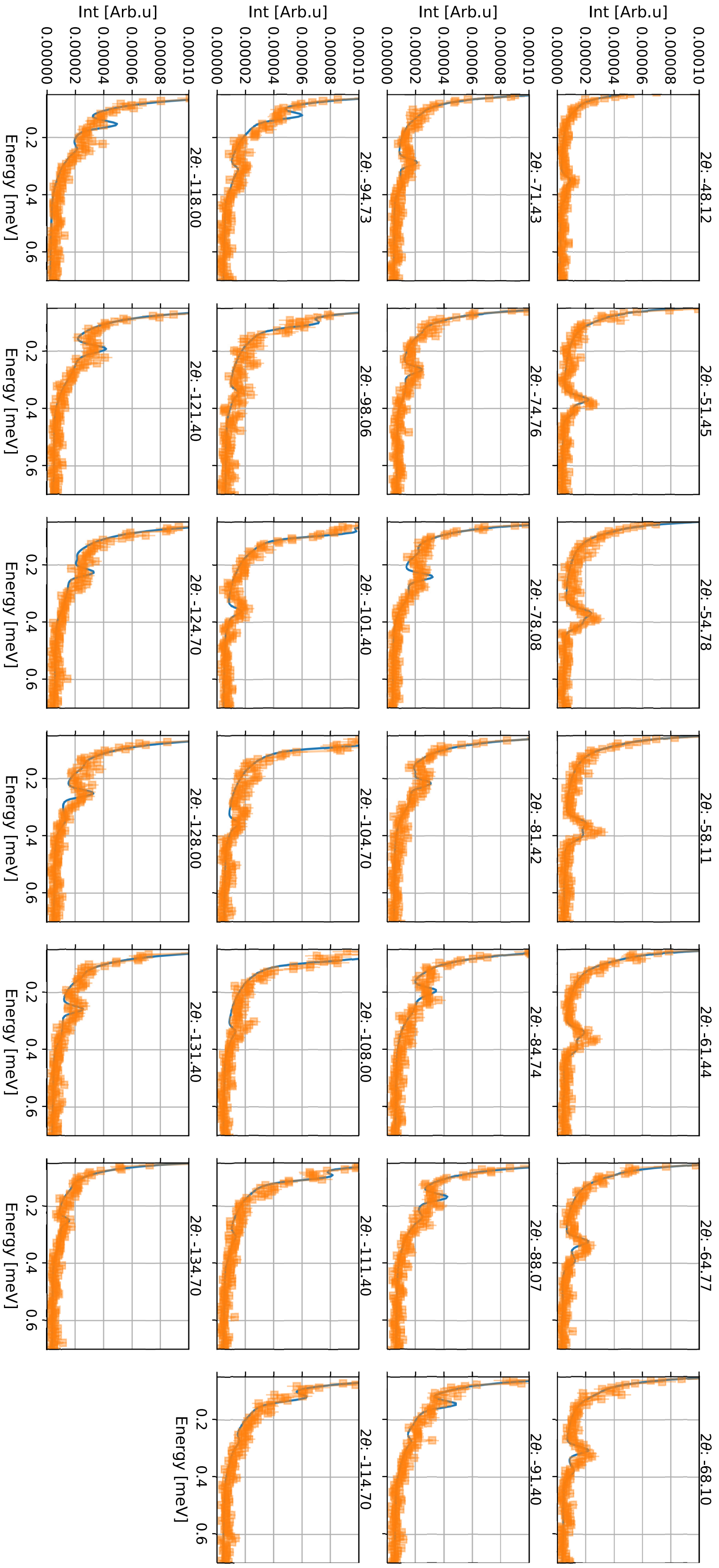

Figure 4.41: Lineshape comparison between the theory and the experiment at ($\Psi = -71.0^\circ$, H=3.5 T) for different detectors labelled by the corresponding scattering angle 2θ.

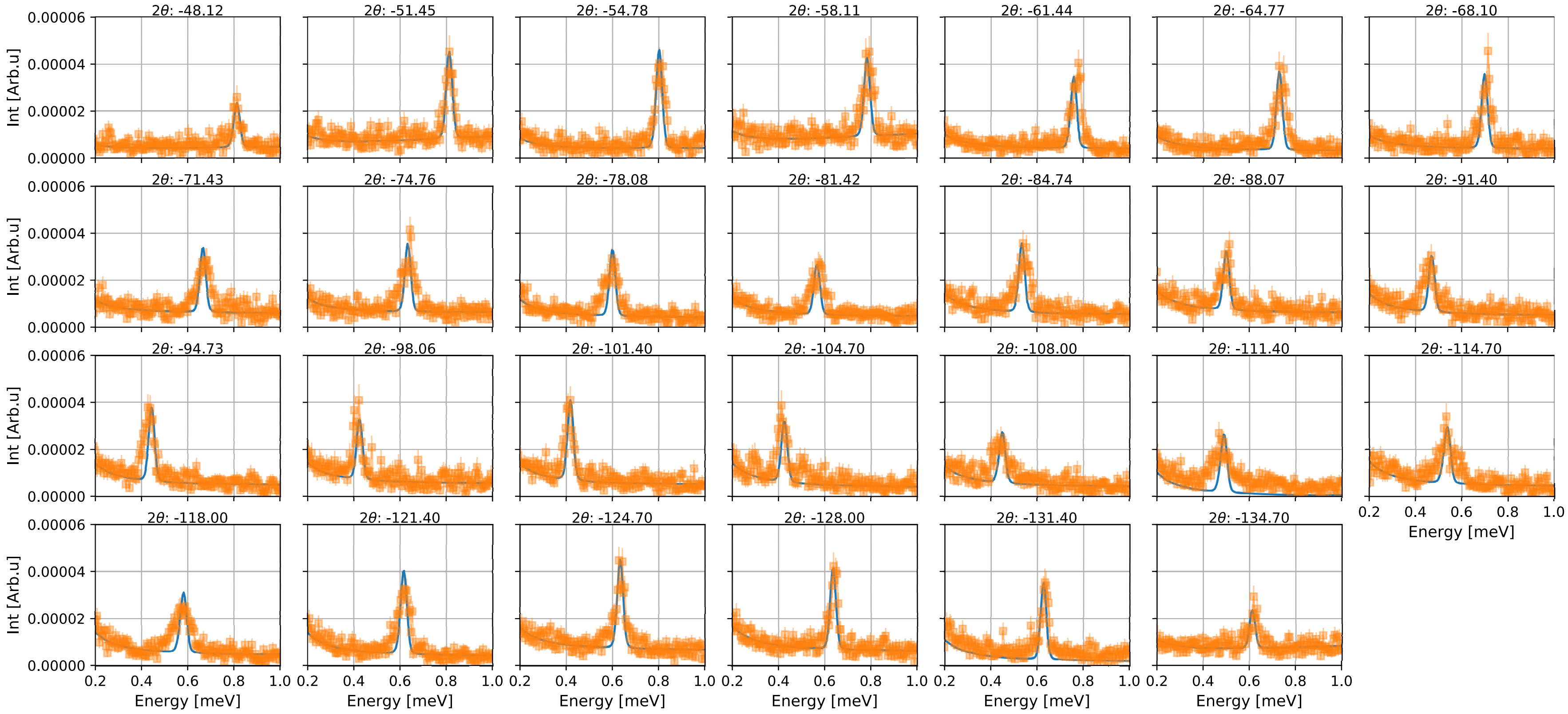

Figure 4.42: Lineshape comparison between the theory and the experiment at ($\Psi = -71.0^\circ$, H=7.0 T) for different detectors labelled by the corresponding scattering angle 2θ.

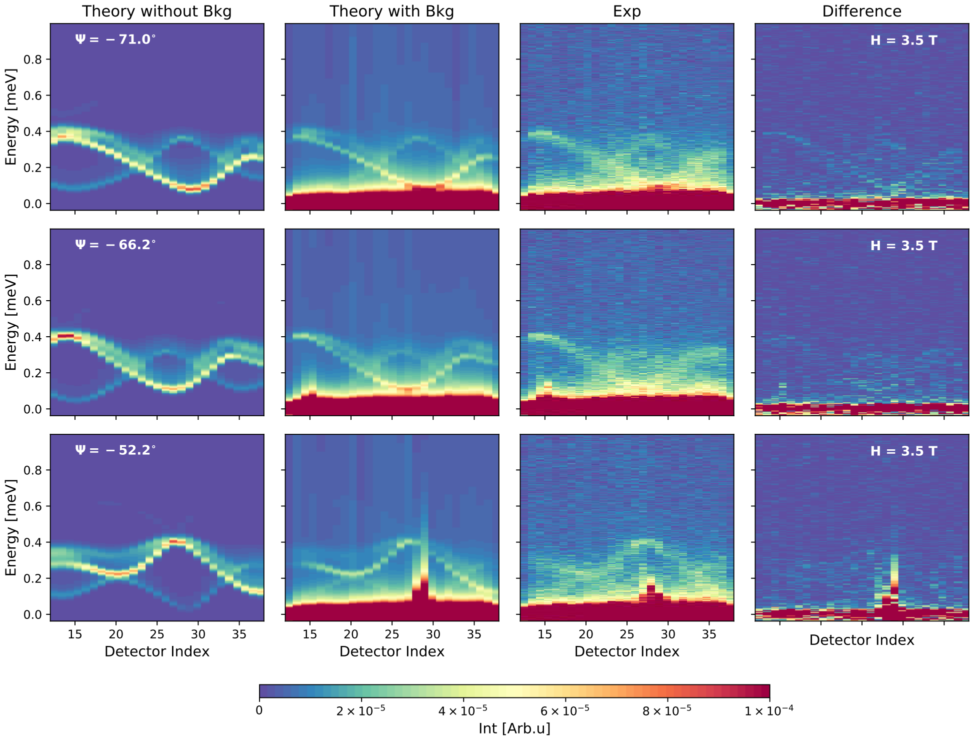

Figure 4.43: The simulated and the experimental spectra for three orientations $\Psi = -71.0°$, $-66.2°$ and $-52.2°$. All data were collected at 3.5 T. The first three columns are the pure theoretical results, the theoretical spectra together with the background contributions and the experimental spectra, respectively. The right most column is the absolute difference between the experimental spectra and the theoretical spectra with the background contributions. The intense blob feature below 0.2 meV located between detector 25 and 30 in the $\Psi = -52.2°$ spectra is a spurion which cannot be captured by either the theoretical model or the background model. As the result, an intense feature shows up at the same region in the difference spectrum.

5 Possible Kitaev Physics in a d^7 Compound Na$_2$Co$_2$TeO$_6$

The honeycomb lattice antiferromagnet Na$_2$Co$_2$TeO$_6$ has been proposed as a possible realization of the Heisenberg-Kitaev model [80, 81] given the high-spin d^7 configuration of Co (II). In this chapter, we present an inelastic neutron scattering study on its crystal field and spin wave excitations. The sections are organized as follow. We start by reviewing the theoretical work on d^7 compounds being possible Kitaev candidates. Next, we discuss the crystal structure and bulk magnetic properties of Na$_2$Co$_2$TeO$_6$. We then present the inelastic neutron scattering spectra and discuss their implications for the ground state properties of Na$_2$Co$_2$TeO$_6$. Finally, we discuss which spin Hamiltonians can host the observed spin excitations.

5.1 Realization of the Kitaev model in d^7 cobalt compounds

The realization of the Kitaev model in d^7 cobalt compounds was first proposed in Refs [80, 81]. In the following we will closely follow Liu and Khaliullin's arguments and summarise their key findings.

Assume that Co (II) ($3d^7$) ions situate in ideal octahedra surrounded by six O^{2-}. To form a honeycomb lattice plane of Co (II), the CoO$_6$ octahedra are arranged in an edge-sharing fashion. Due to the cubic symmetry of the CoO$_6$ octahedron, the energy difference between the split t_{2g} and e_g levels is smaller than the Coulomb interaction strength. The resultant Co (II) is in a high-spin state, i.e. $t_{2g}^5 e_g^2$, characterized by an effective orbital angular momentum $l_{\text{eff}} = 1$ and a spin angular momentum $S = 3/2$. The sizable spin-orbit coupling of $3d$ electrons in Co (II) further splits the high-spin ground state into three manifolds, characterized by effective total angular momenta $J_{\text{eff}} = 1/2$, $3/2$, and $5/2$, respectively, as explained in Chapter 1. The resultant lowest energy levels ($J_{\text{eff}} = 1/2$) are two-fold degenerate and comprise a Kramers doublet.

Unlike d^5 Kitaev materials [33, 82] where the e_g manifold is completely empty, such as α-RuCl$_3$ and Na$_2$IrO$_3$, for the high-spin state of d^7 it is partially filled with electrons. When evaluating the exchange interaction between neighboring Co (II) ions in the honeycomb lattice plane, apart from the commonly considered exchange between t_{2g} manifolds on neighboring ions, two additional exchange paths must be taken into account as well: the

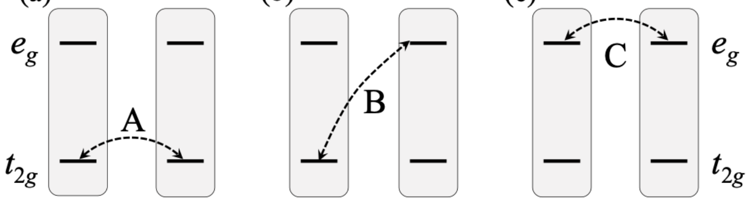

Figure 5.1: Three different categories of exchange processes A, B and C, derived from the interaction between (a) t_{2g} and t_{2g}, (b) t_{2g} and e_g and (c) e_g and e_g manifolds. The figure is taken from Ref [80]

.

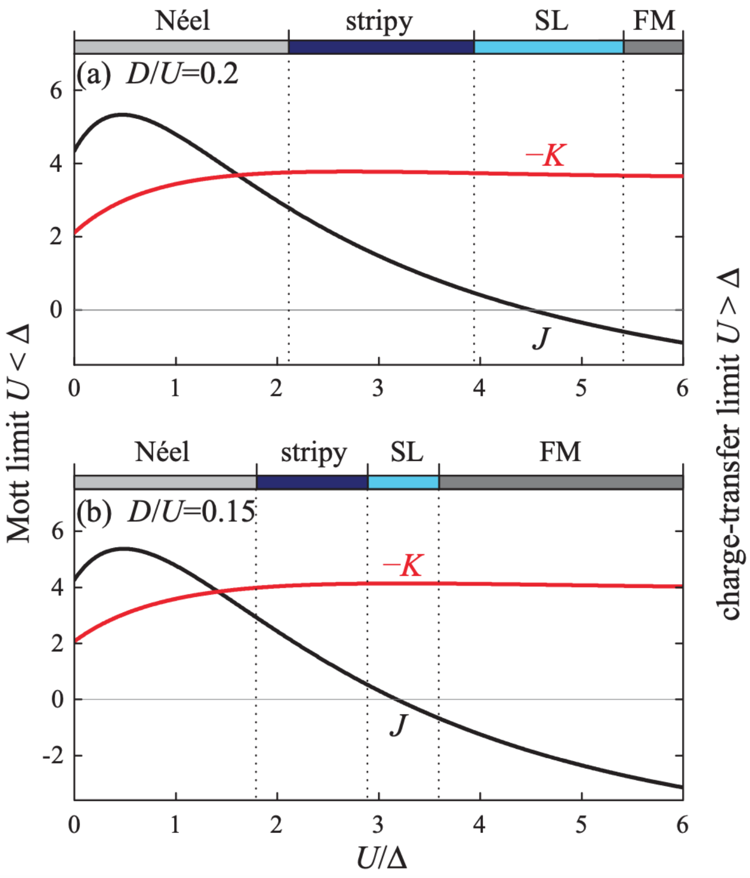

Figure 5.2: Total values of Heisenberg (J) and Kitaev ($-K$) interactions calculated in units of t^2/U as a function of U/Δ for (a) $D/U = 0.2$ and (b) 0.15, where t is the oxygen-mediated hopping amplitude between two adjacent Co (II) ions, U is the Coulomb interaction of Co (II), D is the crystal field splitting between t_{2g} and e_g and Δ is the $p-d$ charge transfer gap between Co and O. SL is the abbreviation for spin liquid state. The figure is taken from [80]

.

exchange between t_{2g} and e_g manifolds and the exchange within e_g manifolds only, see Fig.5.1. Together with the edge-sharing geometry of the neighboring CoO_6 octahedra, the $t_{2g} - e_g$ exchange process dominate over the others. As the result, the nearest neighbor Kitaev interaction K is always ferromagnetic and off-diagonal exchange interactions [83] are negligible. The nearest neighbor Heisenberg interaction J is sensitive to the system being in the Mott or a charge-transfer insulator limit, whose strength might be strongly suppressed, see Fig.5.2. In such a situation, the ratio K/J may become significant enough to stabilize the system in the desired Kitaev quantum spin liquid (SL) phase [19].

5.2 Crystal and magnetic structures of $Na_2Co_2TeO_6$

$Na_2Co_2TeO_6$ crystallizes in hexagonal symmetry with space group P$6_3$22 (No. 182) [84]. At room temperature the lattice constants are $a = 5.2770(2)$ Å and $c = 11.2231(1)$ Å [85]. The crystal structure of $Na_2Co_2TeO_6$ is shown in Fig.5.3(b) which displays a two-layer hexagonal crystal structure. The layers consist of edge-sharing CoO_6 octahedra forming a honeycomb lattice of Co (II) ions, with TeO_6 octahedron sitting at the center of each honeycomb unit. There are two inequivalent Co (II) sites in one unit cell. For both of

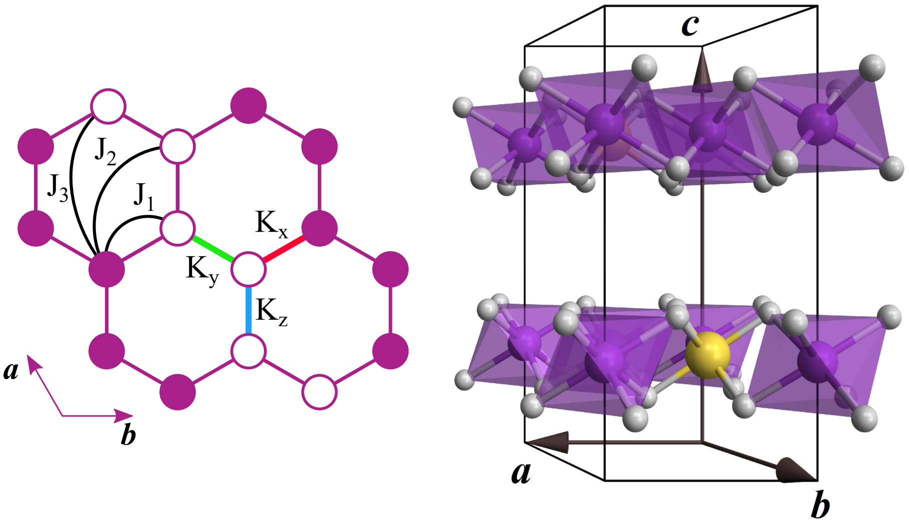

Figure 5.3: (a) Honeycomb layer with the nearest, next-nearest and third-nearest neighbor interactions J_1, J_2, and J_3 indicated. Also shown are the bond-dependent Kitaev interactions K_x, K_y and K_z. (b) Crystal structure of $Na_2Co_2TeO_6$ with sodium ions omitted for clarity. The Co (II) ions (purple sphere) reside inside edgesharing CoO_6 octahedra forming a nearly perfect honeycomb arrangement perpendicular to the crystallographic c-axis. At the center of a honeycomb planquette situated an TeO_6 octahedron where Te ion is represented by an yellow sphere.

them, the CoO_6 octahedra are found to be flattened along the crystallographic **c** axis. This indicates the presence of a trigonal distorted crystal field at the Co (II) sites [85]. Possible exchange paths for the Heisenberg interactions beyond the nearest neighbor type J_1, i.e. the second nearest neighbor J_2 and the third nearest neighbor J_3 are depicted in Fig.5.3(b) as well. Along the **c** axis, the adjacent honeycomb lattice layers are separated by an intermediate layer of Na ions, whose distribution is highly disordered over three triangular prismatic sites connecting the honeycomb layers [85].

Upon cooling, $Na_2Co_2TeO_6$ undergoes an antiferromagnetic phase transition at $T_N \sim 24.8$ K, below which a zigzag ordering, characterized by a propagation vector **k** $= (1/2, 0, 0)$ [85], is developed within the 2D honeycomb lattice plane. Here we stress that, due to a highly disordered distribution of Na, this might cause the variation of interlayer exchange couplings. As the result, the ordering temperature of $Na_2Co_2TeO_6$ could be sample dependent. The Curie-Weiss temperature of $Na_2Co_2TeO_6$ is $T_{CW} \sim 20.9$ K and the effective moment is $\mu_{\text{eff}} = 5.55\ \mu_B$/Co (II) [85, 86], which is larger than the spin-only value (3.87 μ_B) for $S = 3/2$ and more close to the expected moment with full orbital contribution (6.63 μ_B) [87]. The magnetic structure is illustrated in Fig.5.3(a) where the full and empty filled circles represent magnetic moments align along the crystallographic **b** axis [85], respectively. A neutron diffraction study [85, 86] revealed the magnetic moments on Co (II) ions in two sublattices are $M_{\text{Co}_1} = 2.77(3)\ \mu_B$/Co (II) and $M_{\text{Co}_2} = 2.45(2)\ \mu_B$/Co (II), respectively. The significant reduction of the moments from the classical expectation value 3 μ_B/Co (II) implies strong quantum fluctuation persists in the system despite of the occurrence of spontaneous symmetry breaking. Even above the Néel temperature, short range magnetic correlation within the honeycomb lattice plane persists and the correlation length is estimated to be 12 Å at 25 K [85].

5.3 Experimental details

The synthesis of polycrystalline $Na_2Co_2TeO_6$ was carried out by M. Retuerto from Instituto de Catálisis y Petroquímica. For the preparation, Na_2CO_3, $Co(NO_3)_2 \cdot 6H_2O$ and TeO_2 were used as starting materials (all from Alfa Aesar). The compounds were ground in stoichiometric ratio of the cations, but with a 20 % excess of Na_2CO_3 to compensate the partial volatilization of sodium. A first heat treatment in air was performed at 780 $^\circ$C for 12 hours. This was followed by an intermediate grinding phase before a second heat treatment in air at 800 $^\circ$C for 20 hours.

A laboratory powder X-ray diffractometer was used to confirm the structure and investigate the purity of the final product. The oxide obtained was pure but exhibited preferential orientation along the (001) direction, as expected from the symmetry of hexagonal honeycomb-based crystal structure. The refinement of the crystal structure yielded cell parameters $a = 5.278(6)$ Å and $c = 11.252(16)$ Å in good agreement with literature values [88, 86, 85]. The temperature and field-dependence of the magnetization for temperatures lower than 400 K and fields lower than 9 T were measured on a Physical Property Measurement System from Quantum Design, from which the Néel temperature of our sample was determined to be $T_N \sim 27$ K.

To study the magnetic excitations in $Na_2Co_2TeO_6$ below and above the Néel temperature T_N, a neutron scattering experiment was carried out using the direct geometry time-of-flight chopper spectrometer MARI at the ISIS Neutron and Muon Source. The spectrometer was operated using the repetition rate multiplication (RRM) technique [38] in which the choppers are configured to allow the passage of several monochromatic beams onto the sample. This allows simultaneous collection of spectra with different momentum and energy transfer ranges, Q and $\hbar\omega$. For the experiment, a polycrystalline sample of total mass 2.45 g was mounted in an annular geometry inside an Aluminium can, which was connected to the cold-finger of a continuous cycle refrigerator capable of cooling the sample to $T = 5$ K. For background subtraction purposes, the scattering from an empty can was recorded at 60 K. This turned out to be particularly important for distinguishing crystal field levels from phonon contributions in the full excitation spectrum. The MANTID software package was used to process the raw neutron data [89, 90] which were subsequently analyzed using the MATLAB package MSlice and SpinW [24].

5.4 Results and analysis

We start by giving an overview of the excitation spectrum of $Na_2Co_2TeO_6$. The data shown in Fig.5.4(a) were collected at $T = 5$ K using neutrons with $E_i = 70$ meV. Given the detector coverage of the MARI spectrometer, such a configuration allows access to momentum transfers $Q \leq 11$ Å^{-1}.

For energy transfers lower than 40 meV, the high Q part of the spectrum is dominated by scattering from lattice vibrations. This is readily seen from the scattering feature that grows in intensity with increasing Q, consistent with the expectation of scattering from phonons [25]. The phonon scattering contains contributions from both acoustic and optical modes. At momentum transfers close to 7 Å^{-1}, 9 Å^{-1}, and 10 Å^{-1}, the acoustic modes disperse linearly away from nuclear reciprocal lattice vectors. The optical branches are most prominent at energy transfers between 10 meV and 30 meV. Compared with the neutron scattering spectrum from a polycrystalline Al (Fig.2.1), the striking similarities between the two spectra suggest that the phonon excitations shown in Fig.5.4(a) might come from the Aluminium can.

The dominant feature in the raw data obtained with $E_i = 70$ meV neutrons (Fig.5.4(a))

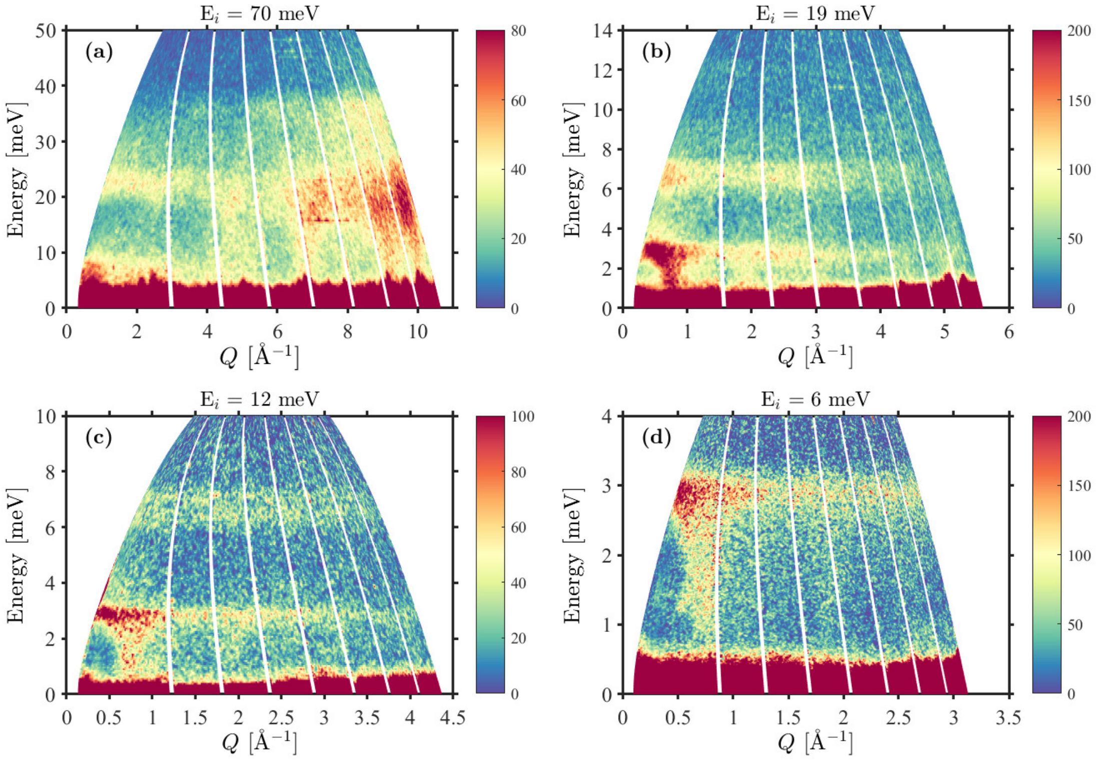

Figure 5.4: Overview of the excitation spectrum of a $\mathrm{Na_2Co_2TeO_6}$ powder sample. The incident energies, E_i, in panels (a)-(d) are 70, 19, 12 and 6 meV, respectively, and the corresponding energy resolutions (FWHM) at the elastic line are 4.66±1.84, 0.77(1), 0.31(2) and 0.30(5) meV. All data were obtained at $T = 5$ K. The white lines represent gaps between the detectors of the MARI spectrometer.

is the phonon scattering at high Q. Close to 20 meV energy transfer, the optical modes are very intense, which could potentially obscure magnetic excitations at the same energy range, but mostly intense at low Q. As mentioned earlier, the phonon scattering might come from the Aluminium can. Therefore, to separate the magnetic and optical phonon excitations, the collected empty Aluminium can data was subtracted from the raw $E_i = 70$ meV spectrum (Fig.2.1). It is important that before the subtraction, the temperature dependent Bose occupation factor of the empty can data must be corrected. Such a subtraction procedure helps us to easily identify the magnetic excitations. At base temperature, a 23 meV peak is clearly visible in the spectrum shown in Fig.5.6(i). The spectrum is a constant momentum cut with $\Delta Q = [1, 3]$ Å^{-1}. Apart from that, a shoulder at 28 meV is also present in the spectrum. The positions of these two peaks are indicated by open and full triangles.

To study the Q dependence of the intensity of the identified magnetic excitations centered at 23 meV and 28 meV, two constant energy cuts with $\Delta E = [21, 25]$ meV and $\Delta E = [28, 32]$ meV, respectively are shown in Figs.5.6(o) and (p). Compared with the Q dependent squared magnetic form factor for a free Co (II) ion, the agreement is excellent and strongly suggests these two excitations are of magnetic origin. Their temperature dependence is shown in Figs.5.6(i) - (n). By tracking the thermal evolution of their peak positions (23 meV: open triangle and 28 meV: full triangle), it is possible to discern that the magnetic excitation at 23 (28) meV slightly increases (decreases) in energy with increasing temperature. Besides that, thermal broadening of the magnetic excitations becomes more obvious at higher temperatures, especially at 60 K. In contrast to the low energy magnetic excitations (one locates at 3 meV and the other is around 7 meV) illustrated in Figs.5.6(i)-(n), whose intensities gradually diminish as the temperature approaches T_N and essentially become indistinguishable from the background at above T_N, the thermal robustness and the almost dispersionless of the magnetic excitations at 23 and 28 meV suggest they are crystal field excitations. The widths of these two modes are somewhat broader than the energy resolution of the MARI spectrometer [FWHM(23 meV) = 3.03 meV and FWHM(28 meV) = 2.77 meV]. This can be ascribed to the weakly coupling between the neighboring Co (II) ions and possibly the exchange-induced mixing of the ground state and the excited states [91, 87].

In Figs.5.4(b)-(d), with improved energy resolutions, low energy scattering below 10 meV is clearly visible at low Q. This is due to scattering from magnons. Fig.5.4(b) shows the data obtained using neutrons with $E_i = 19$ meV and illustrates that the magnon excitations in $\mathrm{Na_2Co_2TeO_6}$ consist of two parts: a dispersionless band close to 7 meV and a dispersive feature below 3 meV. The Q dependence of the intensities of both parts is shown in Fig.5.6(o) and (p), respectively. The observed gradual decrease in intensity with increasing Q is consistent with the expectation for magnetic scattering, which reflects the squared magnetic form factor in the double differential cross-section of neutron scattering (Section 2.3.2). From Fig.5.4(b) and (c), it is possible to discern that the dispersive excitation feature gradually approaches the momenta, where magnetic Bragg peaks occur in neutron powder diffraction experiments [85, 86], as energy transfer approaches zero. Such minimum is most prominent at $Q \simeq 0.7$ Å^{-1}, from which we can infer that low energy dispersive magnetic excitations are close to the magnetic Bragg peaks $\mathbf{Q} = (1/2, 0, 0)$ and $\mathbf{Q} = (1/2, 0, 1)$. A less obvious minimum is observed at Q just below 2 Å^{-1}. This corresponds to magnons close to $\mathbf{Q} = (1/2, 0, 3)$, $\mathbf{Q} = (3/2, -1, 0)$, and $\mathbf{Q} = (1/2, 1, 1)$.

As illustrated in Figs.5.4(b)-(d), the dispersive low energy magnetic excitations disperse away from the Q positions close to magnetic Bragg peaks and terminate at 3 meV energy transfer, at which a flat band is formed. The intensity of the 3 meV flat band decreases

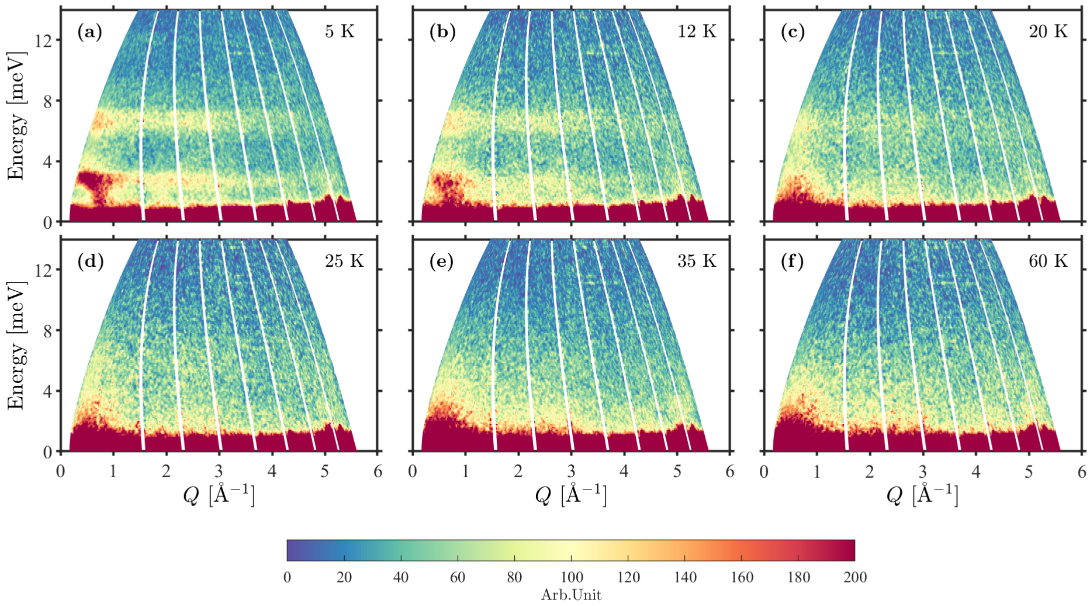

Figure 5.5: Temperature dependence of the spin wave excitation spectrum in $Na_2Co_2TeO_6$ collected at $E_i = 19$ meV for temperatures (a) 5 K, (b) 12 K, (c) 20 K, (d) 25 K, (e) 35 K and (e) 60 K.

gradually with Q increasing. This is illustrated in Fig.5.6(g), in which a constant energy cut with $\Delta E = [2.5, 3.2]$ meV is shown. At $Q = 4$ Å^{-1}, the intensity of the 3 meV flat band is so weak that it is essentially indistinguishable from the background. For the data shown in Fig.5.4(b), the energy resolution of the MARI spectrometer at 3 meV was 0.69 meV and was 0.57 meV at 7 meV energy transfer. It is immediately clear that the flat band at 7 meV is significantly broader than the energy resolution, implying that it contains more than one branch of the spin wave spectrum. In fact, the instrumental energy resolution at 7 meV for the data shown in Fig.5.4(c) was 0.22 meV. This further supports that, what appears to be a single flat band in Fig.5.4(b) has an internal structure and may contain contributions from two magnon branches. We shall return to this in the low energy spin wave part (Section 5.4.2).

Finally, the data shown in Fig.5.4(d) was collected using neutrons with $E_i = 6$ meV, which permits a closer look at the low energy dispersive spin wave excitations. Although the intense elastic scattering centered at $\hbar\omega = 0$ meV partially obscures the data, it is still feasible to infer that a spin wave gap exists at $Q \simeq 0.7$ Å^{-1}, which is close to the magnetic Bragg peak **Q** $= (1/2, 0, 0)$, and is of an order 1 meV. Notice that a spurion is present in the spectrum, locating at $Q \simeq 0.5$ Å^{-1} and $\hbar\omega \simeq 1.5$ meV [92]. Even though it directly lies on top of the dispersive low energy excitations at $Q \sim 0.7$ Å^{-1}, the overall spectrum quality is not severely affected due to the relatively small size of the spurion. Given the flux characteristics of the MARI spectrometer, it was not feasible to obtain data at an even higher resolution.

Having described the salient features of the excitation spectrum at 5 K, now we turn to the thermal evolution of the low energy magnetic excitations. Fig.5.5 and the right-hand panel ((a)-(f)) of Fig.5.6 illustrates how both the dispersive low energy mode and the flat

	Co$_1$	**Co$_2$**	**Co$_{avg}$**
B_2^0 [meV]	3.27	4.03	3.65
B_4^0 [meV]	0.35	0.31	0.33
B_4^3 [meV]	11.03	10.18	10.61

Table 5.1: The first two columns: results of point-charge calculations of Stevens parameters for Co$_1$ and Co$_2$. The last column summarizes the mean values of the Stevens parameters over Co$_1$ and Co$_2$.

band at 7 meV gradually lose definition as the temperature increases. As the temperature approaches the Néel temperature T_N, the 7 meV flat band is no longer discernible and the dispersive low energy mode gradually evolves into a broad intense diffuse scattering with a maximum at low Q, which extends from zero energy transfer to 6 meV. The spectra obtained at 35 and 60 K (Figs. 5.5(d)-(f)) are visually indistinguishable from each other, indicating the essential role of magnetic ordering in determining the magnetic dynamics in Na$_2$Co$_2$TeO$_6$.

5.4.1 Effective spin-1/2 ground state

In this section, we solve for the single-ion levels of Co (II) within an intermediate coupling scheme, as explained in Chapter 1, in a trigonally distorted octahedral crystal field. As the result, the INS spectrum, magnetization, and dc susceptibility can be computed as well. The results were fitted to the experimental data to determine the single-ion ground state of Co (II), which is found to be a Kramers doublet with in-plane anisotropy characterized by an anisotropic g tensor.

Noticed that there are two inequivalent Co (II) sites in the unit cell of Na$_2$Co$_2$TeO$_6$. Their single-ion levels are uniquely determined by the corresponding local coordination geometry. Such inequivalence implies any measured physical quantities contain contributions from both sites and thus it is important to have a qualitatively understanding of how these contributions differ from each other before diving into the experimental data fitting and analysis. For this purpose, we carried out the point-charge calculations as explained in Section 1.2.1 for both Co (II) sites. The Stevens parameters obtained are summarized in Table 5.1 where only the significant terms are listed.

Since the octahedra surrounding both Co ions are locally trigonally distorted, only B_2^0, B_4^0 and B_4^3 are non-vanishing from a group theory perspective. With further inclusion of the spin-orbit coupling for the two Co$_i$ (II) sites ($i = 1, 2$), the final single-ion Hamiltonian takes the form

$$\hat{H}_{\text{ion}}^{(i)} = B_2^{0(i)}\hat{O}_2^0 + B_4^{0(i)}\hat{O}_4^0 + B_4^{3(i)}\hat{O}_4^3 + \lambda^{(i)}\vec{L}\cdot\vec{S} \tag{5.1}$$

where $B_2^{0(i)}$, $B_4^{0(i)}$ and $B_4^{3(i)}$ are the calculated values for the given site i listed in Table 5.1, together with the Stevens operators $\hat{O}_2^0$, $\hat{O}_4^0$ and $\hat{O}_4^3$. The last term in the summation describes the spin-orbit coupling of $3d$ electrons in Co(II) with strength $\lambda^{(i)}$ at the site i.

According to Hunds' rules, the ground state (^4F see Chapter 1) of a free Co (II) ion ($3d^7$) is characterized by two quantum numbers: $(L = 3, S = 3/2)$, and the degeneracy is $(2L + 1)(2S + 1) = 28$. Projecting the Hamiltonian Eq.(5.1) onto the 28-fold ground state manifold ^4F and carrying out exact diagonalization for both sites, assuming that the spin-orbit coupling strength takes the free ion value $\lambda^{(1)} = \lambda^{(2)} = -22$ meV [8], the 28-fold ground state splits into 14 doublets. These are illustrated in Fig. 5.7(d) up to an energy transfer 120 meV for both Co (II) sites. The energy requires to transit from the ground state to the first excited state for both Co (II) sites are $\Delta\mathcal{E}_1 = 33.75$ meV and $\Delta\mathcal{E}_2 = 31.40$ meV,

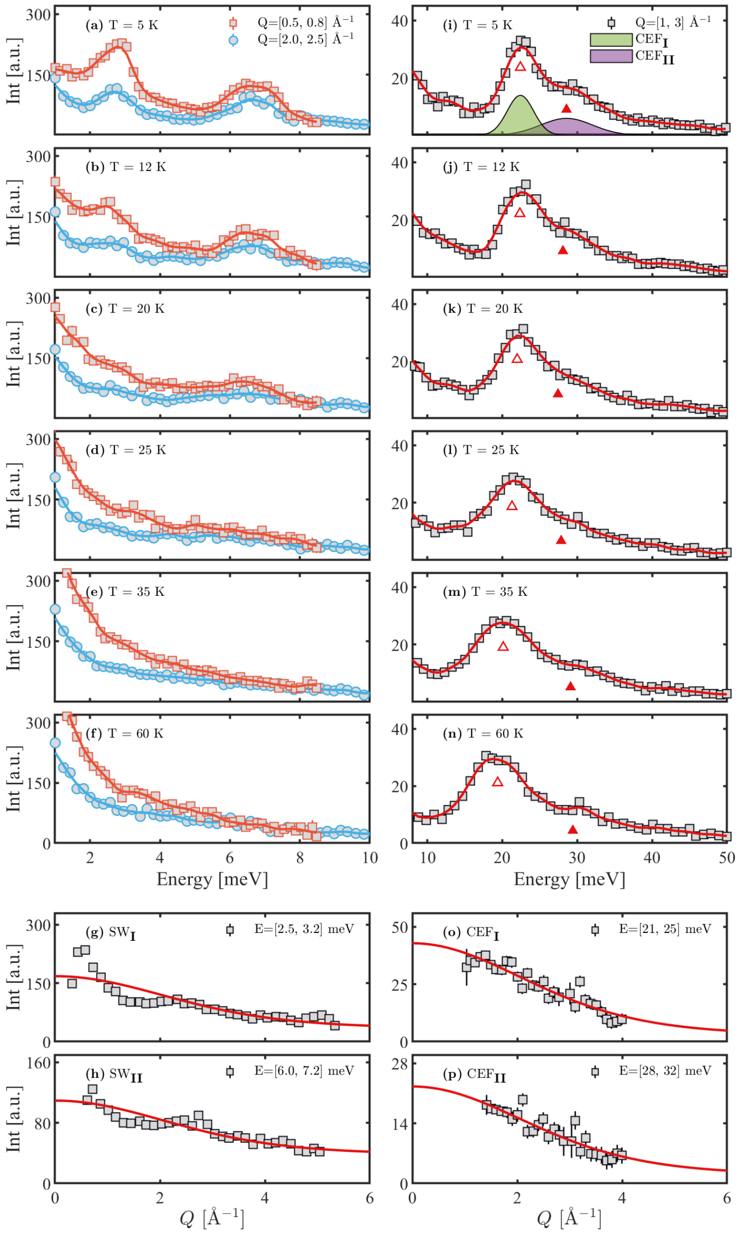

Figure 5.6: Temperature evolution of the magnetic excitations in Na$_2$Co$_2$TeO$_6$. (a)-(f) Constant momentum cuts focusing on the spin wave excitations. The data are taken at $E_i = 19$ meV and averaged over $\Delta Q = [0.5, 0.8]$ Å^{-1} (red squares) and $[2, 2.5]$ Å^{-1} (blue circles) at $T = 5$, 12, 20, 25, 35 and 60 K respectively. (i)-(n) Constant momentum cuts taken at $E_i = 70$ meV focusing on the crystal field excitations with $\Delta Q = [1, 3]$ Å^{-1} at $T = 5$, 12, 20, 25, 35 and 60 K respectively. The solid lines are guides to the eye and the triangles indicate the fitted peak positions as described in the text. (g) and (h) Constant energy cuts averaged over the energy transfer ranges $[2.5, 3.2]$ meV and $[6, 7.2]$ meV corresponding to the dispersive and dispersionless excitations in Fig. 5.4(b). (o) and (p) Constant energy cuts averaged over the energy ranges $[21, 25]$ meV and $[28, 32]$ meV where crystal field excitations are visible in Fig. 5.4(a). The red solid lines represent the squared magnetic form factor of Co (II) ion.

respectively. Both of the two transitions are higher in energy than the observed dispersionless excitations at 23 meV and 28 meV (Fig.5.6(i)), and the energy difference between them is $\Delta\mathcal{E} = \Delta\mathcal{E}_1 - \Delta\mathcal{E}_2 = 2.35$ meV, which is slightly smaller than the MARI's energy resolution at 30 meV (FWHM~2.96 meV). We also tried to decrease λ while keeping the Stevens parameters fixed for both Co (II) sites to move the two transitions close to the observed experimental values. The obtained energy difference between them diminishes with decreasing λ. Considering the energy resolution function of the MARI spectrometer increases with decreasing energy transfer, the contributions from the individual Co (II) sites therefore might be indistinguishable in the current dataset. As mentioned earlier, the two transitions obtained from the point-charge Stevens parameters are higher in energy than the energy levels observed in the INS spectra. This implies both the Stevens parameters and the spin-orbit coupling strength might have to be reduced to match the experimental data. Nevertheless, the results deduced from the point-charge calculation serve as a good starting point for the fitting of the experimental data, as we shall discuss next.

As mentioned above, it is not possible to distinguish the crystal field contributions from the two Co (II) sites separately in our experimental spectra and essentially what we measured were the spectra averaged over the two sites. Moreover, as there are only two peaks observed in the INS spectra, fitting them to a four-parameter (B_2^0, B_4^0, B_4^3 and λ) Hamiltonian is impractical. The fitted values would be strongly influenced by the given initial values, so it is impossible to obtain a unique definite solution. To overcome such a technical difficulty, we used the point-charge model prediction as a starting point by first finding the averaged Stevens parameters of the two sites: $\langle B_2^0\rangle = 3.65$ meV, $\langle B_4^0\rangle = 0.33$ meV and $\langle B_4^3\rangle = 10.61$ meV. Then we fixed their relative ratios and further introduced a global scaling factor p. The averaged single-ion Hamiltonian now reads,

$$\langle\hat{H}_{\text{ion}}\rangle = p \times (3.65\langle\hat{O}_2^0\rangle + 0.33\langle\hat{O}_4^0\rangle + 10.61\langle\hat{O}_4^3\rangle) + \lambda\vec{L}\cdot\vec{S} \tag{5.2}$$

The number of required fitted values is reduced from 4 to 2 with only p and λ left.

To account for the covalency effect between Co (II) and the neighbouring O, an angular momentum reduction factor κ is introduced which modifies the total magnetization from $\mathbf{M} = \mathbf{L} + 2\mathbf{S}$ to $\mathbf{M} = \kappa\mathbf{L} + 2\mathbf{S}$. Normally for Co (II), κ is around 0.8 [8].

For the fitting, we adopted the standard least χ^2 fitting routine. The fitted experimental data not only include the constant Q cut between 1 Å^{-1} and 3 Å^{-1} (Fig.5.6(i)) from the INS spectrum collected at E_i = 70 meV and 5 K, but also contain the dc susceptibility (from 200 K to 400 K) and the magnetization data in the paramagnetic state (measured at 57 K). The calculations of these quantities have already been explained in Chapter 1. The background model for the INS spectrum is a second order polynomial. To remind the reader, the magnetic susceptibility is calculated within a mean-field approximation (Section 1.2.2)

$$\chi_{MF} = \chi_0 + \frac{\chi_{\text{ion}}}{1 + \lambda_W\chi_{\text{ion}}}. \tag{5.3}$$

Here, χ_0 is a diamagentic susceptibility and λ is the Weiss molecular field constant [93]. A positive λ_W indicates antiferromagnetic interactions. The fitted results are shown in Fig. 5.7 and Table 5.2.

As expected, both the Stevens parameters and the spin-orbit coupling strength have to be reduced (the Stevens parameters: $\sim 50\%$ and the spin-orbit coupling: $\sim 10\%$) in order to provide a satisfactory description of the experimental data. The calculation shows the 28-fold ground state (^4F) splits into 14 doublets and the ground state is a Kramers doublet.

	Fitted value
B_2^0 [meV]	1.72 ± 0.034
B_4^0 [meV]	0.16 ± 0.0031
B_4^3 [meV]	4.99 ± 0.10
λ [meV]	-18.45 ± 0.35
κ	0.78 ± 0.0022
χ_0 [emu·Oe^{-1}·mol^{-1}]	$-0.0011 \pm 5.32 \times 10^{-8}$
λ_W	$4.23 \pm 2.99 \times 10^{-4}$

Table 5.2: Best fitted results of the Stevens parameters, the spin orbit coupling λ, the reduction factor κ for orbital angular momentum, the diamagnetic contribution χ_0 and the Weiss molecular field constant λ_W.

The doublet ground state can be described by an effective anisotropic magnetic moment with strength given by the g tensor. Assume the doublet ground state contains the states $|v_1\rangle$ and $|v_2\rangle$. The components of the g tensor can be obtained by projecting the total magnetization operator **M** onto the subspace spanned by the two ground state vectors $|v_1\rangle$ and $|v_2\rangle$ [8],

$$\begin{aligned} g_{xy} &= -2 \langle v_1| M_x |v_2\rangle \\ g_z &= 2 \langle v_2| M_z |v_2\rangle \end{aligned} \tag{5.4}$$

where xy and z represent components parallel and perpendicular to the **a** $-$ **b** plane, respectively. For Na$_2$Co$_2$TeO$_6$ we found $g_{xy} = 5.03$ and $g_z = 3.33$ indicating a strong in-plane anisotropy, which is in good accord with recent single crystal studies [94, 95].

5.4.2 Low energy spin wave excitations

In this section, we will discuss the the spin wave spectrum in Na$_2$Co$_2$TeO$_6$ in relation to three different Hamiltonians: a J_1-J_2-J_3 Heisenberg model, a generalized XXZ model and a Heisenberg-Kitaev Hamiltonian. For a quantitative comparison, we took advantage of having repetition rate multiplication for offering views at different E_i's and extracted six different cuts from the experimental data:

- Two constant energy cuts with $\Delta E = [1.0, 1.4]$ meV and $[1.7, 2.0]$ meV, respectively, from the spectrum collected at $E_i = 6$ meV and $T = 5$ K (Fig.5.4(d)). They are included to select the right model(s) hosting a similar dispersive low energy magnetic excitations.
- A constant momentum cut with $\Delta Q = [0.7, 0.8]$ Å^{-1} from the spectrum collected at $E_i = 6$ meV and $T = 5$ K (Fig.5.4(d)). This is selected due to the ~ 1 meV spin wave gap.
- Two constant momentum cuts with $\Delta Q = [1.0, 1.5]$ Å^{-1} and $[2.0, 2.5]$ Å^{-1}, respectively, from the spectrum collected at $E_i = 12$ meV and $T = 5$ K (Fig.5.4(c)). They are selected because of the 7 meV flat band and the 3 meV dispersionless excitation.
- A constant momentum cut with $\Delta Q = [0.5, 0.8]$ Å^{-1} from the spectrum collected at $E_i = 19$ meV and $T = 5$ K (Fig.5.4(b)). This is selected because of the low Q (< 1 Å^{-1}) intense broad scattering feature at 7 meV.

To further separate the spin wave contribution and the background scattering (including the elastic line at $\hbar\omega = 0$ meV), we carried out a background estimation for the extracted

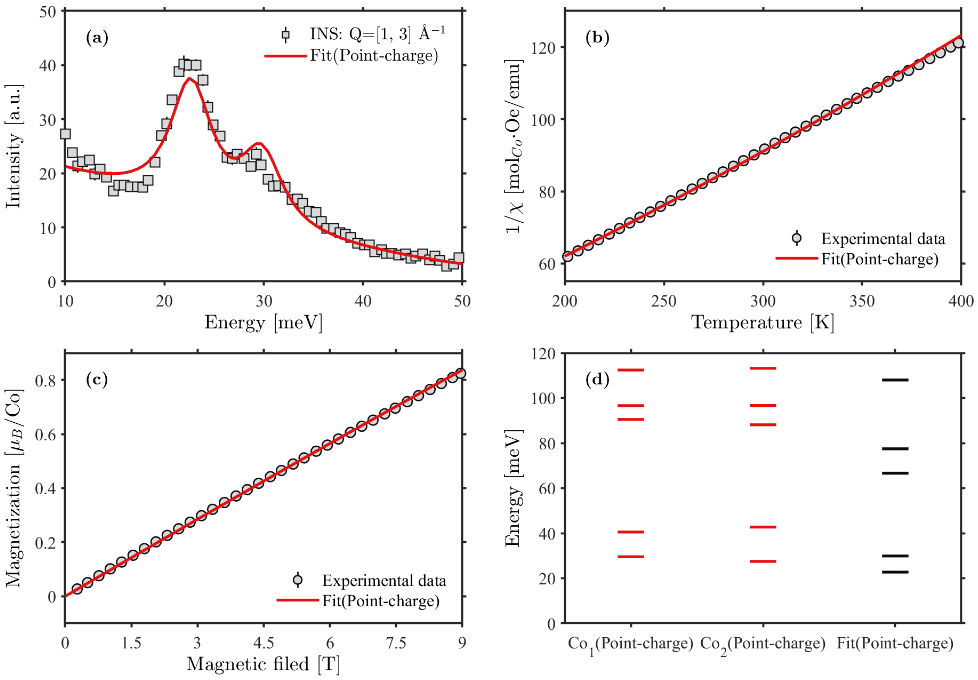

Figure 5.7: Fitted results obtained from the averaged single-ion Hamiltonian Eq.5.2. (a) A constant momentum cut with $\Delta Q = [1, 3]$ Å^{-1} taken from the spectrum measured at 5 K, $E_i = 70$ meV. (b) Inverse dc susceptibility (0.1 T) of $Na_2Co_2TeO_6$, $1/\chi$, collected between 200 K to 400 K. (c) Magnetization of $Na_2Co_2TeO_6$ measured at $T = 57$ K. (d) Energy levels obtained from the point-charge calculations on the two Co (II) sublattices and the best-fitted parameters in Table 5.2. The red solid lines represent the fitted results obtained from the model and parameters described in section 5.4.1

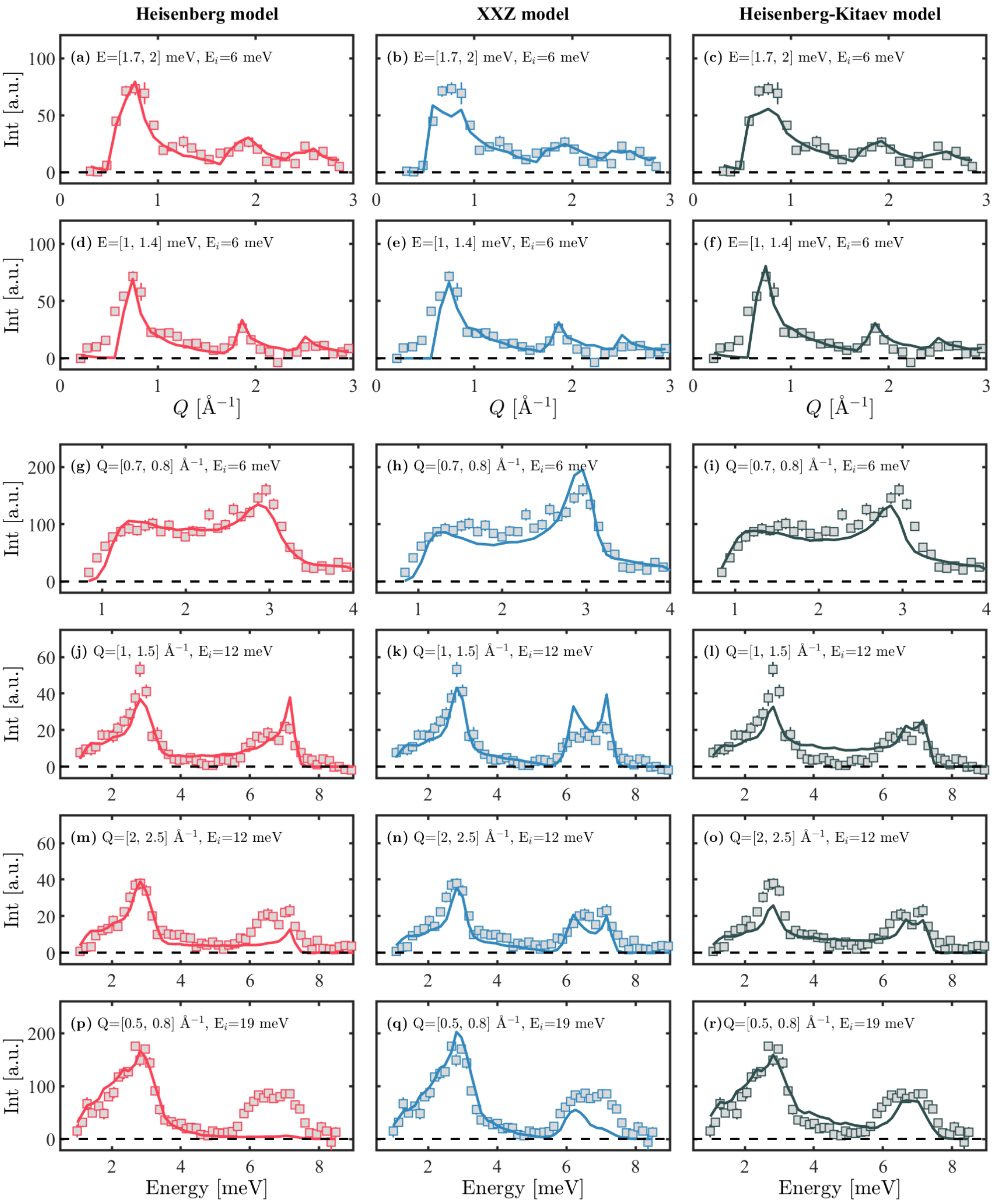

Figure 5.8: Fitted results obtained from the Heisenberg, generalized XXZ, and Heisenberg-Kitaev models. (a)-(f) Constant energy cuts averaged over $[1.7, 2]$ meV (panels (a)-(c)), and $[1, 1.4]$ meV (panels (d)-(f)), which are obtained from the $E_i = 6$ meV spectrum (Fig.5.4(d)). (g)-(r) Constant momentum cuts averaged over $[0.7, 0.8]$ Å^{-1} (panels (g)-(i)) from the $E_i = 6$ meV spectrum (Fig.5.4(d)), $[1, 1.5]$ Å^{-1} (panels (j)-(l)) from the $E_i = 12$ meV spectrum (Fig.5.4(c)), $[2.0, 2.5]$ Å^{-1} (panels (m)-(o)) from the $E_i = 12$ meV spectrum (Fig.5.4(c)), and 0.5 to 0.8 Å^{-1} (panels (p)-(r)) from the $E_i = 19$ meV spectrum (Fig.5.4(b)). The solid lines represent resolution convoluted fits obtained from the Heisenberg (red), the generalized XXZ (blue) and the Heisenberg-Kitaev (black) models, as explained in the text. All the data are obtained at $T = 5$ K.

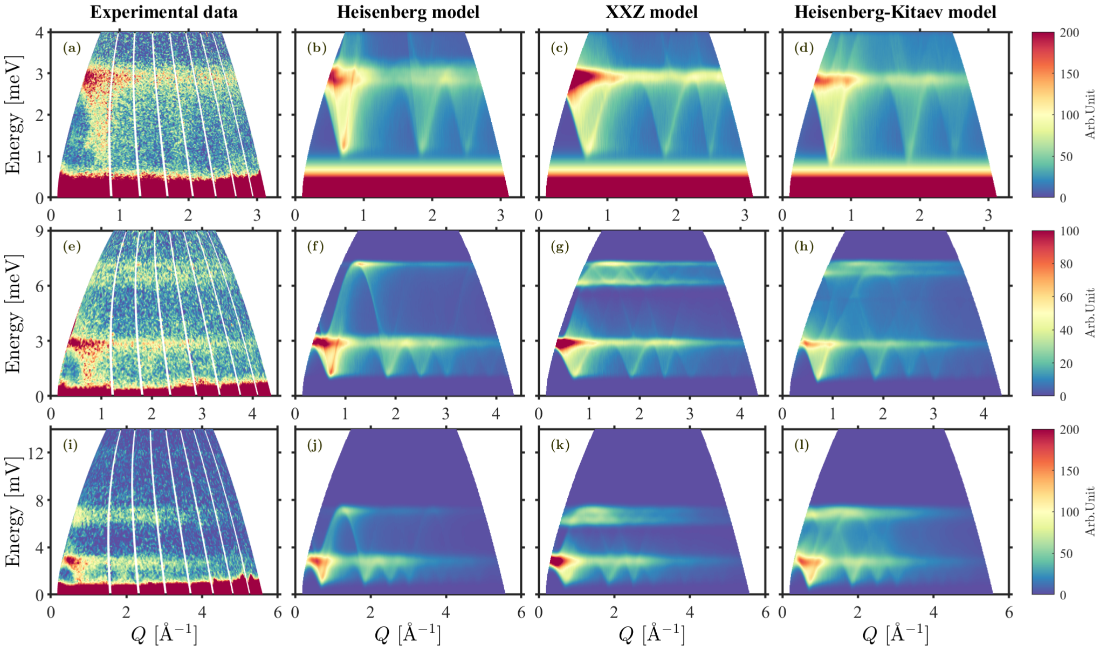

Figure 5.9: Color plots of INS spectra illustrating the agreement between the experimental data (panels (a), (e) and (i) for $E_i = 6$, 12 and 19 meV data, all obtained at $T = 5$ K) and the calculations with the best fitted parameters obtained from the Heisenberg (panels (b), (f) and (j)), the generalized XXZ (panels (c), (g) and (k)) and the Heisenberg-Kitaev (panels (d), (h) and (l)) models, as discussed in the text.

cuts and subsequently subtracted the estimated background lineshapes from the corresponding cuts. The result is six background-free spectra, ready for the next fitting process. For the fitting, the simulated spectra from SpinW [24] were convoluted with the energy resolution of the MARI spectrometer. To obtain the parameters giving the best description of the spectra, we introduced a cost function $J(\{p\})$ ($\{p\}$ representing the fitting parameters)

$$J(\{p\}) = \sum_i \left(\frac{y_i - y_i^{\text{conv}}(x_i; \{p\})}{e_i} \right)^2 \tag{5.5}$$

where $\{x_i\}$, $\{y_i\}$ are data points in the six background-free spectra and $\{e_i\}$ represent the corresponding error bars. $\{y_i^{\text{conv}}\}$ are the convoluted theoretical spectra and the summation is over all the data points in the six background-free spectra. For minimizing $J(\{p\})$, the particle-swarm optimization [76] was applied. The fitted results for three different models are shown in Fig.5.8. The best fitted parameters for the Heisenberg, the generalized XXZ and the Heisenberg-Kitaev models are listed in Table 5.3, 5.4, and 5.5, respectively. Fig.5.9 illustrates the spectra calculated with the best fitted parameters in Table 5.3, 5.4, and 5.5. The meaning of these obtained parameters will be explained in the following sections. Fig.5.10 illustrates the spin wave dispersions along high symmetry directions in the reciprocal space of a 2D honeycomb lattice for the Heisenberg, generalized XXZ, and Heisenberg-Kitaev models.

As a final remark, it is computationally expensive to calculate a powder spectrum. It is thus not feasible to include as many spectra as one wants in the fitting. The calculation of the powder spectra presented in this work was running on a cluster. For each $(\hbar\omega, Q)$ point, a Monte Carlo sampling was applied with 20000 random points. Fitting to one model normally takes a couple of days to finish.

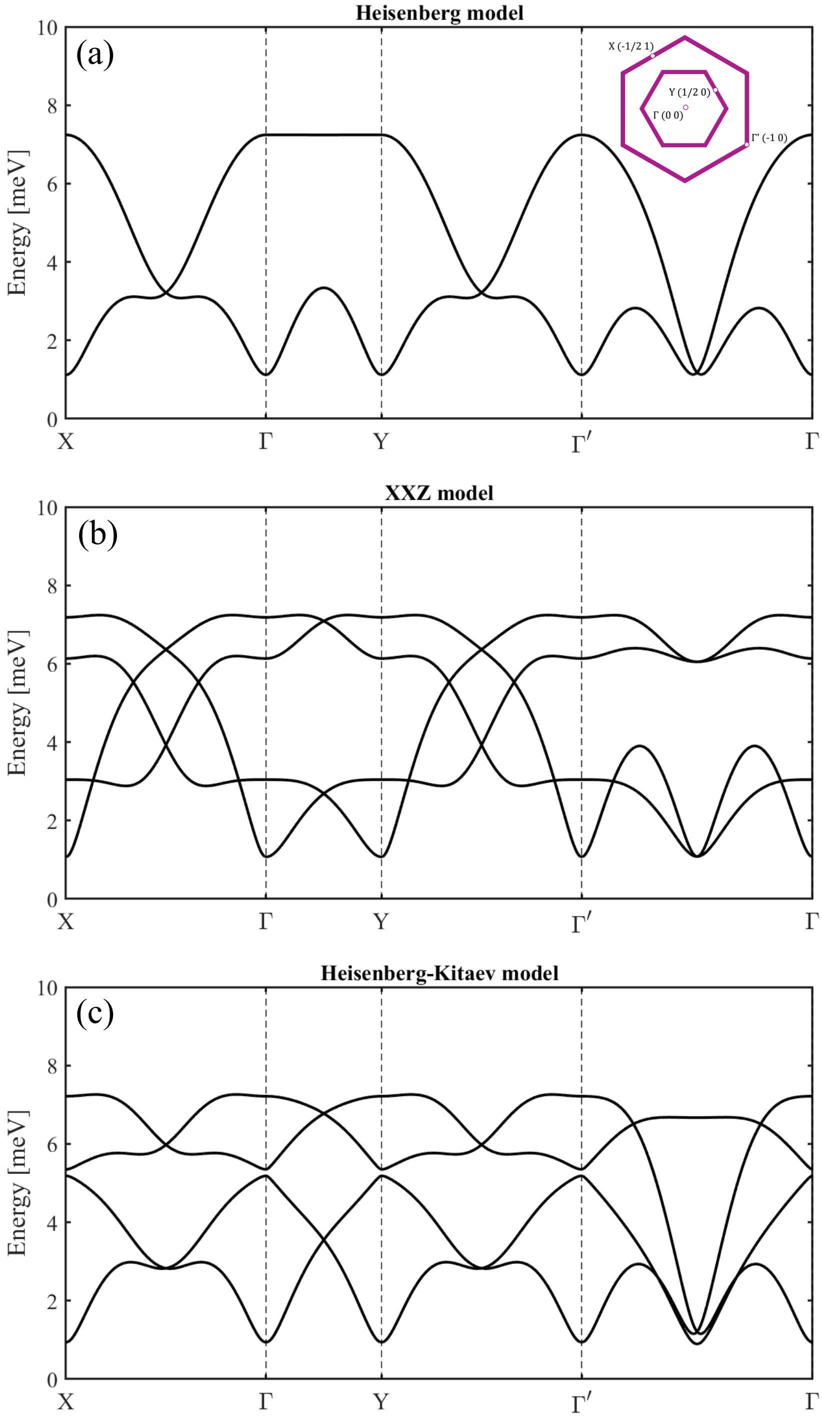

Figure 5.10: Simulated spin wave dispersion relations along high symmetry directions in the reciprocal space of a 2D honeycomb lattice for (a) the Heisenberg model, (b) the generalized XXZ model, and (c) the Heisenberg-Kitaev model as explained in Section 5.4.2. The parameters used for the calculations are listed in Table 5.3, 5.4 and 5.5.

	Best fitted	Standard deviation
J_1 [meV]	-1.95	0.0106
J_2 [meV]	0.799	0.021
J_3 [meV]	1.68	0.0204
D [meV]	0.0483	0.00135

Table 5.3: Parameters of the Heisenberg model used to describe the $Na_2Co_2TeO_6$ spin-wave spectrum.

	Best fitted	Standard deviation
J_1 [meV]	-3.74	0.0120
J_2 [meV]	-0.183	0.00228
J_3 [meV]	1.38	0.00740
D [meV]	0.0393	7.73×10^{-4}
Δ_1 [meV]	0.0156	2.98×10^{-4}
Δ_2 [meV]	0.0435	0.0193
Δ_3 [meV]	0.578	0.00553

Table 5.4: Parameters of the generalized XXZ model used to describe the $Na_2Co_2TeO_6$ spin-wave spectrum.

	Best fitted	Standard deviation
J_1 [meV]	-0.0596	0.0376
J_2 [meV]	0.164	0.0528
J_3 [meV]	1.72	0.0388
K [meV]	-4.40	0.125
D [meV]	-0.149	0.0262

Table 5.5: Parameters of the Heisenberg-Kitaev model used to describe the $Na_2Co_2TeO_6$ spin-wave spectrum.

Heisenberg Hamiltonian

For the Heisenberg model on honeycomb lattice to host a zigzag ordered ground state, the only possible scenario is when the Hamiltonian includes exchange interactions up to the third nearest neighbour [96], see Eq.(5.6).

$$H = J_1 \sum_{\langle i,j \rangle} \mathbf{S}_i \cdot \mathbf{S}_j + J_2 \sum_{\langle\langle i,j \rangle\rangle} \mathbf{S}_i \cdot \mathbf{S}_j + J_3 \sum_{\langle\langle\langle i,j \rangle\rangle\rangle} \mathbf{S}_i \cdot \mathbf{S}_j \tag{5.6}$$

where $\langle i,j \rangle$, $\langle\langle i,j \rangle\rangle$ and $\langle\langle\langle i,j \rangle\rangle\rangle$ represent the nearest neighbour, the second nearest neighbour and the third nearest neighbour illustrated in Fig.5.3, respectively, and J_1, J_2 and J_3 are the corresponding exchange coupling constants.

As stated by the Mermin-Wagner theorem, no long-range ordering occurs at finite temperature for a two-dimensional system with continuous symmetries. Even if Eq.(5.6) is a sufficient description of the Hamiltonian of Na$_2$Co$_2$TeO$_6$, to explain the observed non-zero Néel temperature $T_N \sim 27$ K, the interlayer exchange coupling must also be included in the Hamiltonian to extend the couplings to three-dimension. However due to the disordered distribution of Na ions in between layers [85], the interlayer exchange coupling strength J_{inter} is expected to be relatively small compared to the intralayer couplings. As the result, deducing the exact strength of the interlayer coupling from our measured INS powder spectra is impossible. This is because the existence of small interplane couplings would mostly be reflected from the magnetic excitations close to zero energy transfers. As the MARI spectrometer does not equip with a super high resolution in energy transfer, it is not feasible to extract the interlayer couplings in Na$_2$Co$_2$TeO$_6$ reliably based on the current datasets. For this reason, in the following discussion, the interlayer coupling is neglected and we only focus on the spin wave dynamics originating from the intralayer couplings within the 2D honeycomb lattice plane. In addition, to account for the observed gap (~ 0.1 meV) in the low energy spin wave spectrum, a phenomenological easy-axis single-ion ($D > 0$) anisotropy is added to the Hamiltonian, see Eq.(5.7), which forces spins to align along the crystallographic **b** axis as observed experimentally. In the dynamical structure factor calculation in SpinW [24], the previously obtained anisotropic g tensor from section 5.4.1 was also included.

$$H_{\text{Single-ion}} = \sum_i \begin{bmatrix} S_i^x & S_i^y & S_i^z \end{bmatrix} \begin{bmatrix} -D & \sqrt{3}D & 0 \\ \sqrt{3}D & -3D & 0 \\ 0 & 0 & 0 \end{bmatrix} \begin{bmatrix} S_i^x \\ S_i^y \\ S_i^z \end{bmatrix} \tag{5.7}$$

The best-fitted results of the six background-free spectra are illustrated in the left column of Fig.5.8. The simplest Heisenberg $J_1 - J_2 - J_3 - D$ model offers a satisfactory description of the dispersive low energy magnetic excitations below 3 meV which is evident from the fitted $E_i = 6$ meV spectra (Fig.5.8(a) and (d)). The extra intensity at $Q \simeq 0.5$ Å^{-1} in the data shown in Fig.5.8(b) is due to the spurion in the $E_i = 6$ meV spectrum (Fig.5.4(d)) as explained in Section 5.4. The high energy 7 meV flat band as shown in Fig.5.4(b) features a broader bandwidth compared to the 3 meV mode. The scattering intensity of the 7 meV flat band is most intense at the lowest Q (Fig.5.4(b)). As Q increases, it gradually diminishes in intensity and becomes indiscernible at $Q \simeq 5$ Å^{-1}. It is this 7 meV flat band that the pure Heisenberg model fails to reproduce, especially at low Q. The lineshapes of the high energy spin wave excitations obtained from the linear spin wave theory are much narrower than the experimental spectra and possess a single sharp peak feature at around 7 meV as opposed to the observed broad excitation feature. This is illustrated in the fitted constant energy cuts at $E_i = 12$ meV (Fig.5.8(g) and (j)). The most significant discrepancy between the theory and the experimental data is illustrated in the fitted constant energy cut at $E_i = 19$ meV (Fig.5.8), where the intense high energy excitation feature between 6 meV and 8 meV is completely absent in the theoretical calculation.

In Fig.5.9(b), (f) and (j) we show the simulated INS spectra for $E_i = 6$ meV, 12 meV, and 19 meV, which are calculated with the best fitted exchange parameters of the Heisenberg model (Table 5.3). Compared with the experimental spectra shown in the first column of Fig.5.9 (Fig.5.9(a), (e) and (i)), same as what we concluded from the fitting to the constant momentum and energy cuts at $E_i = 6$ meV, the dispersive low energy spin wave excitations below 3 meV can be well described by the $J_1 - J_2 - J_3 - D$ Heisenberg model. The differences between the theoretical and the experimental spectra become more obvious with increasing energy transfer. In the former at $E_i = 9$ meV and 19 meV (Fig.5.9(f) and (j)), the 3 meV and 7 meV flat bands are connected via an acoustic spin wave branch which disperses away from **Q** $\simeq 0.7$ Å^{-1} and 2 Å^{-1}, and has a finite scattering intensity in the region (3 meV to 7 meV) between the two modes. At $Q \simeq 1.2$ Å^{-1} and $\hbar\omega \simeq 7$ meV, the acoustic spin wave has a relatively intense curved scattering feature. This indicates that the acoustic spin wave terminates at the maximal excitation energy 7 meV, as illustrated in Fig.5.10(a). However such an acoustic spin wave branch is not observable in the experimental spectra. Moreover the theoretical 7 meV flat band has a much narrower width compared to the experimental observation. Most importantly, the theoretical spin wave excitations terminate at $Q \simeq 1.5$ Å^{-1}. This is in sharp contrast to the observed intense scattering feature at 7 meV even at the lowest possible momentum transfer, see Fig.5.9(i).

In Ref [97], M. Songvilay *et al.* reached a similar conclusion when trying to fit the experimental INS spectra of $\mathrm{Na_2Co_2TeO_6}$ to a XXZ Heisenberg model, see Eq.(5.8).

$$H = \sum_{n=1}^{3} J_n \sum_{i,j} \left(S_i^x S_j^x + S_i^z S_j^z + \Delta S_i^z S_j^z \right) \tag{5.8}$$

Here i and j run over the first, second and third nearest neighbor spin pairs, as illustrated in Fig.5.3(a). Δ takes a value between 0 (XY anisotropy) and 1 (Heisenberg). They found such a model fails to capture the observed 7 meV flat band as well with their best fitted exchange parameters: $J_1 = -2.1$ meV, $J_2/J_1 = -0.21$, $J_3/J_1 = 1$ and $\Delta = 0.95$. Notice that their values are comparable with our estimation from the Heisenberg model: $J_1 = -1.95$ meV, $J_2/J_1 = -0.41$, $J_3/J_1 = 0.86$ and $\Delta = 1$.

Generalized XXZ Hamiltonian

Even though the $J_1 - J_2 - J_3 - D$ Heisenberg model provides a satisfactory description of the spin wave excitations below 3 meV, the substantial mismatch between the theory and the experimental data at 7 meV forbids the Heisenberg model to be the rightful candidate for representing the Hamiltonian of $\mathrm{Na_2Co_2TeO_6}$. M. Songvilay *et al.* [97] also showed that even by adding an uniform XY anisotropy Δ in the Hamiltonian, see Eq.5.8, the model still fails to reproduce the experimental data. In this section, we consider a generalized XXZ model in which the XY anisotropies Δ of different neighbor spin pairs are allowed to vary. The generalized XXZ Hamiltonian reads

$$\begin{aligned} H =&J_1 \sum_{\langle i,j \rangle}(S_i^x S_j^x + S_i^y S_j^y + \Delta_1 S_i^z S_j^z) + J_2 \sum_{\langle\langle i,j \rangle\rangle}(S_i^x S_j^x + S_i^y S_j^y + \Delta_2 S_i^z S_j^z) \\ &+ J_3 \sum_{\langle\langle\langle i,j \rangle\rangle\rangle}(S_i^x S_j^x + S_i^y S_j^y + \Delta_3 S_i^z S_j^z) \\ &+ \sum_i \begin{bmatrix} S_i^x & S_i^y & S_i^z \end{bmatrix} \begin{bmatrix} -D & \sqrt{3}D & 0 \\ \sqrt{3}D & -3D & 0 \\ 0 & 0 & 0 \end{bmatrix} \begin{bmatrix} S_i^x \\ S_i^y \\ S_i^z \end{bmatrix} \end{aligned} \tag{5.9}$$

where Δ_1, Δ_2 and Δ_3 are fractions between 0 and 1 representing an in-plane anisotropy. Similar to the Heisenberg model, the nearest neighbor, the second nearest neighbor and the third nearest neighbor exchange constants are J_1, J_2 and J_3, respectively. The last term in the summation is an easy-axis single-ion anisotropy, which aligns the spins along the crystallographic **b** axis and thus opens a gap in the low energy spin wave spectrum. In the dynamical structure factor calculation in SpinW [24], the anisotropic g tensor was included as well. The fitted results of the six-background free spectra are shown in the middle column of Fig.5.8.

Comparing the fitted lineshapes to the constant energy and momentum cuts at $E_i = 6$ meV (Fig.5.8(b), (e) and (h)), similar to what was observed for the $J_1 - J_2 - J_3 - D$ Heisenberg model, the fitting quality provided by the generalized XXZ model is decent as well for the spin wave excitations below 3 meV. The most salient difference between the two models arises from the high energy spin wave excitations at 7 meV. For the generalized XXZ model, the bandwidth of the 7 meV flat band is much larger than that of the Heisenberg model. This is consistent with the experimental spectra shown in Fig.5.8(k) and (n).

Compared to the Heisenberg model, the generalized XXZ model appears to be a more promising candidate for describing the spin wave excitations in $Na_2Co_2TeO_6$. However, discrepancies between the theoretical spectra and the experimental data are still quite obvious. For the constant momentum cut shown in Fig.5.8(k), the calculated intensity for the spin wave excitations between 6 meV and 8 meV is more pronounced than the experimental observation. Moreover, a clear two-peak feature stands out in the theoretical spectrum whereas such a feature is less pronounced in the experimental data. For the constant momentum cut at $E_i = 19$ meV (Fig.5.8(q)), the generalized XXZ model predicts the intensity of the spin wave excitations between 6 meV and 8 meV gradually diminishes with increasing energy. As the result, the spectral lineshape within this energy range is strongly asymmetrical according to the model. This is in contrast to the experimental data where the observed lineshape between 6 meV and 8 meV is more symmetric.

In Fig.5.9(c), (g) and (k), we illustrate the simulated INS spectra calculated with the best fitted parameters listed in Table 5.4. As seen from Fig.5.9(c), the spin wave excitations below 3 meV can be well modeled by the generalized XXZ model judged by the overall spectral lineshape. For the high energy spin wave excitations at 7 meV, what appears to be a flat band at 7 meV as shown in Fig.5.4(b) and (c) actually contains contributions from two spin wave branches. This is more clearly illustrated in the spin wave dispersion of the generalized XXZ model (Fig.5.10(b)). Both of them disperse away from **Q** $= (0, 0)$ (Γ) but along different directions, From Γ to X (**Q** $= (-0.5, 1)$), one of the branch terminates at around 7.2 meV. From Γ to Γ' (**Q** $= (-1, 0)$), the other extends to around 6 meV. The notations used here are in the reciprocal space of a 2D honeycomb lattice. For the generalized XXZ model, the 7 meV flat band is most intense in the region $[1, 2]$ Å^{-1}, especially for the upper spin wave branch. This is likely a feature inherited from the Heisenberg model, in which an intense feature appears at a similar position. At low Q, as seen from Fig.5.9(g) and (k), the generalized XXZ model predicts the two previously identified spin wave branches merge at $Q \simeq 0.8$ Å^{-1} and $\hbar\omega \simeq 6$ meV. This is the consequence of two non-degenerate high energy spin wave modes become degenerate at $\mathbf{Q} = (-1/2, 0)$ (the middle point of Γ and Γ'), as shown in Fig.5.10(b). Such a merging of two spin waves manifests itself as the observed asymmetric lineshape between 6 meV and 8 meV in the theoretical spectrum shown in Fig.5.8(q). Nevertheless, compared with the Heisenberg model, the generalized XXZ model offers a better description of the experimental spectra. It captures nearly all the essential features apart from the intense 7 meV magnetic excitation at the lowest Q.

As a final remark, the idea behind the introduction of the generalized XXZ model is to have a better description of the experimental data. So we will not try to reconcile the best fitted parameters of the Heisenberg model and the generalized XXZ model. In fact, the best fitted values of Δ_1, Δ_2, and Δ_3 (see Table 5.4) indicate significant anisotropies need to be introduced to the system Hamiltonian to give a relatively satisfactory description of the experimental data.

Heisenberg-Kitaev Hamiltonian

At last, we will examine the possibility of the spin wave dynamics in Na$_2$Co$_2$TeO$_6$ is resembled by the Heisenberg-Kitaev Hamiltonian. Due to the previous success with the $J_1 - J_2 - J_3$ type Heisenberg model and its generalized XXZ extension on the low energy spin wave excitations in Na$_2$Co$_2$TeO$_6$, the Heisenberg-Kitaev model we will consider here include exchange couplings up to third nearest neighbors as well, see Eq.(5.10).

$$H = \sum_{\langle i,j\rangle,\gamma} (J_1 \mathbf{S}_i \cdot \mathbf{S}_j + K S_i^\gamma S_j^\gamma) + J_2 \sum_{\langle\langle i,j\rangle\rangle} \mathbf{S}_i \cdot \mathbf{S}_j + J_3 \sum_{\langle\langle\langle i,j\rangle\rangle\rangle} \mathbf{S}_i \cdot \mathbf{S}_j \tag{5.10}$$

Here J_1, J_2 and J_3 are the exchange coupling constants of the nearest neighbor, the second nearest neighbor, and the third nearest neighbor, respectively, as shown in Fig.5.3(a). K denotes the Kitaev interaction and γ represents three different bond directions, see Fig.5.3(a) where the red, green, and blues lines indicate the X, the Y, and the Z bonds, respectively. Notice that such a Hamiltonian is defined within the local cubic coordinate system of an octahedron. This is different from the Heisenberg model and the generalized XXZ model which are defined within a global reference frame. To open a gap in this model, a phenomenological single-ion anisotropy $H_{\text{single-ion}}$ along the cubic Z axis, see Eq.(5.11), is further included in the Hamiltonian. Here $D < 0$.

$$H_{\text{single-ion}} = D \sum_i S_i^{z2} \tag{5.11}$$

The best fitted parameters of the Heisenberg-Kitaev model are listed in Table 5.5. To reproduce most of the features in the experimental spectra, we find that J_1 has to be close to zero and a ferromagnetic K should be the dominant one among all the exchange interactions. The ratio of the best fitted K and J_1 is extremely large, i.e. $K/J_1 \sim 100$, such that, if ignoring J_2 and J_3, theoretically the system should be in a Kitaev quantum spin liquid state at base temperature [98]. However, experimentally the zigzag order [85] sets in at $T_N \sim 27$ K. Based on our best fitted parameters (Table 5.5), we suspect that the zigzag ordered ground state is stabilized due to the sizable long range exchange couplings J_2 and J_3. Our findings support the theoretical prediction made by Liu and Khaliulin [80]. They found that for a d^7 Kitaev material, due to the additional electron hopping processes originating from the e_g manifold, the Kitaev interaction K is always ferromagnetic and the nearest neighbor coupling J_1 might be significantly suppressed.

The six background-free fitted results are illustrated in the right column of Fig.5.8. The overall fitting quality of the Heisenberg-Kitaev model is comparable with the generalized XXZ model. The spin wave excitations below 3 meV are captured relatively well by the Heisenberg-Kitaev Hamiltonian (Fig.5.8(c) and (f)) regarding the peak positions and the overall spectral lineshapes. In 5.8 (l) and (o), we notice the intensity of the 3 meV flat band is significantly suppressed in the Heisenberg-Kitaev model compared to the experimental data. Such a mismatch is due to a spectral weight redistribution. The intensity of the 3 meV flat band partially redistributes over the energies between 4 meV and 6 meV. This is readily seen from the slightly higher intensities of the theoretical lineshapes between 4 meV and 6 meV when compared to the experimental spectra in the same range. For the spin wave excitations at 7 meV, even though the intensities obtained from the Heisenberg-Kitaev model are comparable with the experimental data, the theoretical lineshapes are slightly narrower than the collected spectra, as illustrated in Fig.5.8(l), (o), and (r). This is most obvious for the constant momentum cut at $E_i = 19$ meV (5.8(r)). In Fig.5.9(d), (h) and (l), we illustrate the simulated INS spectra calculated with the best fitted parameters in Table 5.5. Consistent with what we observed in Fig.5.8, the intensity of the 3 meV flat band is less pronounced compared to the experimental data. Even though, the overall lineshapes are well captured by the model. The flat band at 7 meV in the Heisenberg-Kitaev model is slightly narrower than the data. From Fig.5.10(c), it is possible to infer that the 7 meV flat band consists of two contributions: one is from the highest spin wave branch locating at ~ 7.2 meV and the other is the nearly dispersionless spin wave branch at ~ 6.4 meV from $\Gamma' \to \Gamma$. In between the 3 meV and 7 meV excitations, the Heisenberg-Kitaev model predicts a higher spectral weight compared to the Heisenberg and generalized XXZ models.

Apart from our work, several other groups [97, 99, 100] have tried to study the INS spectrum of $Na_2Co_2TeO_6$ in relation to the generalized Heisenberg-Kitaev model, see Eq.(5.12).

$$\begin{aligned} H = & \sum_{\langle i,j\rangle_{r=1,2,3,4}} J_r \mathbf{S}_i \cdot \mathbf{S}_j + \sum_{\langle i,j\rangle_1 \in \{\alpha,\beta,\gamma\}} K S_i^\gamma S_j^\gamma + \\ & \Gamma\left(S_i^\alpha S_j^\beta + S_i^\beta S_j^\alpha\right) + \Gamma'\left(S_i^\alpha S_j^\gamma + S_i^\gamma S_j^\alpha + S_i^\beta S_j^\gamma + S_i^\gamma S_j^\beta\right) \end{aligned} \tag{5.12}$$

As before J_1, J_2 and J_3 are the nearest, the second nearest, and the third nearest neighbor exchange constants, respectively. J_4 is an interlayer coupling, K is the Kitaev interaction, and Γ, Γ' are the two components of an nearest neighbour off-diagonal exchange interaction,

In Table 5.6 we summarize the best fitted parameters from Refs [97, 99, 100]. In our analysis, we didn't include the off-diagonal exchange interaction but our best fitted spectra still provide an overall good description of the experimental data. As pointed out by M. songvilay *et al.* [97], the off-diagonal term Γ is mainly responsible for opening a gap in the spin wave spectrum and has little effect on the spin wave dispersion. Our results tend to agree with their conclusion.

5.5 Discussion and Conclusions

Our results on the magnetic excitations in $Na_2Co_2TeO_6$ provides several key insights to the ground state properties of the system:

- The analysis on the crystal field excitations has established that the ground state of the Co (II) ion is a Kramers doublet with a strong in-plane anisotropy $g_{xy}/g_z \sim$

1.51. Compared with a recent ESR study from which the ratio is found to be ~ 1.80 ($g_{ab} = 4.13$ and $g_c = 2.3$) [101], the two results are at least comparable with each other. The difference between them might relate to the over-simplified treatment of the single-ion physics of Co (II) in $Na_2Co_2TeO_6$ (Section 5.4.1). Nevertheless, with the spin-orbit mixed Kramers doublet ground state and the edge-sharing geometry of neighboring CoO_6 octahedra, $Na_2Co_2TeO_6$ fulfills the essential requirements for hosting Kitaev physics.

- Two main magnetic excitation features are identified in the INS spectra for $Na_2Co_2TeO_6$. One is the dispersive low energy magnetic excitations below 3 meV and the other is the 7 meV flat band. As temperature increases, both features vanish above the Néel temperature $T_N \sim 27$ K, verifying their magnetic origins. To model these excitations, three Hamiltonians are examined: the pure Heisenberg model, the generalized XXZ model, and the Heisenberg-Kitaev model. The Heisenberg model fails to reproduce several features in the experimental spectra, especially the low Q part of the 7 meV flat band. On the contrary, the generalized XXZ model and the Heisenberg-Kitaev model can capture the essential features, i.e. the dispersive low energy excitations below 3 meV and the flat band at 7 meV, of the measured spectra at nearly all Q. Even though at low Q, the intense feature of the 7 meV flat band cannot be well reproduced by both models, they provide an overall much better description of the experimental spectra compared to the Heisenberg model. For the Heisenberg-Kitaev model, our best fitted results indicate the Kitaev interaction K is ferromagentic and dominate over the nearest neighbor interaction J_1 by a factor of ~ 100. These findings support the theoretical prediction made in Ref [80]. At last we suspect that the observed zigzag ordered ground state is due to the existence of sizeable long range interactions J_2 and J_3.

In our analysis, we replace the off-diagonal interaction in the generalized Heisenberg-Kitaev model with the easy-axis single-ion anisotropy. By doing so, we can introduce a gap in the spin wave spectrum phenomenologically. Our results suggest the off-diagonal terms might not be the crucial exchange interaction in determining the magnetic excitation spectrum of $Na_2Co_2TeO_6$. This seems to be a general trend for the models (Model 1, 2, and 4 in Tabel 5.6) having ferromagnetic Kitaev interactions, among which the off-diagonal interaction is never the dominant one and is only a fraction of the Kitaev term. In contrast, for the models (Model 3 and 5) with antiferromagnetic Kitaev interactions, the off-diagonal interaction is sizeable and comparable with the Kitaev strength. This is an interesting observation but for now, we do not understand how the Kitaev interaction and the off-diagonal term correlate with each other in relation to the spin wave spectrum of $Na_2Co_2TeO_6$.

For all the models (Model 1, 2, 4, and 6) with ferromagnetic Kitaev interactions, see Table 5.6, J_1 is close to zero while J_3 is always sizable and antiferromagnetic. Given Model 2 and 3 do not include J_2 at all and the relative small strengths of J_2 for those who included, this suggests J_2 might not a crucial parameter as well in determining the magnetic excitation spectrum of $Na_2Co_2TeO_6$. Summarizing, the minimal Hamiltonian for $Na_2Co_2TeO_6$ with a ferromagnetic Kitaev interaction could be a $K - \Gamma - J_1 - J_3$ type. Here Γ is for opening a gap in the spectrum and K, J_1, and J_3 are for controlling the overall spectral lineshapes.

It should be noted that a triple-**k** ($\mathbf{k}_1 = (1/2, 0, 0)$, $\mathbf{k}_2 = (0, 1/2, 0)$ and $\mathbf{k}_3 = (1/2, -1/2, 0)$) magnetic structure model was recently suggested by Chen *et. al* [102]. In such an arrangement, the magnetic moment will form a vortex pattern in the honeycomb lattice plane with only 3/4 of Co (II) ions carrying ordered moments. Previous neutron powder diffraction experiments [85, 86] cannot distinguish between a multi-**k** structure and a multi-**k** domain contribution. Hence a future single crystal neutron diffraction study would be helpful in distinguishing the two scenarios.

As a conclusion, our results together with the existing studies [97, 99, 100] indicate that $Na_2Co_2TeO_6$ can host Kitaev related physics. This also demonstrates that a high spin Co (II) based materials might become a new platform for studying Kitaev physics in the future. Therefore, a further single crystal study is of necessity to elucidate the accuracy of different models and to fully reveal the potential Kitaev nature of $Na_2Co_2TeO_6$.

Model label	Material	K [meV]	Γ [meV]	Γ' [meV]	J_1 [meV]	J_2 [meV]	J_3 [meV]	J_4 [meV]	D [meV]	Reference
1	Powder	-9	1.8	0.3	-0.1	0.3	0.9	0	0	[97]
2	Powder	-7.4	-0.1	0.05	-0.1	0	1.4	0	0	[99]
3	Powder	3.5	-3	2	-1.2	0	1.6	0	0	[99]
4	Powder	-7	0.02	-0.23	-0.2	0.05	1.2	-0.15	0	[100]
5	Powder	2.7	-2.9	1.6	-3.2	0.1	1.2	-0.4	0	[100]
6	Powder	-4.4	0	0	-0.06	0.16	1.72	0	-0.149	This work

Table 5.6: Parameters of the generalized Heisenberg-Kitaev model used in this and the previous studies to describe the $Na_2Co_2TeO_6$ spin-wave spectrum.

6 Tailoring Magnetism by Metal-organic Framework Engineering

In this chapter, we investigate the magnetic properties of three metal-organic framework compounds CrI$_2$(pyz)$_2$, GaCl$_2$(pyz)$_2$, and CrCl$_2$(pyz)$_2$ (pyz stands for pyrazine C$_4$N$_2$H$_4$). Even though the crystal structures of these three compounds are rather similar, their electronic and magnetic properties vary substantially.

The electronic state of Cr in CrI$_2$(pyz)$_2$ is Cr (II). Whereas for CrCl$_2$(pyz)$_2$, simply by replacing Cl with I, the electronic state of Cr is altered to Cr (III). Such a drastic variation of the electronic state of Cr from CrI$_2$(pyz)$_2$ to CrCl$_2$(pyz)$_2$ is readily observed in their Cr K-edge XAS spectra [103], as shown in Fig.6.1. The K-edge XAS spectrum of CrI$_2$(pyz)$_2$ is similar to the K-edge spectrum obtained from a model compound Cr(III)Br, and for CrCl$_2$(pyz)$_2$ its K-edge XAS spectrum resembles the K-edge lineshape of another model compound Cr(II)I. Normally ligand like Cl or I take one electron away from a central metal ion and form a chemically more stable Cl^{-1} or I^{-1} with a completely filled p shell. Therefore it is easy to infer that, the two pyz ligands in CrI$_2$(pyz)$_2$ carry zero net charges while there is one electron residing on the two pyz rings in CrCl$_2$(pyz)$_2$. In such a scenario, we refer the accumulation of zero net charges on the pyz rings in CrI$_2$(pyz)$_2$ as ligand innocence. On the contrary, ligand non-innocence is present in CrCl$_2$(pyz)$_2$ due to the residing of electrons on the pyz ligands. GaCl$_2$(pyz)$_2$ is similar to CrCl$_2$(pyz)$_2$. The pyz ligands are non-innocent due to that an electron from Ga is shared by two pyz rings in one formula unit. As the result, Ga is in a chemically inert state Ga (III) ($3d^{10}$).

Among the three CrI$_2$(pyz)$_2$ is a quasi-two-dimensional Néel ordered antiferromagnet while GaCl$_2$(pyz)$_2$ is magnetically disordered down to 2 K. Both of them are well placed in an insulating limit showing no evidence of being conductors. Whereas for CrCl$_2$(pyz)$_2$, it is electrically conductive at room temperature and belongs to conducting coordination solids [104, 105, 106]. Moreover, CrCl$_2$(pyz)$_2$ is a ferrimagnet in which the spins on the Cr sites are antiparallel to the radical spins on the pyz ligands [104]. Such a dramatic variation in magnetic properties among CrI$_2$(pyz)$_2$, GaCl$_2$(pyz)$_2$, and CrCl$_2$(pyz)$_2$ signifies the great potential of tailoring magnetism by metal-organic framework engineering.

6.1 A ligand innocent quasi-2D antiferromagnet square lattice CrI$_2$(pyz)$_2$

CrI$_2$(pyz)$_2$ crystallizes in the tetragonal I4/mmm space group (No. 139) and at room temperature its lattice constants are $a = b = 7.0896(3)$ Å, $c = 12.5761(9)$ Å [103]. The crystal structure of CrI$_2$(pyz)$_2$ is illustrated in Fig.6.2(a) which displays a two-layer square lattice crystal structure. The layers consist of corner-sharing CrI$_2$(pyz)$_4$ octahedra, see Fig.6.2(b), forming a 2D square lattice plane of Cr (II) ions ($3d^4$: $S = 2$). For the octahedra, the pyz ligands are bridging between two adjacent Cr (II) ions and are

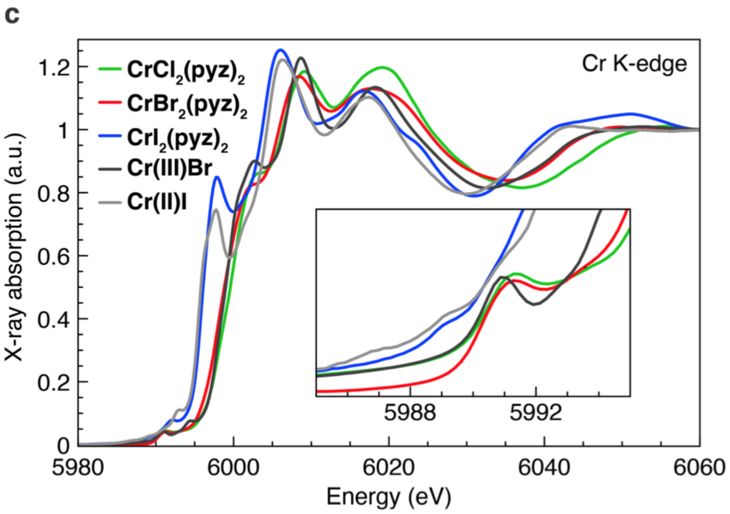

Figure 6.1: Cr K-edge XAS spectra for $CrCl_2$(pyz)$_2$ (green), $CrBr_2$(pyz)$_2$ (red), CrI_2(pyz)$_2$ (blue), Cr(III)Br (dark grey), and Cr(II)I (light grey). The last two curves are reference spectra. The figure is taken from Ref [103].

disordered over two positions, see Fig.6.2(b), while the I^{-1} ligands are non-bridging and extend towards the center of Cr plaquettes in the adjacent layers. From Fig.6.2(b), it is evident the octahedron is significantly elongated along the Cr-I direction. Such a structural distortion is due to the Jahn-Teller effect associated with a high-spin d^4 electronic configuration in an octahedral crystal field [10].

Upon cooling, CrI_2(pyz)$_2$ undergoes a magnetic phase transition at ~ 26 K highlighted by the so-called λ-anomaly in the specific heat data (taken by L. Voigt [103]), see Fig.6.3 [103]. Combined with magnetic susceptibility measurements, its ground state is believed to be antiferromagnetically ordered below $T_N \sim 26$ K characterized by a negative Curie-Weiss temperature $T_{CW} = -39.4 \pm 4.4$ K and an effective moment $\mu_{\text{eff}} = 4.48 \pm 0.03\ \mu_B$ [108], which lies in between the spin-only values for Cr (II), 4.90 μ_B, and Cr (II), 3.87 μ_B [109].

The magnetic structure of CrI_2(pyz)$_2$ is revealed by a neutron powder diffraction study on SPODI [107]. The diffraction patterns are illustrated in Fig.6.2(c). As there are no structural phase transitions occur in CrI_2(pyz)$_2$ upon cooling, from a direct comparison between the 4 K and 60 K data, we can conclude that the weak peaks below 1 Å^{-1} and at around 1.5 Å^{-1} are of magnetic origin. The peaks can be index as $(1/2, 1/2, 0)$ and $(3/2, 1/2, 1)$, respectively, which confirms the antiferromagnetic nature of CrI_2(pyz)$_2$. The refinement of the magnetic structure for CrI_2(pyz)$_2$ was performed by M. Kubus and the resultant magnetic structure is shown in Fig.6.2(d). The magnetic moments of Cr (II) align along the crystallographic **c**-axis but are anti-parallel with any in-plane adjacent Cr (II) sites. Thus the resultant structure is an ideal Néel state within the 2D square lattice

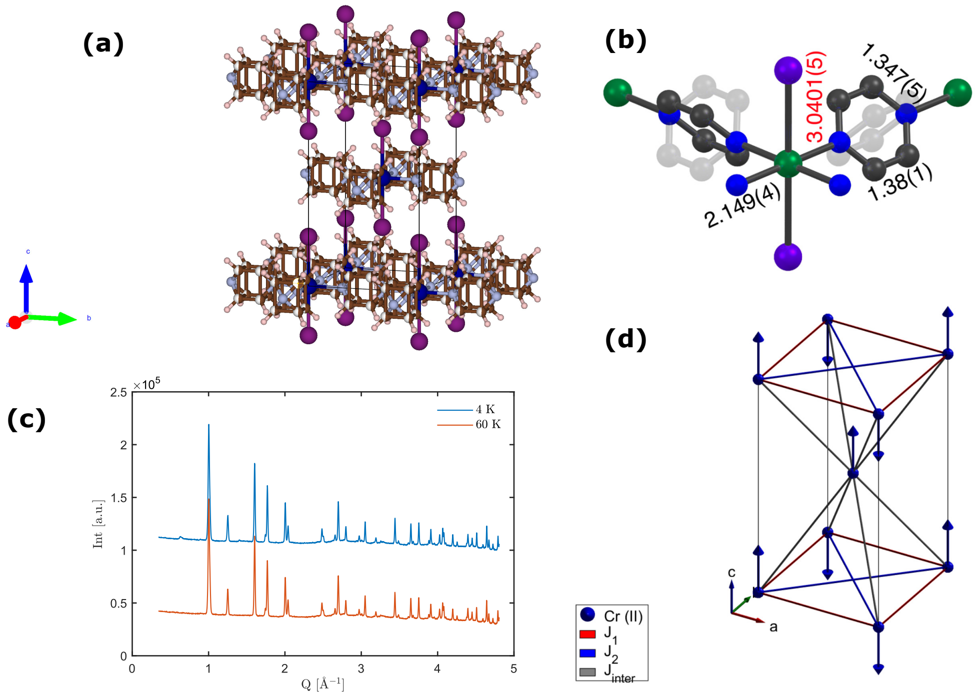

Figure 6.2: (a) Crystal structure of CrI$_2$(pyz)$_2$. The blue and purple spheres represent Cr and I ions respectively. The brown ”cage” represent the disordered state of a pyrazine molecule which is a superposition of two possible orientations of the molecular ring. The figure is taken from Ref [103]. (b) A CrI$_2$(pyz)$_4$ octahedron with a significant elongation along the Cr-I direction. Notice the two possible orientations of pyrazines. The bond lengths are in Å. The figure is taken from Ref [103]. (c) Neutron powder diffraction patterns of CrI$_2$(pyz)$_2$ collected at 4 K and 60 K on SPODI [107] using $\lambda = 2.536$ Å neutrons. The red (60 K) and blue (4 K) curves are displaced for a better comparison. (d) Refined magnetic structure of CrI$_2$(pyz)$_2$. The spins of the in-plane Cr (II) sites form a Néel state and are aligned along the crystallographic **c**-axis. Also shown are the nearest neighbour, the second nearest neighbour and the inter layer exchange interactions J_1, J_2 and J_{inter}.

plane. As a final remark, even though the ordered moment for Cr (II) is close to 4 μ_B, there is a substantial difference in intensity between the structural and magnetic diffraction patterns illustrated in Fig.6.2(c). This might relate to the highly symmetric nuclear structure and the significant amount of atoms in the unit cell of CrI$_2$(pyz)$_2$. As the result, the phase factors in the nuclear structure factor of CrI$_2$(pyz)$_2$ add up coherently and this leads to a significant increase of the allowed nuclear peaks' intensities. Thus the final nuclear scattering signals are way more pronounced than the scattering signals from the magnetic structure.

6.1.1 Experimental details

The synthesis of polycrystalline CrI$_2$(pyz-D$_4$)$_2$ (pyz-D$_4$: C$_4$D$_4$N$_2$) was carried out by L. Voigt from DTU chemistry. To check the sample quality, she also performed a powder X-ray diffraction on the synthesized material. The collected spectrum is in good agreement with the simulated X-ray diffraction pattern. This confirms a high degree of purity and crystallinity of the sample.

To study the spin excitations in CrI$_2$(pyz-D$_4$)$_2$ below and above the Néel temperature $T_N = 26$ K, a neutron scattering experiment was carried out using the direct geometry time-of-flight chopper spectrometer MARI at the ISIS Neutron and Muon Source. The spectrometer was operated using the repetition rate multiplication technique [38] with the incident neutron energy E_i set to 19 meV and the chopper spinning at 200 Hz. This allows simultaneous collection spectra with different energy and momentum transfers at $E_i = 9$ meV, 19 meV, and 70 meV, respectively. For the experiment, a polycrystalline sample of total mass 3.025 g was mounted in an annular geometry inside an Aluminium can, which is connected to the cold-finger of a continuous circle refrigerator capable of cooling the sample to $T = 6$ K. Six sets of data were collected at 6 K, 15 K, 30 K, 60 K, and 100 K, respectively. It turned out the 100 K data are particularly useful for background subtraction purposes, allowing us to distinguish spin excitations from phonon contributions in the full excitation spectra. The MANTID software package was used to process the raw neutron data [89, 90] which were subsequently analyzed using the MATLAB programs MSlice and SpinW [24].

6.1.2 Results and analysis

We start by giving an overview of the excitation spectrum of CrI$_2$(pyz-D$_4$)$_2$. The data shown in Fig.6.4(c) are obtained with neutrons of incident energy $E_i = 70$ meV collected at $T = 6$ K which is far below $T_N \sim 26$ K. Given the detector coverage of the MARI spectrometer, this configuration allows to probe momentum transfers up to 11 Å^{-1}. It is evident from Fig.6.4(c) there are no obvious scattering features in the region between 5 meV and 10 meV energy transfers at $Q \leq 3$ Å^{-1}, while above that the spectrum is dominated by features that grow in intensity as momentum transfer Q increases. Such behavior is consistent with the expectation of scattering from lattice vibrations or phononic excitations [25]. Thus the spin excitations in CrI$_2$(pyz-D$_4$)$_2$ must reside below 5 meV and are hidden by the elastic line in the $E_i = 70$ meV spectrum, hindering the observability.

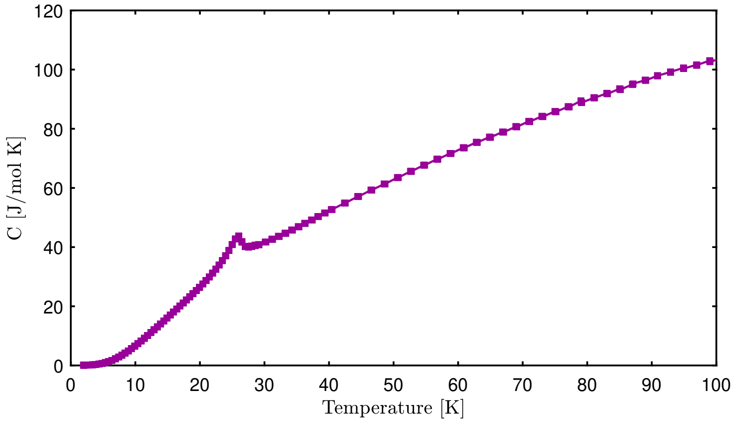

Figure 6.3: Specific heat of CrI$_2$(pyz)$_2$ measured from 2 K to 100 K. The λ-anomaly at around 26 K indicates the onset of an antiferromagnetic ordering upon cooling. The data is from Ref [103].

The $E_i = 19$ meV spectrum is illustrated in Fig.6.4(b), similar to what was observed in the $E_i = 70$ meV data, the spectrum is dominated by phonon scattering at energy transfers above 8 meV. Below that the most prominent feature is the intense scattering feature at energy transfers $\hbar\omega \approx 4$ meV. The intense feature can be divided into two parts, of which the intensities follow different trends. Above $Q \sim 3$ Å^{-1}, the feature gradually becomes more pronounced in intensity as Q increases, which can be again attributed to the scattering from phonons in CrI$_2$(pyz-D$_4$)$_2$. Below ~ 3 Å^{-1}, the feature acquires more intensity as Q decreases and is most prominent at low Q, contrary to the characteristic feature of phonon scattering [25]. Such an observation is in good accord with features of scattering from spin excitations whose intensity falls off as Q increases. This is due to the intensity modulation from the squared magnetic form factors of the magnetic ions inside the material under study [25].

In Fig.6.4(a), we present a closer look at the spin excitations in CrI$_2$(pyz-D$_4$)$_2$ in the $E_i = 9$ meV spectrum with a much better resolution at low Q. It is clear that the spin excitations extend from ~ 1 meV to ~ 4.5 meV and the most salient feature is the nearly flat mode at ~ 4.5 meV, which gradually becomes weaker as Q increases and blends into the background at $Q \sim 3.5$ Å^{-1}. It is possible to discern that the dispersive spin excitations below the flat mode stem from the positions where magnetic Bragg peaks occur in the neutron powder diffraction experiment. The most prominent such minimum occurs around $Q \sim 0.5$ Å^{-1}, which corresponds to **Q** $= (1/2, 1/2, 0)$. This reflects the antiferromagnetic nature of the spin wave excitations. It is evident in the spectrum there is a ~ 1 meV gap between zero energy transfer and the minimum of the spin excitations at the magnetic Bragg peak **Q** $= (1/2, 1/2, 0)$. This indicates no gapless Goldstone magnons exist in CrI$_2$(pyz-D$_4$)$_2$ and the spin Hamiltonian of CrI$_2$(pyz-D$_4$)$_2$ cannot possess continuous three dimensional rotational symmetry. Notice that there are two stripy

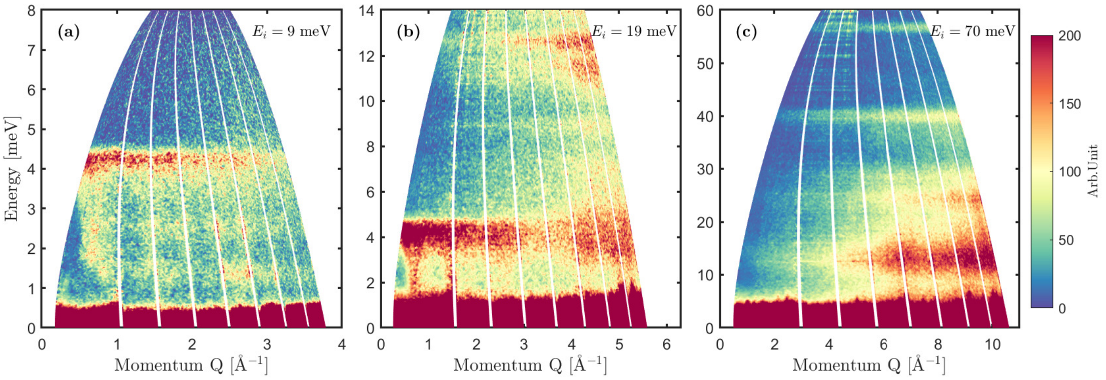

Figure 6.4: Overview of the excitation spectrum of a CrI$_2$(pyz-D$_4$)$_2$ powder sample. The incident energies E_i in panels (a)-(c) are 9, 19 and 70 meV, respectively, and the corresponding energy resolutions (FWHM) at the elastic line are around 0.28, 0.79 and 4.17 meV. All data were obtained at T = 6 K. The white lines represent gaps between the detectors of the MARI spectrometer.

features in the spectrum locating at around 1.5 meV and 2.5 meV, respectively. These are spurions of the MARI spectrometer parasitizing scattering spectra but with relatively discernible shape features. From a private communication with the MARI beamline scientist Duc Le, the plausible spurion scenario is that the sample or Aluminum can Bragg peaks scatter neutrons up. The scattered neutrons hit something then scatter elastically incoherently back down and are detected at a later time than expected. Therefore they appear to be scattered inelastically from the sample. However, the reasoning behind the temperature dependent behavior of these spurions is still unclear.

The thermal evolution of the spin and lattice excitations in CrI$_2$(pyz-D$_4$)$_2$ below and above the Néel temperature $T_N \sim 26$ K is illustrated in Fig.6.5 in which only the spectra collected at $E_i = 9$ meV and 19 meV are included. As temperature increases, the excitations from lattice vibrations grow stronger in intensity and eventually dominate the whole spectra, especially at temperatures above T_N. This is clearly observable from the spectra collected at $E_i = 19$ meV, see Fig.6.5(f)-(j). The spin excitations below 4 meV persist up to 60 K, and at 60 K or above ($> 2T_N$) they are no longer discernible at look (see Fig.6.5(a)-(e))). The prominent 4.5 meV flat mode at 6 K gradually loses definition and completely disappears at 30 K, just above T_N, so does the 1 meV energy gap. From 30 K and above, the gapless spin excitations are softened as the increase in temperature and start merging with the elastic line at 100 K.

Due to the substantial contributions from lattice vibrations in the 100 K spectrum, the thermal evolution of the spin excitations in CrI$_2$(pyz-D$_4$)$_2$ becomes clearer after subtracting it (with the Bose factor corrected) from the rest of the spectra. The result is illustrated in Fig.6.6. The phonon scattering cannot be completely eliminated from the spectra (the residual intensity is still seen at energy transfers below 4 meV and above 8 meV at $Q \geq 4$

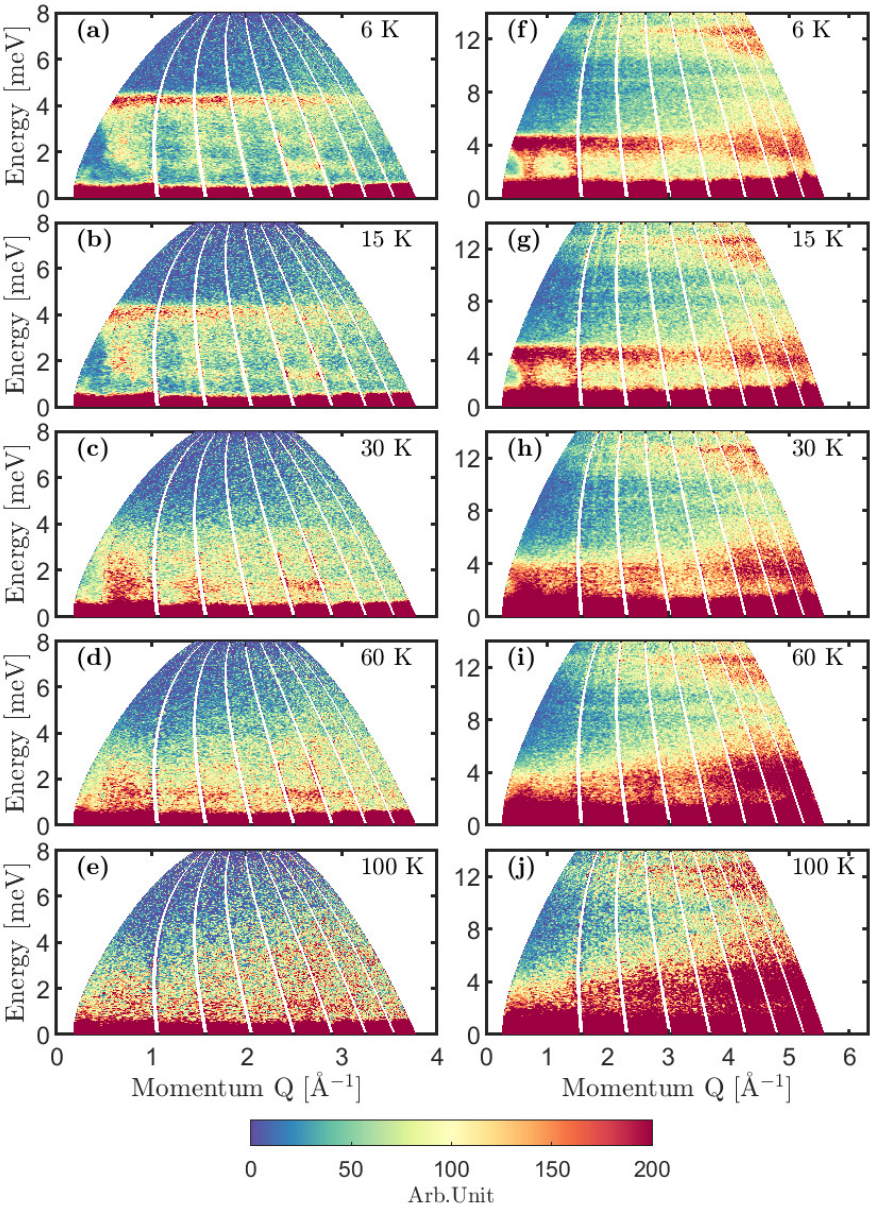

Figure 6.5: Temperature dependence of the spin excitation spectra and the lattice vibration excitation spectra in CrI$_2$(pyz-D$_4$)$_2$ collected at $E_i = 9$ meV ((a) - (e)) and 19 meV ((f) - (j)), for temperatures (a)(f) 6 K, (b)(g) 15 K, (c)(h) 30 K, (d)(i)60 K and (e)(j) 100 K. The Néel temperature of CrI$_2$(pyz-D$_4$)$_2$ is around 26 K.

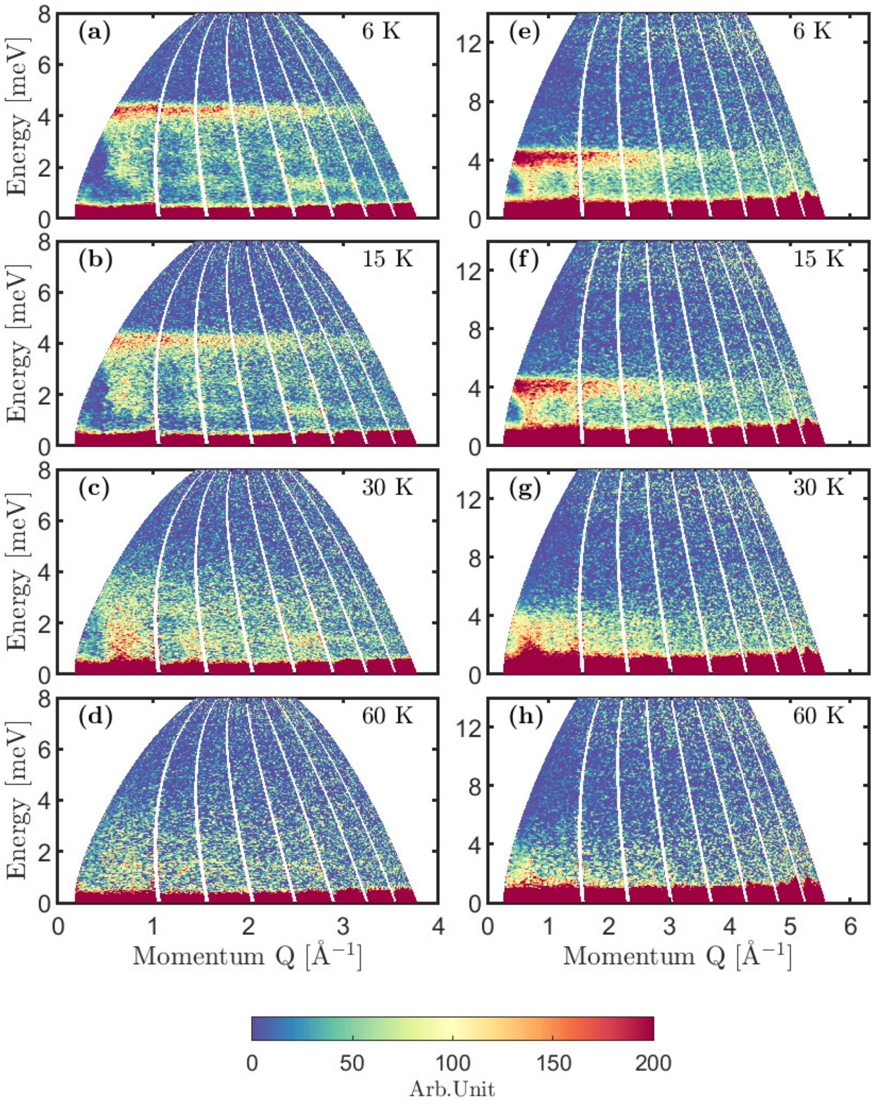

Figure 6.6: Spin wave spectra of CrI$_2$(pyz-D$_4$)$_2$ for $E_i = 9$ meV ((a) - (d)) and 19 meV ((e)-(h)), for temperatures (a)(e) 6 K, (b)(f) 15 K, (c)(hg 30 K and (d)(h) 60 K after subtracting the 100 K data corrected for the Bose occupation factor.

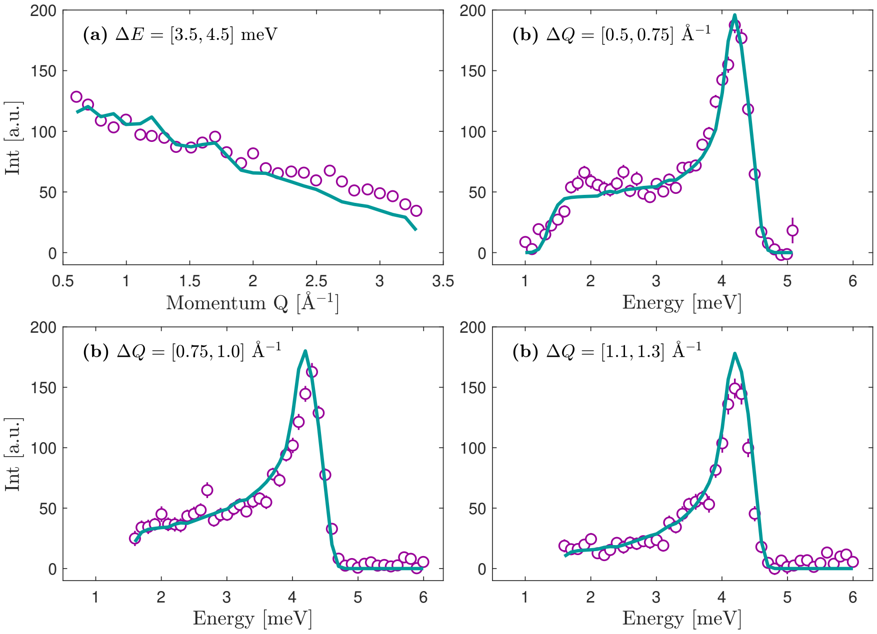

Figure 6.7: Comparison between the $J_1 - J_2 - D$ Heisenberg model (green lines) and the experimental data (purple open circles) through (a) a constant energy cut between 3.5 meV and 4.5 meV, (b) a constant momentum cut between 0.5 Å^{-1} and 0.75 Å^{-1}, (c) a constant momentum cut between 0.75 Å^{-1} and 1.0 Å^{-1} and (d) a constant momentum cut between 1.1 Å^{-1} and 1.3 Å^{-1}.

Å^{-1} in the $E_i = 19$ meV spectra, as seen from Fig.6.6(e)-(h)). However, this is not a big concern as after subtraction, the spin excitations dominate the spectra whose intensity is much more pronounced than the residue phonons. Thus it is relatively easy to distinguish the spin excitations from the residual phonon modes. Consistent with what was observed before, the spin excitations in CrI$_2$(pyz-D$_4$)$_2$ are robust against thermal fluctuations and indeed survive above T_N. Even though the prominent 4.5 meV flat mode and the 1 meV excitation gap gradually diminish when approaching T_N and are completely vanished in the paramagnetic phase, there still exists a broad diffuse scattering extending from zero energy transfer to 4 meV, see Fig.6.6(c) and (g). The diffuse scattering directly emerges from the positions where magnetic Bragg peaks situate, among which the most prominent one is at **Q** $= (1/2, 1/2, 0)$. This implies the spin-spin correlation length in the 2D square lattice plane is still finite just above T_N. At 60 K, the diffuse scattering from the spin excitations is considerably weakened, see Fig.6.6(d) and (h). This indicates that the correlation length between spins in CrI$_2$(pyz-D$_4$)$_2$ is significantly reduced.

Having described the salient features of the spin excitations of CrI$_2$(pyz-D$_4$)$_2$, the next step is to determine the spin Hamiltonian. As previously explained, the Hamiltonian

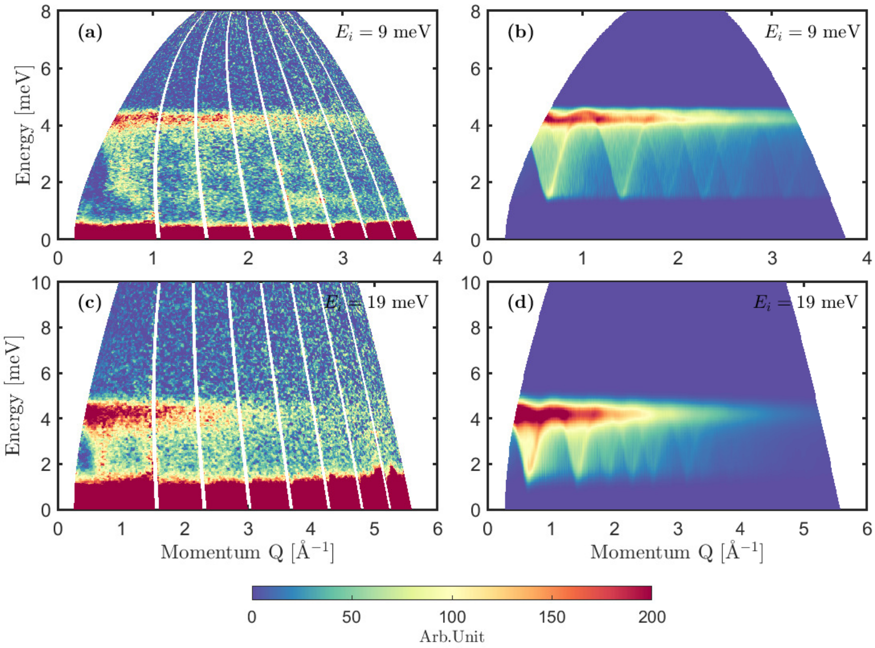

Figure 6.8: (a)(c) Powder INS spectra of CrI$_2$(pyz-D$_4$)$_2$ collected at $T = 6$ K using $E_i = 9$ meV and 19 meV. (b)(d) Calculated powder INS cross-section for the $J_1 - J_2 - D$ Heisenberg model with the optimized parameters listed in Table 6.1 for $E_i = 9$ meV and 19 meV.

possesses no continuous three dimensional rotational symmetry. Given that the ordered moments are along the crystallographic **c**-axis, a $J_1 - J_2 - D$ Heisenberg model is adopted for describing the spin excitation spectrum in CrI$_2$(pyz-D$_4$)$_2$, see Eq.(6.1).

$$H = J_1 \sum_{\langle i,j \rangle} \mathbf{S}_i \cdot \mathbf{S}_j + J_2 \sum_{\langle\langle i,j \rangle\rangle} \mathbf{S}_i \cdot \mathbf{S}_j + \sum_i D \left(S_i^z\right)^2 \tag{6.1}$$

Here the first two summations are over the nearest neighbors and the second nearest neighbors of spins in the 2D square lattice plane, and the corresponding exchange constants are J_1 and J_2, respectively. In Fig.6.2(d), they are represented by the red and blue solid lines. The last term in the summation is a single-ion anisotropy with $D < 0$, which dictates spins to align parallel to the **z**-axis in the laboratory frame or the crystallographic **c**-axis of CrI$_2$(pyz-D$_4$)$_2$. Here we ignore the interlayer exchange couplings between the adjacent Cr (II) square lattice planes as the strengths are expected to be significantly lower than the intralayer couplings due to the large separation between the layers and the absence of direct bond connections between the adjacent layers.

Calculations of the spin wave dispersion and the powder INS cross-section for the given Hamiltonian Eq.(6.1) are conducted by linear spin wave theory using SpinW [24]. The resultant spectrum is fitted to the $E_i = 9$ meV, $T = 6$ K spectrum shown in Fig.6.6(a). For the fitting, four different cuts from the experimental spectrum are selected, (i) a constant energy cut with $\Delta E = [3.5, 4.5]$ meV and (ii) three constant momentum cuts with $\Delta Q = [0.5, 0.75]$ Å^{-1}, $[0.75, 1.0]$ Å^{-1} and $[1.1, 1.3]$ Å^{-1}, respectively. The first energy cut is used to constrain the Q-dependent intensity variation of the $J_1 - J_2 - D$ Heisenberg model. The constant momentum cut with $\Delta Q = [0.5, 0.75]$ is used to determine the size of the spin wave gap or to constrain the value of D. The last two constant momentum cuts are included to constrain the value of J_1 and the relative ratio between J_1 and J_2. The simulated spectrum obtained from SpinW is convoluted with the energy resolution function of MARI spectrometer and the final spectrum is used in the fitting process. Minimization of the χ^2 cost function of the fitting is achieved by the particle swarm optimization [76] and the optimized parameters (J_1, J_2, D) are summarized in Table 6.1. A direct comparison between the experimental data and the best fitted results is shown in Fig.6.7. It is evident that the model captures the main features of the spin excitations in terms of peak positions and spectral lineshapes. Because of the easy-axis single-ion anisotropy D in the spin Hamiltonian, the observed ~ 1 meV gap is faithfully reproduced. This is evident from the constant momentum cut with $\Delta Q = [0.5, 0.75]$ Å^{-1} shown in Fig.6.7(b). In Fig.6.8, we present the calculated powder INS spectra based on the $J_1 - J_2 - D$ Heisenberg model with the optimized parameters for $E_i = 9$ meV and 19 meV, respectively. Again, the model spectra well reproduce the observed spin excitations and the ~ 1 meV excitation gap.

In Fig.6.9, we show the spin wave dispersion calculated from the $J_1 - J_2 - D$ Heisenberg model along the high symmetry directions in the reciprocal space of a 2D square lattice, as illustrated in Fig.4.1a, using the best fitted parameters in Table 6.1. From the calculation we obtain the size of the spin wave gap at (π, π), which is 1.37 meV.

	Fitted value
J_1 [meV]	0.447 ± 0.0045
J_2 [meV]	-0.0429 ± 0.0022
D [meV]	-0.0634 ± 0.0047

Table 6.1: Parameters of the $J_1 - J_2 - D$ Heisenberg model used to describe the $CrI_2(pyz\text{-}D_4)_2$ spin wave spectrum.

Along the zone boundary direction, i.e. $(\pi/0) \rightarrow (\pi/2, \pi/2)$, unlike the 2DQHAFSL case (see Fig.4.1b), linear spin wave theory predicts the dispersion is no longer flat. The spin wave energy at $(\pi, 0)$ is slightly higher than that at $(\pi/2, \pi/2)$ ($\Delta\hbar\omega = 0.34$ meV). Such a difference is due to the existence of finite J_2.

As a final remark, we tried to extend the Hamiltonian with the inclusion of the interlayer coupling J_{inter}, indicated by the grey lines in Fig.6.2(d), and hoped to find its value based on the 6 K dataset. However the best optimized J_{inter} is two orders magnitude smaller than J_1 and there is no significant improvement of the fitting quality, which justifies the previous neglection of interlayer couplings. Apart from that, we also examined whether a minimal $J_1 - D$ Heisenberg model is enough to faithfully reproduce the experimental spectra. However, the optimized $\chi^2 = 10.3$ is around two times larger than the best-fitted $\chi^2 = 4.9$ from the $J_1 - J_2 - D$ Heisenberg model. This directly supports the necessity of including J_2 in the spin Hamiltonian.

Our results indicate $CrI_2(pyz\text{-}D_4)_2$ is close to a realization of the 2D $S = 2$ Heisenberg antiferromagnet on a square lattice ($J_2/J_1 \approx -0.1$) with easy-axis anisotropy as the interlayer couplings are negligible. Due to the ferromagnetic J_2, no frustration is present in the system and the Néel order is further stabilized. Ignoring the easy-axis anisotropy D, the Curie-Weiss temperature calculated from the fitted parameters in Table 6.1 is $T_{CW} = \frac{S(S+1)}{3k_B}(4J_1 + 4J_2) = -37.6$ K, which agrees well with the measured value -39.4 K. For a high spin d^4 state ($t_{2g}^3 e_g^1$) the angular orbital moment is quenched [10]. Thus similar to CrI_3, the observed single-ion anisotropy in $CrI_2(pyz\text{-}D_4)_2$ may arise from the large spin-orbit coupling strength in I [110] which dictates the preferred spin orientations of Cr (II) ions.

6.2 Ligand non-innocence in $GaCl_2(pyz)_2$

$GaCl_2(pyz)_2$ crystallizes in the orthorhombic space group Immm (No. 71). Similar to $CrI_2(pyz)_2$, $GaCl_2(pyz)_4$ octahedra coordinate in a corner-sharing fashion with the pyz ligands bridging two adjacent Ga ions [103]. As the result, Ga ions form a nearly ideal 2D square lattice plane with lattice constants $a = 6.8809$ Å and $b = 7.0730$ Å [103]. The square lattice planes are stacked along the crystallographic **c**-axis with lattice constant $c = 10.7563$ Å, such that the Cl ligands extend towards the center of Ga plaquettes in the adjacent layers. In Fig.6.10, we illustrate the crystal structure of $GaCl_2(pyz)_2$. Unlike $CrI_2(pyz)_2$, for every formula unit of $GaCl_2(pyz)_2$ an electron is transferred from Ga (II) to one of the pyz rings, yielding a chemically inert ion Ga (III) ($3d^{10}$). Moreover, as

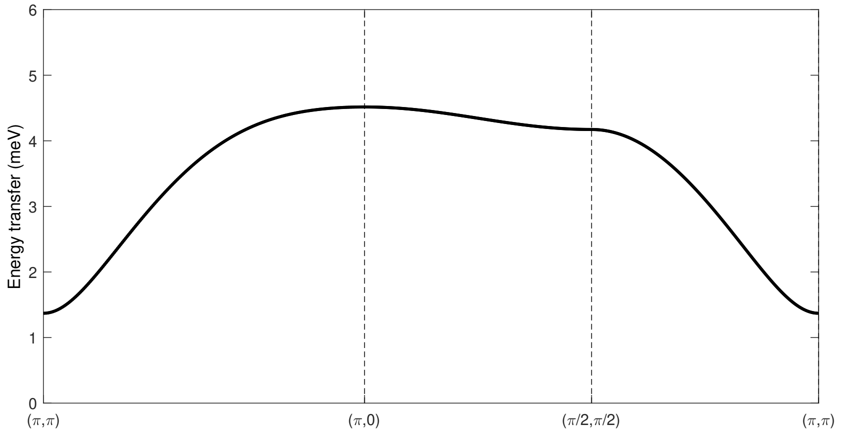

Figure 6.9: Spin wave dispersion of CrI$_2$(pyz-D$_4$)$_2$ along high symmetry directions in the reciprocal space of a 2D square lattice calculated from the best fitted parameters listed in Table 6.1. The high symmetry directions in the reciprocal space are illustrated in Fig.4.1a.

visible in Fig.6.10(b) a width reduction of the pyz ligands occurs in the crystallographic **a** direction, along which the pyz ligands are in closer contact with Ga (III) ions than along the crystallographic **b** direction. This can be inferred from the bond lengths analysis: in the **a** direction Ga-N distance is 2.027(4) Å, C-C distance is 1.366(5) Å and in the **b** direction Ga-N distance is 2.138(4) Å, C-C distance is 1.39(1) Å [103].

6.2.1 Magnetic susceptibility and specific heat

GaCl$_2$(pyz)$_2$ exhibits a strong ESR signal which yields a g-factor of 2.0048, close to the value of a free electron ($g_e = 2.002319$) [103]. This supports the physical picture of having an electron situated on the pyz ligand in a unit formula of GaCl$_2$(pyz)$_2$. In contrast, the g-factor of a Ga (II) ion is expected to lie close to or below 2 as previously reported [112]. A magnetic susceptibility measurement on GaCl$_2$(pyz)$_2$ is illustrated in Fig.6.11 (conducted by L. Voigt [103]), in which the temperature range extends from 1.5 K to 300 K. A simple Curie-Weiss fit (from 100 K to 280 K, see Fig.6.11(a)) to the data yields a negative Curie-Weiss temperature $T_{CW} = -8.60$ K, indicating the dominant interaction present in the system is antiferromagnetic type, and a Curie constant $C = 0.3559$ cm^3 K mol^{-1} which is close to the value for a $S = 1/2$, $g = 2$ system ($C = 0.3751$ cm^3 K mol^{-1}). Recalling the pyz ligands in the crystallographic **a** direction are considerably reduced and are in more close contact with the Ga (III) ions, the transferred electrons may be mainly localized on the pyz rings along the **a** direction. This would cause stronger exchange interactions along the **a** axis compared to the exchange strengths in the crystallographic **b** direction. As the result, this would imply a system consisting of $S = 1/2$ antiferromagnetic chains along the **a** axis which are weakly coupled along the **b** axis.

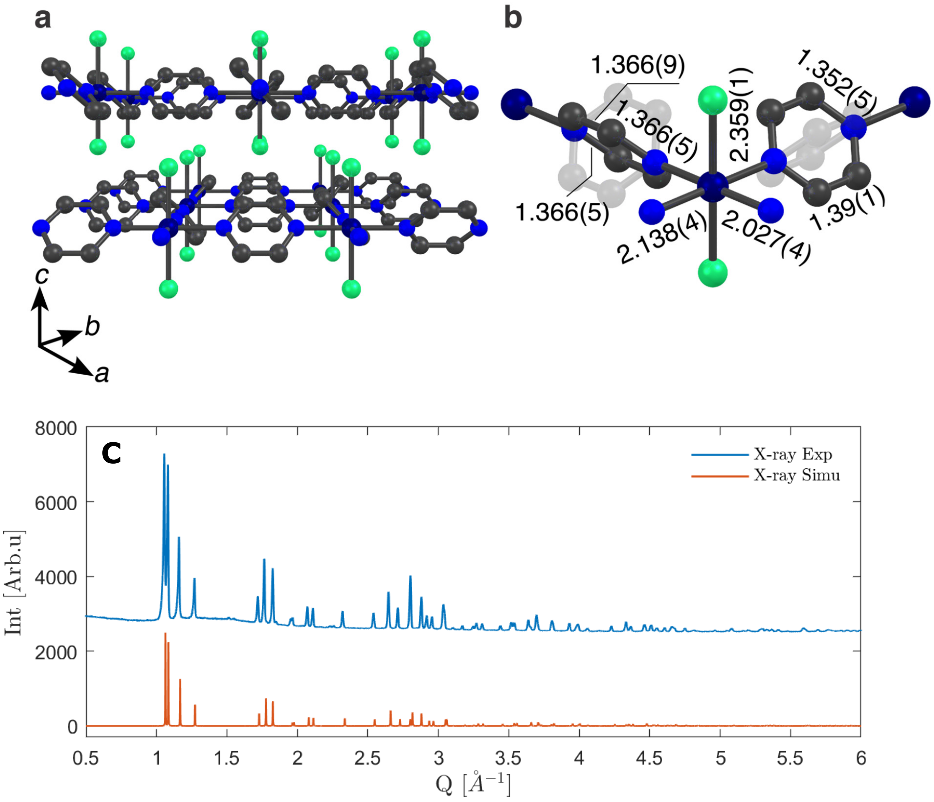

Figure 6.10: (a) Crystal structure of GaCl$_2$(pyz)$_2$ at 120 K. Ga: dark blue, Cr: dark green, Cl: light green, N: blue and H is emitted for clarity. (b) A GaCl$_2$(pyz)$_4$ octahedron with bond lengths in Å. The two possible orientations of pyrazines are illustrated as well. (a) and (b) are taken from Ref [103]. (c) Experimental (taken by H. Chen from DTU Chemistry) and simulated X-ray powder diffraction pattern (calculated from Vesta [111]) for GaCl$_2$(pyz)$_2$ calculated from the crystal structure presented in Ref [103]. An overall good agreement in terms of the peak positions is reached between the two spectra. A clear difference arises at $Q = 1.5$ Å^{-1} in which a two-peak feature is present in the experimental spectrum but not in the simulated pattern.

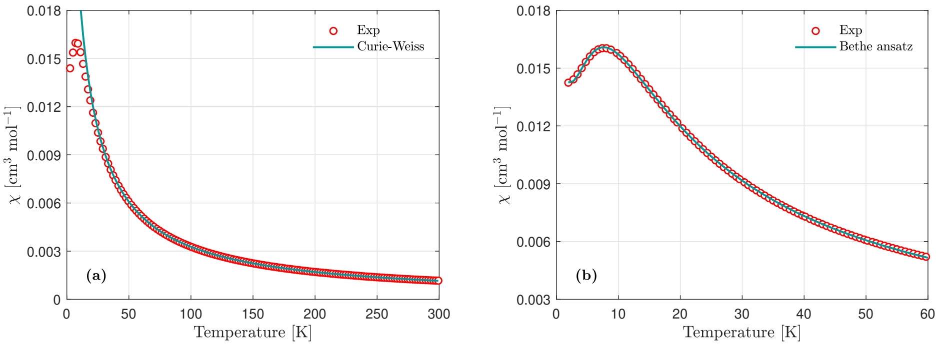

Figure 6.11: (a) Measured magnetic susceptibility of GaCl$_2$(pyz)$_2$ and the Curie-Weiss fit. (b) Below 60 K, the magnetic susceptibility of GaCl$_2$(pyz)$_2$ can be well described by a weakly coupled $S = 1/2$ antiferromagnetic chain, see Section 2.1 for more details.

	Fitted value
J [meV]	1.06 ± 0.0029
λ [meV]	0.22 ± 0.0048
χ_0 [cm^3 mol^{-1}]	$-3.20 \times 10^{-4} \pm 9.09 \times 10^{-6}$
C_{impurity} [cm^3 K mol^{-1}]	$0.0027 \pm 6.54 \times 10^{-5}$

Table 6.2: Parameters of the susceptibility model, see Eq.(6.2), used to describe the measured susceptibility below 60 K for GaCl$_2$(pyz)$_2$.

To model the susceptibility of such a system, Eq.(6.2) is adopted.

$$\chi(T) = \chi_0 + \frac{C_{\text{impurity}}}{T} + N\mu_B^2 g^2 \frac{\chi_{\text{1D}}(T)}{1 + 4\lambda\chi_{\text{1D}}(T)} \tag{6.2}$$

Here χ_0 is a constant to account for a temperature independent para- or dia- magnetic contribution. The second term in the summation is the response of paramagnetic impurities to magnetic field and the last term is a mean-field result of the susceptibility for a weakly coupled antiferromagnetic $S = 1/2$ chain system whose interchain couplings are absorbed in 4λ (λ represents the sum of all the exchange couplings for a single site at one side of a chain) in the denominator [113]. $\chi_{\text{1D}}(T)$ is the susceptibility of an antiferromagnetic Heisenberg $S = 1/2$ chain calculated from the Bethe ansatz with an intrachain coupling J (Eq.(50) in Ref [114] which is valid for the temperature range $0.01J \leq T \leq 5J$). N is the Avogadro constant, μ_B is the Bohr magneton and $g = 2.0048$ is the g-factor of GaCl$_2$(pyz)$_2$. Eq.(6.2) is fitted to the susceptibility curve of GaCl$_2$(pyz)$_2$ (from 1.79 K to 60 K) and the fitted result is shown in Fig.6.10(b). In Table 6.2 we summarize the best fitted parameters of Eq.(6.2). Notice that the fitted λ takes a positive value, indicating the chains are antiferromagnetically coupled [87].

Even though antiferromagnetic interactions are evident from the magnetic susceptibility data, it is not sufficient to investigate whether long range ordering occurs in GaCl$_2$(pyz)$_2$.

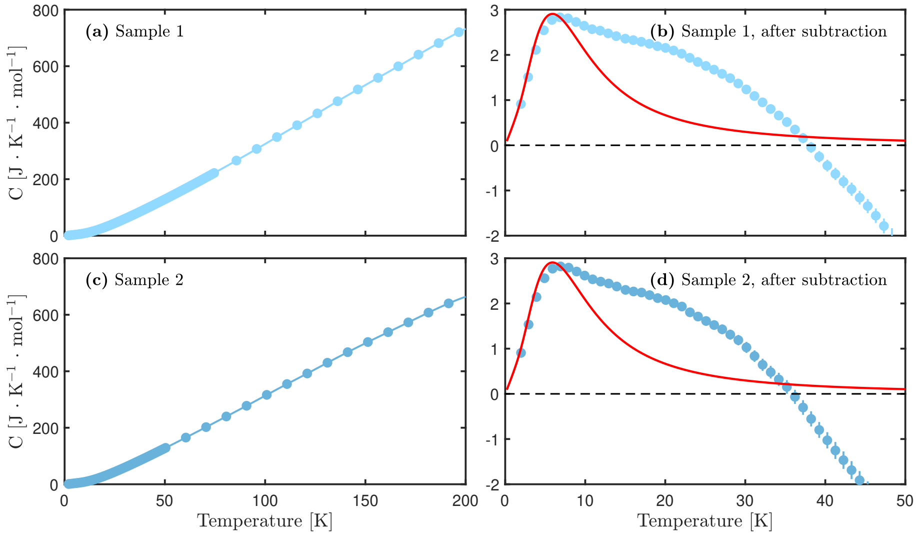

Figure 6.12: (a)(c) Specific heat for Sample 1 and Sample 2 from 2 K to 200 K. (b)(d) $ZnCl_2(pyz)_2$ subtracted specific heat for both Sample 1 and Sample 2. Also shown is the theoretical specific heat obtained from the Bethe ansatz for a Heisenberg $S = 1/2$ chain with an intrachain coupling $J = 1.06$ meV and without interchain coupling (red solid lines).

To this end, we conducted a specific heat measurement on $GaCl_2(pyz)_2$ searching for any signatures of phase transitions at low temperatures. During the experiment, two powder pellets of $GaCl_2(pyz)_2$ weighted 5.7 mg and 5.0 mg were measured, labeled as Sample 1 and Sample 2 respectively. In addition, an iso-structural non-magnetic compound $ZnCl_2(pyz)_2$ was measured as well for phonon subtraction purposes. Datasets at five different field values, 0 T, 2 T, 6 T, 10 T, and 14 T, were collected for Sample 2.

In Fig.6.12, we illustrate the zero field specific heat results for Sample 1 and Sample 2, see Fig.6.12(a) and (c). Due to the air sensitive nature of $GaCl_2(pyz)_2$, the samples were immersed in an excessive amount of grease during the experiment for protection purposes ($ZnCl_2(pyz)_2$ was also immersed in grease). The measured specific heats in such a situation contain contributions from the samples, the grease, and the platform for placing the samples (see Fig.3.1). The side effect of this is obvious: the measured specific heat contains contributions from the grease and the platform, which in total are significantly larger than the contribution from the sample itself. This is readily observed in the data. As the heating up of the sample, the measured values increase significantly (compared to the specific heat of $CrI_2(pyz)_2$ shown in Fig.6.3, $GaCl_2(pyz)_2$ takes value close to 400 J · K^{-1} · mol^{-1} at 100 K while $CrI_2(pyz)_2$ is only around 100 J · K^{-1} · mol^{-1} at the same temperature). No clear λ-anomaly features are observed in the accessible temperature range from 2 K to 200 K, implying that no phase transitions occur upon cooling and that $GaCl_2(pyz)_2$ is magnetically disordered even at 2 K. In Fig.6.12(b) and

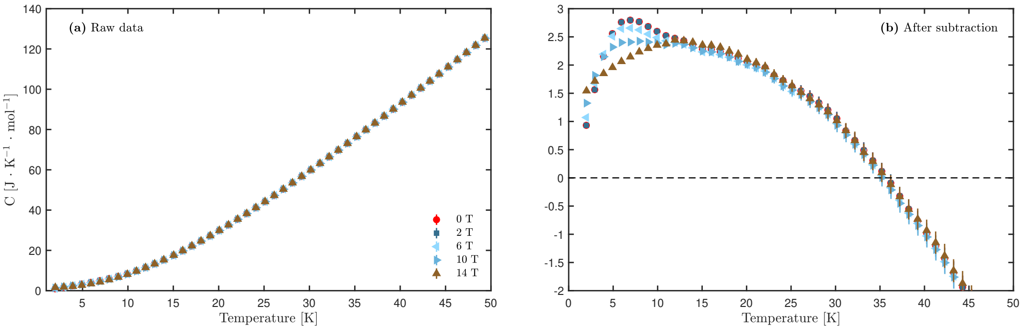

Figure 6.13: (a) Specific heat of Sample 2 at 5 different fields 0 T, 2 T, 6 T, 10 T and 14 T. (b) $ZnCl_2(pyz)_2$ subtracted specific heat at the five different fields for Sample 2.

(d) we illustrate the specific heat for Sample 1 and Sample 2, respectively, after subtracting the specific heat of $ZnCl_2(pyz)_2$. In principle, such a subtraction procedure should remove most of the phonon contributions from the $GaCl_2(pyz)_2$ specific data due to the isostructural relation between $GaCl_2(pyz)_2$ and $ZnCl_2(pyz)_2$ and the contribution from the platform. However, as evident in both Fig.6.12(b) and (d), the simple removal method fails above 40 K where an over-subtraction occurs resulting in negative specific heat. Under such a circumstance how can we even be sure the residual positive part of the subtracted data is the true magnetic contribution?

Luckily a clear distinction between magnetic and phonon contributions is that they have different responses to magnetic field. For phonons, as long as couplings between magnetic degree of freedom and lattice vibrations are negligible, their contribution to specific heat should be magnetic field independent. By contrast, the magnetic contribution is dynamic and changes with different field strengths. For the contribution from the platform, we expect it to be field independent. In Fig.6.13(a) and (b), we illustrate the field evolution of the specific heat for Sample 2 with and without the $ZnCl_2(pyz)_2$ subtraction. As seen from the raw data in Fig.6.13(a), the pure magnetic contribution is hidden behind the large specific heat of grease and the platform, making it impossible to identify any field dependent changes in the data. After subtracting the $ZnCl_2(pyz)_2$ data, see Fig.6.13(b), it is obvious the most dramatic changes occur at temperatures below 10 K where the maximum of the specific heat at zero field gradually decreases and eventually vanishes around 10 T. Above 10 T, the specific heat at around 5 K decreases rapidly. In contrast, the specific data lying in between 15 K and 35 K show only slight variations as the increase of the field. Especially above 25 K, the specific data collected at five different fields are almost field independent. This implies the $ZnCl_2(pyz)_2$ subtracted data in Fig.6.12(b) and (d) are likely under-subtracted and dominated by the remnant phonon, grease, or platform contribution in the region between 15 K and 35 K. Otherwise given their relatively large values, the field evolution of the specific heat should have a much more pronounced variation in the temperature range from 15 K to 35 K.

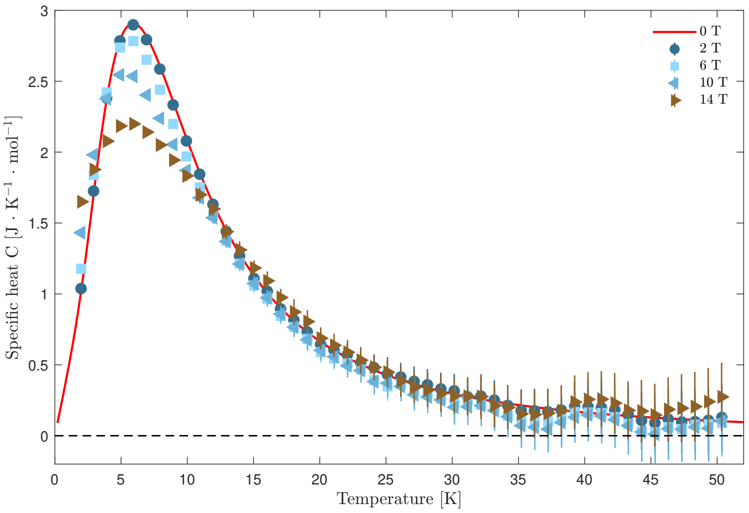

Figure 6.14: Specific heat of Sample 2 at four different fields, 2 T, 6 T, 10 T and 14 T, after subtracting the effective background contribution as described in the text. The red solid line represents the specific heat calculated from the Bethe ansatz for a Heisenberg $S = 1/2$ chain model with an intrachain coupling $J = 1.06$ meV. The interchain coupling for the spin chains is absent.

Having established the ZnCl$_2$(pyz)$_2$ subtraction method does not work as expected and given the prior that the magnetic susceptibility of GaCl$_2$(pyz)$_2$ can be well reproduced by a $S = 1/2$ antiferromagnetic Heisenberg chain model with weak interchain couplings, a natural question is whether the spin chain model describes the collected specific data as well? In Fig.6.12(b) and (d), we plot the theoretical specific heat calculated from the Bethe ansatz (Eq.(54) in Ref [114] valid for the temperature range $0.01J \leq T \leq 5J$) for a $S = 1/2$ Heisenberg chain with $J = 1.06$ meV without interchain coupling. As seen in Fig.6.12(b) and (c), it is clear the theoretical lines match relatively well with the subtracted data below 8 K irrespective of which sample is under investigation. Whereas above 10 K, the theoretical values are considerably lower than the subtracted data, consistent with our expectation that there is an under subtraction in the plotted data between 15 K and 35 K as previously explained.

If we assume the Heisenberg $S = 1/2$ antiferromagnetic chain model offers a satisfactory description of the zero field specific heat, it can be used to construct an effective specific heat background containing contributions from phonons in GaCl$_2$(pyz)$_2$, the grease of Sample 2 and the platform. Such an effective background can be obtained by subtracting the calculated theoretical specific heat (the red solid line in Fig.6.12(d)) from the raw experimental data for Sample 2. Having identified the non-magnetic specific background, the obtained background curve is further subtracted from the raw specific heat data collected at different fields. The resultant data (interpreted to be purely mag-

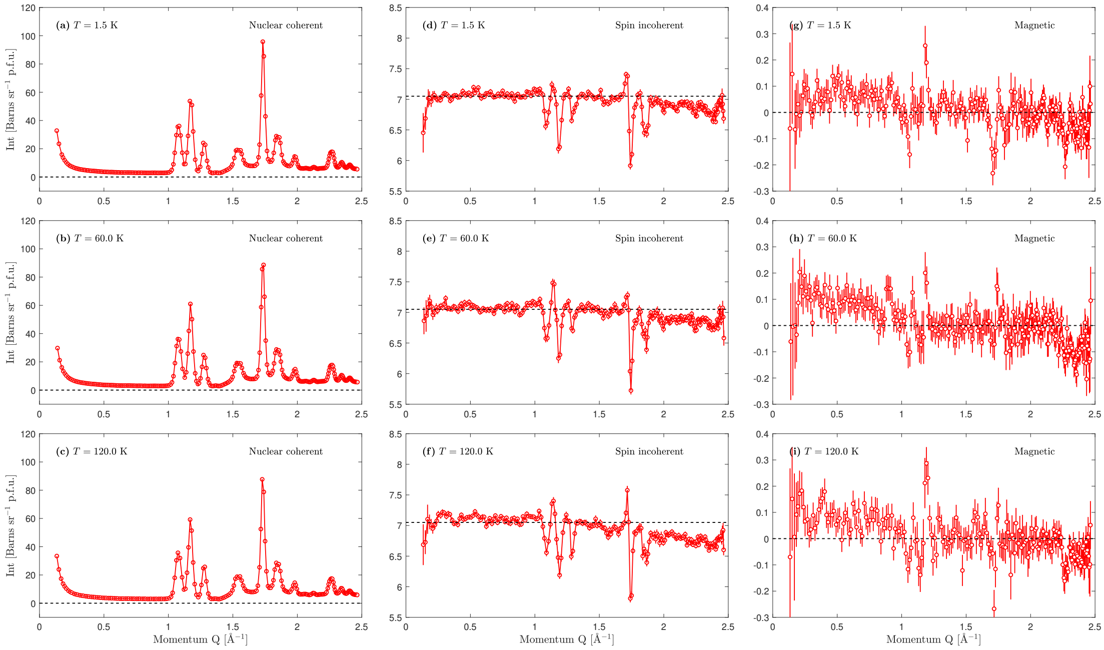

Figure 6.15: Nuclear coherent scattering spectra ((a)-(c)), spin incoherent scattering spectra ((d)-(f)) and magnetic scattering spectra ((g)-(i)) of GaCl$_2$(pyz-D$_4$)$_2$ obtained from the D7 experiment. The measurement was conducted at three different temperatures, (a)(d)(g) 1.5 K, (b)(e)(h) 60 K and (e)(f)(j) 120 K.

netic) are illustrated in Fig.6.14. At all fields, the magnetic specific heat approaches zero at around 50 K and its intensity gradually decreases as the field increases. At zero field, the maximum of the specific heat is close to 3 J·K^{-1}·mol^{-1} whereas at 14 T it is only around 2.1 J·K^{-1}·mol^{-1}, displaying a $\sim 30\%$ reduction in intensity. Moreover, the position of the maximum specific heat seems to shift towards a lower temperature as the field increases. This has been observed before in a field dependent study of the specific heat of Cu(C$_4$H$_4$N$_2$)(NO$_3$)$_2$ [115], which manifests itself to be a perfect realization of the $S = 1/2$ antiferromagnetic Heisenberg chain. Although this effect is minor for GaCl$_2$(pyz)$_2$, it is still worth pointing out that such a trend exists in the data which requires a more detailed specific heat study in the future.

6.2.2 Polarized neutron powder diffraction on GaCl$_2$(pyz-D$_4$)$_2$

Having studied the specific heat and magnetic susceptibility of GaCl$_2$(pyz)$_2$ and found no evidence for long range ordering down to 2 K, the next step is to investigate the magnetic correlation in GaCl$_2$(pyz)$_2$. For such a purpose, a polarized neutron powder diffraction was conducted. A deuterated polycrystalline sample of GaCl$_2$(pyz)$_2$ was prepared by H. Chen from DTU Chemistry and the total sample weight is 7.738 g. The experiment was performed on a diffuse scattering spectrometer D7 [116] at the Institut Laue-Langevin using $\lambda = 4.8707$ Å. The polycrystalline sample was sealed in an

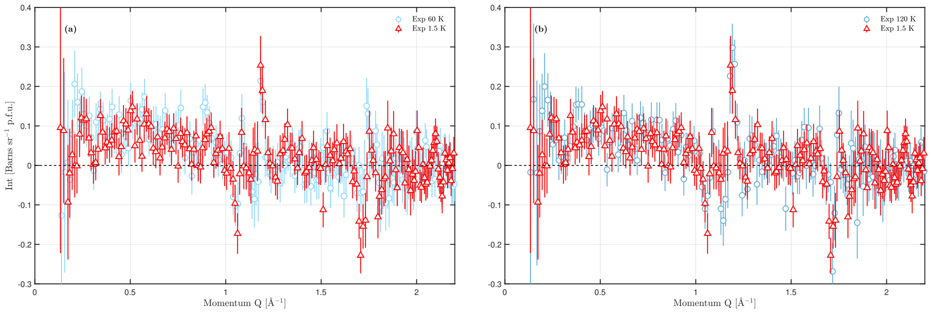

Figure 6.16: Magnetic scattering spectra collected at (a) 1.5 K (red) and 60 K (light blue), (b) 1.5 K (red) and 120 K (light blue).

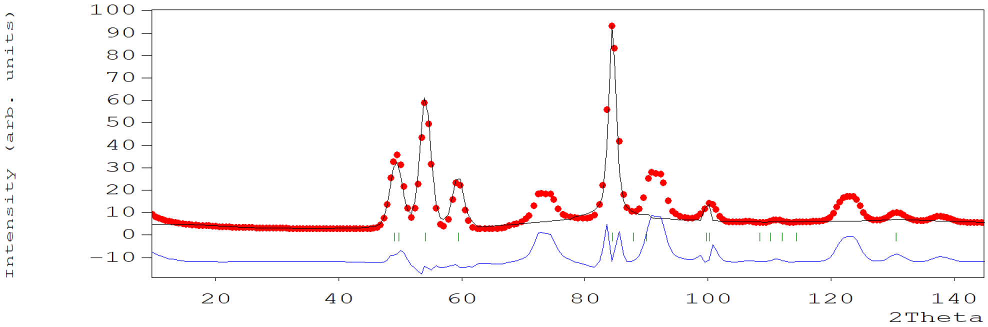

Figure 6.17: The nuclear coherent scattering spectrum of GaCl$_2$(pyz-D$_4$)$_2$ collected at 1.5 K is fitted with the nuclear structure of GaCl$_2$(pyz)$_2$ solved from a X-ray powder diffraction. The black solid line represent the calculated neutron diffraction pattern using the X-ray refined crystal structure of GaCl$_2$(pyz)$_2$ and the green lines indicate the positions of the allowed Bragg reflections.

annular geometry inside an Aluminium can, which is placed inside a Helium-4 cryostat capable of cooling the sample down to 1.5 K. For the experiment, the XYZ polarization analysis was conducted to separate nuclear coherent, spin incoherent, and magnetic contributions to the total differential cross-section. Three sets of data were collected at 1.5 K, 60 K, and 120 K, respectively.

The thermal evolution of the nuclear coherent, spin incoherent, and magnetic scattering spectra of GaCl$_2$(pyz-D$_4$)$_2$ is illustrated in Fig.6.15. As seen from Fig.6.15(a)-(c), the absence of new nuclear Bragg peaks developing in the nuclear coherent channel upon heating indicates that no structural phase transition occurs in GaCl$_2$(pyz-D$_4$)$_2$ between 1.5 K and 120 K, consistent with the specific heat study in which no obvious λ-anomalies were observed below 200 K. In the spin incoherent channel, see Fig.6.15(d)-(f), a sudden decrease of the intensity at momentum transfers $Q \sim 1.2$ Å^{-1} and ~ 1.75 Å^{-1} is evident at all measured temperatures. Comparing the sudden intensity drop Q positions in Fig.6.15(d)-(f) to the locations of the strong nuclear Bragg peaks in Fig.6.15(a)-(c), it is clear these features in the spin incoherent channel are artifacts due to the subtraction procedure of the XYZ polarization analysis, in which an over-subtraction occurs at the Q positions where strong nuclear Bragg peaks are present, see Section 2.4. Apart from the sudden intensity decrease at the strong nuclear Bragg positions, the spin incoherent scattering signals, in general, show very little Q variation. At 1.5 K, the spin incoherent spectrum is almost a constant at ~ 7.05 Barns sr^{-1} p.f.u. (p.f.u.: per formula unit) below $Q \sim 1.5$ Å^{-1}. Above 1.5 Å^{-1} there is a slight decrease in intensity in the collected 1.5 K spectrum. Upon heating, the spin incoherent scattering intensity starts at ~ 7.05 Barns sr^{-1} p.f.u. at the lowest Q as well, but at high Q the intensity has a more rapid decay especially at 120 K where the falling trend is visible. The almost Q-independent behavior of the spin incoherent spectrum at base temperature is consistent with the expectation that theoretically its intensity should be a constant [34]. The rapid falling trend at high Q can be attributed to the Debye-Waller factor due to the unsettled motions of atoms inside a crystal, which takes an exponential decay form in the neutron scattering cross-section. Since this decay trend is more prominent at high temperatures [25], it could explain the rapid falloff at high temperatures. In Fig.6.15(g)-(i), we illustrate the magnetic scattering spectra collected at three different temperatures 1.5 K, 60 K, and 120 K. The data presented here are the final averaged results of the magnetic scattering spectra from both spin-flip and non spin-flip channels. It is immediately clear that the magnetic scattering is weak in GaCl$_2$(pyz-D$_4$)$_2$. For all three temperatures, the magnetic scattering signal is close to zero even at low Q. The maximum intensity is around 0.2 Barns sr^{-1} p.f.u. at $Q \sim 0.25$ Å^{-1} in both 60 K and 120 K spectra. Sudden increases and decreases in intensity occur at $Q \sim 1.2$ Å^{-1} and ~ 1.75 Å^{-1} in all spectra. These changes happen at the same Q positions where the subtraction artifacts from the XYZ polarization analysis are present. Thus we do not consider that these features correspond to any sharp features in the magnetic scattering spectrum of GaCl$_2$(pyz-D$_4$)$_2$. A systematic negative intensity in the magnetic spectra above 2.2 Å^{-1} is present across all three temperatures. This is likely due to a failure of the subtraction method of the XYZ polarization analysis. As such a negative intensity only happens at high Q, it does not impair the analysis of magnetic scattering which is most relevant at low Q [25]. From the data presented in Fig.6.15(g)-(i), even though the scattering intensity in magnetic channel is non-zero at 1.5 K, which indicates the existence of finite spin-spin correlation in GaCl$_2$(pyz-D$_4$)$_2$, it is not feasible to observe any fine structure in the 1.5 K magnetic scattering spectrum besides an overall intensity decay trend. In Fig.6.16(a) and (b), we present a detailed view of the magnetic scattering spectrum at 1.5 K and compare it to the magnetic scattering at 60 K and 120 K, respectively. At low Q, i.e. $Q < 0.8$ Å^{-1}, the scattering intensity at 1.5 K is only slightly lower than the intensities at 60 K and 120 K. No significant temperature dependent intensity variation of the magnetic scattering is observed as the temperature increases. The difference between either 1.5 K and 60 K, or 1.5 K and 120 K is within the intensity error bars. It is evident that the magnetic scattering spectra at three different temperatures display a similar trend at high Q. At above 1 Å^{-1}, the magnetic scattering intensities approach zero in a nearly identical way

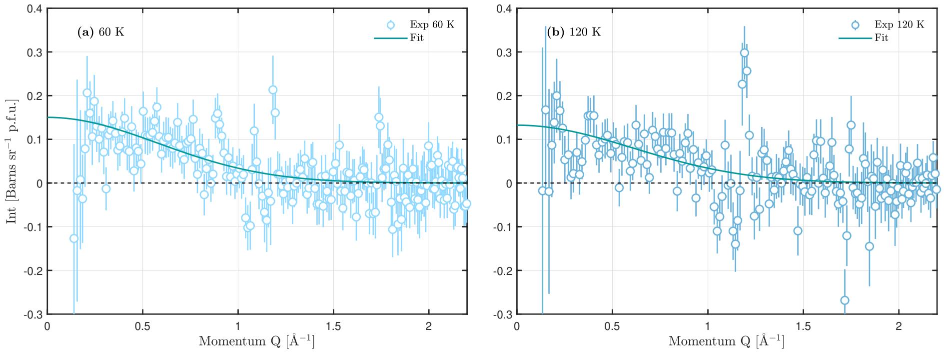

Figure 6.18: Fitted magnetic scattering spectra using Eq.(6.5) for (a) 60 K and (b) 120 K.

for all three temperatures. Given at temperatures above 50 K the magnetic susceptibility of GaCl$_2$(pyz)$_2$ closely follows the Curie-Weiss law, see Fig.6.11, it is reasonable that the observed decay of the magnetic scattering at 60 K and 120 K closely resembles the magnetic scattering from a paramagnetic ion whose intensity is proportional to the magnetic form factor square of the ion [25]. For GaCl$_2$(pyz-D$_4$)$_2$, the ”paramagnetic ion” is a pyz ring with an additional electron.

As the first step of the data analysis, we fitted the nuclear coherent diffraction pattern at 1.5 K using FullProf [117] using the nuclear crystal structure solved by a powder X-ray diffraction for GaCl$_2$(pyz)$_2$. The result is presented in Fig.6.17. It is immediately evident that the prominent Bragg peaks at $2\theta \sim 75°$ (1.57 Å^{-1}), $\sim 90°$ (1.82 Å^{-1}) and $\sim 122°$ (2.26 Å^{-1}) can not be assigned to any allowed nuclear Bragg peaks in GaCl$_2$(pyz-D$_4$)$_2$, indicated by the green lines in Fig.6.17. This is quite surprising as no such pronounced extra structural Bragg peaks were observed in the X-ray diffraction pattern, see Fig.6.10(c). In the spectrum, there exist two small structural peaks at around $Q \sim 1.5$ Å^{-1} which are also forbidden by the Immm space ground (compared with the theoretical X-ray diffraction pattern shown below, calculated from Vesta [111]). Their positions coincide with the extra pronounced peak (at 1.5 Å^{-1}) observed in the nuclear coherent channel but in contrast, the intensities are orders of magnitude smaller compared to the structural Bragg peaks of GaCl$_2$(pyz-D$_4$)$_2$ in the X-ray scattering pattern and are almost negligible. We do not yet understand the origin of these extra nuclear Bragg peaks and this will require further investigations in the future. The refined amplitude Amp from FullProf is 0.24 [per formula unit] which is close to the theoretical value 0.2538 [per formula unit] calculated from Eq.(6.3) [118].

$$\text{Amp} = \frac{45\lambda^3}{2\pi^2 N_{\text{spins}} V} \tag{6.3}$$

where λ is the neutron wavelength at D7, V is the volume of the unit cell of GaCl$_2$(pyz-D$_4$)$_2$, N_{spins} is the number of spins in a unit cell and for GaCl$_2$(pyz-D$_4$)$_2$ it is 2 as there

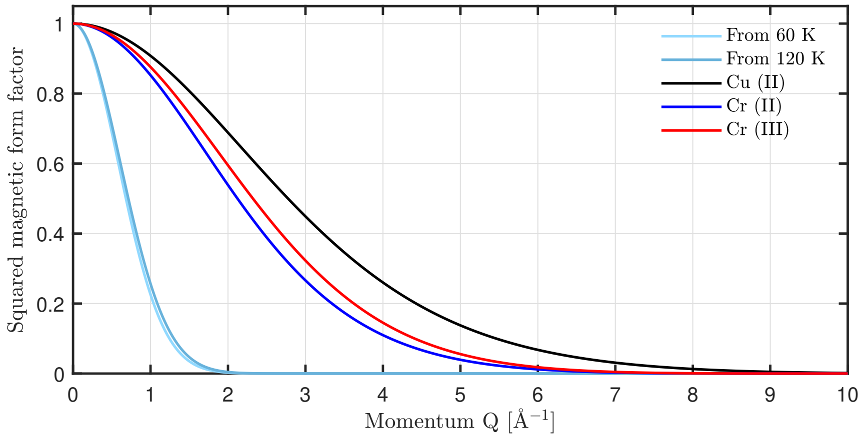

Figure 6.19: Squared effective magnetic form factors of a pyz ring with an extra electron extracted from 60 K (light blue), 120 K (blue). For comparison, we also show the squared magnetic form factor of Cu (II) (black), Cr (II) (blue), and Cr (III) (red) ions.

are two unit formulas per one unit cell. The proximity of the refined and the theoretical amplitude values indicates that, even if previously described extra nuclear peaks came from impurities, the sample quality of GaCl$_2$(pyz-D$_4$)$_2$ was not severely affected.

As previously discussed, the starting value of the spin incoherent scattering in Fig.6.15(d)-(f) is around 7 Barns sr^{-1} p.f.u., for all three temperatures. However the expected spin incoherent scattering value for GaCl$_2$(pyz-D$_4$)$_2$ is 2.3211 Barns sr^{-1} p.f.u., which can be obtained via Eq.(6.4) [25, 28].

$$\frac{d\sigma_{\text{SI}}}{d\Omega} = \frac{n_{\text{Ga}} b^2_{\text{Inc(Ga)}} + n_{\text{Cl}} b^2_{\text{Inc(Cl)}} + n_{\text{C}} b^2_{\text{Inc(C)}} + n_{\text{D}} b^2_{\text{Inc(D)}} + n_{\text{N}} b^2_{\text{Inc(N)}}}{n_{\text{Ga}} + n_{\text{Cl}} + n_{\text{C}} + n_{\text{D}} + n_{\text{N}}} \tag{6.4}$$

where n_{X} (X: Ga, Cl, C, N D) is the number of atom X in a unit formula and $b_{\text{Inc(X)}}$ is the corresponding bound incoherent scattering length for X. It is not clear yet where such a significant difference may come from. Together with the observation that extra structural Bragg peaks are much more pronounced in the neutron diffraction spectra compared to the X-ray diffraction spectrum, see Fig.6.15(a)-(c) and Fig.6.10(c), this indicates there may exist excess H in the sample, which are nearly invisible to X-ray but not to neutron and substantially increase the spin incoherent scattering intensity. However, it is still not clear what kind of structures these excessive H are formed that give rise to the prominent additional Bragg peaks observed in the nuclear coherent scattering channel.

As previously explained, the decaying trend in the magnetic scattering spectra collected at 60 K and 120 K is related to the squared magnetic form factor of the pyz ring with one extra electron. To model such the data, a single exponential decay function, as illustrated in Eq.(6.5), is fitted to the magnetic scattering data collected at 60 K and 120

	$S(S+1)$
60 K	0.7709 ± 0.099
120 K	0.6791 ± 0.097

Table 6.3: Obtained total spin moment from Eq.(6.7) for 60 K and 120 K.

K. The fitted results are summarized in Fig.6.18.

$$\frac{d\sigma_M}{d\Omega} = \left(Ae^{-aQ^2}\right)^2 \tag{6.5}$$

In theory, the differential scattering cross-section of neutrons scattered from non-interacting paramagnetic ions in a polycrystalline form can be written as [25, 28]

$$\frac{d\sigma_M}{d\Omega} = \frac{2}{3}p^2g^2f^2(Q)S(S+1) = 0.0485 \times g^2f^2(Q)S(S+1) \tag{6.6}$$

where $p = 0.2696 \times 10^{-12}$ cm, g is the g-factor, $f(Q)$ is the magnetic form factor of the ion in question and S is the spin value of the ion. Combining Eq.(6.6) with Eq.(6.5), at $Q = 0$, the following equality holds

$$A^2 = 0.0485 \times g^2S(S+1) \Rightarrow S(S+1) = \frac{A^2}{0.0485 \times g^2}. \tag{6.7}$$

Hence from Eq.(6.7), we can directly deduce the total spin angular momentum $S(S+1)$ per unit formula for GaCl$_2$(pyz-D$_4$)$_2$ given the g-factor of GaCl$_2$(pyz)$_2$ is 2.0048. In Table 6.3, we listed the extracted values of $S(S+1)$ from Eq.(6.7) for 60 K and 120 K, respectively. As seen in the table, the values obtained agree well with a $S = 1/2$ situation in which $S(S+1) = 0.75$. From the fits to Eq.(6.5), we can obtain the squared effective magnetic form factor of a pyz ring with an additional electron. The results are shown in Fig.6.19 for both 60 K and 120 K. In addition, we further illustrate in Fig.6.19 the squared magnetic form factors of a common $S = 1/2$ ion Cu (II), a $S = 2$ ion Cr (II) and a $S = 3/2$ ion Cr (III) [119]. It is obvious that, compared to Cu (II), Cr (II), and Cr (III), the squared magnetic form factor of the pyz ring with an extra electron decays much faster. At $Q = 2$ Å^{-1}, there is an only around 30%-45% reduction in intensity for Cu (II), Cr (II) and Cr (III) whereas for the pyz ring the intensity has essentially vanished. Such a rapid reduction in intensity for the pyz ring is consistent with the fact that a single electron is more delocalized in a pyz ring compared to residing in $3d$-orbitals.

As a final remark, it would be interesting to test whether the Heisenberg $S = 1/2$ antiferromagnetic chain model with an intrachain coupling strength $J = 1.06$ meV is sufficient to describe the magnetic scattering spectrum presented in Fig.6.15(g). This will be left for future study.

6.3 Ligand non-innocent ferrimagnet CrCl$_2$(pyz)$_2$

The crystal structure of CrCl$_2$(pyz)$_2$ is similar to GaCl$_2$(pyz)$_2$. As shown in Fig.6.20, CrCl$_2$(pyz)$_2$ crystallises in a layered structure in the orthorhombic Immm space group

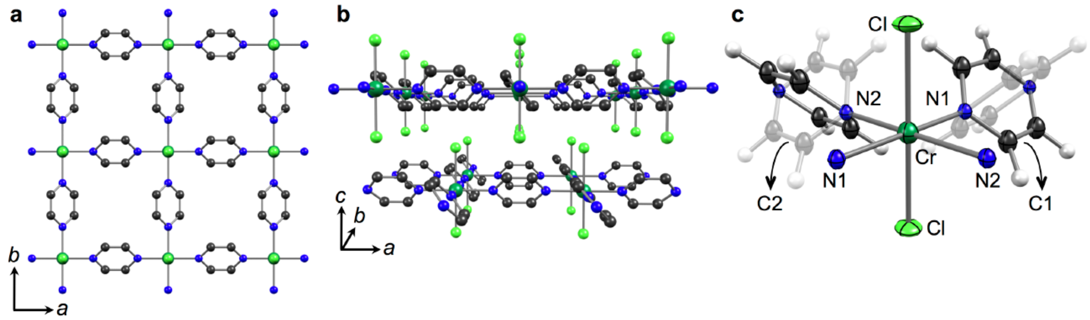

Figure 6.20: Crystal structure of CrCl$_2$(pyz)$_2$. (a) Fragment of the layered structure perpendicular to the crystallographic **c** axis. (b) View of the staggered stacking of the layers along to the crystallographic **c** axis. (c) A CrCl$_2$(pyz)$_4$ octahedon showing the two possible orientations of the pyz rings. Cr dark green, Cl light green, Cl blue, N dark grey. H is emitted for clarity. The figures are taken from Ref [104].

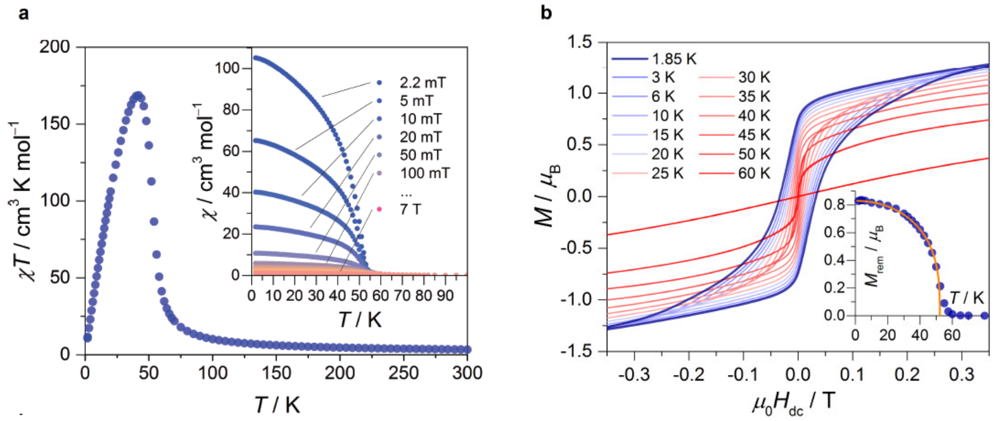

Figure 6.21: (a) Temperature dependence of the χT product for CrCl$_2$(pyz)$_2$. Inset: A selection of $\chi(T)$ measurements at different magnetic fields. (b) Field dependence of the magnetization for CrCl$_2$(pyz)$_2$ at various temperatures. Inset: Temperature dependence of the remnant magnetization for CrCl$_2$(pyz)$_2$. The solid line is a simulation result. For details see Ref [104]. The figures are taken from Ref [104].

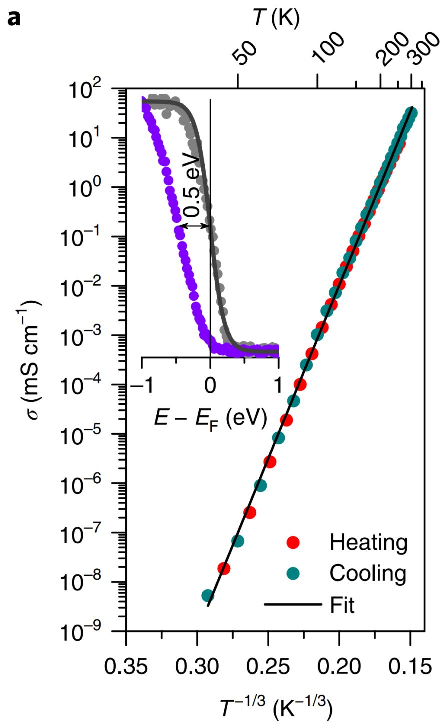

Figure 6.22: Temperature dependence of the two-contact conductivity of $CrCl_2(pyz)_2$. The solid line is the best fit to the 2D Mott law, for details see in Ref [104]. Inset: Fermi edge region of the UV photoelectron spectrum of $CrCl_2(pyz)_2$ (purple) and the metallic reference Mo (grey). The figure is taken from Ref [104].

(No. 71) with lattice constants $a = 6.90351(4)$ Å, $b = 6.97713(4)$ Å and $c = 10.82548(6)$ Å [104]. Within each layer, Cr ions sit in an octahedral environment in which the pyz ligands are disordered among two possible positions imposed by the symmetry of Immm space group, see Fig.6.20. A previous X-ray absorption spectroscopy (XAS) study [104] (Fig.6.1) found the oxidation state of Cr in $\mathrm{CrCl_2(pyz)_2}$ is +3 instead of +2 as one might expect from the chemical formula. This indicates the non-innocent role of the pyz ligands who "kidnap" one electron from the e_g manifold of Cr (II) ion per formula unit. The electron is transferred to one of the unoccupied orbitals of the two pyz rings or even both of them during the synthesis.

The striking feature of this material is that $\mathrm{CrCl_2(pyz)_2}$ not only exhibits long range magnetic ordering but also is electrically conductive at room temperature. Previous magnetic susceptibility measurements [104] suggest that, upon cooling long range magnetic ordering takes place at 55 K based on a sudden increase of the measured susceptibility, see Fig.6.21 [104]. However, the high temperature region of the susceptibility is poorly described by the Curie-Weiss law. Even when extending the measured temperature to 400 K, a clear linear behavior of χ^{-1} vs T is still absent [104, 108]. A hysteretic behavior is observed in the field dependence of the magnetization of $\mathrm{CrCl_2(pyz)_2}$ and the remnant magnetization persists until 55 K [104], supporting the assignment of a magnetic ordering transition at 55 K. The saturation magnetization of $\mathrm{CrCl_2(pyz)_2}$ at 7 T and 1.85 K amounts to $1.8\ \mu_B$ [104], which is significantly lower than the expected value $\sim 3\ \mu_B$ for a Cr (III) ion, but is close to the value $\sim 2\ \mu_B$ expected for antiferromagnetically coupled Cr (III) - pyz spins. The above results unambiguously indicate $\mathrm{CrCl_2(pyz)_2}$ is a ferrimagnet below 55 K where in the 2D square lattice plane the spins on the Cr (III) ions are antiferromagnetically coupled to the spins on the pyz ligands and such a coupling is strong enough to affect the high temperature behavior of susceptibility. The temperature dependence of the electrical conductivity σ of $\mathrm{CrCl_2(pyz)_2}$ [104] is illustrated in Fig.6.22. The room-temperature conductivity of $\mathrm{CrCl_2(pyz)_2}$ is $\sigma_{\mathrm{RT}} = 32$ mS cm^{-1}, which places $\mathrm{CrCl_2(pyz)_2}$ among one of the conducting coordination solids reported so far [105, 106]. It is not clear yet whether $\mathrm{CrCl_2(pyz)_2}$ is semiconducting, metallic, or even half-metallic (predicted by DFT calculations, see Ref [120, 121]).

6.3.1 Experimental details

To study the thermal evolution of the spin excitations in $\mathrm{CrCl_2(pyz)_2}$ below and above the transition temperature 55 K, an inelastic neutron scattering experiment was performed on a time-of-flight spectrometer LET at the ISIS Neutron and Muon Source. A polycrystalline deuterated sample of $\mathrm{CrCl_2(pyz)_2}$ was prepared by L. Voigt from DTU chemistry. The total sample weight was around 3 grams. The LET spectrometer was operated using the repetition rate multiplication technique [38] with the incident neutron energy set to 2 meV and the choppers spinning at 240 Hz. This allows simultaneous collection spectra with different momentum and energy transfers at $E_i = 3.6$ meV, 6.4 meV and 17.4 meV. The sample was mounted in an annular geometry inside a Aluminium can and connected to the cold finger of a continuous cycle refrigerator capable of cooling the sample down to 2 K. Data at five different temperatures were collected, i.e. 2 K,

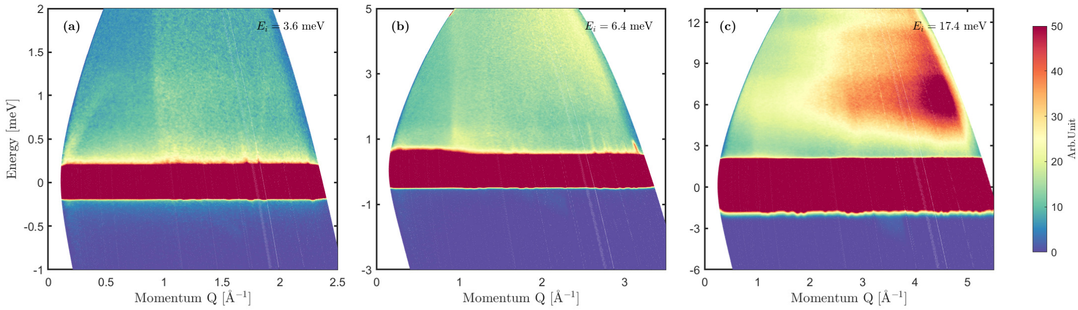

Figure 6.23: Spin and lattice vibration excitations in CrCl$_2$(pyz-D$_4$)$_2$ collected at 2 K using E_i: (a) 3.6 meV, (b) 6.4 meV and (c) 17.4 meV.

15 K, 30 K, 45 K, and 60 K, for investigating the temperature dependence of the spin excitations in CrCl$_2$(pyz-D$_4$)$_2$. For investigation of the high energy spin excitations in CrCl$_2$(pyz-D$_4$)$_2$, we performed an inelastic neutron scattering on a time-of-flight spectrometer MAPS at the ISIS Neutron and Muon Source. The neutron incident energy was set to 400 meV and 800 meV with the choppers spinning at 600 Hz. The same sample used for the LET experiment was again sealed in an Aluminium can and mounted in an annular geometry. Only two temperatures were measured during the experiment, one is 3.5 K and the other is 300 K. The MANTID software package was used to process the raw neutron data [89, 90] which were subsequently analyzed using the MATLAB programs MSlice.

6.3.2 Results and analysis

The spectra collected at 2 K using three different E_i's: 3.6 meV, 6.4 meV and 17.4 meV are summarized in Fig.6.23(a)-(c). It is immediately evident that there is an intense scattering feature located at high Q in the $E_i = 17.4$ meV spectrum extending from 3 meV to 12 meV. Noticing that its intensity increases significantly as Q becomes larger, we can attribute such an intense scattering feature to the lattice vibrations in CrCl$_2$(pyz-D$_4$)$_2$. Apart from the high Q phonon scattering, a nearly vertical (in the low E_i data we see it curving) scattering feature close to $Q = 1$ Å^{-1} extends from 0.25 meV to around 6 meV is observed in all three spectra. This feature is likely associated with the scattering from acoustic phonon branches in CrCl$_2$(pyz)$_2$.

Recalling that magnetic scattering is most prominent in the low Q part of a spectrum [25, 28], this is where we expect to see spin excitations in a ferrimagnet. However in our collected data at different E_i's, the low Q region of the spectra is relatively clean showing no traces of any pronounced magnetic scattering signals (compared to the spin excitation spectrum of CrI$_2$(pyz-D$_4$)$_2$, see Fig.6.4). Upon a further inspection, a weak scattering feature is spotted in the $E_i = 3.6$ meV spectrum at momentum transfers below $Q = 0.5$ Å^{-1} and energy transfers below $E = 1$ meV. This weak scattering signal originates from the position close to $Q = 0$ Å^{-1} and $E = 0$ meV and its excitation energy increases

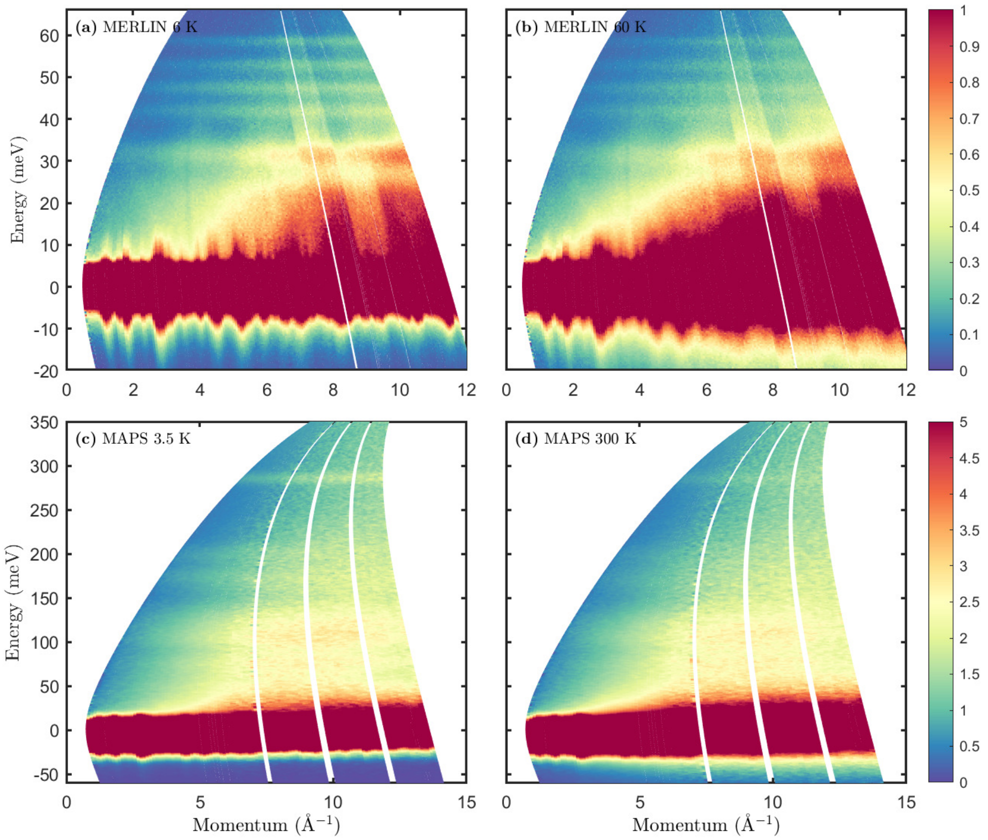

Figure 6.24: Lattice excitations in CrCl$_2$(pyz-D$_4$)$_2$ collected at (a) 4 K, (b) 60 K, (c) 3.5 K, and (d) 300 K. Spectra shown in (a) and (b) are from the MERLIN spectrometer using neutrons with $E_i = 78$ meV. (c) and (d) are from the MAPS spectrometer using neutrons with $E_i = 400$ meV.

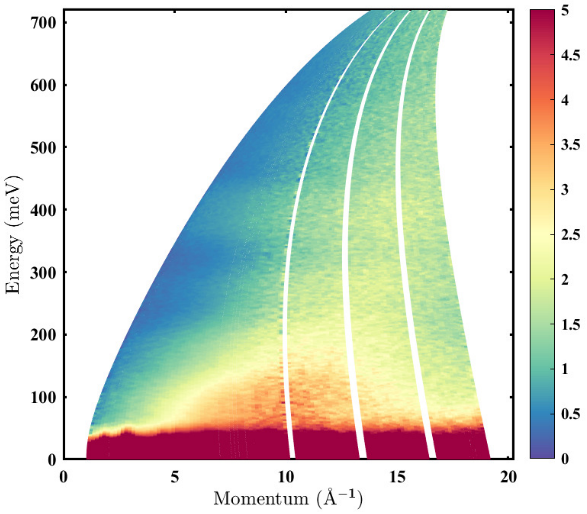

Figure 6.25: Lattice excitations in $CrCl_2(pyz\text{-}D_4)_2$ collected at 3.5 K on MAPS using $E_i = 800$ meV.

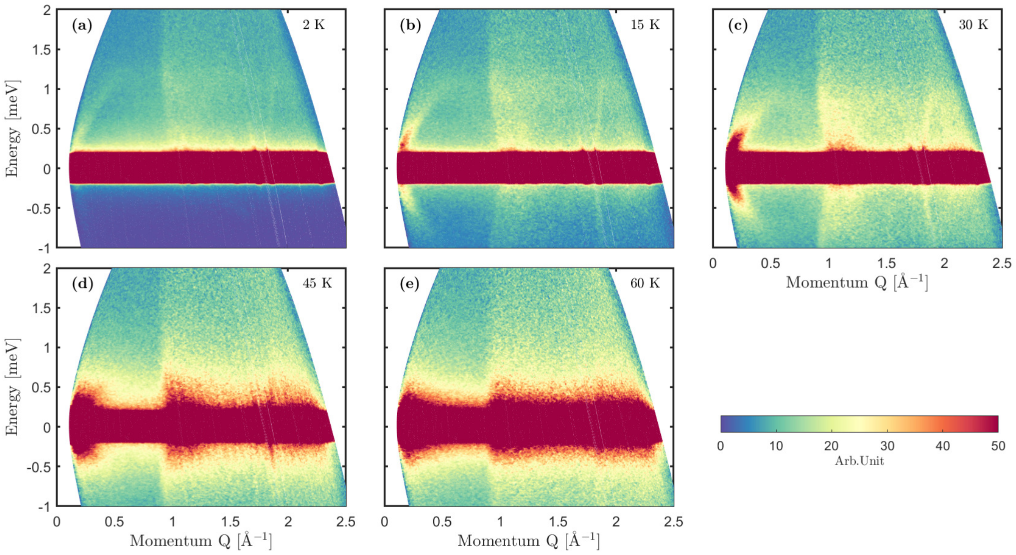

Figure 6.26: Thermal evolution of the spin and lattice vibration excitations in $CrCl_2(pyz\text{-}D_4)_2$ collected at (a) 2 K, (b) 15 K, (c) 30 K, (d) 45 K and (e) 60 K using $E_i = 3.6$ meV.

monotonically as the momentum transfer moves away from $Q = 0$ Å^{-1}. Intensity-wise, the weak scattering feature decreases monotonically with increasing momentum transfer. At around $Q \sim 0.5$ Å^{-1} and $E \sim 1$ meV, it is no longer discernible and completely vanished from the $E_i = 3.6$ meV spectrum. The observed intensity decrease with Q is consistent with the behavior expected from the squared magnetic form factor variation of the magnetic cross-section [25, 28]. Summarizing, the only spin excitations observed in the spectra at $E_i = 3.6$ meV, 6.4 meV and 17.4 meV are the weak scattering feature below $E \sim 1$ meV and $Q \sim 0.5$ Å^{-1}.

In Fig.6.24 and Fig.6.25, we illustrate the spectra collected with higher E_i's on MAPS and MERLIN. The MERLIN experiment was performed by the MERLIN beamline scientist H. Walker before the start of this Ph.D. project. Spectra at two temperatures, 6 K and 60 K, were collected and the neutron incident energy was set to 78 meV. The sample used for the MERLIN experiment is the same sample for the later LET and MAPS experiments. It is evident that the scattering from the lattice vibrations in $CrCl_2(pyz\text{-}D_4)_2$ dominates the MERLIN spectra, as seen in Fig.6.24(a) and (b). These phonon excitations are most prominent at the high Q part of the spectra and their intensities increase with the increase of temperature from 6 K to 60 K. The nearly equal-distant flat modes from 40 meV to 60 meV observed in Fig.6.24(a) and (b) belong to the optical phonon branches of $CrCl_2(pyz\text{-}D_4)_2$ and may closely resemble the quantum harmonic oscillator scenario explained in Ref [122]. In their study, the equal-distant modes observed in UN are attributed to the vibrations of a N ion which situates inside an octahedral U cage. It is not clear yet where the equal-distant optical phonon modes come from in $CrCl_2(pyz\text{-}D_4)_2$. One possible explanation is that these are the vibrations of the Cr ion inside a $Cr(pyz\text{-}D_4)_4Cl_2$ octahedron due to the rigidity of rather large molecular pyz rings. At the low Q part of the MERLIN spectra, the only visible excitations are those acoustic phonon branches locating at around 1 Å^{-1}, 1.7 Å^{-1} and 3 Å^{-1}, and the optical phonon modes extending from 10 meV to around 30 meV. Apart from that, no spin excitations are observed up to 65 meV in $CrCl_2(pyz\text{-}D_4)_2$.

In Ref [104], K. Pedersen *et al* performed a DFT calculation to determine the antiferromagnetic exchange coupling strength J between Cr and pyz. They found the coupling strength is extremely large and estimated around $J \sim 505$ meV [104]. If there exists a strong coupling between Cr and pyz in $CrCl_2(pyz\text{-}D_4)_2$, the spin excitations associated with such a coupling in principle should be observable in the MAPS data due to the large incident neutron energies (400 meV and 800 meV) applied during the experiment. However, as shown in Fig.6.24(c) and (d), again scattering from the lattice vibrations of $CrCl_2(pyz\text{-}D_4)_2$ dominate the spectra. This is readily seen from the enhanced intensity of these scattering features as the temperature increases from 3.5 K to 300 K. The flat mode at around 300 meV likely belongs to one of the vibrational modes of pyz ring. Apart from that, there is no clear evidence of the existence of spin excitations in the spectra. In Fig.6.25, we show the spectrum collected at 3.5 K using $E_i = 800$ meV on MAPS. Similar to the $E_i = 400$ meV data, the spectrum is dominated by phonon scatterings. At low Q where we expect to see any spin excitations if they exist, the spectrum

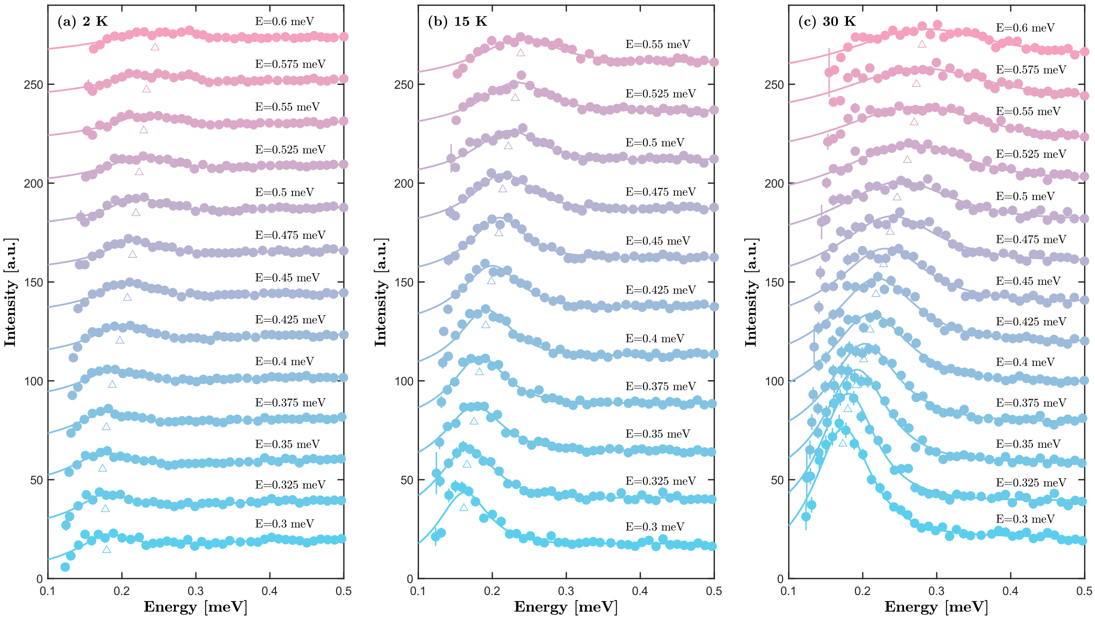

Figure 6.27: Fitted constant energy cuts taken from the $E_i = 3.6$ meV spectra collected at (a) 2 K, (b) 15 K and (c) 30 K for energy transfers below 0.6 meV using Eq.(6.8). The triangular markers indicate the fitted peak positions.

is fairly clean. The stripy feature at around 400 meV likely resembles some vibrational modes of pyz ring. It is thus impossible to spot any spin excitations in the $E_i = 800$ meV spectrum. Summarizing, the spin excitations of CrCl$_2$(pyz-D$_4$)$_2$ are absent in the MAPS data up to 720 meV. One possible explanation for such an absence is that the squared magnetic form factor of pyz vanishes at $Q = 2$ Å^{-1}, see Fig.6.19. Even though the squared magnetic form factor of Cr (III) is still finite at $Q = 5$ Å^{-1} ($\sim 85\%$ intensity reduction compared to $Q = 0$ Å^{-1}), the intensity of the spin excitations associated with the antiferromagnetically coupled Cr (III) and pyz spins is significantly suppressed to approach zero at $Q > 2$ Å^{-1} due to the pyz. As the result, this leads to the vanish of spin excitations in the MAPS spectra.

In Fig.6.26, we illustrate the thermal evolution of the previously identified weak spin excitations below and above the ordering temperature 55 K. It is obvious from Fig.6.26(b) and (c), that upon heating, the spin excitations in CrCl$_2$(pyz-D$_4$)$_2$ gain intensity and become more pronounced in the collected spectra at 15 K and 30 K compared to 2 K. This is a manifestation of the Bose factor in the neutron magnetic scattering cross-section [25, 28] whose value is enhanced as the temperature increases. Because the spin excitations lie below 1 meV such an enhancement becomes easily visible at 15 K and 30 K, when the generalized susceptibility is not significantly altered compared to 2 K. As the temperature approaches the transition temperature 55 K, the damping of the spin excitations is more severe and their width in Q increases substantially. Together with the noticeable softening of the excitation energy with increasing temperature, the spin excitations eventually disappear when crossing the ordering temperature 55 K. At 60 K, no more spin excitations are discernible at low Q, and the spectrum is left with a quasi-elastic scattering signal only, which is centered at zero energy transfer.

To extract the peak positions in Q of the spin excitations at different temperatures, lineshapes described by Eq.(6.8) were fitted to constant energy cuts taken below the energy transfer $E = 0.6$ meV.

$$y(Q) = \frac{\text{Amp}}{\pi\gamma} \frac{\gamma^2}{(Q - Q_0)^2 + \gamma^2} + AQ + BQ^2 \tag{6.8}$$

where the first term in the summation is a Lorentzian lineshape characterized by the amplitude Amp, the center of the peak Q_0 and the half width half maximum (HWHM) γ. The term $AQ + BQ^2$ is an effective background model with two free parameters A and B. As the spin excitations are strongly damped and broadened at 45 K, we only extracted the thermal evolution of the peak positions of the spin excitations up to 30 K. The fitted spectra are presented in Fig.6.27 for the constant energy cuts taken at $T = 2$ K, 15 K and 30 K, respectively.

In Fig.6.28 and Fig.6.29, we present the E-dependent fitted peak positions and peak widths in Q of the spin excitations at 2 K, 15 K, and 30 K, labeled by the blue circles, yellow squares, and red triangles, respectively. Compared to the color plots in Fig.6.26, it is more evident that a softening of the spin excitations occurs as the temperature increases. At 30 K, there is a significant reduction in the excitation energy especially at $Q = 2.5$ Å^{-1}, at which the spin excitation energy shifts from ~ 0.6 meV at 2 K to ~ 0.5 meV at 30 K. This amounts to ~ 17 % reduction in energy. As seen in Fig.6.29, there is no significant difference in width between the spin excitation at 2 K and 15 K. In fact, their widths are comparable to each other. This indicates the damping is not severe as the temperature increases from 2 K to 15 K. Whereas at 30 K, there is a substantial increase of the width of the spin excitation, especially at $Q > 0.2$ Å^{-1}. This agrees with the color plot shown in Fig.6.26.

To further quantify the dispersion relations of the spin excitations at different temperatures, the following equation is fitted to the extracted peak positions

$$\mathcal{E} = \alpha Q^{\beta} \tag{6.9}$$

where $\mathcal{E}$ is the energy of the spin excitations, Q is the extracted momentum transfers, and α, β are for parameterization of the dispersion. The fitted results are shown in Fig.6.28 and the best fitted parameters are listed in Table 6.4. Both α and β decrease monotonically as the temperature increases. This is consistent with the temperature-softening behavior of the spin excitations in $\text{CrCl}_2(\text{pyz-D}_4)_2$. In addition, the best fitted $\beta = 1.92 \pm 0.071$ at 2 K is close to a ferromagnetic scenario in which the dispersion at small Q limit scales as $\mathcal{E} \sim Q^2$ [23]. Together with the temperature dependence of the spin excitations, the $\mathcal{E} \sim Q^2$ behavior and the saturation moment $1.8\ \mu_B$ at 7 T

	α	β
2 K	9.26 ± 1.03	1.92 ± 0.071
15 K	4.79 ± 0.37	1.50 ± 0.048
30 K	3.48 ± 0.17	1.39 ± 0.032

Table 6.4: Best fitted parameters α and β in Eq.(6.9) at 2 K, 15 K and 30 K.

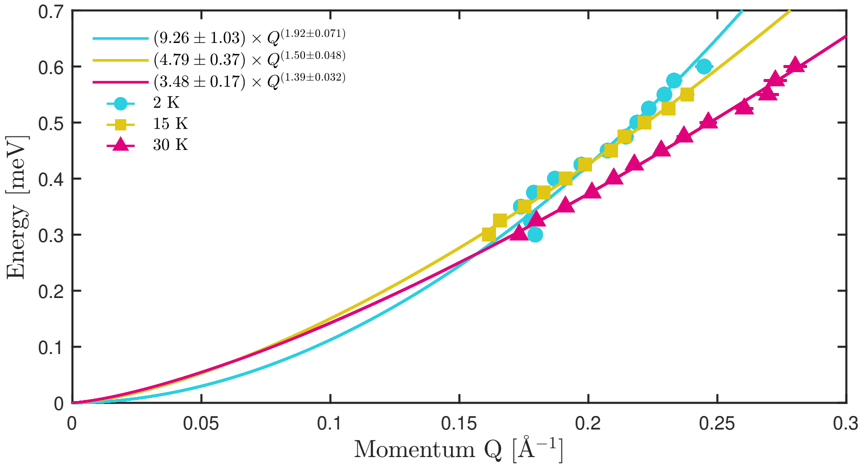

Figure 6.28: Extracted peak positions of the spin excitation using Eq.(6.8) at three temperatures: 2 K (blue), 15 K (yellow) and 30 K (red). Also shown are the best fitted results using Eq.(6.9), see the blue (2 K), yellow (15 K) and red (30 K) solid lines.

(see Fig.6.21) unambiguously support CrCl$_2$(pyz)$_2$ is a ferrimagnet below 55 K whose uncompensated $S = 1$ degree of freedoms at the Cr (III) sites are ferromagnetically coupled, giving rise to a ferromagnetic type spin wave dispersion at low Q region. For a ferromagnet in an ideal square lattice, the theoretical value for α is JSa_0^2 where J is the nearest neighbor exchange interaction, S is the spin value associate with each lattice site and a_0 is the lattice constant of the square lattice [23]. For CrCl$_2$(pyz)$_2$, the square lattice slightly deviates from the ideal case whose two lattice constants $a = 6.90351$ Å and $b = 6.97713$ Å are not equivalent. To estimate J, we take the averaged lattice constant of a and b for a_0. Given $S = 1$, the estimated J is -0.19 ± 0.021 meV, which is significantly lower than the 55 K ordering temperature ($|4JS| \sim 5.97$ K). Clearly, the nearest neighbor ferromagnetic coupling J alone cannot support the observed 55 K ordering temperature. The mechanism behind the ferrimagnetic ordering phenomenon is not fully understood yet which requires future investigations.

As a final remark, in Fig.6.29 we illustrate the constant energy cuts at 2 K and 60 K from the $E_i = 3.6$ meV spectra with $\Delta E = [-0.2, 0.2]$ meV. Such cuts resemble the elastic scattering patterns of CrCl$_2$(pyz-D$_4$)$_2$ below and above the ordering temperature 55 K. It is immediately evident that no obvious differences are discernible between the

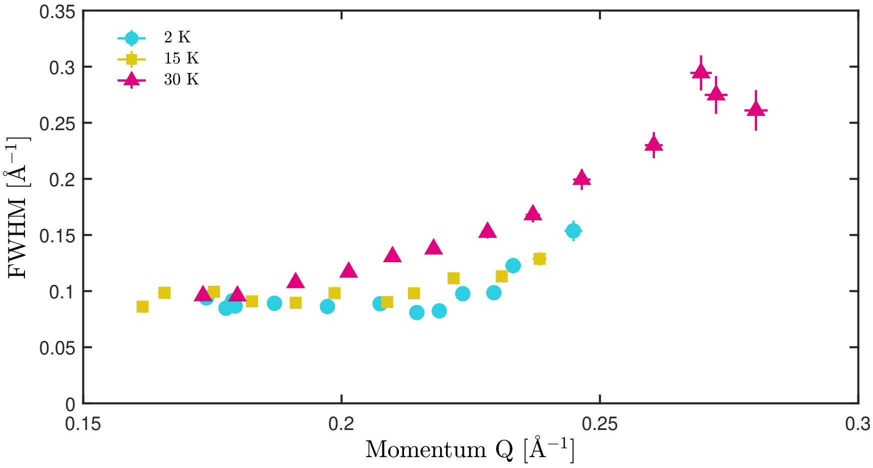

Figure 6.29: Extracted peak FWHMs of the spin excitation using Eq.(6.8) at three temperatures: 2 K (blue), 15 K (yellow) and 30 K (red).

2 K spectrum and 60 K spectrum. Thus the peaks presented in Fig.6.29 belong to the nuclear Bragg peaks of CrCl$_2$(pyz-D$_4$)$_2$. Similar to GaCl$_2$(pyz-D$_4$)$_2$, the two peaks at $Q \sim 1.57$ Å^{-1} and 1.83 Å^{-1} are not allowed by the Immm space group and the origin of these peaks remain a mystery which requires further investigations in the future as well.

6.4 Conclusions

In this chapter, we studied the magnetic properties of three isostructural metal-organic framework compounds: CrI$_2$(pyz)$_2$, GaCl$_2$(pyz)$_2$, and CrCl$_2$(pyz)$_2$. Despite sharing a similar crystal structure, their magnetic properties vary substantially.

CrI$_2$(pyz)$_2$ is a quasi two dimensional $S = 2$ antiferromagnet on a square lattice with a Néel temperature of $T_N \sim 26$ K. Inelastic neutron scattering study shows that the dominant interaction in the system is an in-plane nearest neighbor exchange coupling $J_1 = 0.447(4)$ meV and the exchange interaction J_2 associated with in-plane second nearest neighbor Cr (II) ions is only $\sim 10\%$ of J_1. A spin wave gap ~ 1 meV is observed in the inelastic neutron spectrum using $E_i = 9$ meV (Fig.6.4(a)). This can be explained by including an easy-axis anisotropy D (along the crystallographic **c** direction) in the spin Hamiltonian with $D = -0.063(4)$ meV. The obtained exchange coupling constants J_1 and J_2 are in good accord with the measured Curie-Weiss temperature of CrI$_2$(pyz)$_2$. It is, therefore, safe to conclude that CrI$_2$(pyz)$_2$ is a conventional antiferromagnet on a square lattice.

Magnetism in GaCl$_2$(pyz)$_2$ originates from its non-innocent pyz ligands. For every formula unit of GaCl$_2$(pyz)$_2$, an electron is transferred from Ga to one of the pyz ligands, and it is the transferred electron which localize on a pyz ring that determines the magnetic property of GaCl$_2$(pyz)$_2$. Magnetic susceptibility measurement indicates the mag-

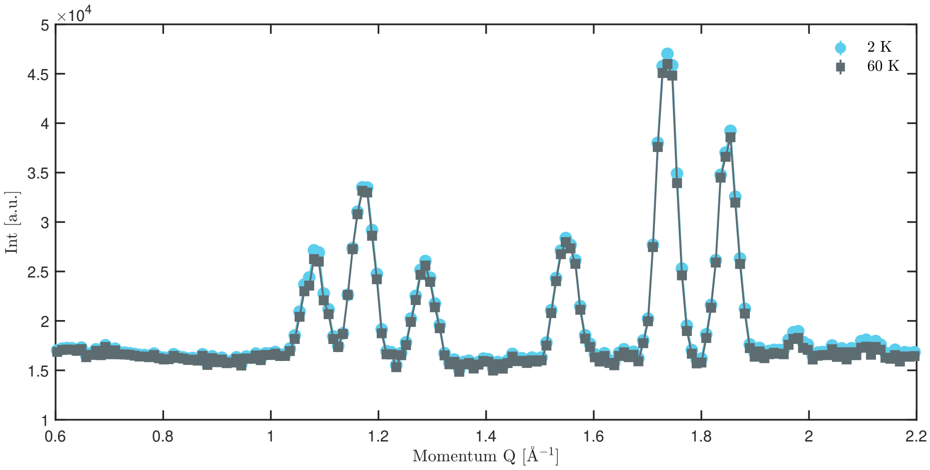

Figure 6.30: Constant energy cuts taken from the $E_i = 3.6$ meV spectra collected at 2 K and 60 K with $\Delta E = [-0.2, 0.2]$ meV.

netism in GaCl$_2$(pyz)$_2$ closely resembles a $S = 1/2$ scenario, which supports the picture of having a localized electron on a pyz ring per formula unit. Specific heat study shows no long range ordering occurs in GaCl$_2$(pyz)$_2$ down to 2 K. To study the spin-spin correlation in GaCl$_2$(pyz)$_2$, a polarized neutron powder diffraction was performed, from which the magnetic contribution to the total cross-section can be obtained (Section 2.4 in Chapter 2). The measured magnetic cross-sections of GaCl$_2$(pyz)$_2$ at 1.5 K, 60 K, and 120 K are very small (but still finite) and nearly indistinguishable (Fig.6.16). The three spectra all show a characteristic feature that the scattering intensity decays with increasing Q. At $Q > 1$ Å^{-1}, it is essentially zero. The scattering spectra at 60 K and 120 K are expected to follow the cross-section of a paramagnetic ion, from which the total spin angular momentum $S(S+1)$ per formula unit for GaCl$_2$(pyz)$_2$ can be extracted. The values (Table 6.3) we found agree well with the $S = 1/2$ situation. In addition, the squared magnetic form factor per formula unit for GaCl$_2$(pyz)$_2$ can also be extracted, see Fig.6.19. Compared to the squared magnetic form factors of $3d$ transition metal ions, such as Cu (II), Cr (II), and Cr (III), it decays more rapidly and becomes essentially zero at $Q > 2$ Å^{-1}. Such a rapid and fast decay is consistent with the picture that an electron residing on a pyz ring. In such a scenario, the wavefuntion of the electron is more delocalized compared to the more localized $3d$ orbitals.

We analyzed the magnetic susceptibility and specific heat of GaCl$_2$(pyz)$_2$ with a strongly theory-oriented approach. The results indicate GaCl$_2$(pyz)$_2$ might be decomposed into weakly coupled $S = 1/2$ antiferromagnetic Heisenberg chains. The field dependence of the specific heat shown in Fig.6.14 shares some similarities with a previous study on the $S = 1/2$ antiferromagnetic Heisenberg chain [115]. Even though it is far from conclusive that GaCl$_2$(pyz)$_2$ resembles the $S = 1/2$ antiferromagnetic Heisenberg chain scenario, it might be worthy to pursue this direction in the future. A more detailed specific heat study is necessary, especially to carefully separate apart magnetic and non-magnetic contributions. It might also be interesting to study the spin excitations in GaCl$_2$(pyz)$_2$ even for a polycrystalline sample. If GaCl$_2$(pyz)$_2$ indeed were a quasi-1D system, the method presented in Ref [123] could be applied and the resultant spectrum would show signatures of spinons [124].

Both CrI$_2$(pyz)$_2$ and GaCl$_2$(pyz)$_2$ are well placed in an insulating limit. In contrast CrCl$_2$(pyz)$_2$ is electrically conductive at room temperature. Similar to GaCl$_2$(pyz)$_2$, the ligands in CrCl$_2$(pyz)$_2$ are non-innocent as well. The two pyz in one formula unit take one electron away from the Cr ion. Such an electron transfer surprisingly leads to antiferromagnetically coupled Cr (III) ($S = 3/2$) and pyz ($S = 1/2$) spins, such that below ~ 55 K the system is ferrimagnetically ordered [104] with an ordered moment $1.8\ \mu_B$. Inelastic neutron scattering shows that the only observed spin excitation locates below 1 meV and its intensity is fairly weak (Fig.6.26), in sharp contrast to CrI$_2$(pyz)$_2$. At low Q, i.e. $Q < 0.3$ Å^{-1}, the energy of the spin excitation increases quadratically in Q at 1.5 K. This signifies the uncompensated $S = 1$ degree of freedom ($3/2 - 1/2 = 1$) at Cr (III) sites are ferromagnetically coupled, which consistent with the ferrimagnetic picture. However, the estimated exchange constant $J = -0.19$ meV is much smaller than the ordering temperature 55 K. Such a discrepancy we do not understand at the current stage. Several DFT calculations [120, 121] have pointed out CrCl$_2$(pyz)$_2$ is likely to be half-metallic. The orbitals from pyz form spin-polarized conduction bands at the Fermi level and it is the electrons from these conduction bands that induce the observed ferrimagnetism. Since the conduction electrons are itinerant and the spins on Cr (III) are localized, it might be meaningful to examine in such a scenario whether Kondo related physics could exist [125] (more precisely, the situation here is more close to an underscreened Kondo lattice model [126]). This will be left for future study.

Bibliography

[1] Martin Mourigal et al. "Fractional spinon excitations in the quantum Heisenberg antiferromagnetic chain". In: *Nature Physics* 9.7 (2013), pp. 435–441.

[2] Kei Yosida. *Theory of magnetism*. Vol. 122. Springer Science & Business Media, 1998.

[3] Robert Eder. "Multiplets in Transition-Metal Ions and Introduction to Multiband Hubbard Models". In: *Quantum Materials: Experiments and Theory* (2016).

[4] Frank De Groot. "Multiplet effects in X-ray spectroscopy". In: *Coordination Chemistry Reviews* 249.1-2 (2005), pp. 31–63.

[5] Sadamichi Maekawa et al. *Physics of transition metal oxides*. Vol. 144. Springer Science & Business Media, 2013.

[6] Adelsindo Liberato de Brito. "FORTRAN program for the integral of three spherical harmonics". In: *Computer Physics Communications* 25.1 (1982), pp. 81–85.

[7] Daniel I Khomskii. *Basic aspects of the quantum theory of solids: order and elementary excitations*. Cambridge University Press, 2010.

[8] Anatole Abragam and Brebis Bleaney. *Electron paramagnetic resonance of transition ions*. OUP Oxford, 2012.

[9] Fang Wen. "Octahedral crystal-field splitting in non-conventional coordinate system". In: *Optik* 203 (2020), p. 163871.

[10] Daniel Khomskii. *Transition metal compounds*. Cambridge University Press, 2014.

[11] M T Hutchings. "Point-charge calculations of energy levels of magnetic ions in crystalline electric fields". In: *Solid state physics*. Vol. 16. Elsevier, 1964, pp. 227–273.

[12] K Stevens. "Matrix elements and operator equivalents connected with the magnetic properties of rare earth ions". In: *Proceedings of the Physical Society. Section A* 65.3 (1952), p. 209.

[13] Douglas John Newman and Betty Ng. *Crystal field handbook*. Cambridge University Press, 2007.

[14] Allen Scheie. "PyCrystalField: software for calculation, analysis and fitting of crystal electric field Hamiltonians". In: *Journal of Applied Crystallography* 54.1 (2021).

[15] Alan Robert Edmonds. *Angular momentum in quantum mechanics*. Princeton university press, 2016.

[16] Christopher Bradley and Arthur Cracknell. *The mathematical theory of symmetry in solids: representation theory for point groups and space groups*. Oxford University Press, 2009.

[17] Jens Jensen and Allan R Mackintosh. *Rare earth magnetism*. Clarendon Press Oxford, 1991.

[18] Erik Koch. "Exchange mechanisms". In: *Correlated electrons: from models to materials* 2 (2012), pp. 1–31.

[19] Alexei Kitaev. “Anyons in an exactly solved model and beyond”. In: *Annals of Physics* 321.1 (2006), pp. 2–111.

[20] G. Jackeli and G. Khaliullin. “Mott Insulators in the Strong Spin-Orbit Coupling Limit: From Heisenberg to a Quantum Compass and Kitaev Models”. In: *Phys. Rev. Lett.* 102 (1 Jan. 2009), p. 017205.

[21] Hidenori Takagi et al. “Concept and realization of Kitaev quantum spin liquids”. In: *Nature Reviews Physics* 1 (Mar. 2019), p. 1.

[22] Michael E Fisher. “Relation between the specific heat and susceptibility of an antiferromagnet”. In: *Philosophical Magazine* 7.82 (1962), pp. 1731–1743.

[23] Steven M Girvin and Kun Yang. *Modern condensed matter physics*. Cambridge University Press, 2019.

[24] S Toth and B Lake. “Linear spin wave theory for single-Q incommensurate magnetic structures”. In: *Journal of Physics: Condensed Matter* 27.16 (2015), p. 166002.

[25] Gordon Leslie Squires. *Introduction to the theory of thermal neutron scattering*. Courier Corporation, 1996.

[26] Stephen W Lovesey. “Theory of neutron scattering from condensed matter. Vol. 1: Nuclear scattering”. In: (1984).

[27] Stephen W Lovesey. “Theory of neutron scattering from condensed matter. Vol. 2: Polarization effects and magnetic scattering”. In: (1984).

[28] Albert Furrer, Joel F Mesot, and Thierry Strässle. *Neutron scattering in condensed matter physics*. Vol. 4. World Scientific Publishing Company, 2009.

[29] Jens Als-Nielsen and Des McMorrow. *Elements of modern X-ray physics*. John Wiley & Sons, 2011.

[30] E Ressouche. “Reminder: Magnetic structures description and determination by neutron diffraction”. In: *École thématique de la Société Française de la Neutronique* 13 (2014), p. 02001.

[31] Andrew T Boothroyd. *Principles of Neutron Scattering from Condensed Matter*. Oxford University Press, 2020.

[32] Daniel L Roach et al. “The interpretation of polycrystalline coherent inelastic neutron scattering from aluminium”. In: *Journal of applied crystallography* 46.6 (2013), pp. 1755–1770.

[33] A Banerjee et al. “Proximate Kitaev quantum spin liquid behaviour in a honeycomb magnet”. In: *Nature materials* 15.7 (2016), pp. 733–740.

[34] J Ross Stewart. “Disordered materials studied using neutron polarization analysis”. In: *Collection de la Société Française de la Neutronique*. Vol. 7. EDP Sciences. 2007, pp. 173–197.

[35] G Ehlers et al. “Generalization of the classical xyz-polarization analysis technique to out-of-plane and inelastic scattering”. In: *The Review of scientific instruments* 84 (Sept. 2013), p. 093901. DOI: 10.1063/1.4819739.

[36] Quantum Design. *Vibrating Sample Magnetometer (VSM) Option User’s Manual*.

[37] Quantum Design. *Physical Property Measurement System Heat Capacity Option User’s Manual*.

[38] F Mezei, M Russina, and S Schorr. “The multiwavelength cold neutron time-of-flight spectrometer project IN500 at LANSCE”. In: *Physica B: Condensed Matter* 276-278 (2000), pp. 128–129.

[39] Ruben Verresen, Frank Pollmann, and Roderich Moessner. “Quantum dynamics of the square-lattice Heisenberg model”. In: *Phys. Rev. B* 98 (15 Oct. 2018), p. 155102.

[40] Efstratios Manousakis. “The spin-½ Heisenberg antiferromagnet on a square lattice and its application to the cuprous oxides”. In: *Rev. Mod. Phys.* 63 (1 Jan. 1991), pp. 1–62.

[41] N. B. Christensen et al. “Quantum dynamics and entanglement of spins on a square lattice”. In: *Proceedings of the National Academy of Sciences* 104.39 (2007), p. 15264.

[42] Bastien Dalla Piazza et al. “Fractional excitations in the square-lattice quantum antiferromagnet”. In: *Nature Physics* 11.1 (2015), p. 62.

[43] M. Powalski, K. P. Schmidt, and G. S. Uhrig. “Mutually attracting spin waves in the square-lattice quantum antiferromagnet”. In: *SciPost Phys.* 4 (1 2018), p. 001.

[44] Hui Shao et al. “Nearly Deconfined Spinon Excitations in the Square-Lattice Spin-$1/2$ Heisenberg Antiferromagnet”. In: *Phys. Rev. X* 7 (Dec. 2017), p. 041072.

[45] H Burger N. Fuess and P. Burlet. “SNeutron diffraction study of the antiferromagnetic phase of copper formate tetradeuterate”. In: *Solid State Comm.* 34 (1980), p. 883.

[46] R. L. Martin and Hanneke Waterman. “269. Magnetic studies with copper(II) salts. Part IV. Remarkable magnetic behaviour of copper(II) formate and its hydrates”. In: *J. Chem. Soc.* (1959), p. 1359.

[47] Kazuo Yamagata and Tooru Sakai. “Magnetization Process of Nearly 2-Dimensional $Cu(HCOO)_2{\cdot}4H_2O$ and $Cu(HCOO)_2{\cdot}2(NH_2)_2CO{\cdot}2H_2O$. I Mechanism of the Field-Induced Transition”. In: *Journal of the Physical Society of Japan* 49.6 (Dec. 1980), p. 2165.

[48] Kazuo Yamagata, Yoshinari Kozuka, and Takashi Morita. “Magnetization Process of Nearly 2-Dimensional $Cu(HCOO)_2{\cdot}4H_2O$ and $Cu(HCOO)_2{\cdot}2(NH_2)_2CO{\cdot}2H_2O$. II Estimation of Magnetic Parameters”. In: *Journal of the Physical Society of Japan* 50.2 (1981), p. 421.

[49] R Coldea et al. “Spin waves and electronic interactions in La_2CuO_4”. In: *Physical review letters* 86.23 (2001), p. 5377.

[50] Ruben Verresen, Roderich Moessner, and Frank Pollmann. “Avoided quasiparticle decay from strong quantum interactions”. In: *Nature Physics* 15 (Aug. 2019).

[51] M. E. Zhitomirsky and A. L. Chernyshev. “Instability of Antiferromagnetic Magnons in Strong Fields”. In: *Phys. Rev. Lett.* 82 (22 May 1999), pp. 4536–4539.

[52] S. M. Hayden et al. “High-energy spin waves in La_2CuO_4”. In: *Phys. Rev. Lett.* 67 (25 Dec. 1991), pp. 3622–3625.

[53] Anders W. Sandvik. “Stochastic method for analytic continuation of quantum Monte Carlo data”. In: *Phys. Rev. B* 57 (17 May 1998), pp. 10287–10290.

[54] Olav F. Syljuåsen. “Using the average spectrum method to extract dynamics from quantum Monte Carlo simulations”. In: *Phys. Rev. B* 78 (17 Nov. 2008), p. 174429.

[55] Anders W. Sandvik. “Computational Studies of Quantum Spin Systems”. In: *AIP Conference Proceedings* 1297.1 (2010), pp. 135–338.

[56] Peter Hasenfratz and Ferenc Niedermayer. “The exact correlation length of the antiferromagnetic d= 2+ 1 Heisenberg model at low temperatures”. In: *Physics Letters B* 268.2 (1991), pp. 231–235.

[57] Jae-Kwon Kim and Matthias Troyer. “Low Temperature Behavior and Crossovers of the Square Lattice Quantum Heisenberg Antiferromagnet”. In: *Phys. Rev. Lett.* 80 (12 Mar. 1998), pp. 2705–2708.

[58] H. M. Rønnow, D. F. McMorrow, and A. Harrison. “High-Temperature Magnetic Correlations in the 2D $S = 1/2$ Antiferromagnet Copper Formate Tetradeuterate”. In: *Phys. Rev. Lett.* 82 (15 Apr. 1999), pp. 3152–3155.

[59] Martin Mourigal. *Effect of Magnetic Field on Dynamics of Antiferromagnets*. Master thesis, École Polytechnique Fédérale de Lausanne, 2008.

[60] M. Mourigal, M. E. Zhitomirsky, and A. L. Chernyshev. “Field-induced decay dynamics in square-lattice antiferromagnets”. In: *Phys. Rev. B* 82 (14 Oct. 2010), p. 144402.

[61] Olav F. Syljuåsen. “Numerical evidence for unstable magnons at high fields in the Heisenberg antiferromagnet on the square lattice”. In: *Phys. Rev. B* 78 (18 Nov. 2008), p. 180413.

[62] Andreas Lüscher and Andreas M. Läuchli. “Exact diagonalization study of the antiferromagnetic spin-$\frac{1}{2}$ Heisenberg model on the square lattice in a magnetic field”. In: *Phys. Rev. B* 79 (19 May 2009), p. 195102.

[63] W. T. Fuhrman et al. “Dynamical structure factor of quasi-two-dimensional antiferromagnet in high fields”. In: *Phys. Rev. B* 85 (18 May 2012), p. 184405.

[64] M. E. Zhitomirsky and A. L. Chernyshev. “Colloquium: Spontaneous magnon decays”. In: *Rev. Mod. Phys.* 85 (1 Jan. 2013), pp. 219–242.

[65] T. Masuda et al. “Instability of magnons in two-dimensional antiferromagnets at high magnetic fields”. In: *Phys. Rev. B* 81 (10 Mar. 2010), p. 100402.

[66] Philip R. Hammar et al. “Magnetic studies of the two-dimensional, S=1/2 Heisenberg antiferromagnets (5CAP)$_2$CuCl$_4$ and (5MAP)$_2$CuCl$_4$”. In: *Journal of Applied Physics* 81.8 (1997), pp. 4615–4617.

[67] F. C. Coomer et al. “Neutron diffraction studies of nuclear and magnetic structures in the $S = 1/2$ square Heisenberg antiferromagnets $(\mathrm{d}_6{-}5\mathrm{CAP})_2\mathrm{Cu}X_4$ ($X =$ Br and Cl)”. In: *Phys. Rev. B* 75 (9 Mar. 2007), p. 094424.

[68] Henrik Bruus and Karsten Flensberg. *Many-body quantum theory in condensed matter physics: an introduction*. OUP Oxford, 2004.

[69] Ken Andersen, D. Marero, and Michael Barlow. “The OSIRIS diffractometer and polarisation-analysis backscattering spectrometer”. In: *Applied Physics A: Materials Science and Processing* 74 (Dec. 2002), s237–s239.

[70] Mark. T. F. Telling and Ken. H. Andersen. “Spectroscopic characteristics of the OSIRIS near-backscattering crystal analyser spectrometer on the ISIS pulsed neutron source”. In: *Phys. Chem. Chem. Phys.* 7 (6 2005), pp. 1255–1261.

[71] Stefan Paul Gosuly. “Neutron Scattering Studies of Low-Dimensional Quantum Spin Systems”. English. PhD thesis. 2016.

[72] F. Demmel and K. Pokhilchuk. “The resolution of the tof-backscattering spectrometer OSIRIS: Monte Carlo simulations and analytical calculations”. In: *Nuclear Instruments and Methods in Physics Research Section A: Accelerators, Spectrometers, Detectors and Associated Equipment* 767 (2014), pp. 426–432. ISSN: 0168-9002.

[73] Peter Kjær Willendrup and Kim Lefmann. “McStas (ii): An overview of components, their use, and advice for user contributions”. In: *Journal of Neutron Research* Preprint (2020), pp. 1–21.

[74] Franz Demmel. *Private Communication*. May 2021.

[75] Paul Glasserman. *Monte Carlo methods in financial engineering*. Vol. 53. Springer, 2004.

[76] Mykel J Kochenderfer and Tim A Wheeler. *Algorithms for optimization*. Mit Press, 2019.

[77] Diptiman Sen and R. Chitra. “Large-U limit of a Hubbard model in a magnetic field: Chiral spin interactions and paramagnetism”. In: *Phys. Rev. B* 51 (3 Jan. 1995), pp. 1922–1925.

[78] Jung Hoon Han, Jin-Hong Park, and Patrick A. Lee. “Consideration of thermal Hall effect in undoped cuprates”. In: *Phys. Rev. B* 99 (20 May 2019), p. 205157.

[79] Rhine Samajdar et al. “Enhanced thermal Hall effect in the square-lattice Néel state”. In: *Nature Physics* 15.12 (2019), pp. 1290–1294.

[80] Huimei Liu and Giniyat Khaliullin. “Pseudospin exchange interactions in d^7 cobalt compounds: Possible realization of the Kitaev model”. In: *Phys. Rev. B* 97 (1 Jan. 2018), p. 014407.

[81] Ryoya Sano, Yasuyuki Kato, and Yukitoshi Motome. “Kitaev-Heisenberg Hamiltonian for high-spin d^7 Mott insulators”. In: *Phys. Rev. B* 97 (1 Jan. 2018), p. 014408.

[82] Sae Hwan Chun et al. “Direct Evidence for Dominant Bond-directional Interactions in a Honeycomb Lattice Iridate Na_2IrO_3”. In: (Apr. 2015).

[83] Stephen M Winter et al. “Models and materials for generalized Kitaev magnetism”. In: *Journal of Physics: Condensed Matter* 29.49 (2017), p. 493002.

[84] L Viciu et al. “Structure and basic magnetic properties of the honeycomb lattice compounds $Na_2Co_2TeO_6$ and $Na_3Co_2SbO_6$”. In: *Journal of Solid State Chemistry* 180.3 (2007), pp. 1060–1067.

[85] A. K. Bera et al. “Zigzag antiferromagnetic ground state with anisotropic correlation lengths in the quasi-two-dimensional honeycomb lattice compound $Na_2Co_2TeO_6$”. In: *Phys. Rev. B* 95 (9 Mar. 2017), p. 094424.

[86] E. Lefran çois et al. “Magnetic properties of the honeycomb oxide $Na_2Co_2TeO_6$”. In: *Phys. Rev. B* 94 (21 Dec. 2016), p. 214416.

[87] K. A. Ross et al. “Single-ion properties of the $S_{\text{eff}} = \frac{1}{2}$ XY antiferromagnetic pyrochlores NaA'Co$_2$F$_7$ ($A' =$ Ca^{2+}, Sr^{2+})”. In: *Phys. Rev. B* 95 (14 Apr. 2017), p. 144414.

[88] L. Viciu et al. “Structure and basic magnetic properties of the honeycomb lattice compounds $Na_2Co_2TeO_6$ and $Na_3Co_2SbO_6$”. In: *Journal of Solid State Chemistry* 180.3 (2007), pp. 1060–1067.

[89] O. Arnold et al. “Mantid—Data analysis and visualization package for neutron scattering and μSR experiments”. In: *Nuclear Instruments and Methods in Physics Research Section A: Accelerators, Spectrometers, Detectors and Associated Equipment* 764 (2014), pp. 156–166.

[90] *Mantid (2013): Manipulation and Analysis Toolkit for Instrument Data*. Mantid Project, 2013.

[91] Bo Yuan et al. “Spin-orbit exciton in a honeycomb lattice magnet $CoTiO_3$: Revealing a link between magnetism in d- and f-electron systems”. In: *Phys. Rev. B* 102 (13 Oct. 2020), p. 134404.

[92] Duc Le. *Private Communication*. May 2019.

[93] Robert M White, Robert M White, and Bradford Bayne. *Quantum theory of magnetism*. Vol. 1. Springer, 1983.

[94] Guiling Xiao et al. “Crystal growth and the magnetic properties of $Na_2Co_2TeO_6$ with quasi-two-dimensional honeycomb lattice”. In: *Crystal Growth & Design* 19.5 (2019), pp. 2658–2662.

[95] Weiliang Yao and Yuan Li. “Ferrimagnetism and anisotropic phase tunability by magnetic fields in $Na_2Co_2TeO_6$”. In: *Phys. Rev. B* 101 (8 Feb. 2020), p. 085120.

[96] Fouet, J. B., Sindzingre, P., and Lhuillier, C. “An investigation of the quantum J1-J2-J3 model on the honeycomb lattice”. In: *Eur. Phys. J. B* 20.2 (2001), pp. 241–254.

[97] M Songvilay et al. “Kitaev interactions in the Co honeycomb antiferromagnets $Na_3Co_2SbO_6$ and $Na_2Co_2TeO_6$”. In: *Physical Review B* 102.22 (2020), p. 224429.

[98] Ji ří Chaloupka, George Jackeli, and Giniyat Khaliullin. “Zigzag Magnetic Order in the Iridium Oxide Na_2IrO_3”. In: *Phys. Rev. Lett.* 110 (9 Feb. 2013), p. 097204.

[99] Chaebin Kim et al. “Antiferromagnetic Kitaev interaction in $J_{\text{eff}} = 1/2$ cobalt honeycomb materials $Na_3Co_2SbO_6$ and $Na_2Co_2TeO_6$”. In: *arXiv preprint arXiv:2012.06167* (2020).

[100] Anjana M. Samarakoon et al. “Static and dynamic magnetic properties of honeycomb lattice antiferromagnets Na$_2M_2$TeO$_6$, M = Co and Ni”. In: *arXiv e-prints* (May 2021). eprint: 2105.06549.

[101] Gaoting Lin et al. “Field-induced quantum spin disordered state in spin-1/2 honeycomb magnet $Na_2Co_2TeO_6$ with small Kitaev interaction”. In: *arXiv preprint arXiv:2012.00940* (2020).

[102] Wenjie Chen et al. “Spin-orbit phase behavior of $Na_2Co_2TeO_6$ at low temperatures”. In: *arXiv: Strongly Correlated Electrons* (2020).

[103] Laura Voigt. “Radical architectures in two dimensions”. English. PhD thesis. 2020.

[104] Kasper S Pedersen et al. “Formation of the layered conductive magnet $CrCl_2(pyrazine)_2$ through redox-active coordination chemistry”. In: *Nature chemistry* 10.10 (2018), pp. 1056–1061.

[105] Gonzalo Givaja et al. “Electrical conductive coordination polymers”. In: *Chemical Society Reviews* 41.1 (2012), pp. 115–147.

[106] Lei Sun, Michael G Campbell, and Mircea Dincă. “Electrically conductive porous metal–organic frameworks”. In: *Angewandte Chemie International Edition* 55.11 (2016), pp. 3566–3579.

[107] Markus Hoelzel, Anatoliy Senyshyn, and O. Dolotko. “SPODI: High resolution powder diffractometer”. In: *Journal of large-scale research facilities JLSRF* 1 (Aug. 2015).

[108] Jonatan Olsen and Martin Schjeldrup Jessen. *Characterization of the magnetic properties of $CrX_2(pyz)_2$, X = {Cl,Br,I}*. Bachelor thesis, Technical Univeristy of Denmark, 2018.

[109] Stephen Blundell. *Magnetism in condensed matter*. 2003.

[110] J. Lado and J. FernÃ¡ndez-Rossier. “On the origin of magnetic anisotropy in two dimensional CrI_3”. In: *2D Materials* 4 (Apr. 2017).

[111] Koichi Momma and Fujio Izumi. “*VESTA3* for three-dimensional visualization of crystal, volumetric and morphology data”. In: *Journal of Applied Crystallography* 44.6 (Dec. 2011), pp. 1272–1276.

[112] Andrey Protchenko et al. “Stable GaX_2, InX_2 and TlX_2 radicals”. In: *Nature chemistry* 6 (Apr. 2014), pp. 315–9.

[113] Marc Bocquet et al. “Finite-temperature dynamical magnetic susceptibility of quasi-one-dimensional frustrated spin-$\frac{1}{2}$ Heisenberg antiferromagnets”. In: *Phys. Rev. B* 64 (9 Aug. 2001), p. 094425.

[114] D. Johnston et al. “Thermodynamics of Spin $S = 1/2$ Antiferromagnetic Uniform and Alternating-Exchange Heisenberg Chains”. In: *Physical Review B* 61 (Apr. 2000).

[115] Oliver Breunig et al. “Quantum criticality in the spin-$1/2$ Heisenberg chain system copper pyrazine dinitrate”. In: *Science Advances* 3 (Sept. 2017).

[116] J. Stewart et al. “Disordered materials studied using neutron polarization analysis on the multi-detector spectrometer, D7”. In: *Journal of Applied Crystallography - J APPL CRYST* 42 (Feb. 2009), pp. 69–84.

[117] Juan Rodriguez-Carvajal. “Recent developments of the program FULLPROF, commission on powder diffraction”. In: *IUCr Newsl.* 26 (Jan. 2001).

[118] Joe Paddison. “Absolute Data Normalisation Using FullProf”. In: (Mar. 2016).

[119] *Magnetic Form Factors*. https://www.ill.eu/sites/ccsl/ffacts/.

[120] Wentao Hu et al. “2D hybrid $CrCl_2(N_2C_4H_4)_2$ with tunable ferromagnetic half-metallicity”. In: *Journal of Materials Chemistry C* 9 (Jan. 2021).

[121] Huanhuan Xie et al. “Two-dimensional $CrCl_2(pyrazine)_2$ monolayer: High-temperature ferromagnetism and half-metallicity”. In: *Journal of Physics: Condensed Matter* 32 (Nov. 2019).

[122] Adam A Aczel et al. “Quantum oscillations of nitrogen atoms in uranium nitride”. In: *Nature communications* 3.1 (2012), pp. 1–7.

[123] K. Tomiyasu et al. “Conversion method of powder inelastic scattering data for one-dimensional systems”. In: *Applied Physics Letters* 94 (Mar. 2009).

[124] Jonathan Leiner et al. “Magnetic Excitations of the Cu^{2+} Quantum Spin Chain in Sr$_3$CuPtO$_6$”. In: *Physical Review B* 97 (Sept. 2017).

[125] Piers Coleman. “Heavy fermions and the Kondo lattice: a 21st century perspective”. In: *arXiv preprint arXiv:1509.05769* (2015).

[126] Natalia B Perkins et al. “Underscreened Kondo lattice model applied to heavy fermion uranium compounds”. In: *Physical Review B* 76.12 (2007), p. 125101.

Technical
University of
Denmark

Fysikvej, building 311
2800 Kgs. Lyngby
Tlf. 4525 1700

https://www.fysik.dtu.dk